

THE UNIVERSITY OF HULL

**DEVELOPMENT AND APPLICATION OF A
COMPUTATIONAL MODEL FOR SCOUR
AROUND OFFSHORE WIND TURBINE
FOUNDATIONS**

Being a Thesis submitted for the Degree of

Doctor of Philosophy

to the University of Hull

by

Carl Collins, MEng

November 2017

Contents

CONTENTS	II
LIST OF FIGURES	I
ACKNOWLEDGMENTS.....	V
ABSTRACT	VI
NOMENCLATURE	VII
CHAPTER 1 INTRODUCTION.....	1
1.1 MOTIVATION	5
1.2 OBJECTIVES.....	6
1.3 THESIS OUTLINE.....	6
CHAPTER 2 THE PHENOMENA OF SCOUR	8
2.1 OFFSHORE FLOW CONDITIONS	8
2.2 EROSION.....	13
2.3 SCOUR.....	27
CHAPTER 3 GRAVITY BASE FOUNDATION EXPERIMENT	56
3.1 FACILITY	56
3.2 SETUP.....	57
3.3 PROCEDURE.....	58
3.4 RESULTS.....	60
CHAPTER 4 COMPUTATIONAL FLUID DYNAMICS.....	74
4.1 TURBULENCE MODELS	75
4.2 DISCRETIZATION	77
4.3 WALL TREATMENT.....	79
4.4 TEMPORAL RESOLUTION	80
4.5 MORPHING METHODOLOGY	81
4.6 MULTIPHASE FLOW	82
4.7 SUMMARY	85
CHAPTER 5 SCOUR MODEL LITERATURE REVIEW.....	88
5.1 MORPHOLOGICAL MODELS	88
CHAPTER 6 HYDRODYNAMICS OF FOUNDATION STRUCTURES	94
6.1 MONOPILE INVESTIGATION	94
6.2 ALTERNATE PILE SHAPE INVESTIGATION	104
CHAPTER 7 SCOUR MODEL DEVELOPMENT	130
7.1 SCOUR MODEL COMPOSITION	130
7.2 SINGLE PHASE MODEL	139
7.3 TWO PHASE MODEL	159

CHAPTER 8 MORPHOLOGICAL INVESTIGATION.....	168
8.1 SUCTION CAISSONS	168
CHAPTER 9 CONCLUSION	174
9.1 FUTURE WORK.....	177
REFERENCES.....	178

LIST OF FIGURES

Figure 1-1 – Cumulative Installation of EU Wind Power (EWEA, 2016)	1
Figure 2-1 – Live-bed Equilibrium Scour Depth around a Pile (Sumer and Fredsøe, 2001).....	9
Figure 2-2 - Fully Developed Velocity Profile in Smooth Flow (Liu, 2001)	10
Figure 2-3 – Shields Diagram (U.S. Army Corps of Engineers, 1994)	13
Figure 2-4 - Varying Angle of Repose (Graf and Yulistiyanto, 1998)	16
Figure 2-5 - Sediment Transport Modes	17
Figure 2-6 - Rouse Formula Concentration Profiles	18
Figure 2-7 – Critical Shields Parameter Diagrams (Dey, 1999)	21
Figure 2-8 - Lee-Wake Vortex Shedding Sequence	30
Figure 2-9 - Strouhal Number vs. Reynolds Number (Sumer and Fredsøe 2006).....	31
Figure 2-10 - Cylinder Separation Angle vs. Reynolds Number (Achenbach, 1968)	32
Figure 2-11 - Boundary Layer Separation	33
Figure 2-12 - Mounted Cylinder Flow Mechanisms	33
Figure 2-13 - Horseshoe Vortex Modes (Huang et al., 2014).....	34
Figure 2-14 - Equilibrium Scour Depth	36
Figure 2-15 - Clear-Water Scour Development	37
Figure 2-16 - Cylinder-Scour Development Stages	38
Figure 2-17 – Developing Horseshoe Vortex Strength for Two Cases	39
Figure 2-18 – Excess Shear effect upon Time and Depth (Kang and Yeo, 2012)	41
Figure 2-19 – Blockage Ratio effect on Bed forms	42
Figure 2-20 – Live-bed and Clear-water scour development.....	42
Figure 2-21 – Experimental Live-bed and Clear-Water scour development	43
Figure 2-22- Transitioning Live-Bed Bed Form Height (Chiew, 1984).....	44
Figure 2-23 - Transitioning Live-Bed Scour Depth (Chiew, 1984).....	44
Figure 2-24 – Fluctuations in developing scour depth (Link and Zanke, 2004)	45
Figure 2-25 – Geometry Implications Upon Shear Stress (Sumer and Fredsøe, 2002)	47
Figure 2-26 – Collar Protection against Horseshoe Vortices and Flow Acceleration	48
Figure 2-27 – Gravity Base Examples	49
Figure 2-28 – Experimental scour depth around different foundations (Larsen and Frigaard, 2005)	50
Figure 2-29 – Suction Caisson Diagram	51
Figure 2-30 – Caisson Parameter Effect on Scour depth. Data: (Melville, 2008)	51
Figure 2-31 – Tripod Foundation (Subsea World News, 2014).....	52
Figure 2-32 – Tri-pile Foundation (Brickwell, 2012)	52
Figure 3-1- TES Facility, Hull.	56
Figure 3-2 – Flume Setup	57

Figure 3-3 – Gravity Base Foundation Model	58
Figure 3-4 – Measurement Positions	59
Figure 3-5 – Velocity Profiles showing under-developed upstream flow	60
Figure 3-6 – Velocity (V_x) Reduction due to Obstruction, 1m Upstream.....	61
Figure 3-7 – Velocity Profiles along the Centreline	61
Figure 3-8 – Vertical Velocities surrounding Gravity Base Foundation	62
Figure 3-9 – Experimental Velocity Profile Development	63
Figure 3-10 – RMS Local Velocity Magnitude Fluctuations (X-Y Plane).....	64
Figure 3-11 – RMS Local Velocity Magnitude Fluctuations (X-Z Plane)	64
Figure 3-12 – FFT Analysis of Velocity (X-Dir) at x, y, z/h of 0.18 m, 0.3 m, 0.114.....	65
Figure 3-13 – Scour after 2 hrs	66
Figure 3-14 – Scour after 3 hrs 10 min	67
Figure 3-15 – Scour after 7 hrs	68
Figure 3-16 – Bed Formations	69
Figure 3-17 – Local Bed form changes.....	69
Figure 3-18 – Scour Depth Contours (Top View)	70
Figure 3-19 – Final Scour Depth along Centreline	71
Figure 3-20 – Downstream Pitting.....	72
Figure 6-1 – Geometry Setup.....	96
Figure 6-2 – Mesh Refinement	96
Figure 6-3 – Turbulence Model Comparison, Q Criterion	98
Figure 6-4 – Turbulence Model Comparison, Reversed Flow.....	99
Figure 6-5 – Turbulence Model Comparison, Surrounding Max. Wall Shear.....	100
Figure 6-6 – Turbulence Model Comparison, Wall Shear Stress	101
Figure 6-7 – Strake Parameterisation.....	105
Figure 6-8 – Strake Testing Domain.....	106
Figure 6-9 – Strake Testing Mesh – Base Design.....	107
Figure 6-10 – Strake Pitch Impact	108
Figure 6-11 – Number of Strakes Impact.....	108
Figure 6-12 – Velocity Magnitude Contour Plots, 10m and 45m pitch.....	109
Figure 6-13 – Strake Radius Impact	110
Figure 6-14 – Strake Geometry Converging and Diverging Sides	110
Figure 6-15 – Impact of Strake Thickness	111
Figure 6-16 – End Plate Width Impact.	111
Figure 6-17 - Strakes – Larger End Plate Flow Attachment	112
Figure 6-18 - End Plate Width Effect on Wall Shear Stress	112
Figure 6-19 – Strake Height Impact.....	112
Figure 6-22 – Strake Geometry Conical Effect.....	113

Figure 6-21 – Strake Angle Impact.....	113
Figure 6-20 – Strake Rotation Angle	114
Figure 6-23 – Changing Strake AOA	114
Figure 6-24 – Optimal Strake Geometry.....	115
Figure 6-25 – Optimal Strake Geometry Shear Stress Comparison	115
Figure 6-26 – Suction Caisson Testing Domain	118
Figure 6-27 – Suction Bucket Base Designs.....	118
Figure 6-28 – Single Rib Geometry	120
Figure 6-30 – Single Rib – Hole Size Averaged Value	121
Figure 6-30 – Single Rib – Plate Width Averaged Values	121
Figure 6-31 – Single Rib Hole Size Effect	122
Figure 6-32 – Single Rib – Hole Size Effect on Accelerated Flow and Blockage	124
Figure 6-33 – Single Rib - Hole Size Effect on Accelerated Flow and Blockage	125
Figure 6-34 – Impact of Multiple Ribs	127
Figure 6-35 – Low Blockage Factor Design	127
Figure 6-36 – Average values across all Multi-rib structures	128
Figure 7-1 – Angle of Repose Model Characteristics.....	132
Figure 7-2 – Simplified Flow diagram of the single and two-phase model.....	134
Figure 7-3 – Meshing procedure for complex structures	136
Figure 7-4 – Face Validity Example	137
Figure 7-5 – Cell Skewness Diagram	138
Figure 7-6 – Converged and Course Mesh	140
Figure 7-7 – Monitored values when testing the required upstream domain size.....	141
Figure 7-8 –Case 1 Boundary Conditions.....	142
Figure 7-9 – Case 1 Empirical Formula Testing Results	143
Figure 7-10 – Case 1 Lowest Point Development Mesh Comparison	144
Figure 7-11 – Case 1 Scour Gradient Comparison	144
Figure 7-12 - Case 1 Developing Radial Topology	145
Figure 7-13 – Case 2 Fluid Domain.....	147
Figure 7-14 – Case 2 Scour Development Results	148
Figure 7-15 – Case 3 Hourly Scour	150
Figure 7-16 – Case 3 Scour Development	151
Figure 7-17 – Case 3 Normalised Topology Along Symmetry Plane	151
Figure 7-18 – Normalised Scour Topology	152
Figure 7-19 – Suction Caisson Position Extremes.....	154
Figure 7-20 – Pile-Cap Elevation Scour Development.....	155
Figure 7-21 - Pile-Cap Elevation Final Topology.....	155
Figure 7-22 – Excess Shear Stress effect on Suction Caisson Scour Depth	156

Figure 7-23 – Deviating Scour Topology with Pile-Cap Depth	157
Figure 7-24 – Simulation Setup	159
Figure 7-25 – Straight Uniform Channel Domain	160
Figure 7-26 – Sectional Concentration Results.....	160
Figure 7-27 – Continuous Concentration Results	161
Figure 7-28 – Trench Setup	163
Figure 7-29 – Trench Simulation Domain	163
Figure 7-30 – Concentration Profiles along a Trench.....	165
Figure 7-31 – Two-Phase Morphological Results	166
Figure 8-1 – Continued mesh resolution as scour progresses	168
Figure 8-2 – Suction Bucket Scouring – Maximum Depth.....	170
Figure 8-3 - Suction Bucket Scouring – Scour Volume	170
Figure 8-4 – Final Scour Contours.....	172

ACKNOWLEDGMENTS

My PhD has been an unforgettable challenge and experience, which has been aided by many people along the way for which I am truly grateful, with specific thanks to the following;

Prof. Philip A. Rubini, for his constant availability and dependable guidance, support and patience, over the many years as my supervisor.

Dr. Stuart McLelland, Brendan Murphy and Brian Houston for the collaborative experimental work capturing the scour around a gravity base foundation; as detailed in Chapter 3.

The University of Hull, for the opportunity, scholarship and support enabling me to complete my PhD.

My existing and past colleagues, especially Brian, Esther, Jianguo, Imran and Qin whom provided friendship, feedback and importantly regular entertainment.

To my friends outside of University, who have remained supportive and positive, and provided essential distractions from my PhD.

Lastly, a big heartfelt thanks to all my family, who have as always, provided constant and invaluable support, motivation and positivity.

ABSTRACT

There is a constant requirement to understand scour especially regarding its prevention, due to the potential impact and disastrous consequences. The installation of offshore wind turbines is haunted by scour mitigation and at the start of the offshore wind turbine boom in the early 2000's this was achieved using overzealous amounts of rock armour. However, as investment and cost efficiency has increased, protection methods have been refined, but, there remains significant room for improvement.

Research into offshore sediment dynamics has benefited greatly by computational advancements providing a greater understanding of processes and the driving mechanisms; leading to protection method improvements and reductions in environmental impact. The premise of this study is to push this knowledge further, by developing and validating a novel scour model within CFD software that can be used to simulate and analyse offshore scour; specifically, the scour around complex, new offshore wind turbine foundation geometries.

NOMENCLATURE

<i>Symbol</i>	<i>Description</i>
d_*	Dimensionless grain diameter
d_{50}	Grain size - 50 th percentile
c	Concentration
c_a	Reference concentration at 'a'
S	Scour depth
k_s	Nikuradse roughness height
γ	Porosity
q_{bc}	Volume Flux of Bedload Transport due to current
u	Velocity
u_∞	Free-stream Velocity
u_*	Shear Velocity
u_c	Critical Velocity
u_{cw}	Velocity due to current and waves
w_s	Settling Velocity
θ_{cr}	Critical Shields Parameter
τ_{cr}	Critical Shear Stress
$\tau_{cr, \neq}$	Critical shear stress on a slope
A	Area
D	Diameter
Fr	Froude Number
L	Length Scale
Re_p	Particle Reynolds Number
Re	Reynolds Number
St	Strouhal Number
d	Grain size
f	Frequency
g	Gravity
s	Specific Gravity
t	Time
y	Water Depth
KC	Keulegan–Carpenter number
z	Distance from Wall/Bed
α	Angle between velocity vector and β vector
β	Steepest angle from horizontal
δ	Boundary Layer Thickness
μ	Dynamic Viscosity
ρ	Fluid Density
ρ_s	Sediment Density
ν	Viscosity
ϕ	Angle of repose
σ_s	Standard Deviation of Sediment Diameter Range

Chapter 1 Introduction

The past two decades have borne witness to an exponential increase in cleaner and renewable energy sources due to the global concern of limited fossil fuels and the environmental impact of today's main energy production methods. However, current renewable energy methods are dominated by mainstream, problematic energy production methods and more work is required to drive renewable sources through increased energy efficiency, cost efficiency and investment.

A 2009 European Environmental Agency Technical Report (EAA, 2009) showed a tremendous growth potential for onshore and offshore wind power. In 2007, the European Union outlined a roadmap to increase the amount of energy generated by renewable sources to 20% by the year 2020. This initially equated to 180 GW with a 12% contribution from wind energy but was increased in 2011 to 230 GW (EWEA, 2011).

To provide an update of the progression towards these aims, 12.8 GW of wind power was installed in 2015 making it the third annual increase, Figure 1-1, totalling 142 GW with 8.4% located offshore (EWEA, 2016). This was supported by €26.4 billion of investment from the EU which has increased year upon year since 2012; however, despite this the 2020 outlook varies significantly depending on the source.

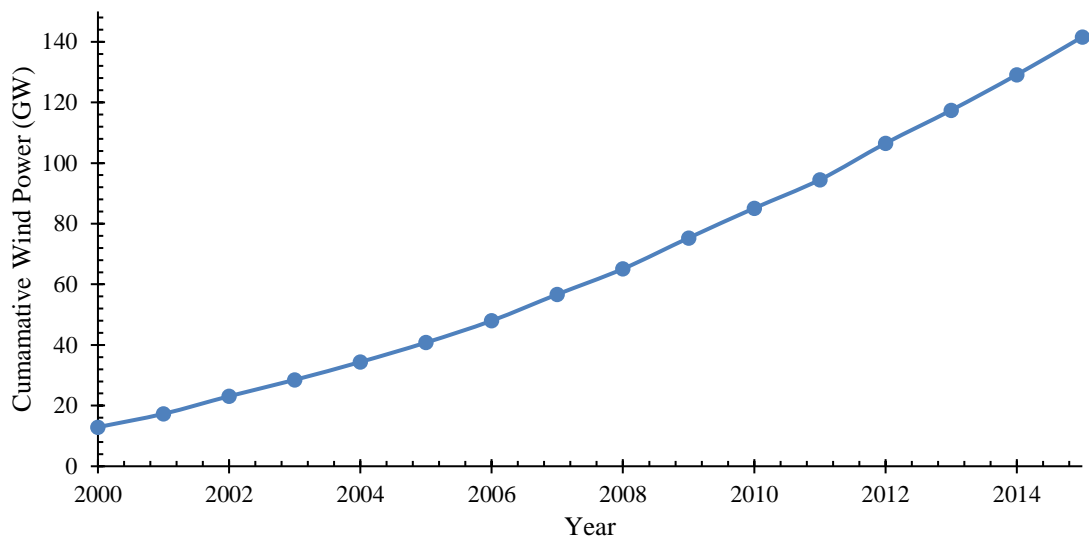


Figure 1-1 – Cumulative Installation of EU Wind Power (EWEA, 2016)

A European Wind Energy Association Report (EWEA, 2014) states, “given the increase of 9.3 GW in 2010 and that wind energy is the most competitive of the renewable energy technologies in most Member States, 180 GW of wind power in the EU is likely to be achieved well before 2020”. However, contrary to this a European Commission progress report that includes a 2020 forecast shows that targets will not be met; especially in onshore and offshore wind sectors due to reduced national efforts and poor infrastructure (European Commission,

2013). The European Commission supports this claim in 2015 with data from additional years projecting 2020 targets to be missed by 8.7% in onshore wind and a staggering 80.3% in offshore wind, (European Commission, 2015).

The 2020 forecast is threatened by economic, social and environmental factors. The economic issues are significant (EAA, 2009) and can be alleviated by improving the investment potential of wind energy. This can be achieved by improving the efficiency and reducing the costs that have been continuous over the last decade, however; it is imperative this continues in order to improve the 2020 outlook.

Energy efficiency improvements include technological advancements, as demonstrated by General Electric in 2014 by increasing the total output of a turbine by 15% by improving turbine components and advancements in system control (GE Power and Water, 2013). Also, increasing the size of the turbine can improve efficiency as it enables the use of the higher and faster winds and more energy is obtainable from a single machine. The average turbine size has continually increased over the past 15 years (EWEA, 2014) and the onshore turbine size has now stabilized, leaving the offshore market to drive this size trend (EWEA, 2004). The most powerful wind turbines at the end of 2015 were the 10MW Seatitan and ST Sway Turbine.

As the number of offshore wind turbines has increased so has the environmental diversity and the variety of foundation types. Existing types vary considerably from shallow water gravity base designs to the latest deep-water floating foundations (EWEA, 2013) that enable the use of deeper less restricted waters (EAA, 2009).

EU statistics for offshore wind turbines show that the monopile foundation design remains the most common at 76%, but alternate designs are becoming more popular as they enable the of diverse environments and can improve efficiency. These alternative foundations consist of gravity base foundations at 12%, and a combined 12% of jacket, tripod, and tri-pile foundations (EWEA, 2014).

Diversification from the widely used and researched monopile to increasing popular, alternate foundation types invokes the reassessment of many factors, due to both structural changes affecting installation, stability and maintenance, in addition to environmental changes due to the use of new locations. Furthermore, geometric differences between these alternate foundation types compared to the typical monopile raises questions about the change in flow around these structures, which changes the bed shear stresses and therefore scour.

Scour is the specific term for the localised erosion of sediment around a structure such as a bridge pier, pipe or offshore wind turbine foundation. It is the result of high shear stresses produced by increased velocities and turbulence, which enable sediment grains on the seabed to be dislodged

and removed. The scouring underneath and around structures can cause structural instability or even failure and is therefore of serious concern.

There is far more that can be learned about alternate foundation structures (gravity base, tripod, tri-pile and jacket structures) compared to monopiles, as there is comparatively little research on the surrounding flow or scour. Furthermore, due to their increased complexity, there is speculatively far more understanding and knowledge to uncover, in comparison to the basic monopile.

Existing research on scouring around alternate designs includes a sparse number of journal papers, ranging to research on relatable geometries which include the basic monopile; which can be used to understand the flow around more complex structures if features are similar.

Research on gravity bases, similar to suction buckets, includes design comparisons provided by (Larsen and Frigaard, 2005), whom study the scour around three very different designs which enables the top-level differences in scour to be understood. A comprehensive study is also provided by Melville (2008) which includes the scouring results given a range of suction bucket geometry changes. This research is extremely useful when analysing the effect of current suction bucket and gravity base geometries, which are typically more complex due to the inclusion of structural supports, extra lips (essentially small collars) and intermediate cylindrical sections. However, this is where relatable research is extremely useful, as the effect of these individual features can aid the understanding of the overall structure. This includes research on topics such as conical structures and monopiles with collars; for which a large amount of research exists as discussed in Chapter 2. However, few studies have analysed the differences of detailed suction bucket geometry on the transient flow dynamics and scour.

This trend of few specific studies alongside many potentially supportive studies is also true for tripods and tri-piles, however supportive studies have a more direction relationship due to the geometric similarities. For example, Stahlmann (2012, 2013) presents two rare analyses on the scour around tripod based offshore wind turbine foundations, which can be simplified or supported by research on grouped monopile foundations (Li et al., 2016).

There is a huge gap in knowledge on the detailed analysis around these alternate structures that has the potential to provide knowledge that can alter the potential scour, the magnitude of scour protection and the migration of sediment. Scour protection methods can be active or static, where active methods reduce shear stresses by altering the fluid dynamics using geometric changes or the use of devices such as strakes. Static methods involve devices or structures that protect the sediment bed against the high shear stresses such as rock armour, or rubber mats. There is limited research on the use of alternative protection methods (other than rock armour) around offshore wind turbines, especially active methods. This is however not the case for bridge piers, as alternate

methods for both active and static methods are common in both research and application, such as rubber mats, collars and sand-filled sacks (McGovern et al., 2012, Huisman et al., 2009, Peters and Werth, 2012).

The main flow mechanisms which drive the scour process are the horse-shoe vortex, flow acceleration and vortex shedding; all of which increase the shear stress and therefore bed erosion rates. As scour develops, these fluid dynamic mechanisms evolve along with the shear stress induced by each mechanism, upon the sediment bed. These evolving shear stresses are key to the scouring process and are dependent on the geometry of the structure.

Offshore wind turbines are typically protected from scour using rock armour, which consists of hundreds of tonnes of rock placed on the seabed around the turbine. This method has remained unchanged despite continued development in other areas such as foundation design, energy efficiency and turbine size. This therefore raises the question, is this historic and crude method the optimal solution, or are there better options?

Rock armour is used for other applications such as coastal erosion and bridge piers, however; alternate methods are also used in these instances, e.g. sand bags and concrete units such as tetrapod's, tribars and 'A-Jacks®' (Federal Highway Administration, 2009). Offshore wind turbines typically use one layer of large rock or several layers of smaller sized rock; ranging in diameter from 0.15 to 0.45m (Matutano et al., 2013). This equates to approximately 500-1500 tonnes of rock around a typical monopile foundation (Huisman et al., 2009).

The paths available to investigate the flow, scour and protection around these alternate structures, include numerical modelling, scaled experiments and in-situ monitoring. Firstly, in-situ monitoring records variables around a full-scale structure in its intended environment, offering the most realistic results, however repeatability is a problem. Furthermore, there is very little or no control of input variables, it is extremely expensive and monitoring the changes in flow and topology can be challenging due to both offshore conditions and available monitoring methods.

Scaled experiments hold a high level of accuracy and there is greater control over variables, but the validity is dependent on the scaled parameters. Many variables only require simple linear scaling; however, others are difficult to scale due to complex mechanisms such as waves. Scaling issues can also arise due to physical limitations, for example sediment grain size.

The final method, numerical modelling, has very different attributes to full-scale monitoring and scaled experiments. The validity and accuracy are highly dependent on the numerical models used, but, remain lower than physical methods due to the assumptions implied to reduce computational time and power costs. However, there is a far greater control over variables which alongside the ease of implementation makes this approach ideal for running a range of different scenarios. Furthermore, numerical simulations allow a more detailed and insightful analysis of

results at a high resolution and a wide range of variables are available. These are often difficult or impossible to obtain with physical modelling, especially without disturbing the flow.

If alternate designs and protection methods are to be tested experimental and numerical methods are best due to the control over variables and ease of monitoring. Design investigations typically require a number of design iterations and testing scenarios which are easier to implement using numerical modelling. However, due to the current accuracy of numerical modelling, experimental studies are still necessary to validate models and provide confidence in results. Computational scour models are generally suited to the scale of the application, ranging from several metres around a structure to kilometres along a coastline. This also commonly changes the method of computation, from erosion formulae combined with complex 3D fluid dynamics for small scale to 2D calculations for large scale; primarily due to the computational expense.

Simulation of the flow around offshore foundation structures requires relatively small-scale simulations as it is necessary to capture of complex fluid dynamics in order to compute the scour correctly. The fluid dynamic models and methods to achieve this are advancing quickly with improved accuracy, extended physics models and reduced computational cost. As a result, it would be beneficial to develop a scour model with a genericity that allows integration within many computational fluid dynamic codes, both commercial and open-sourced, exploiting their continued advancement and ease of implementing additional physical factors.

1.1 Motivation

The hydrodynamics and scour around the classic monopile is a well-researched topic, especially compared to the new and upcoming designs including the gravity base, tri-piles and jacket foundations. Furthermore, due to the increased geometric complexity, there is even more to learn about these structures compared to the classic monopile. This gap in research drives the first question, what more is there to learn about the flow and erosion around these alternate offshore wind turbine foundations? This question is extremely open, and therefore to tailor this research, the additional knowledge should be generated with the aim of exploring improvements in scour mitigation, through active methods, static methods or both.

To carry out this investigation, a numerical approach will be used due to the discussed advantages. Computational scour models are developed on common frameworks, but many have also been built stand-alone (as reviewed in Chapter 5). A fundamental part of scour modelling is the capture of the fluid dynamics and therefore it is logical to aid this foundation and support the extended use of such a model, by building it within a comprehensive commercial computational fluid dynamic software. There are two key advantages to this method, firstly, commercial CFD software is one of the first to demonstrate and include new technologies, algorithms and methods, allowing models to be ‘upgraded’ efficiently, therefore supporting future use. Secondly, the modules and features retained in commercial software mean that additional features, such as free-

surfaces, waves and phase interaction models have already been incorporated, and only a final setup and tuning are required before they can be included within a scour model.

1.2 Objectives

The motivation to explore the potential scour mitigation around new, alternate foundation geometries drives several key objectives. The first is to analyse the flow around these structures, as there is currently limited research on the resultant flow trends and features, which is paramount to understanding the resultant scour development. Obtaining an understanding of the scour around these structures is the second aim, specifically the developing topology, in relation to the attributable geometric features. This process can be extremely complex, due to the flow resulting from interaction with several geometric features, fluid dynamic phenomenon (e.g. the horseshoe vortex) given a non-uniform, transitioning velocity profile.

Once the developing flow and scour around these structures is understood, methods and techniques to reduce the scour can be deduced, marking the third aim.

The fourth aim, which is key to this project's success is to develop a computational scour model capable of predicting offshore scour, specifically around offshore wind turbine foundations. This will enable the scour analysis, understanding and proposed mitigation to be investigated. To ensure the model successfully enables the first three objectives, it will undergo regular validation during model composition and verification during model development. This is because, as it will become clear, scour models can range significantly and could therefore potentially undermine the work carried out, or at the other end of the scale, unnecessarily complicate and increase the necessary time and resource. The model will be implemented, developed and tested within the commercial fluid dynamic software package Star-CCM+ (Star-CCM+, 2014).

1.3 Thesis Outline

This thesis begins with the foundation knowledge required to understand and analyse the physical phenomena of scour. The chapter starts with offshore conditions concentrating heavily on velocity profiles and free-surface effects. This is followed by sediment erosion mechanisms leading onto scour, detailing the transient scour topology and prediction formulae for a range of offshore wind turbine foundation geometries.

Chapter 3 features a novel experiment capturing the scour around, and underneath a scaled gravity base foundation. This is performed in a large flume facility and enables 3D topological scans of the final geometry to be directly compared to simulation results aiding the verification process.

The computational aspect of this thesis begins in Chapter 4 where the computational fluid dynamic parts of the model are explored and assessed. This includes an analysis of potential turbulence models, multiphase models and discretization choices.

Existing scour models are reviewed in Chapter 5, with ranging model complexity, flexibility and application. The discussed sample models are analysed in conjunction with the modelling choices in Chapter 4. However, further work is necessary to conclude specific aspects, which is carried out in Chapter 6, prior to verification of the model in Chapter, 7.

Chapter 6 contains three sections that are prerequisites to the development chapter and final chapter. The first section investigates the fluid dynamics and resultant wall shear stress differences around a pile on a flat bed when using different turbulence models. The second and third sections investigate the geometric effects upon the wall shear stress around a monopile and suction caisson, using a sensitivity study and DOE (design of experiments) analysis. This allows a fewer number of scour simulations in the final investigative Chapter.

Chapter 7 forms a large section of this thesis and contains a comprehensive analysis of results using the developed single and two-phase models using several cases including a simulation that replicates the experiment in Chapter 3.

Chapter 8 utilises the validated model in Chapter 7 to simulate a focused set of scour simulations, selected using the results from the steady-state suction-caisson DOE results in Chapter 6.

Lastly, Chapter 9 summarises and concludes the thesis, followed by a brief discussion on the potential further use and development of the scour models.

Chapter 2 The Phenomena of Scour

The knowledge required to analyse and investigate the phenomena of scour stems from two main topics, fluid dynamics and sediment transport. The specific theory required from each of these topics is dependent on the scour scenario; however, the majority are present during the erosion around a simple monopile and as a result, this is used to describe and relate theory throughout this chapter. The sections are introduced in a progressive order; beginning with the typical upstream flow from a monopile and the resultant sediment transport mechanisms in an open expanse of water. This progresses onto a detailed account of the complex flow around a cylinder, including flow dependent mechanisms as the bed topology and scour develops. In addition, prediction formulae for the developing and resultant scour around a cylinder are provided. Lastly, the flow and scour around other shapes are examined in comparison to a surface mounted cylinder.

2.1 Offshore Flow Conditions

Offshore sea conditions can vary significantly due to the combination of current velocity, wave velocity and height, and the relative direction, all effecting the scour rate and equilibrium depth. Furthermore, the variation and frequency of these features are rarely constant, therefore adding a level of complexity to scour prediction. However, this is not the final layer of complexity, as natural phenomena such as tidal variations and storm conditions can affect the scour process (Stide, 1982) and are even more sporadic. These factors can therefore make scour prediction complex and challenging.

However, given the research objectives to develop a scour model and use it to investigate the hydrodynamics and scour around alternate structures, with the aim to reduce scour, it becomes feasible to mitigate these complexities, as explained in the following.

A large factor which supports a more simplistic approach is condition independence, as there are many active and static scour prevention methods that have a positive impact despite the flow conditions, even if the percentage difference may vary. For example, despite flow conditions, the correct use of a simple collar (de Sonneville et al., 2010) or increasing the size of the pile (Melville and Chiew, 1999) will always reduce the scour depth. However, either an extensive range of conditions must be tested or the resultant change in hydrodynamics must be understood before this can be concluded.

The second main reason is based around the impact of additional flow conditions, as they are not always present or sometimes have no impact on the scour. This includes the dampening effect deep water has on conditions at the free surface, due to waves or storm conditions. Furthermore, if the worse-case scenario is to be concentrated on waves can be dismissed as currents have a

significantly greater impact on equilibrium scour depth, regardless of the change in direction between current and waves as shown by Figure 2-1.

The previous two points defend the model’s simplifications based on worse-case scenario and condition-universal scour improvements, however, in support of the model’s genericity and use of the model to predict scour under very specific conditions, the model is still developed with flexibility and genericity in mind. Examples of this include the script of code written to re-mesh the bed surface, which can easily be changed to rotate the bed surface by 180°, in addition to implementation of a time-dependent velocity inlet to simulate tidal conditions. Furthermore, considering the simplifications made, the benefits of implementation within a commercial code mean that a free-surface, waves and air velocity can be added with relative ease, if imperative. Lastly, due to the numerical formulation of the model, it is possible to define areas of different sized sediment, for example to represent different sediment layers. However, it should be noted that even though these features can be added with relative ease, the resultant flow and scour under their use has not been tested in this study.

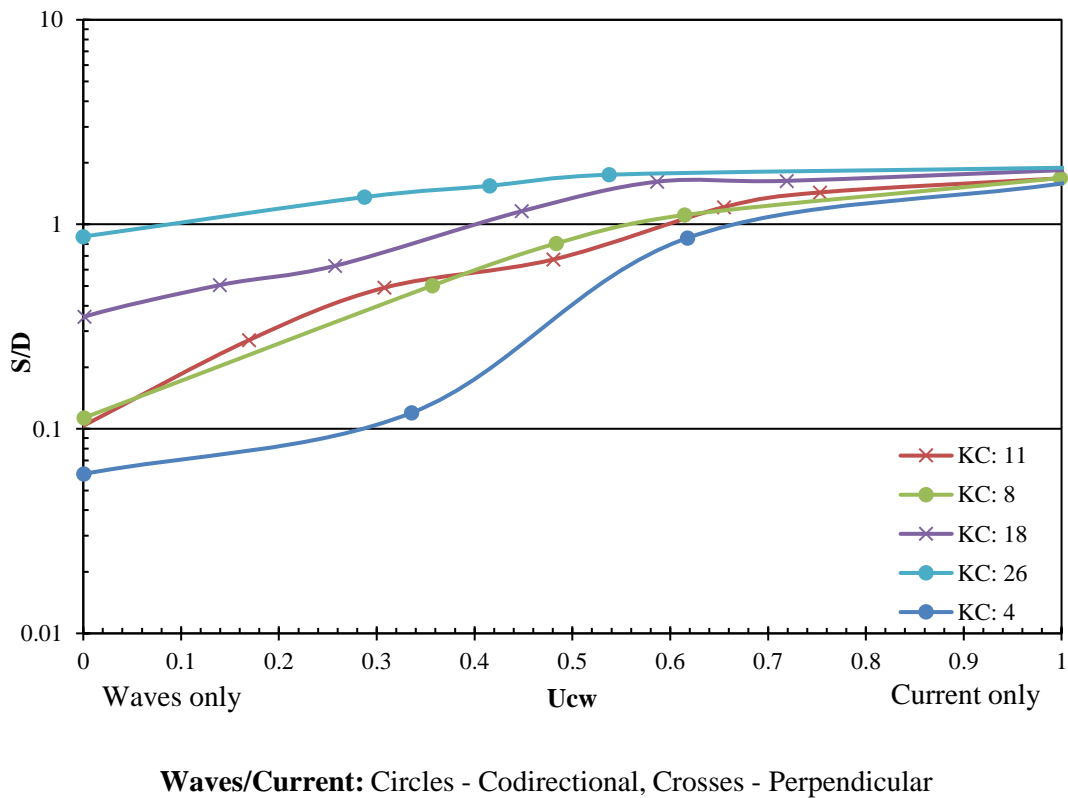


Figure 2-1 – Live-bed Equilibrium Scour Depth around a Pile (Sumer and Fredsøe, 2001)

Figure 2-1 compares the scour depth, S , normalised by the pile diameter, D , to the wave-current ratio, $U_{cW} = \frac{U_c}{U_c + U_m}$, whereby U_c is the undisturbed current velocity at a bed height of half the pile diameter and U_m is the undisturbed orbital velocity just above the wave boundary layer. The different series represent different Keulegan–Carpenter (KC) values, where by $KC = \frac{U_m T}{D}$. This

figure shows that for a unidirectional current and case-varying unidirectional waves, currents have a greater impact on the equilibrium scour depth.

The flow upstream of offshore structures is considered fully developed for the premise of this thesis as in open offshore waters there is nothing to disturb the flow and any transitions that may change the flow such as bed composition or water depth are gradual enough to neglect. The resultant fully developed velocity profile under a current-only condition is dependent on the sediment bed composition, mean flow velocity and water depth. These are discussed within because as it will become apparent, the velocity profile and boundary layer height have a significant impact on scour.

2.1.1 Velocity Profile

In a simplified scenario with a smooth bed surface, the water column comprises of four layers. The first is an extremely small viscous sub-layer, whereby turbulent fluctuations are present but dominated by viscous forces. The layer above this is the transition layer and constitutes the remainder of the boundary layer; acting as buffer layer between the viscous dominated sub-layer and the turbulent dominated outer layer, otherwise known as the wake region. This layer contains small turbulent eddies and more turbulent kinetic energy than the outer layer, Figure 2-2. In a more realistic scenario with a rough bed surface the viscous sub-layer is disrupted and deemed negligible, as the rough surface below protrudes through this layer (Graf and Altinakar, 1998) causing the turbulent buffer layer to dominate this region. The two types described are based on a deep-water assumption, whereby the depth is great enough for all three layers to exist. If the water is respectively shallow, then the turbulent outer layer will become very small and the effects caused by the free surface will become more prominent.

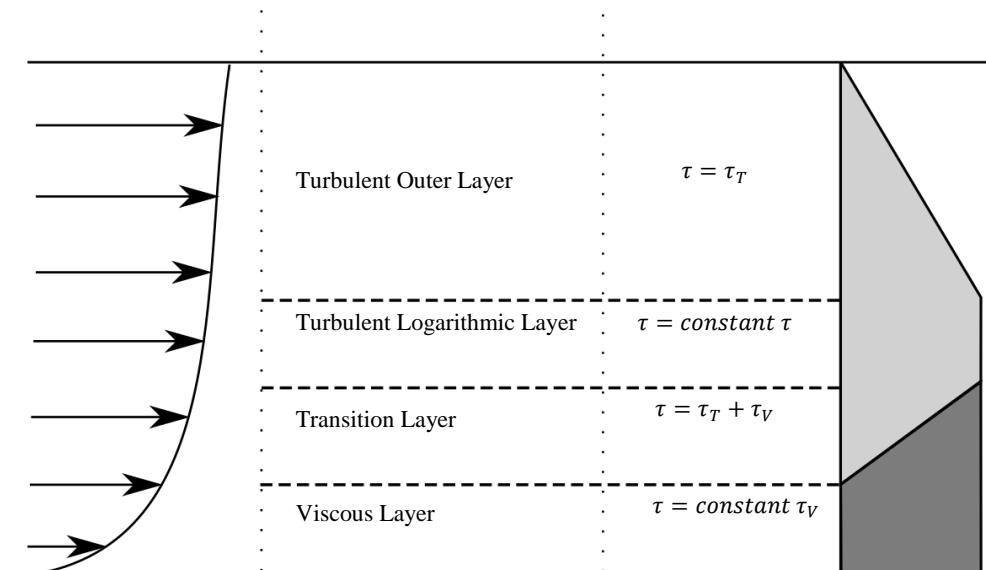


Figure 2-2 - Fully Developed Velocity Profile in Smooth Flow (Liu, 2001)

2.1.2 Free-Surface Effects

If the free surface and therefore difference in velocity between the air and water phase impinges on the turbulent layer it can impact the whole velocity profile, influencing the bed shear stress. For example, in shallow flume experiments there is often a stagnant air phase above, which due to the shear forces between the two phases causes a reduction in free-surface water velocity. This difference in velocity creates a boundary layer at the free surface, that when merged with the bed-boundary layer changes the velocity over the whole of the water column.

2.1.3 Roughness

The rough sediment bed and its apparent roughness directly impacts the velocity profile as the friction and resultant turbulence determine the viscous sub-layer, impacting the rest of the boundary layer. The roughness of a sediment bed is typically represented by an average, specifically, the Nikuradse roughness height, k_s . The roughness height directly impacts the viscous sub-layer, and therefore directly affects the shear stress, which in this study is used to compute the erosion rates. Camenen et al. (2006) assesses existing roughness height formulae and derives a new empirical equation based on a larger data set. A comparison of all the contained formulae to experimental data shows a poor correlation of less than 60% for all formulas, without any noticeable advantages of using specific formulae under limited scenario ranges.

The Nikuradse roughness height is up to 5 times the average grain diameter depending on the grain configuration and the bed forms present. A value of 2.5 is typically used for rough flow on a flat bed (Yalin, 1992), however, because the roughness height has a significant influence on the flow and is difficult to predict correctly many sediment transport models tune the roughness height to suit the results.

2.1.4 Velocity Profile Representation

The turbulent velocity profile produced by a single non-slip surface can be approximated using a logarithmic or power-law formula (Cui, 2011).

The Prandtl-Von Karman, logarithmic velocity formula, is perhaps the most famous. It was originally formulated for pipe flow and extended by Vanoni (1941) for open channel use, Equation 1 (Cui, 2011).

$$\frac{u}{u^*} = \frac{1}{k} \ln \frac{zu^*}{\nu} + B$$

Equation 1

(For turbulent smooth flow ($Re \leq 5$) $B = 5.5$ and turbulent rough flow ($Re \geq 70$) $B = 8.5$, (Dyer, 1986). Also, (Graf and Altinakar, 1998) provides a wider range and more specific constants including high and low levels of smooth and rough surfaced turbulent flows and transitional flows)

Application of the log-law extends beyond the simple calculation of velocity profiles in a channel as it is also used within computation fluid dynamics (Versteeg and Malalasekera, 1995). This is because the numerical resolution necessary to accurately calculate a boundary layer using the governing fluid dynamics equations is computationally expensive and alternatively the log-law can be used to predict the boundary layer with a low grid resolution. Furthermore, the formula can be used in the opposite direction, to estimate the roughness length and shear velocity in experiments using velocity data. This is achieved by using a line of best fit through a semi-log plot of $\ln(z)$ against velocity; whereby the intercept is equal to $\ln(z_0)$, z_0 is the roughness height, and the gradient is equal to κ/u_* .

The classic power-law profile formula was initially developed for pipe flow and extended to channels, (Schlichting, 1979). The power law is easier to apply and simpler than the log-law, but less accurate (Cui, 2011), Equation 2;

$$\frac{u}{u_{\max}} = \left(\frac{z}{y}\right)^{\frac{1}{m}}$$

Equation 2

Where z is the distance from the bed, u_{\max} is the maximum velocity at z_{\max} and m is the power law index which ranges from 4.5-8 depending on surface roughness and Reynolds number (Cheng, 2007).

The log and power law neglect the free surface and are therefore only applicable in deep waters, because as described the free surface can affect the velocity profile.

2.2 Erosion

2.2.1 Physics

Sediment Transport

This section provides an overview of the well-documented sediment transport process, beginning with individual sediment and bulk sediment-bed properties. The physics behind incipient motion, modes of sediment transport and the deposition of sediment are then discussed followed by prediction formulae.

Sediment Properties

Sediment characteristics have a significant impact on erosion rates, as shown with the sediment size in the Shields diagram, Figure 2-3. This figure shows that a reduction in sediment size or density initially reduces the force required for incipient motion. However, at extremely small sediment sizes the threshold increases due to sediment cohesion.

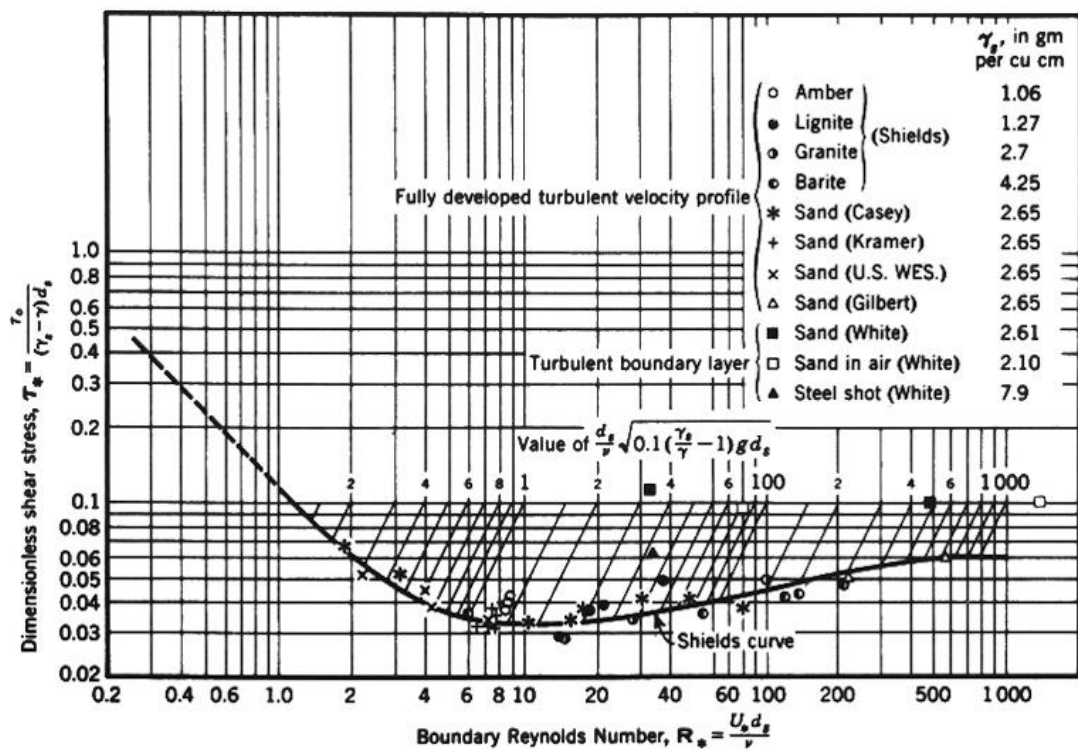


Figure 2-3 – Shields Diagram (U.S. Army Corps of Engineers, 1994)

Cohesive and Non-cohesive

Cohesive and non-cohesive define the two main types of sediment. Small particles with a diameter less than 0.06 mm (Camenen and Larroude, 2003) are defined as clays or silts and classed as cohesive. This is because the distance between particles is so small that the inter-particle forces have a greater effect and raise the erosion threshold. Cohesive sediments can also include larger sediment particles but only when organic matter is present (Partheniades, 2009) as the organic matter essentially bonds sediment particles together.

Marine sediment can be cohesive, non-cohesive or a combination; however, only non-cohesive sediment is considered for the remainder of this study. This is for two reasons, firstly the scour formed in non-cohesive and cohesive scour is proportional; this is clear from the fundamental relationships between the sediment types such as the excess shear stress required to initial motion. Therefore, any new mitigation methods or discoveries will also apply to cohesive sediment beds. The second reason is that a larger number of empirical formulae are available, and they have been subject of more development and research, and due to this and the simpler physics these formulae are more accurate. Therefore, for these two reasons, both model development and the search for innovative active or static methods can be performed with either sediment type.

Sediment Size, Density and Shape

Sediment beds both inland and offshore comprise of layers, each containing a different range of sediment types. In experimental modelling, this can be problematic and as a result the sediment bed is often simplified to one composition of sediment with a limited range of sediment size and density. Numerical modelling and empirical formulae simplify this further, by representing the composition with a single median grain size d_{50} and a constant density, although sometimes lower and higher percentiles or standard deviation from the 50th percentile is also considered.

Wu et al., (2004) demonstrated that the use of a single value to represent non-uniform sediment within a bed load formula can lead to underprediction; as natural flows typically result in a sediment size distribution skewed towards the smaller particle size. Furthermore, it is shown that bed load predictions can be improved if the particle size distribution is known; by splitting the distribution into groups and calculating the bed load for each group individually, taking into account the frequency of each size range and applying a correction factor. This provides a simple and effective way to improve bed load predictions. However, its implementation within a numerical model is meaningless if used with only a single grain diameter.

An alternative is to follow the approach of Ackers and White (1973) and use a value offset from the median, in the case of Ackers and White (1973) this is d_{35} , the grain diameter 35% finer than the median value. Furthermore, if a grain diameter of d_{35} does not increase the cohesive nature of the sediment this provides a factor of safety, as the scour will be greater compared to predictions using the typical d_{50} value.

A universal approach would argue that the best grain diameter size is one which best represents the sediment bed, which then impacts the flow resistance and bedload removal rate. However, it is not this simple as the formulae used to predict the friction on the bed (roughness height formulae) and bedload removal rate (bedload transport formulae) are typically empirical and therefore already tuned based on a range of sediment sizes, or specific grain diameter percentile. Therefore, the choice of diameter in reference to the median will be based on advisory values for each specific formula; however, the use of alternate sizes should not be dismissed as can be used for model tuning; a method used to account for primarily the inaccuracy of model elements and the inability of empirical formula to be consistently accuracy in all scenarios. This is referred to in more detail later in the study.

In respect to individual grains, the size and density are the most influential parameters followed by particle shape; which can affect the sediment threshold and angle of repose. Friedman and Robinson (2002) show that the difference in angle of repose between a course and smooth spherical particle can be up to 20 degrees. The angle of repose is one of the sediment parameters applicable to a bed of particles, in addition to packing density or closely linked bed porosity, and roughness height.

Bed Packing Density

The sediment packing density is directly related to the bed porosity, which describes the voids between sediment grains and is quantified as a volume fraction of void volume to total volume (sediment and voids). The packing density is dependent on sediment size distribution, shape and any compression the bed has undergone. However, the bed porosity is not very sensitive to these values as seen from Table 2-1, resulting in a typical void fraction of 0.4 (40%) for natural sediment mixtures.

		Distribution		
		Well-Sorted	Average	Well-Mixed
Packing	Loosely Packed	0.46	0.43	0.38
	Average	0.42	0.4	0.33
	Densely Packed	0.4	0.37	0.3

Table 2-1 - Porosity of natural sand beds (Soulsby, 1998)

The bed porosity impacts the incipient motion and therefore erosion rate, as it is directly related to the angle between sediment grains and therefore, the resistance to motion. It also has a significant impact for numerical modelling as changes in bed height that are computed using volumetric sediment flux must also incorporate the void fraction. Furthermore, based on Table 2-1 the maximum difference is a change of packing density of 0.16, relating to a maximum possible change in mass flux of 30%, based on Equation 4 – Simplified Exner Equation.

Angle of Repose

The angle of repose or critical angle is important for sediment slopes such as those met in scour scenarios, as it defines the angle that sediment will start to slide down a slope due to gravity. This is typical between 30 and 43 degrees, which for non-cohesive sediment is dependent on the same factors as packing density. Also, similar to packing density, the angle of repose does not vary significantly for fine sands as shown in Figure 2-4 and an angle of 32 degrees is generally accepted.

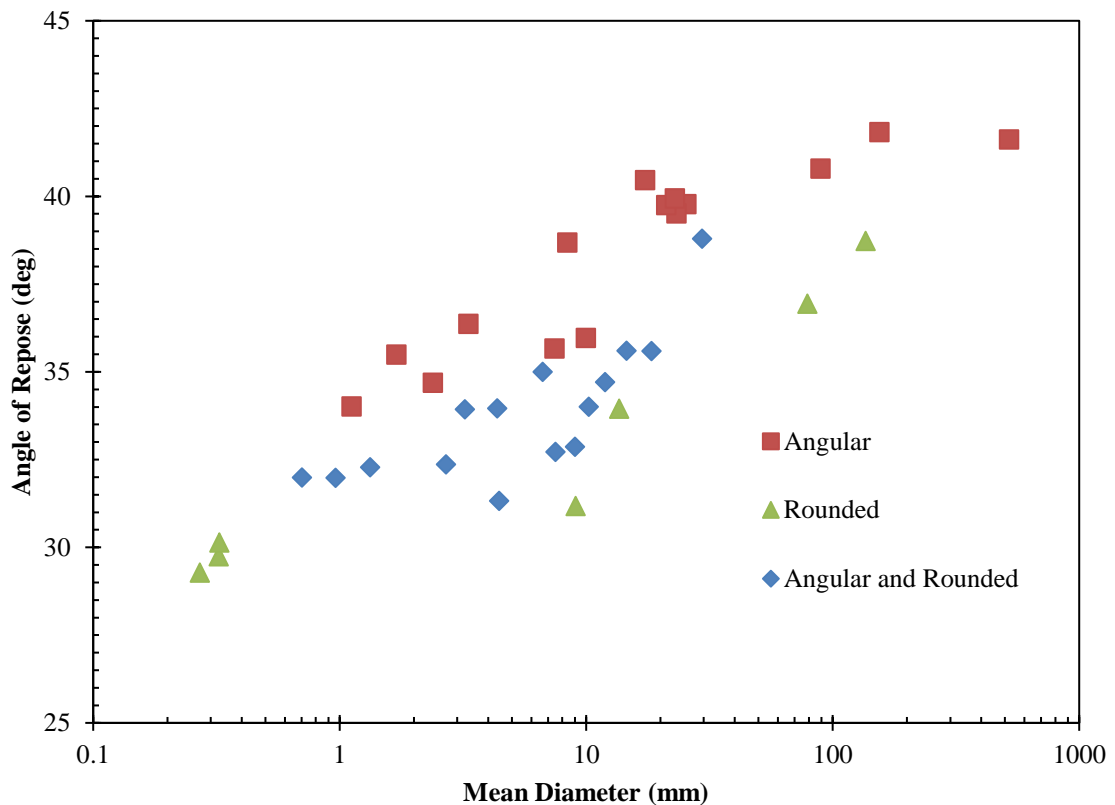


Figure 2-4 - Varying Angle of Repose (Graf and Yulistiyanto, 1998)

The angle of repose is not constant for all slopes, as this is based on a no-flow condition. If an up-sloping flow is present, the flow will oppose the gravitation forces upon sediment grains and stop sediment sliding at the angle of repose and conversely, a down-sloping flow will promote the sliding of grains at a lower angle.

Erosion

The incipient motion of sediment is the instance that hydrodynamic lift and drag forces exerted upon a sediment particle balance with the resistive forces opposing motion (Julien, 1988). The resistive forces include gravitational mass in all sediment types and additional inter-granular attractive forces in cohesive sediment.

The initiation of motion is followed by the transportation of sediment in one of two modes, bed-load and suspended load transport, Figure 2-5.

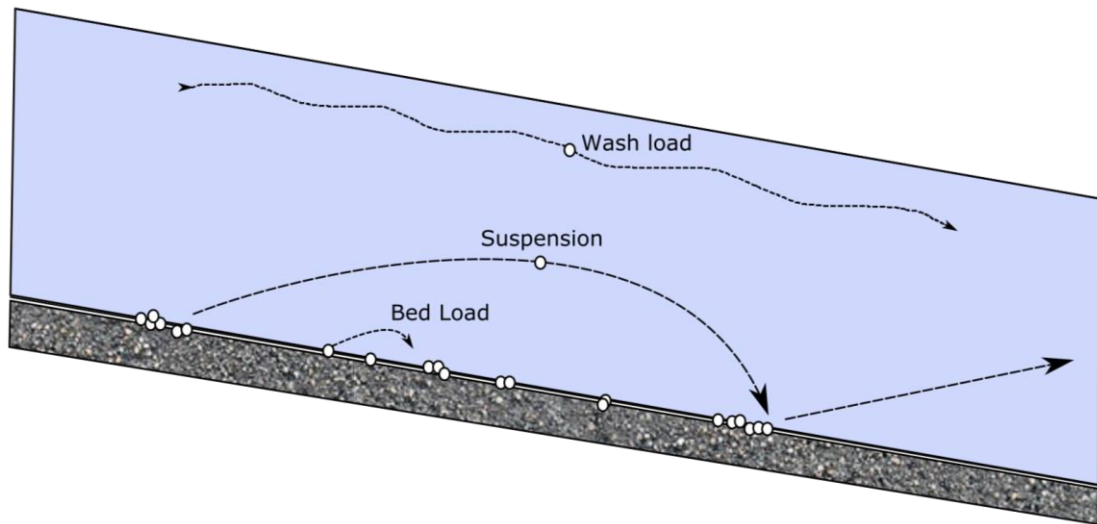


Figure 2-5 - Sediment Transport Modes

Bed load transport includes two mechanisms known as rolling and saltation. These motions are contained within the bed load layer, adjacent to the bed surface and typically only 2 grain-diameters thick (Julien, 1988). The first mechanism, rolling, occurs when the bed shear stress initially exceeds the critical stress causing grains to dislodge and roll downstream to new positions. The second mechanism, saltation, is triggered when additional energy is provided resulting in additional lift and drag forces in the form of impulses (Dyer, 1986) causing grains to 'jump' from the bed surface to new positions further downstream.

The entrainment of particles into the suspended load layer involves grains jumping from the bed load layer into the suspended load layer; therefore, requiring additional force compared to bed load transport. For particles to remain in this suspended state, the frictional velocity must exceed the fall velocity (Sumer and Fredsøe, 2002).

The fall velocity of a single particle is dependent on the drag forces upon that particle, influenced by the flow speed, relative density, fluid viscosity, particle size and shape. In a sediment-laden flow, the fall velocity is reduced as the concentration of sediment increases the mixture density, raising the buoyancy force; this is known as hindered settling (Mazumder and Ghoshal, 2006).

In a simple sediment-laden channel, the logarithmic velocity profile, turbulence and hindered settling results in a parabolic sediment concentration distribution. Rouse (1936) produced one of the first formulae, Equation 3 (illustrated in Figure 2-6) to predict the sediment concentration distribution that remains valid today despite the large amount of research that has followed leading to more accurate formula (Cheng et al., 2013)

$$\frac{c}{c_a} = \left(\frac{y-z}{z} - \frac{a}{y-a} \right)^\xi$$

Equation 3

Where $\xi = \frac{w}{u^* \kappa}$, c is the concentration, a is the reference height, y is the total height and z is the distance from the reference height.

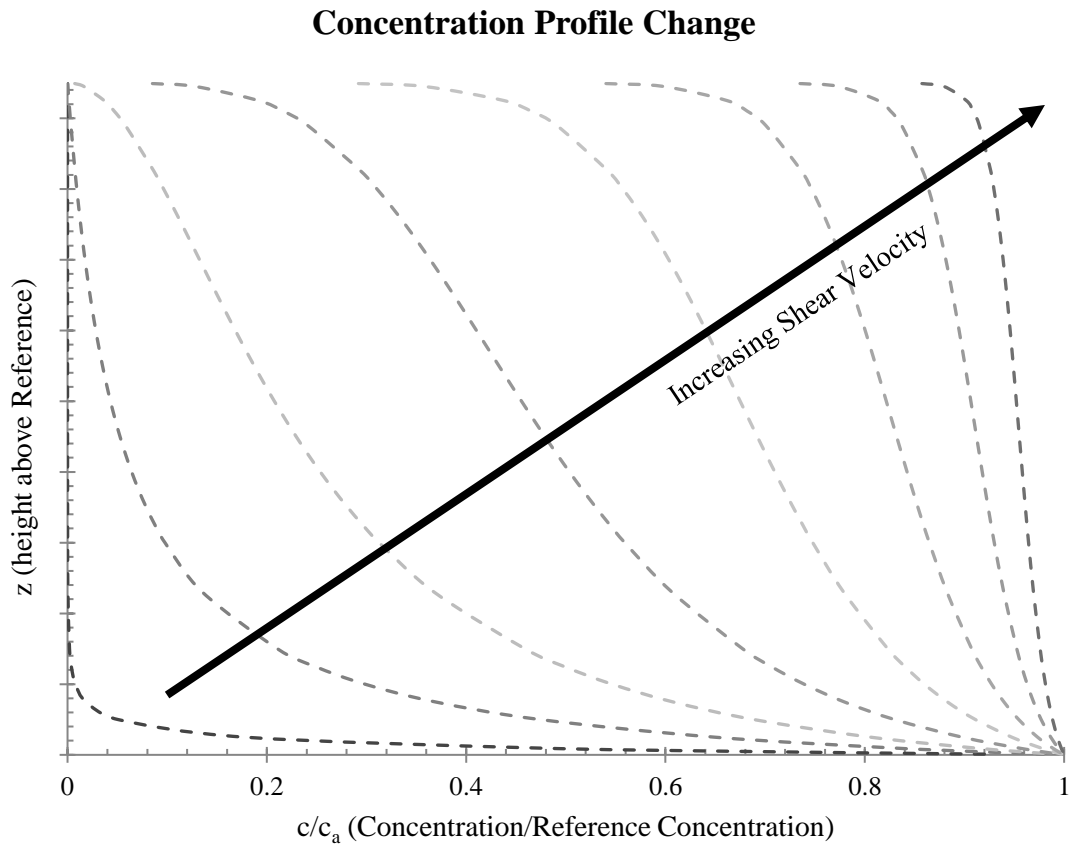


Figure 2-6 - Rouse Formula Concentration Profiles

2.2.2 Representation

There are a number of methods to calculate erosion within a sediment transport model. The most basic method is to use empirical bed load formula, satisfying the mass of sediment removed per unit length per second (q_b), to directly change the bed height which neglects the existing concentration of sediment within the bed load or suspended load layer, following the original form of the Exner equation, Equation 4 (Amoudry, 2008).

$$\frac{\Delta z}{\Delta t} = \left(\frac{1}{1 - \gamma} \right) (q_b)$$

Equation 4 – Simplified Exner Equation

Typically, additional source terms are used to compute sediment mass in the bedload and/or suspended load layer leading to the alternate form of the Exner equation shown in Equation 5 (Amoudry, 2008);

$$\frac{\Delta z}{\Delta t} = \left(\frac{1}{1 - \gamma} \right) (-\nabla \cdot \mathbf{q}_b + \textit{Deposition} - \textit{Erosion})$$

Equation 5 – Expanded Exner Equation

The bed flux term, q_b is always included, however the inclusion and calculation of deposition and erosion differs from model-to-model. The erosion and deposition of sediment can be computed using several different methods, but usually entails empirical concentration formula for the bed and suspended load sections. This is also common in two-phase CFD simulations, as the grid resolution is not always fine enough to model the near-bed sediment gradient accurately (Zhao et al., 2010). The formulae available for bedload and suspended load concentration are also discussed in this section.

The bed-flux is normally calculated from empirical bedload flux or concentration formula, which also requires values to be predicted for sediment threshold. The first part of this section describes the options available to predict both of these values.

Concentration predictions within single-phase simulations are for equilibrium conditions and often do not consider the previous concentration. This is highlighted in Khosronejad et al. (2012) that alternatively uses the concentration at the last time step to compute the concentration during the current time step, this significantly improves the accuracy however its benefit given the additional cost is not always justified.

The Exner equation can be used to compute both the erosion and deposition of sediment, because as stated in Graf and Altinakar (1998) the bed flux provides the capacity of sediment under equilibrium flow. However, if the sediment discharge is not equal to the capacity, erosion or deposition can occur, whereby:

- “
- if the capacity is larger than the supply, erosion and transportation occurs,
 - if the supply is larger than the capacity, deposition and transportation occurs,
 - if the supply is equal to the capacity, transport without erosion or deposition occurs,
- “

Initiation of Motion

The sediment threshold defines the force required to exceed the incipient motion of sediment. Several theories exist to predict the sediment threshold with the most common based on the threshold bed shear stress, which is the theory followed throughout this study. Alternate theories are based on critical velocity (Yang, 2006) and parameters formulated from principal flow conditions (Beheshti and Ataie-Ashtiani, 2008). Formulae used for predicting the threshold of non-cohesive sediments are more common and avoid the added complexity associated with cohesive sediment. Ternat et al. (2008) investigates the threshold for cohesive sediment grains and reveals the added complexity; concluding that for flows of a specific salinity and pH, the additional cohesive forces are dependent on surrounding sediment grain size, distance, packing density and bed porosity.

In the case of non-cohesive sediment, Shields (1936) produced one of the first theories based on excess shear stress that remains popular despite wide criticism (Dey, 1999).

Early incipient motion theories for non-cohesive sediment provide diagrams to predict the critical shear stress from the boundary or grain Reynolds number. However, several equations have since been published that fit these diagrams and are extremely useful in computational modelling. This includes several that represent the original Shields data (Beheshti and Ataie-Ashtiani, 2008, Singh, 2002).

There are also other equations which follow the same trend as Shields as seen in Figure 2-7, including many that report improvement to the original Shields diagram, including (Alfadhi et al., 2012, Vanoni and Parker, 2008). Due to their typical empirical formulation, these equations are heavily dependent on the data used to derive them and therefore perform better in specific scenarios.

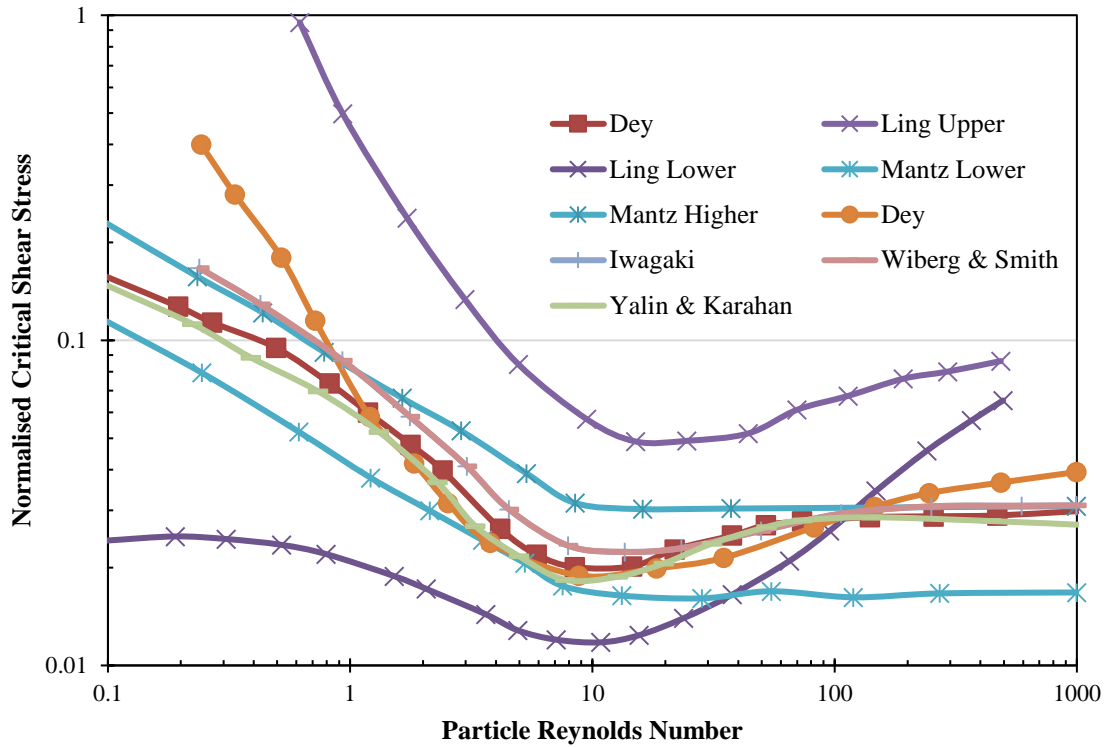


Figure 2-7 – Critical Shields Parameter Diagrams (Dey, 1999)

The difference in critical shear stress between the original shields equation and improved formula is investigated. Equation 6 represents the Hunter-Rouse Diagram (Guo, 2002) that follows the original Shields Diagram and has been used in both computational fluid dynamic software FLOW-3D (Brethour and Burnham, 2010) and computational scour models (Tulimilli et al., 2011).

$$\theta_{cr} = \frac{0.23}{d_*} + 0.054 \left[1 - \exp\left(-\frac{d_*^{0.85}}{23}\right) \right]$$

Equation 6 – Hunter-Rouse Critical Shear Stress Formula

In Equation 6, the Rouse Reynolds Number is calculated using $d_* = \left(\frac{(s-1)g}{\nu^2}\right)^{\frac{1}{3}} d$, where s is the specific gravity ($\rho_s - \rho$).

The ‘Modified Brownlie-Shields’ Equation 7, claims to provide an improvement to the original shields formula, accounting for its common over-prediction (Vanoni and Parker, 2008).

$$\theta_{cr} = 0.5 \left(0.22 \text{Re}_p^{-0.6} + 0.06 \cdot 10^{-7.7 \cdot \text{Re}_p^{-0.6}} \right)$$

Equation 7 – Modified Brownlie-Shields Critical Shear Stress Formula

A comparison of the two formulas uncovered a difference in critical shear stress of 50%. This significant variation is also evident in other formulas as shown in Figure 2-7. Therefore, these

equations are investigated and assessed in a later section by implementing them into a numerical model.

Slope Effects

Critical threshold and sediment load formulae are typically derived for near-horizontal bed surfaces with $\tan \beta < 10^{-3}$ ($< 0.0057^\circ$), (Van Rijn et al., 2006). However, when a slope exceeds this limit the force balance becomes more complex, as gravitational force is no longer perpendicular to the bed. As a result, the force required to move a grain is either increased or decreased, depending on whether there is a downslope or upslope.

To account for these changes correction coefficients are applied to the sediment threshold value, calculated from formulae using the slope and the angle of repose.

Existing formula which account for three-dimensions use the transverse and lateral angle between the flow and steepest slope separately or use the angle between the flow vector and the steepest slope vector. Additionally, it is apparent that not all formulae include empirically based constants. A range of the most recent and common formulae are shown by Equation 8 to Equation 11.

Lesser et al. (2004) presents Equation 8 which is similar to the equation proposed by Bagnold (1963) and one of the simplest, accounting for slope and flow direction upon the slope.

$$\theta_{cr} = \theta_{cr,0} \frac{\tan(\phi)}{(\tan(\phi) - \tan(\alpha)) \cos(\alpha)}$$

Equation 8 – Lesser et al. (2004) Critical Shields Parameter Slope Correction

In Equation 8, ϕ = angle of repose, α = Angle between velocity vector and β vector, where β is the steepest angle from the horizontal.

Van Rijn et al. (2006) includes Equation 9 which is slightly modified from that presented in (Dey, 2003). It is shown that the equation matches well to experimental results, however it is limited to one-directional flow.

$$\theta_{cr} = \theta_{cr,0} \left(1 - \left(\frac{\tan(\beta)}{\tan(\phi)}\right)\right)^{0.75} \left(1 - \left(\frac{\tan(\gamma)}{\tan(\phi)}\right)\right)^{0.37}$$

Equation 9 – Van Rijn et al. (2006) Critical Shields Parameter Slope Correction

Where γ = lateral angle between flow direction and steepest slope.

Equation 10 and Equation 11 are presented by Liu and Garcia (2006) and Roulund et al.(2005) respectively and demonstrate the extended number of available formulae.

$$\theta_{cr} = \theta_{cr,0} \frac{\sin(\alpha - \text{sgn}(\vec{\tau} \cdot \vec{S})\phi)}{\sin(\phi)}$$

Equation 10

Where $\vec{\tau}$ and \vec{S} represent the shear stress and slope vectors.

$$\theta_{cr} = \theta_{cr,0} \left(\cos(\beta) \sqrt{1 - \frac{\sin^2 \alpha \tan^2 \beta}{\phi^2}} - \frac{\cos(\alpha) \sin(\beta)}{\phi} \right)$$

Equation 11

Transport Load

The sediment transport rate is defined as the total weight of grains passing through a unit width per unit time. Formulae are available for predicting the amount of bed-load, suspended-load and total load. These formulae range considerably, with one of the most fundamental differences being the derivation approach (Yang, 2006) with the most common being probabilistic and energetic .

Generally only bed-load formulas are used for sediment transport modelling and suspended-load formulas are usually replaced by suspended-concentration formula, whereby a concentration is predicted just above the bed-load layer that is used to predict the sediment falling onto the bed. A large number of suspended load formulae are presented in (Van Rijn, 1993).

A common weakness of all formulae is the use of experimental data to define equation coefficients, as the data used is limited which reduces formula performance outside of this range (Dyer, 1986). This is evident from comparison studies such as (Camenen and Larroudé, 2003) which investigates the sensitivity of several formulae to dependent factors including wave period, sediment grain size and steady current speed. This study also reports on the accuracy of different formulas under different ranges of dependent parameters; for example, one outcome is that the Ribberink (1998) formula performs worse out of the tested formulas, when the scour is formed by a low wave velocity.

Due to the differences in data used to compose formulae they are best chosen using the application conditions to gain the best accuracy (Camenen and Larroude, 2000, Camenen and Larroudé, 2003). The outcome of different formula once implemented into numerical scour models is shown by (Karami et al., 2012, O'Neil, 2002) and a later section in this study (Chapter 7, Single Phase , Case 1 – Preliminary Scouring around a Simple Monopile).

In addition to formula accuracy, another important factor is the necessary variables. Knighton (1998) indicates that formula can be grouped by the relation of sediment transport rate per unit width to excess shear stress, excess discharge or excess stream power. This classification is

significant when developing numerical models as specific variables are not always available or are difficult to extract; one example of this is the depth averaged velocity (required for the formula in (Bangold, 1966)) which can be difficult to obtain with some numerical codes, especially for every spatially discretized location, or variables averaged over several wave periods (Bailard, 1981) .

Shear stress based formulae are more common and were developed following the early works of (Meyer-Peter and Müller, 1948, Einstein, 1948). However, they are widely criticised due to their simple flow limitations (Camenen and Larson, 2005) due to the weak relationship between shear stress and transport rate; especially in comparison to other variables such as stream power.

These formulae are of the form $q = M \cdot (\tau - \tau_c)^n$, containing two constants, M, n, and the excess bed shear stress; formulated using shear stress τ and critical shear stress τ_c . This type of formula follows the theory that erosion is only initiated once the critical shear stress is exceeded, which is not strictly true as sediment motion is evident before the threshold value as discussed in (Van Rijn, 1993). However, the original notion is generally accepted and is adequate for sediment transport models.

Despite the weaknesses evident with excess shear stress based formula they have been proven to be satisfactory for numerical scour models, providing agreeable results in a number of instances. Tulumilli et al. (2010) presents a 3D scour model designed to capture the scour under bridges during flood conditions. The erosion formula uses a fraction of the excess shear stress present, accounting for other parameters, and adjusts the bed according to this with a maximum depth change of one grain diameter. The results are promising as closely match the profile and depth of experimental results, however the scour is significantly smoother than the experimental result and only one comparison is made.

A journal article by Hsu et al. (2004) concentrates on two-phase heavy-concentration sheet flow and calculates the non-dimensional total load by multiplying the excess shear stress by a constant, to the power of a constant. These constants do not appear to be confidently defined in the model, and despite positive outcomes the author expresses the requirement for further work on the model. Warner et al. (2008) demonstrates the capability of a multi-environment capable model using a number of validation cases (described in the later Chapter 5, Scour Model Literature Review). The model concentrates on the use of a layered domain for both sediment and water phases and computes the sediment load by using the excess shear stress in equations to estimate the active layer thickness and erosion mass flux.

The final example of excess shear stress use, (Khosronejad et al., 2012), is similar to this study as predicts the 3D erosion around bridge piers, using a single phase model. (Khosronejad et al.) uses

the excess shear stress to compute sediment concentration at a reference depth, which is integrated to compute the bed mass flux, using a formula in (Van Rijn, 1993).

Bed layer load

There are many excess shear stress bed load formulae available, which as discussed are best chosen based on the flow conditions. This study requires a formula that performs well under a range of current speeds without waves and based on the results of Camenen and Larroudé (2003) the Van Rijn (1991) formula, Equation 12 was chosen. This is also supported by its successful use in (Karami et al., 2012) providing an average coefficient of determination of 0.82 when comparing simulation to experiment for a range of flow velocities, outperforming all other tested formulas.

$$q_{bc} = 0.25 \cdot d_{50} \cdot d_*^{-0.3} \cdot \left(\frac{\tau}{\rho}\right)^{0.5} \cdot \left(\frac{\tau - \tau_{cr}}{\tau_{cr}}\right)^{1.5}$$

Equation 12

A second formula that has provided accurate scour predictions is Meyer-Peter and Müller (1948), Equation 13, as demonstrated by (Warner et al., 2008) using a variety of scenarios; these are discussed in detail in the later Chapter 5, Scour Model Literature Review.

$$q_{bc} = 8(\theta - \theta_{cr})^{1.5} \cdot \sqrt{(s - 1)gd_{50}^3}$$

Equation 13

The third formula presented by Einstein (1948) has been preliminary selected as it shear stress based and the only changing variable is the Shields Parameter θ , therefore reducing the formulas sensitivity when used within numerical software and simplifying its implementation.

$$q_{bc} = \left(40 \cdot \left(\sqrt{\frac{2}{3} \left(\frac{36v^2}{(s-1)gd_{50}^3} \right)} - \sqrt{\frac{36v^2}{(s-1)gd_{50}^3}} \right) \theta^3 \right) d \sqrt{(s-1)gd}$$

Equation 14

In addition to the critical shear stress formula, these equations are also tested once implemented into the later numerical model.

Sediment Concentration

Sediment concentration in the bed load layer is strongly related to the bedload flux as the concentration gradient in the bed-load layer is assumed constant. The relation, and consequently conversion requires prediction of a bed load layer height using empirical formula.

This is dependent on the grain size and shear stress and is sometimes simply approximated as several times the grain diameter; however formulae are available from Van Rijn (1984) and Einstein (1950).

As discussed, the most accurate reference location for the suspended load concentration is just above the bed load layer, as it is required to predict the sediment exchange between the bed load and suspended load layers. The derivation of suspended load concentration formulae is similar to bed load or concentration formulae, as excess stress, velocity or power is often used to quantify the additional energy necessary to transport and retain sediment in suspension. There are few suspended load concentration formulae compared to bed load and typically, the formula of Van Rijn is used.

2.3 Scour

2.3.1 Physics

Research on the scouring around cylindrical structures has increased significantly in recent decades, firstly because of raised interest into the scour around bridge piers due to increased failure, for example in America 600 bridges have failed in the last 30 years due to scour (Prendergast and Gavin, 2014). Also, as the premise of this project has depicted, the last decade has seen a rapid increase in offshore wind turbines, which has introduced additional complexities including waves, severe weather and different pile sizes and shapes.

Early literature mainly concentrates on the final scour topology using experiment methods, and the development of empirical formulae to describe various scour parameters. The most common are on the maximum scour depth and equilibrium time, however, as shown at the end of this chapter others are available including scour hole width, length, and formulae to describe the maximum scour depth over time. More recently within the last 15-20 years, advancements in experimental measurement techniques and computational fluid dynamics have allowed for more detailed and comprehensive analyses; leading to a more comprehensive understanding of the scour process.

This section provides an in-depth analysis of the scouring around surface mounted structures, concentrating mainly on cylinders. The first part provides an in-depth analysis of the flow around surface mounted cylinders at different Reynolds Numbers with no scouring; enabling the fundamental flow mechanisms that are primarily responsible for scour to be examined. This is followed by the transient and final scour topology around cylinders and finally a section summarising the scour around alternate shaped structures.

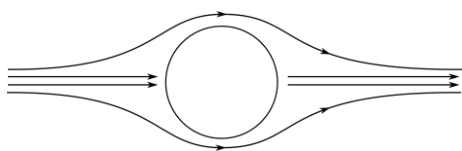
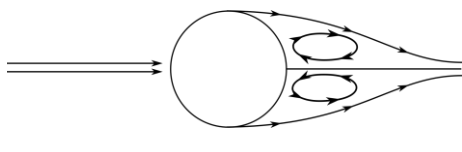
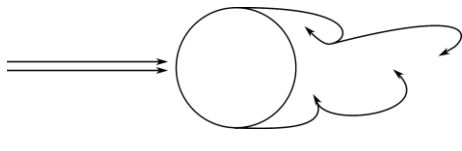
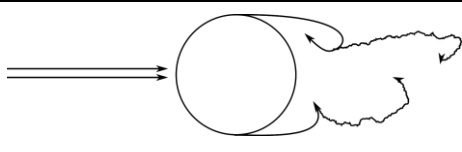
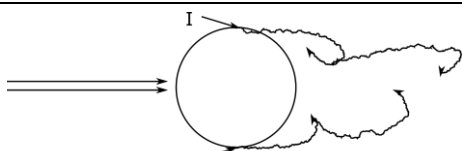
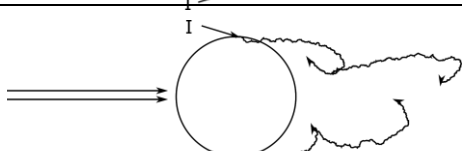
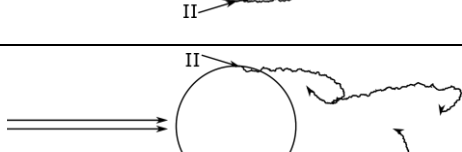
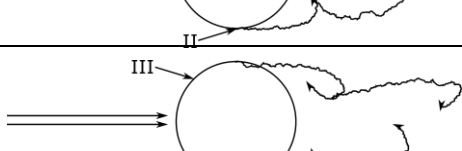
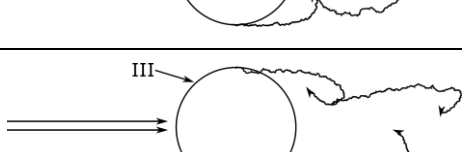
Scour around a cylinder

Flow on a Flat Bed

The flow around a surface mounted cylinder is a traditional topic in fluid dynamics. The resultant hydrodynamics are complex and include three main mechanisms; a horseshoe vortex, flow acceleration and lee-wake vortices. The shape and size of these mechanisms are largely dependent on the Reynolds Number and are discussed in this section.

The flow acceleration and lee-wake vortices can be represented two-dimensionally and are shown in Table 2-2 (based on Schlichting (1979)) over a wide range of Reynolds Numbers using well-defined regimes, .

These regimes vary over a large range of Reynolds Numbers; however, in marine environments Reynolds Numbers greater than 300 are most common. This is particularly true with offshore wind turbines because of their size and exposed current speeds, with monopiles ranging in diameter from 3-6 m and gravity base structures approximately 30 m. As a result, only the regimes of subcritical and above are considered.

$Re < 5$		No Separation
$5 < Re < 40$		Symmetric pair of fixed vortices
$40 < Re < 200$		Laminar Street Vortex
$200 < Re < 300$		Vortex wake transitions to turbulent
$300 < Re < 3 \times 10^5$ Subcritical		Completely turbulent wake with laminar boundary separation (I)
$3 \times 10^5 < Re < 3.5 \times 10^5$ Critical (Lower Transition)		Partial turbulent boundary layer separation (I/II) however the boundary layers remain laminar
$3.5 \times 10^5 < Re < 1.5 \times 10^6$ Supercritical		Turbulent boundary layer separation (II). Partial turbulent boundary layer
$1.5 \times 10^6 < Re < 4 \times 10^6$ Upper transition		Boundary layer completely turbulent at one side (III)
$4 \times 10^6 < Re$ Trans critical		Boundary layer turbulent at both sides (III)

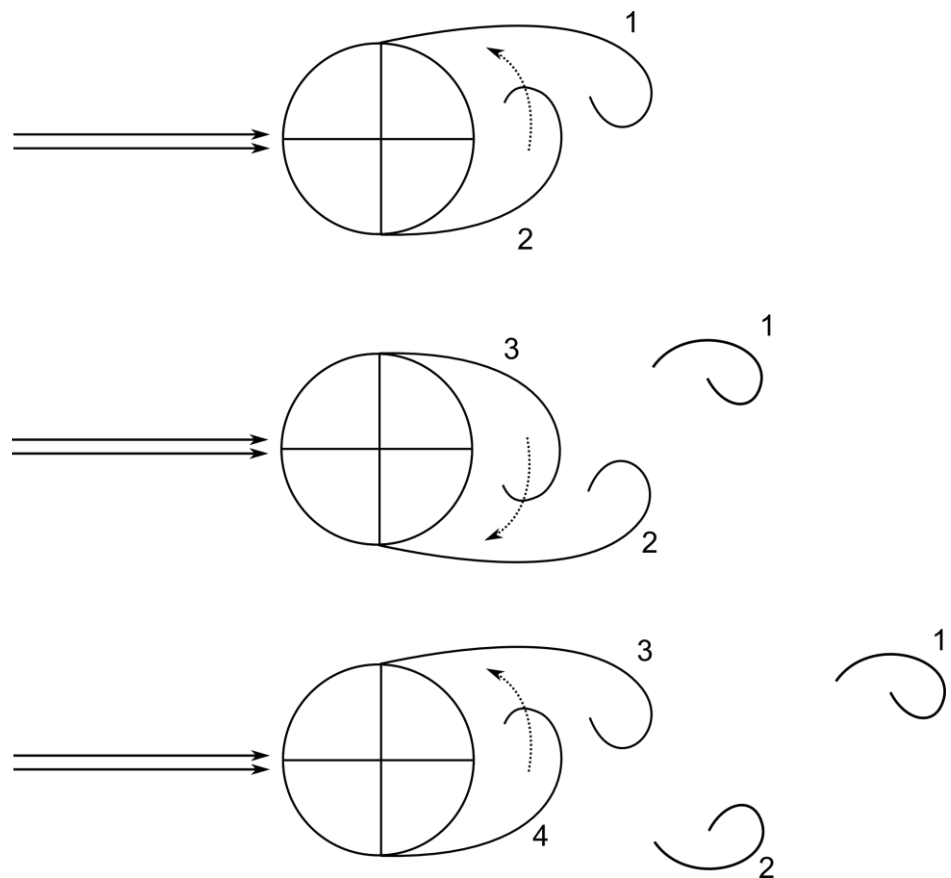
Note: I, II, III denote laminar, partially turbulent and fully turbulent boundary layer separation.

Table 2-2 – Vortex Shedding Regimes

2D Flow Mechanisms

Vortex shedding is evident in all turbulent regimes and initiated by boundary layer separation from the surface of the cylinder; caused by an opposing adverse pressure gradient originating from the lee-wake region behind the cylinder.

This separation leads to the rolling-up of the shear layers into vortices due to the significant levels of vorticity present (Sumer and Fredsøe 2006) which then travel downstream with a dissipating velocity and vorticity. Unsteady and unsymmetrical flow initiates the alternate shedding of vortices. This is then propagated as during shedding the larger more developed vortex attracts the other vortex across the back of the cylinder, until the larger vortex then separates, and then process is reversed, Figure 2-8..



Note: Numbers dictate the order of shedding vortices

Figure 2-8 - Lee-Wake Vortex Shedding Sequence

Research on vortex shedding around cylinders is common and has resulted in striking techniques in order to visualise the effects, such as dye-injected flows (Rao et al., 2004) and the hydrogen bubble method (Huang et al., 2014).

The vortex shedding frequency is typically described using the non-dimensional Strouhal Number, Equation 15 (Sumer and Fredsøe 2006).

$$St = \frac{fD}{u}$$

Equation 15 – Strouhal Number

In Equation 15 f is the shedding frequency, D or sometimes L is the diameter of the pile or reference length and u is the free-stream velocity.

As the Reynolds Number increases, the Strouhal number remains fixed at approximately 0.2 alongside a constant separation angle of 80° .

This remains true until the flow transitions into the critical region at approximately $Re\ 3.5 \times 10^5$, when both vortex shedding frequency (Figure 2-9) and average separation angle (Figure 2-10) increase significantly due to the increased turbulence.

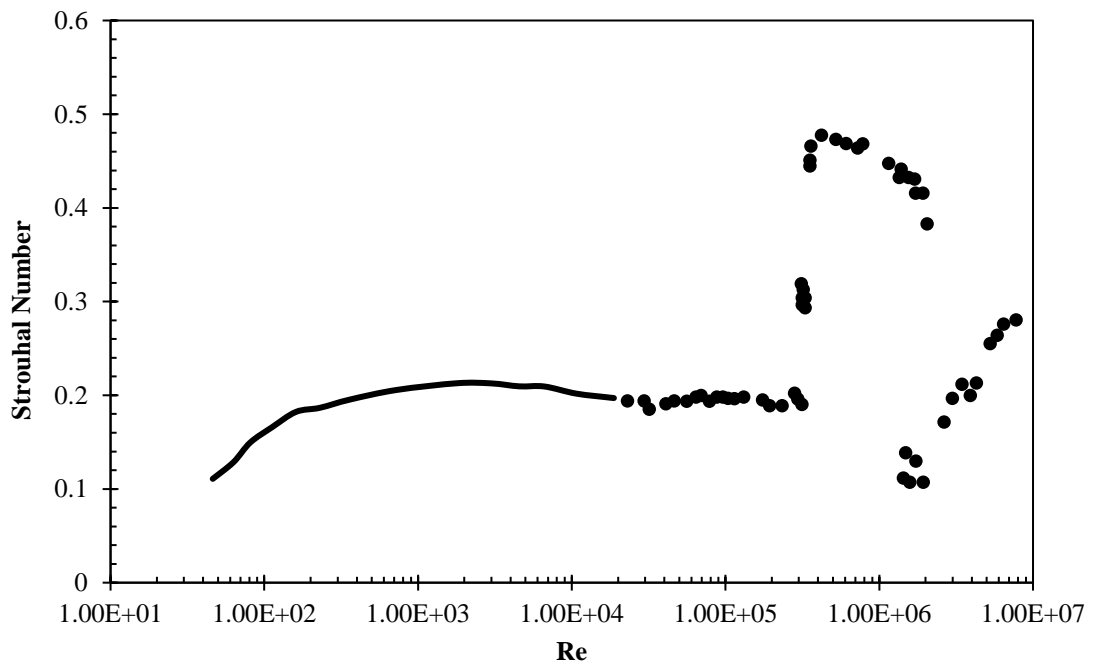


Figure 2-9 - Strouhal Number vs. Reynolds Number (Sumer and Fredsøe 2006)

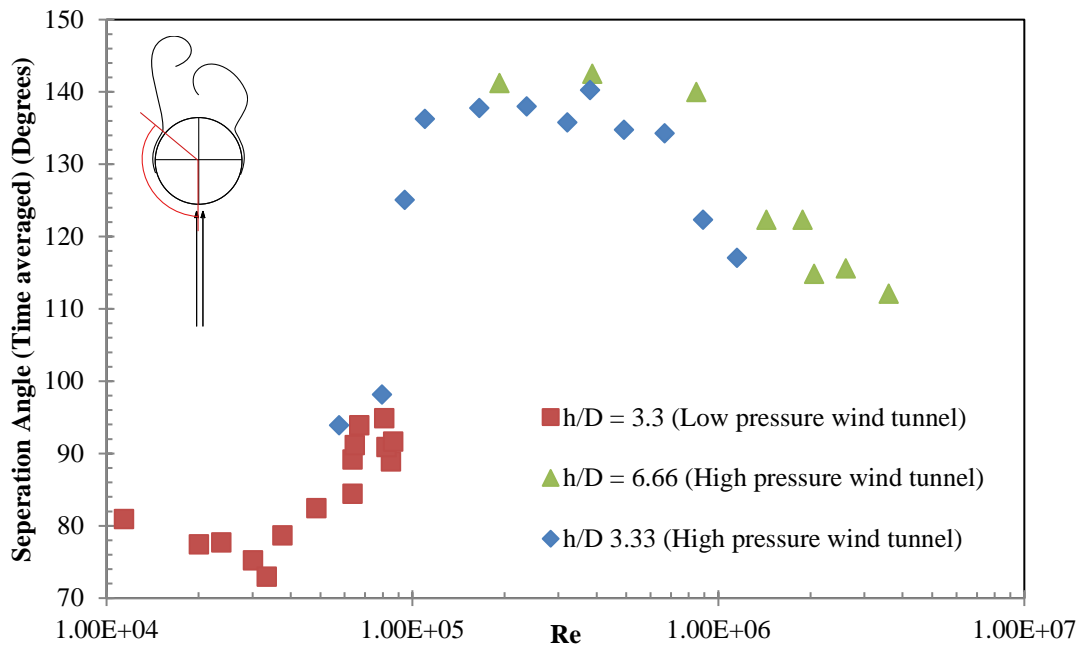


Figure 2-10 - Cylinder Separation Angle vs. Reynolds Number (Achenbach, 1968)

The increased turbulence originates from the wake region, first affecting the boundary layer by providing more energy. This allows for a delay in boundary layer separation to 140° as the additional turbulent energy allows the boundary layer to reattach at a later point. Consequently, the reduced distance between separation points means that the shedding vortices are also closer, resulting in a faster interaction and an increase in vortex shedding frequency.

The increased turbulence progresses further upstream through the boundary layer, until levels of turbulence either side become asymmetric causing irregular and slow vortex shedding in conjunction with a reduced separation angle. Both characteristics continue to decrease as the boundary layer becomes increasingly turbulent until the formation of a fully turbulent boundary layer.

Accelerated Flow

The acceleration of flow around a structure is inevitable due to the resultant displacement. The point of maximum velocity around a cylinder is at $45 - 90^\circ$ either side of the stagnation point, adjacent to the cylinder surface. Achenbach (1968) provides skin-friction results around a cylinder that shows that the position of maximum shear stress and therefore velocity moves downstream around the cylinder as Reynolds Number increases; based on the relationship between velocity and shear stress.

3D Flow Mechanism - Horseshoe Vortex

Horseshoe vortices form in front of cylinders and other structures because of boundary layer separation. Similar to separation at the side of a cylinder, the velocity adjacent to the surface is significantly reduced. The velocity approaches zero and then detaches and travels backwards, resulting in a vortex, as shown in Figure 2-11 based upon (Schlichting, 1979).

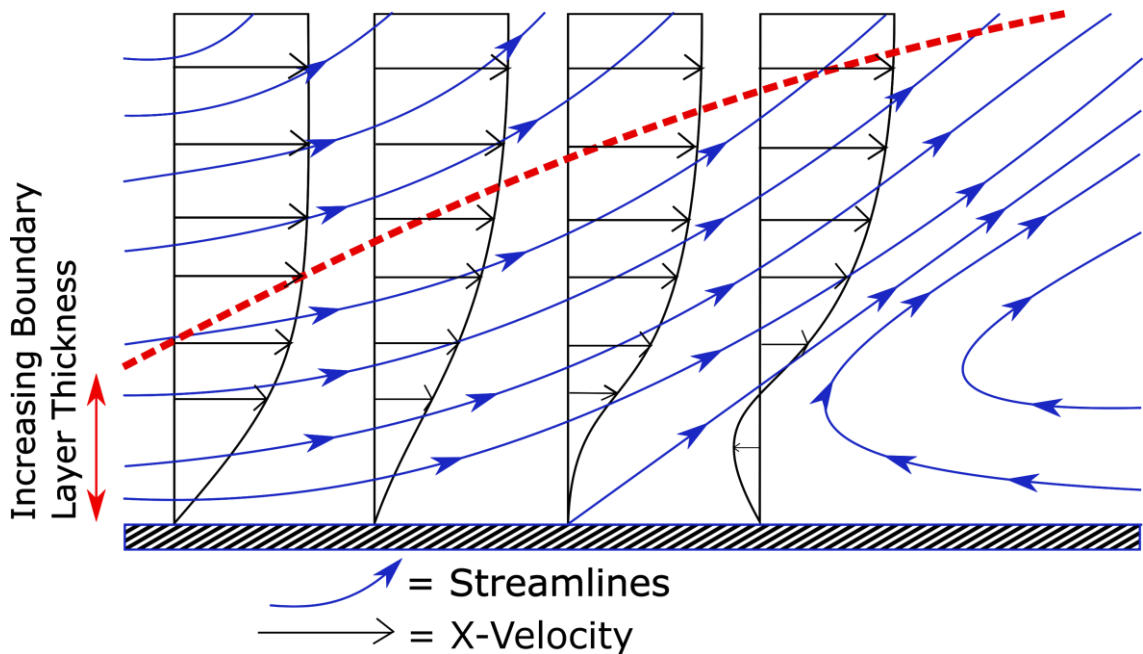


Figure 2-11 - Boundary Layer Separation

The vortex formed in front of surface mounted cylinder typically trails around the entire front half and then dissipates in the downstream direction, hence the name 'horseshoe' vortex, Figure 2-12, based on (Sumer and Fredsøe, 2002). The horseshoe vortex is one of the primary contributors to scour as the formed vortices raise the shear stresses on the bed due to the increased velocity adjacent to the bed surface.

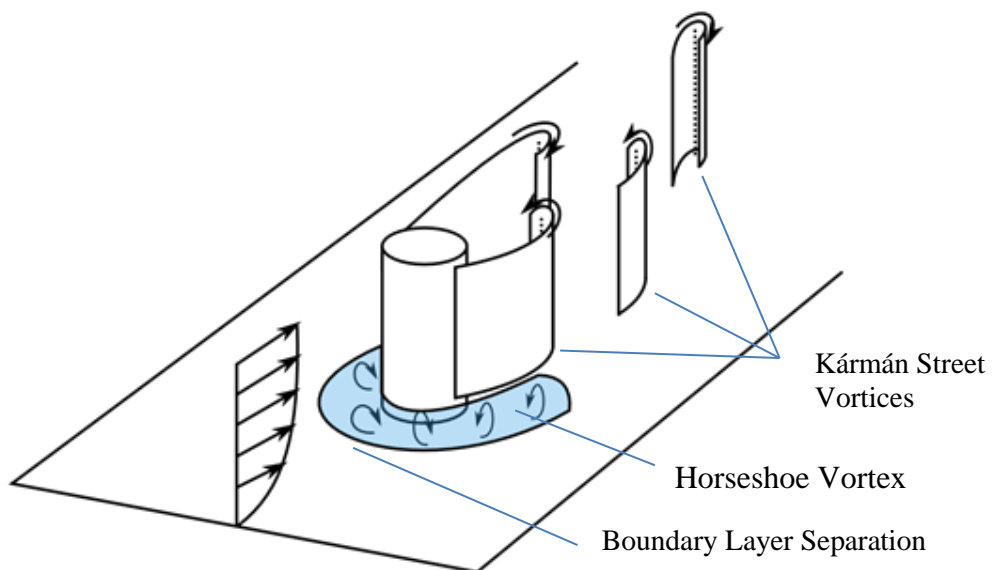


Figure 2-12 - Mounted Cylinder Flow Mechanisms

Horseshoe Vortex Modes

For simplicity, it is perceived that only one horseshoe vortex is present in front of a surface mounted cylinder; however, there is usually one larger vortex with several others upstream and downstream. The number of smaller vortices is dependent on the Reynolds Number and boundary layer thickness as shown in Figure 2-13.

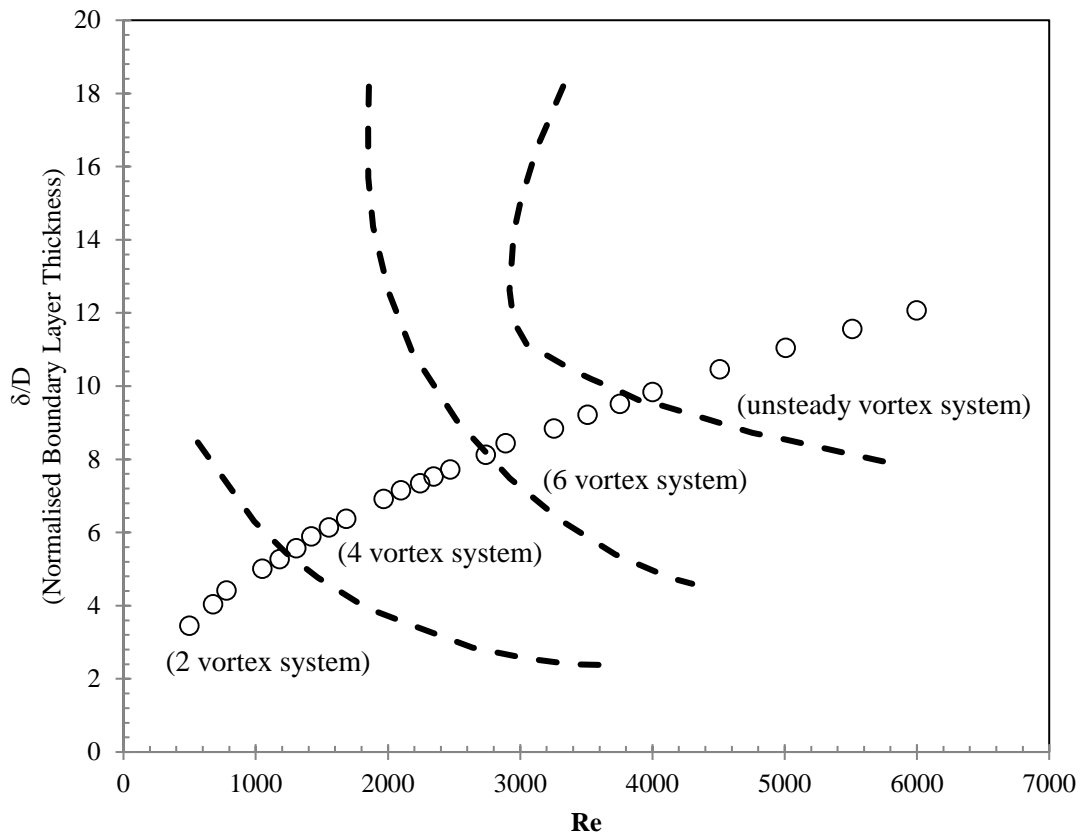


Figure 2-13 - Horseshoe Vortex Modes (Huang et al., 2014)

Escauriaza and Sotiropoulos (2011) studied the horseshoe vortex system at Reynolds Numbers of 2.0×10^4 and 3.9×10^4 using computational methods; specifically using high accuracy detached eddy simulation. The horseshoe vortex system was successfully captured displaying a primary vortex and smaller vortices.

The resolution and capture of many smaller vortices is often neglected, as it is extremely computationally expensive requiring an extremely fine spatial resolution and a turbulence solver that can accurately resolve the complex turbulent flow. However, it is possible to retain scour accuracy despite a loss in turbulence and wall shear stress accuracy, as the time-averaged results do not differ greatly when generated from lower accuracy grids and turbulence models, as seen by studies such as Escauriaza and Sotiropoulos (2011).

Horseshoe vortices are one of the main contributors to scour around a cylinder and using the generalised view of only one main vortex, the strength and resultant wall shear stress can be related to the boundary layer thickness and Reynolds Number (Re_D).

A vortex formed from a laminar boundary layer will increase in size with the Reynolds Number, as this increases the opposing adverse pressure gradient and therefore the distance from the cylinder to the separation point (Sumer and Fredsøe, 2002). Similarly, an increase in boundary layer thickness will also increase the vortex size as shown by Baker (1979).

However, given a turbulent boundary layer, this relationship is reversed, whereby it is shown that an increase in Reynolds Number or boundary layer thickness decreases the size of the horseshoe vortex (Sumer and Fredsøe, 2002). An increase in turbulent energy levels allows the boundary to remain attached for longer, valid up to a Reynolds Number of 1×10^4 when the value remains constant (Muzzammil and Gangadhariah, 2003).

The bed shear stress due to the horseshoe vortices are shown to increase up to approximately $Re_D = 10^4$ (Ozturk et al., 2008, Muzzammil and Gangadhariah, 2003, Das et al., 2013) with a decreasing dimensionless vortex strength ($\Gamma/\pi UD$); where Γ is a product of vortex velocity and mean vortex size, and U and D are the free-stream velocity and the pile diameter. There are fewer reports on the strength after $Re_D = 10^4$ however Muzzammil and Gangadhariah (2003) concludes that the dimensionless strength remains constant at approximately $0.1 Re_D$.

In addition to the boundary layer height, two other boundary layer factors affect the strength of the horseshoe vortex. The first is the water depth, because as discussed previously if the water depth is equal to the boundary layer height, the boundary layer will change in maximum velocity and height which influences the horseshoe vortex. The second is a secondary vortex that forms adjacent to the free-surface and in front of the cylinder, known as a 'surface-roller' or bow-wave. This vortex rotates in the opposite direction and can reduce the effect of the bed-horseshoe vortex if it intersects (Melville and Chiew, 1999).

The Scour Process

The developing and equilibrium scour topology around a cylinder is dependent on the cylinder diameter, flow velocity, boundary layer thickness, grain size and sediment gradation. For a clear water scenario (whereby the free-stream bed shear stress is less than critical) with no upstream sediment load from either supply or erosion, the influence of the factors on the wall shear stress can be reflected by the equilibrium scour depth. This is demonstrated by the relationship between excess velocity and equilibrium scour depth in Figure 2-14 based upon the illustration in (Melville, 2008).

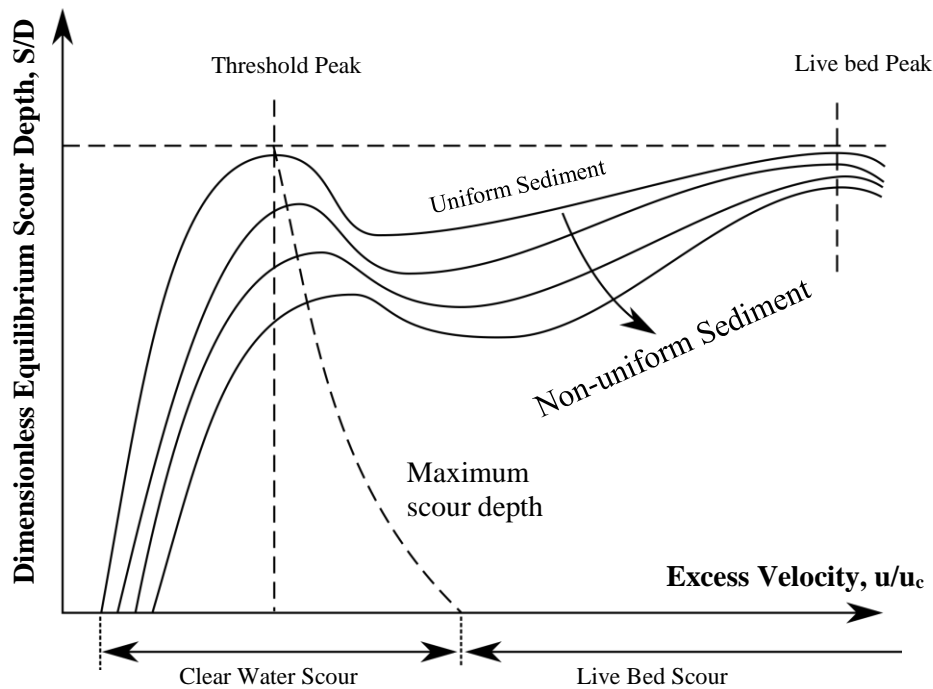


Figure 2-14 - Equilibrium Scour Depth

The relationship between flow variables and scour depth in a live-bed scenario (whereby the free-stream bed shear stress is above critical) is more complex. Figure 2-14 illustrates that at the start of the live-bed region, an increase in excess shear stress initially decreases the maximum scour depth, as the additional stresses do not outweigh the additional sediment load. However, further increases in excess shear stress raise the maximum scour, but only to a maximum similar to the maximum clear water scour depth; the reason behind this is explained later in this section.

As the effect of the dependent variables in clear-water and live-bed scenarios are significantly different they are discussed individually in the following sections. Each section first describes the developing topology and changes in flow and then progresses onto how the dependent variables affect the flow, resultant scour rate, maximum depth and time.

Clearwater Scour

Developing Topology

The clear-water scouring around a cylinder due to unidirectional currents always progresses through the same topological stages, an example of these developments extracted from a later CFD simulation is shown in Figure 2-15.

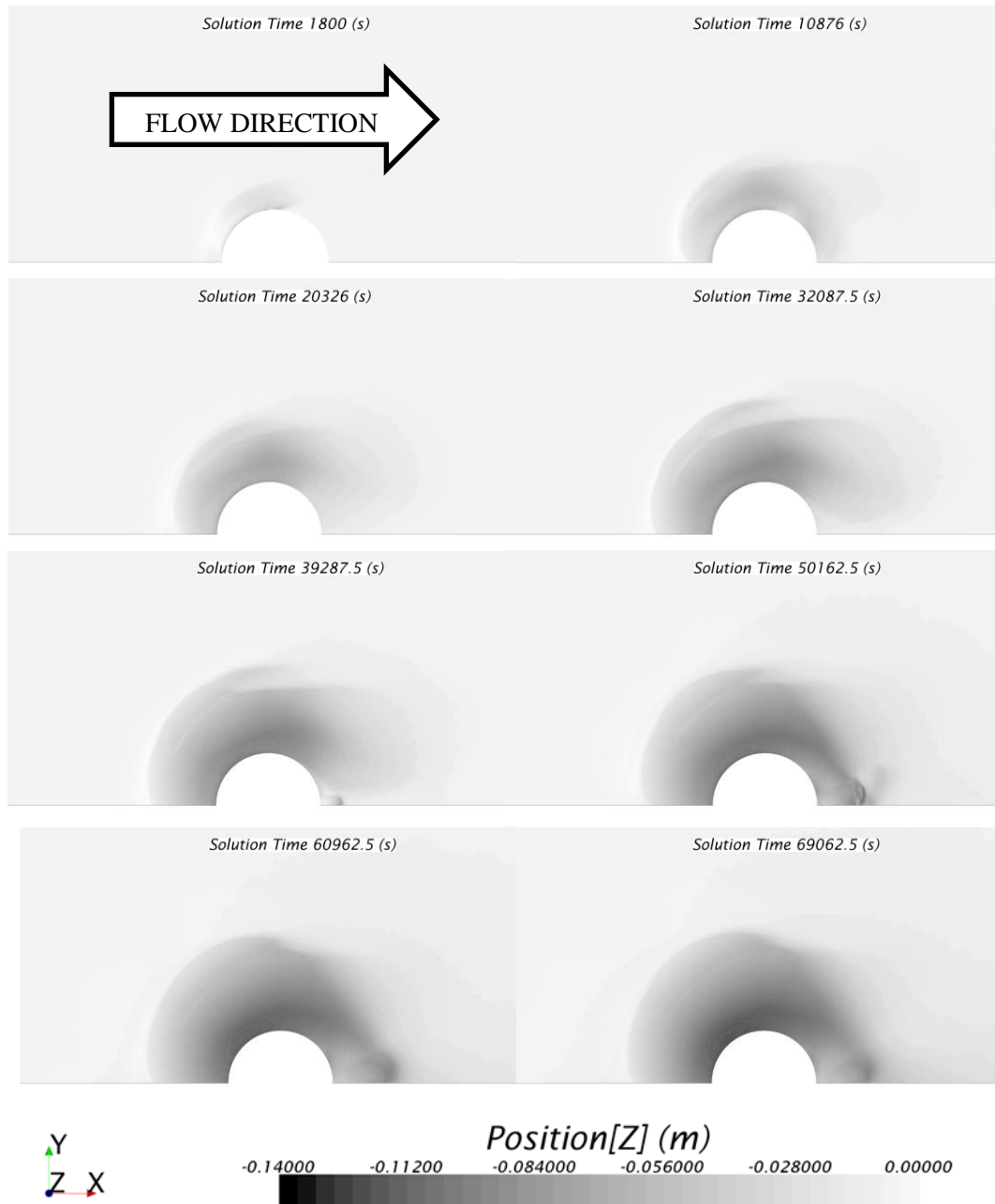


Figure 2-15 - Clear-Water Scour Development

Scour progression from flat-bed to equilibrium has been previously divided into three stages by Ettema (1980) and more recently into four stages by Link (2006). Figure 2-15 shows that in this instance, scour initiates at the sides of the cylinder. The initial scour topology around a cylinder is rarely concentrated on however several studies provide the temporal development of scour in

different axial planes (Link et al., 2008, Whitehouse, 2004, Diab, 2011). These all agree with the above results but the position of maximum scour and the delay in scour between the front and side varies, see Figure 2-16 based on Link et al. (2008). This is because the horseshoe vortex and flow acceleration responsible for this change in strength and position. Furthermore, they do not change together as their relationship to flow variables differ.

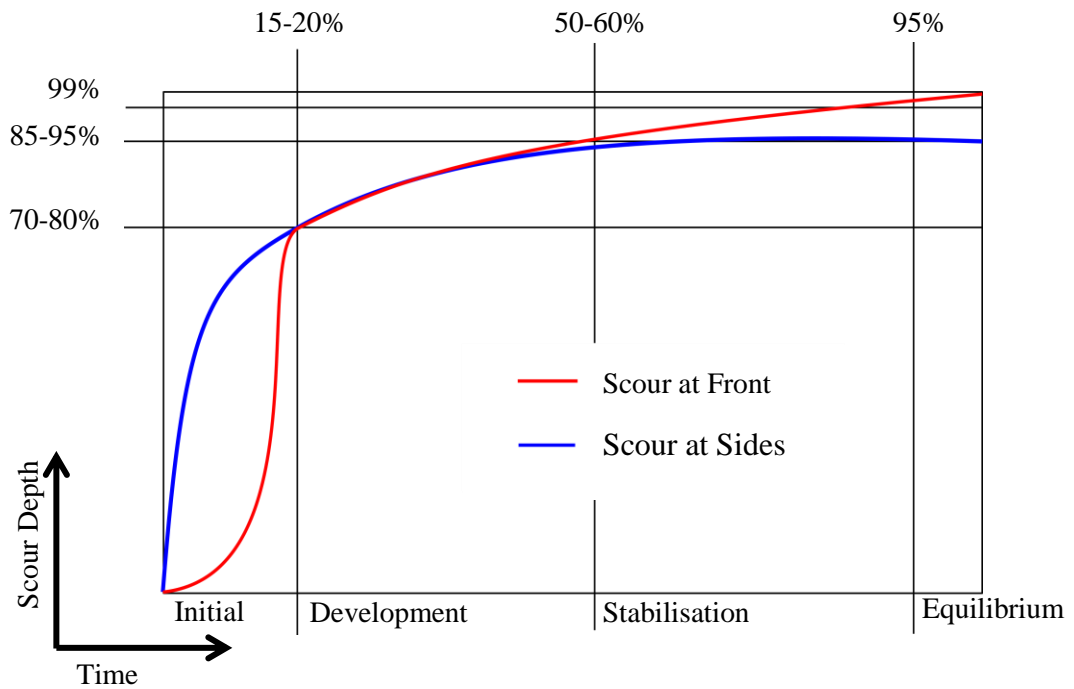


Figure 2-16 - Cylinder-Scour Development Stages

1. Initial Stage

The initial scour stage includes the greatest scour rate at the front and sides of the cylinder. The exponential scour development at the sides is as expected, as given an increase in scour depth and volume the relative blockage is decreased which lowers the velocity and bed shear stress. The scour at the sides appears to govern the scour for the majority of the process, evident from the sudden change in scour at the front between the initial and development stage; when the scouring at the front reaches a similar level to that at the sides.

In the initial stage, the scouring due to the horseshoe vortex at the front takes time to develop. This can be explained using the results in Muzzammil and Gangadhariah (2003) that presents the shear stresses underneath a horseshoe vortex during scour development. The resultant equations proposed by Muzzammil and Gangadhariah (2003) that represents the data of two developing vortices is shown in Figure 2-17. These results also align with those provided by Zhao and Huhe (2006).

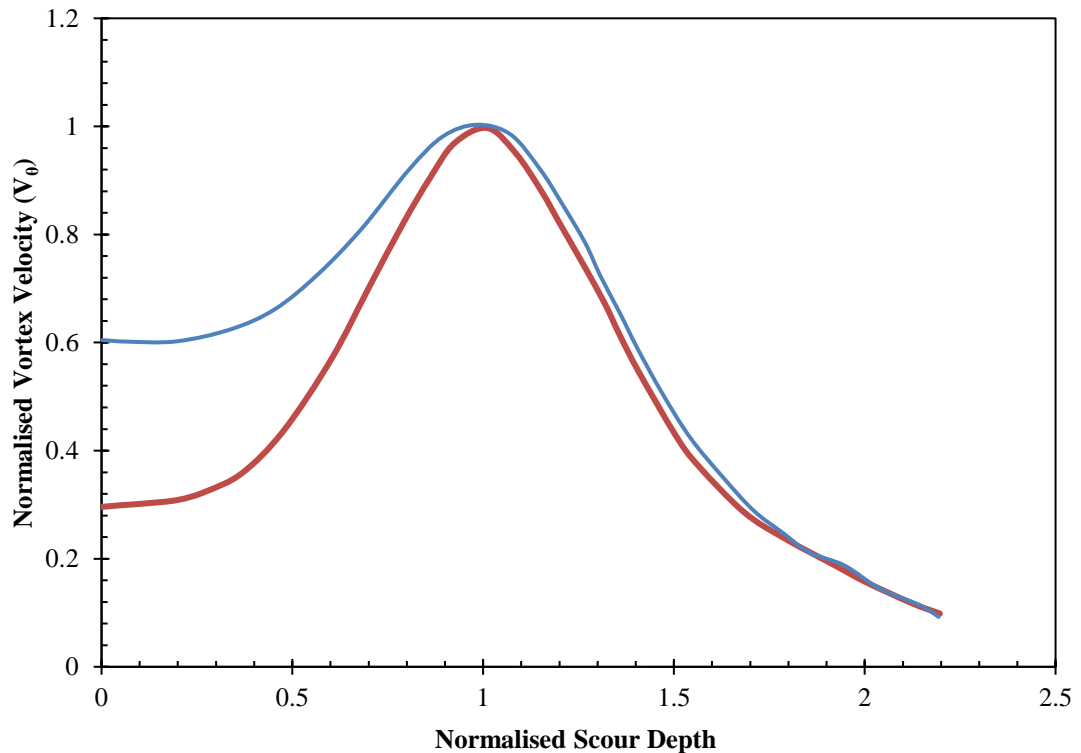


Figure 2-17 – Developing Horseshoe Vortex Strength for Two Cases

In Figure 2-17, (Muzzammil and Gangadhariah, 2003), the vortex velocity is calculated by multiplying π by the vortex core rotation frequency and the average vortex diameter. The scour depth on the x-axis is normalised using the scour depth that corresponds to the maximum vortex strength. The graph shows an initial rise due to the change in flow caused by the scouring at the sides as this reduces the resistance for the horseshoe vortex. This explains both the initial slow development of scour at the front and the transition from initial to development stage, because the rate decreases when the scouring at the front reaches a similar depth to the sides; which lowers the slope between the two areas, constricting the horseshoe vortex and lowering the scour rate.

2. Development Stage

The development stage occurs at a slower rate than the initial stage, during which the scour at the front and sides develops at the same rate (Whitehouse, 2004, Diab, 2011, Muzzammil and Gangadhariah, 2003). The scour topology during this stage is characterised by a relatively uniform scour depth around the front half of the cylinder with a sediment slope at the angle of repose; resulting in the continual sliding of sand as scour adjacent to the pile progresses.

3. Stabilisation Stage

It is deduced from these findings that the stabilisation stage is triggered by the ceasing of scour at the sides, creating more resistance for the horseshoe vortex until equilibrium when the strength of the horseshoe vortex is reduced below the erosion threshold.

4. Equilibrium-Stage

Equilibrium is defined as the state when a balance is achieved, in this case the balance of incoming and outgoing sand. However, this is rarely reached experimentally due to the asymptotic trend. Instead, scour experiments are usually stopped when one of the various equilibrium scour definitions are met. These are typically defined as a percentage of flow or geometric variable over a long period, as shown in Table 2-3 below, sourced from (Diab, 2011). An appreciation of the possible difference in experimentally defined equilibrium is important for the model development and validation process, given the ‘equilibrium’ scour depth stated in experimental results. Furthermore, the reason for this variation is the exponential decay in maximum scour gradient, which also exists in real-life scenarios where it can be equally as difficult to establish.

Source	Definition of equilibrium time
(Ettema, 1980)	The time at which the change of scour hole is no more than 1 mm in a timeframe of 4 hours
(Raudkivi, 1986)	After laboratory test duration of 50 hours
(Melville and Chiew, 1999)	The time at which the rate of change of scour depth doesn't exceed 5% of the pier diameter in the succeeding 24-hour period
(Link, 2006)	The time at which the scour rate is less than d_{50} per hour

Table 2-3 - Definitions of Equilibrium Scour

Scour at the rear of the cylinder

The scour at the rear of a cylinder has not been discussed, as the scour pattern is dependent on the flow conditions unlike the scouring at the front and sides. The downstream erosion, either side of the cylinder always occurs due to residual stresses from the flow acceleration and the trailing horseshoe vortex, but also partially due to lee-wake vortex shedding. The area directly behind the cylinder has been shown to change considerably (Qi and Gao, 2014) and is highly dependent on the lee-wake vortex shedding. Zhao et al.(2010) presents the results for several current-only scour experiments around a cylinder, revealing a ‘V’ shape left behind the cylinder at a low Reynolds Number. As the Reynolds Number is increased the volume of sand within the ‘V’ section decreases and for very high Reynolds Numbers no ‘V’ section exists and only an upwards slope is present, for an example see Qi and Gao (2014).

Dependent Factors

Irrespective of the flow conditions, the progression of maximum scouring depth around a cylinder in a clear-water, current-only environment remains exponential and follows the previously discussed development stages. However, the exponential growth, decay and asymptotic value vary. One of the primary variables is the excess shear stress that when raised, increases the initial scour rate, equilibrium time and depth, Figure 2-18.

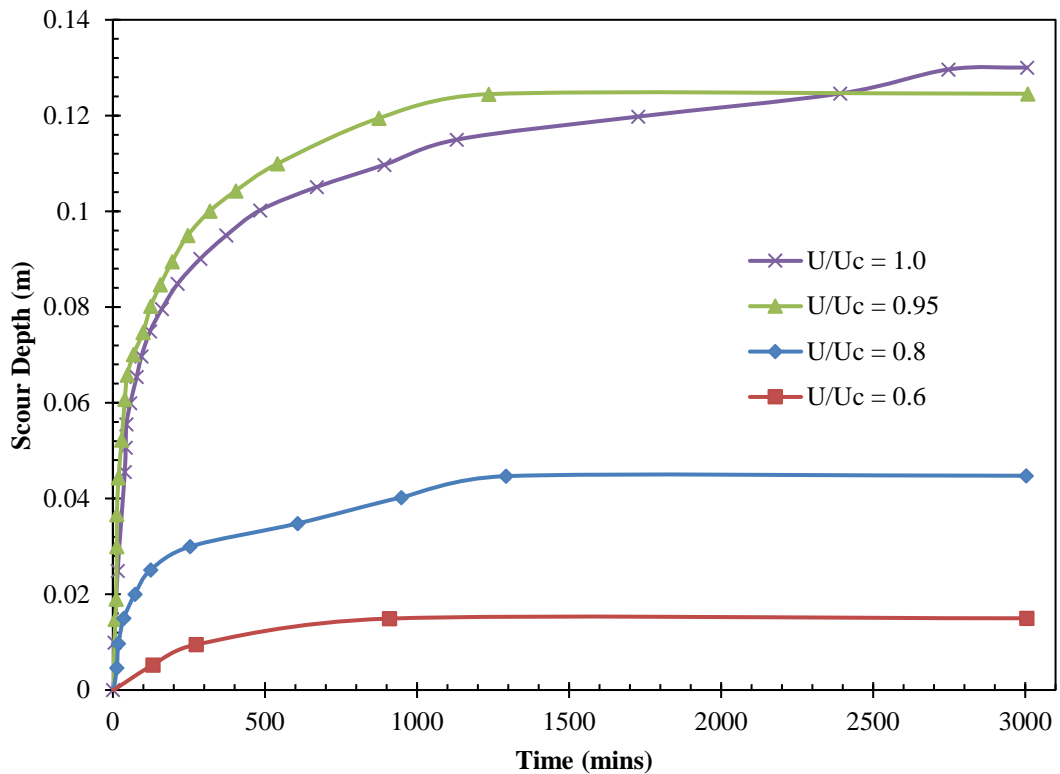


Figure 2-18 – Excess Shear effect upon Time and Depth (Kang and Yeo, 2012)

Furthermore, given a fixed excess shear stress the boundary layer height and water depth also affect the scour progression and equilibrium time and depth. This is due to the changes in wall shear stress as discussed previously due to change in upstream separation point, horseshoe vortex size and velocity, and vortex on the free-surface.

Live-Bed Scour

Developing Topology

In a live bed scenario, bed forms prevail due to tiny fluctuations of relief on the sediment bed. Travelling in the same direction as the current bed forms move through areas of scour, however their transition as they travel through the scour hole is dependent on the blockage ratio (Chiew, 1984), see Figure 2-19. The blockage ratio is the area blocked in the free-stream direction as a percentage of the total flow area. The difference in blockage is not as applicable in offshore, open waters unless other structures cause the effect, however may be important for the experiments used to validate the contained computational model.

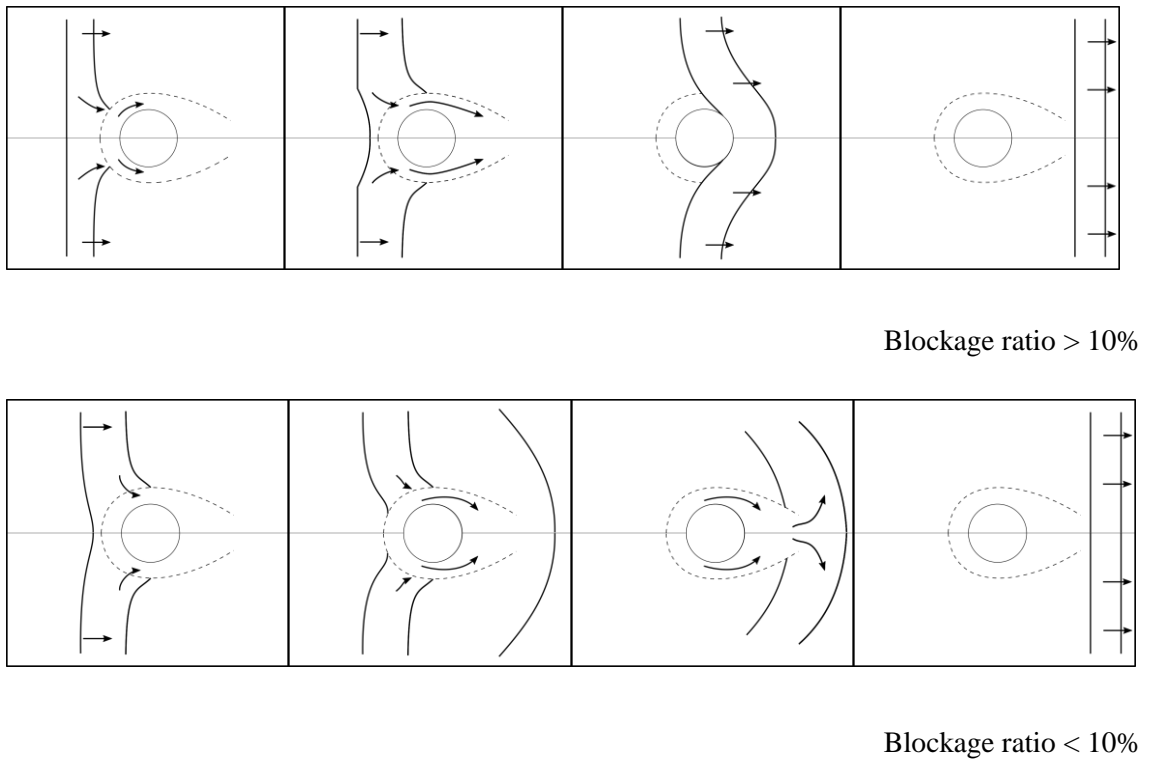


Figure 2-19 – Blockage Ratio effect on Bed forms

Bedforms are present during scour development but are more noticeable when a mean equilibrium value has been reached, as the shear forces within the scour hole are lower and therefore affect the bed forms less. Therefore, due to the fluctuations, equilibrium values for live-bed scenarios are based on a mean value, as shown in Figure 2-20, after (Richardson and Davis, 2001).

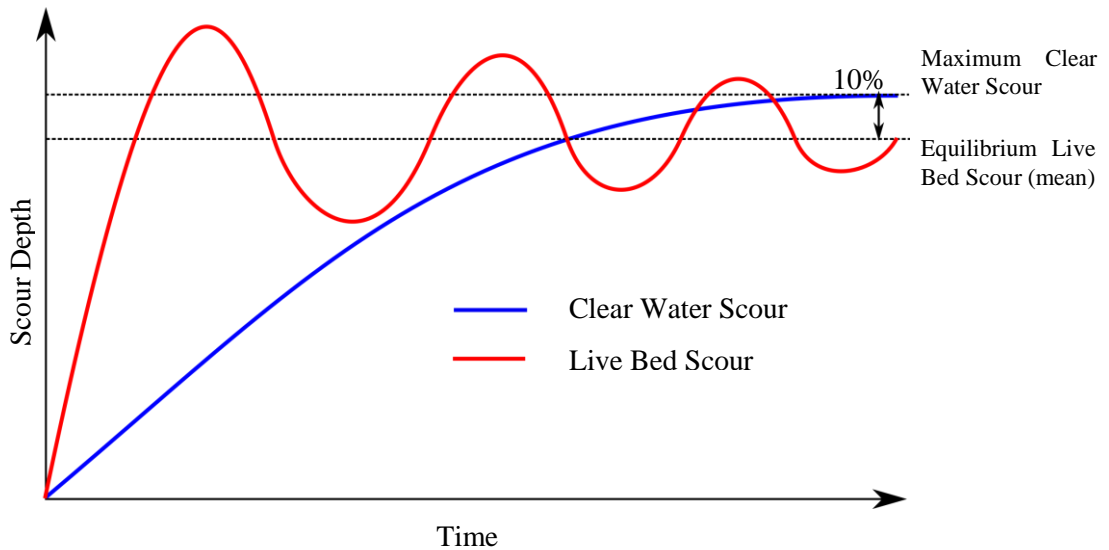
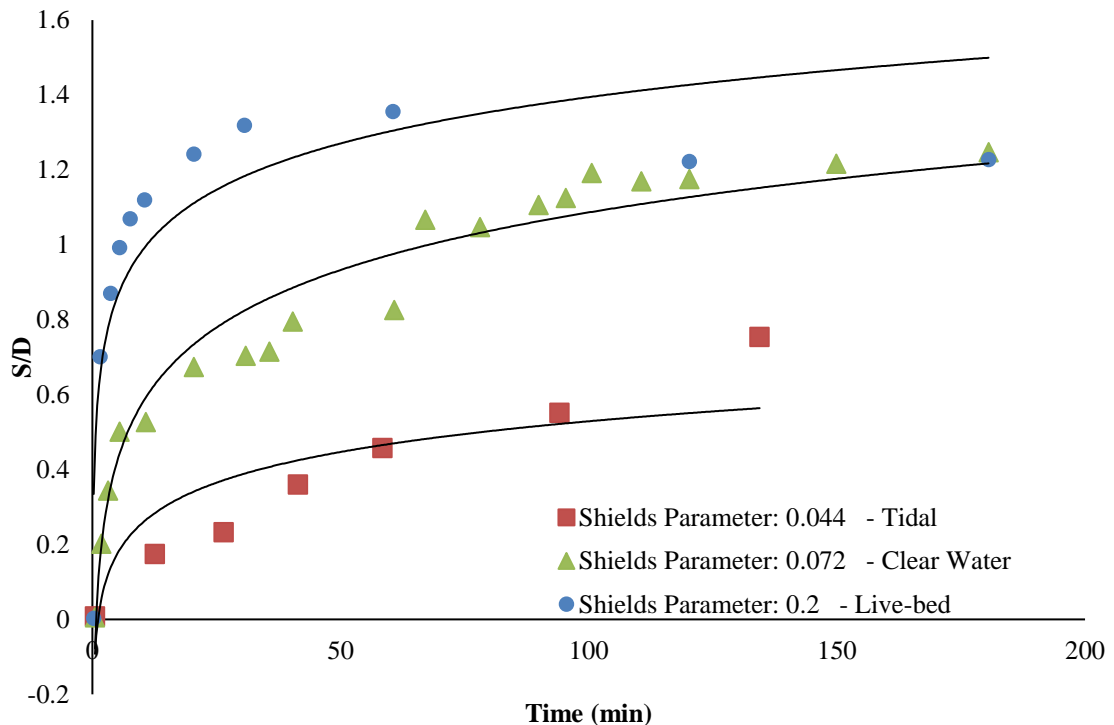


Figure 2-20 – Live-bed and Clear-water scour development

The development rate of live-bed scouring varies more than clear water scour because the excess shear stress range is significantly greater ($0 < \frac{\tau}{\tau_c} > 1$ compared to $1 < \frac{\tau}{\tau_c} > \infty$). Live-bed scour with a relatively low excess shear stress develops similar to clear water scour as demonstrated in

(Whitehouse, 2004) including; exponential development, deepest scour at the sides followed by the front and the removal of sediment from the back due to the high excess shear stress. However, in greater excess shear stress scenarios the scour rate is high for the majority of the scour process; removing the previous distinction between phases, Figure 2-21.



**Figure 2-21 – Experimental Live-bed and Clear-Water scour development
(McCann Thomsen, 2006)**

Dependent Factors

The equilibrium scour depth in live-bed conditions does not change considerably in comparison to clear-water, as the sediment transported out of the scour hole is matched by sediment into the scour hole.

Figure 2-23 shows an example of this, demonstrating the relationship between equilibrium scour depth and excess velocity as an initial decrease and then a climb to a depth approaching the maximum clear-water equilibrium.

The reason for this fluctuation is the bed forms, as the influx of sediment into the scour hole is determined by their height, shape and frequency; all of which change as the critical velocity is increased (Chiew, 1984). Figure 2-24 demonstrates the severe effect bed forms can have on the scour hole volume, followed by Figure 2-22 that shows the changes in bed form height as excess velocity is increased.

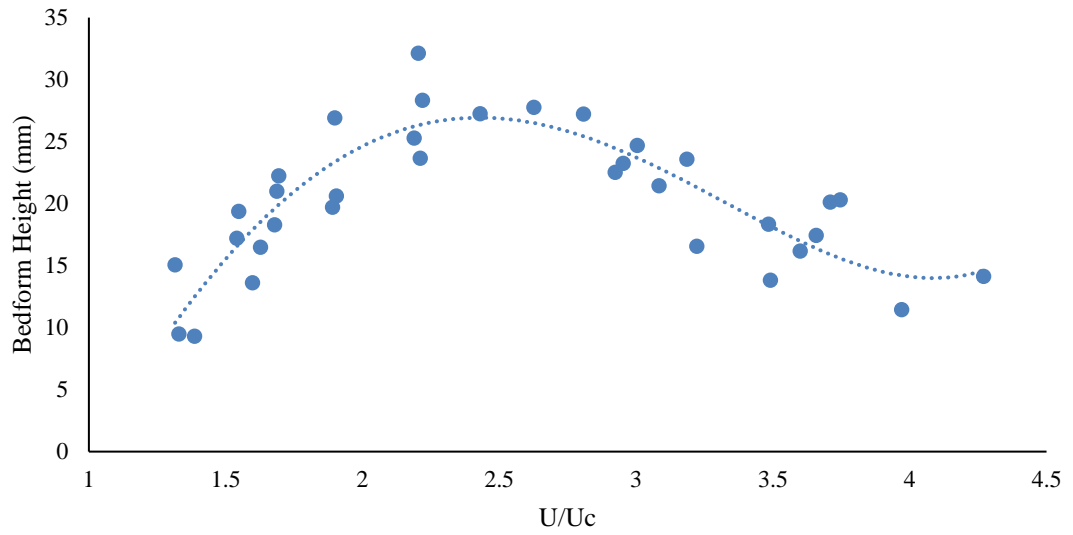


Figure 2-22- Transitioning Live-Bed Bed Form Height (Chiew, 1984)

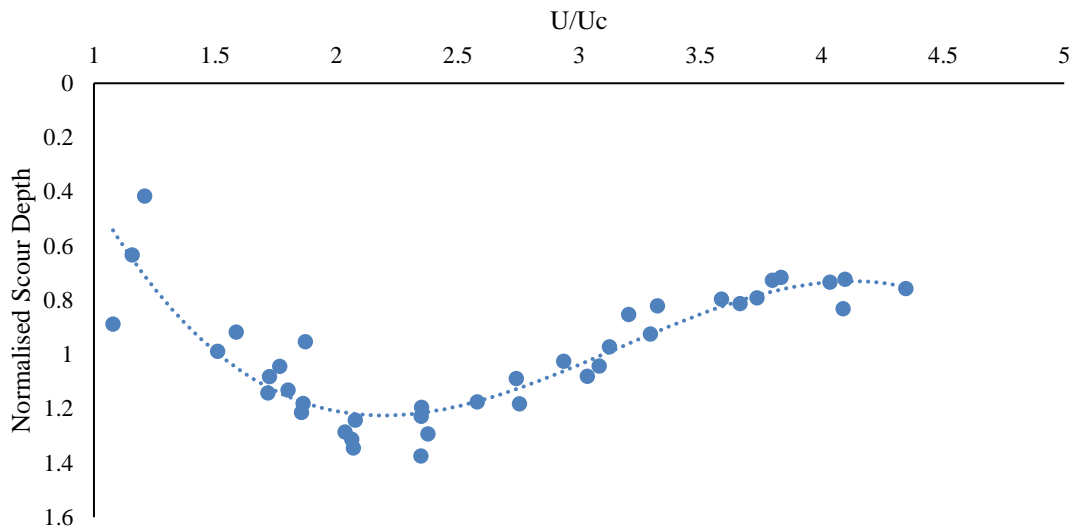


Figure 2-23 - Transitioning Live-Bed Scour Depth (Chiew, 1984)

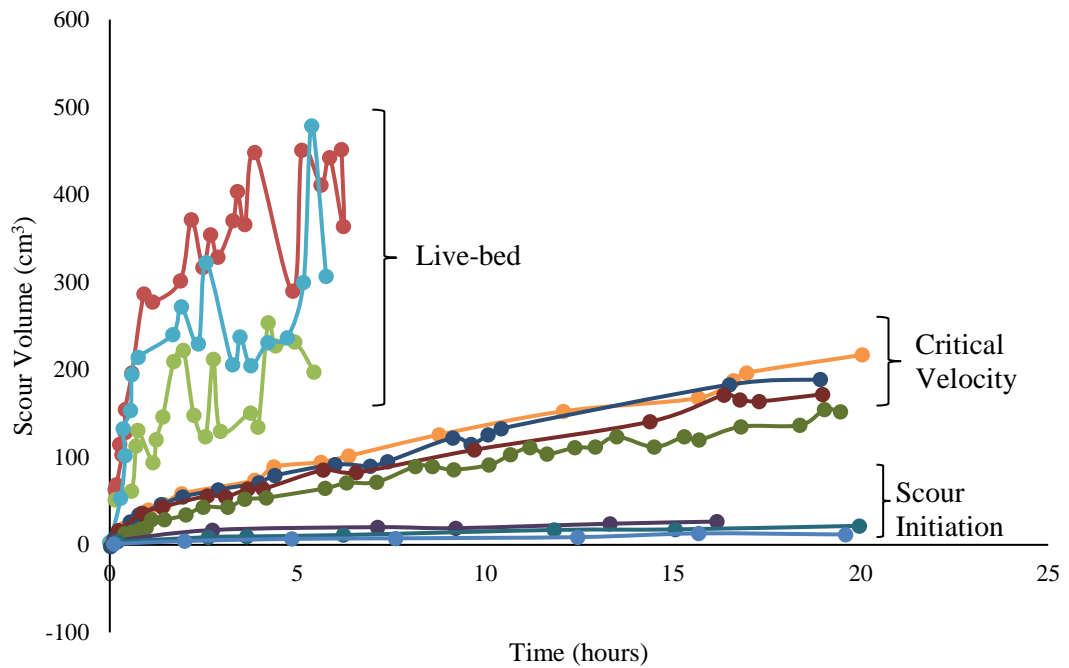


Figure 2-24 – Fluctuations in developing scour depth (Link and Zanke, 2004)

The effect of factors such as boundary layer height and water depth are the same as in clear-water conditions due to the reduction in critical shear stress, resulting in a lower equilibrium depth (Chiew, 1984). However, the scour rate has been shown to increase with critical velocity but with trivial effect on the equilibrium depth. As a result, equilibrium time decreases as the critical velocity increases, opposite to clear water conditions.

Scour around a Cylinder Summary

The scouring around a cylinder is primarily a result of the excess shear stress and Reynolds number, affecting the initial scour rate, equilibrium scour depth and time. Secondary to these the upstream flow profile can significantly affect the scour, specifically the boundary layer in terms of both height and profile. Other factors such as the sediment gradation and size affect both scour and erosion rates in any scenario in exactly the same way and therefore any changes are relatively simple.

The most complex and varied parameter is the scouring time, this varies significantly and given an increase in excess shear stress can increase or decrease depending on a clear-water or live-bed condition. The topological development is dependent on the balance between the scouring at the front and sides, due to the huge effect the scour at the sides has on the horseshoe vortex (HSV). Finally, the normalised equilibrium scour pattern at the front and sides does not change significantly regardless of flow conditions; however, the scour at the back differs due to the changes in lee-wake vortices.

Scour around Alternate Shapes

The horseshoe vortex, accelerated flow and lee-wake vortices are responsible for the highest wall shear stresses around a cylinder and consequently the maximum scour. Analysis of these mechanisms is common around mounted cylinders, however, they are also the main scour mechanisms around a variety of other shaped structures such as square and rectangular piles (El-Ghorab, 2013), gravity base foundations (Whitehouse et al., 2010), buried spheres (Dixen et al., 2013) and cones (Sumer et al., 1994) . The following section examines the differences in wall shear stress and scour between various surface-mounted geometries in comparison to a simple cylinder.

Square Piles

It is clear that under a current-only condition the equilibrium scour around square piles is deeper than at a cylinder, at all angles of attack (El-Ghorab, 2013, Sumer and Fredsøe, 2002). Khosronejad et al.(2012) compares the scour between a cylinder and two square piles at 45° and 90° under steady currents, revealing the changes in scour pattern; displaying the greatest scour point around a diamond at the side, square pile at the front edge and corner, and circular pile at the front between 0-80 deg.

The maximum scour depth around both square and circular piles is located at the front due to flow acceleration and the horseshoe vortex. (Raikar and Dey, 2008) investigates the developing horseshoe vortex as scour progresses around a square pile. The monitored turbulence in the horseshoe vortex region is compared to a similar study with a cylinder by Dey and Raikar (2007) revealing that the square pile increases the Reynolds stresses and vortex core size; this also agrees with the scour data in (Khosronejad et al., 2012).

The flow acceleration which contributes to scour around a circular pile is not present in the same sense around a square pile, as the blunt shape does not encourage an increase in velocity. Raised velocities are still present around a square cylinder due to the blockage caused; however, the scouring surrounding the front corners is due to shedding shear layers. This factor is more obvious when a square pile is at 45°.

The scour at the front of a square pile at 45° is minimal and suggests that the diamond shape weakens or irradiates the horseshoe vortex. A study by Richardson and Davis (2001) primarily based on abutments clarifies this, stating that due to reductions in the horseshoe vortex, the maximum scour around a sharp-nosed pier is 10% less than a cylindrical nose and 20% less than a square-nose. The greatest scour is instead located at the side corners due to shedding shear layers (Khosronejad et al., 2012). The resultant scour is evidently stronger than at the corners of a 90° square pile, as velocities are increased due to the removal of the horseshoe vortex and the front face is more streamline.

The difference in maximum scour depth between a cylinder and the discussed square pile orientations is represented in many equilibrium scour depth equations as a shape correction factor. The typical values are shown in Table 2-4.

Shape of Pier Nose	Shape Factor
Square	1.1
Round	1.0
Sharp	0.9
Circular	1.0

Table 2-4 – Pier Nose Shape Factors

In addition, (Richardson and Davis, 2001) provides additional shape factors for live-bed scenarios evidencing more variation between the cylinder and square shapes, with 1.3 for square nose, 1.0 for cylinder and 0.7 for diamond nose.

Cones

Sumer et al.(1994) and Hakimzadeh et al. (2012) show that cones scour less than cylinders. This is confirmed by Figure 2-25 which shown that scouring is reduced further if the angle of the cone is decreased as the upstream pressure gradient is reduced, which lowers the strength of the horseshoe vortex, flow acceleration and lee-wake vortex shedding (Sumer and Fredsøe, 2002).

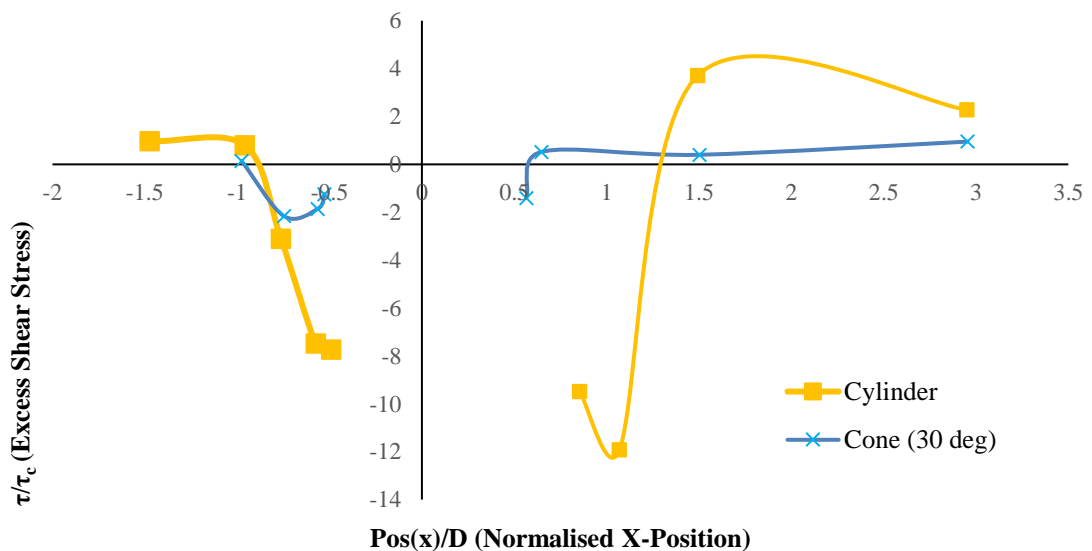


Figure 2-25 – Geometry Implications Upon Shear Stress (Sumer and Fredsøe, 2002)

Cylinders with collars

The prevention of scour using a simple collar is effective given a certain size as unanimously evidenced by (de Sonneville et al., 2010, Jahangirzadeh et al., 2014, Alabi, 2006, Garg et al., 2005). This is because collars primarily stop scouring due to the protection provided against the

horseshoe vortex and accelerated flow, Figure 2-26, but also in some cases protection from lee-wake vortices (Jahangirzadeh et al., 2014).

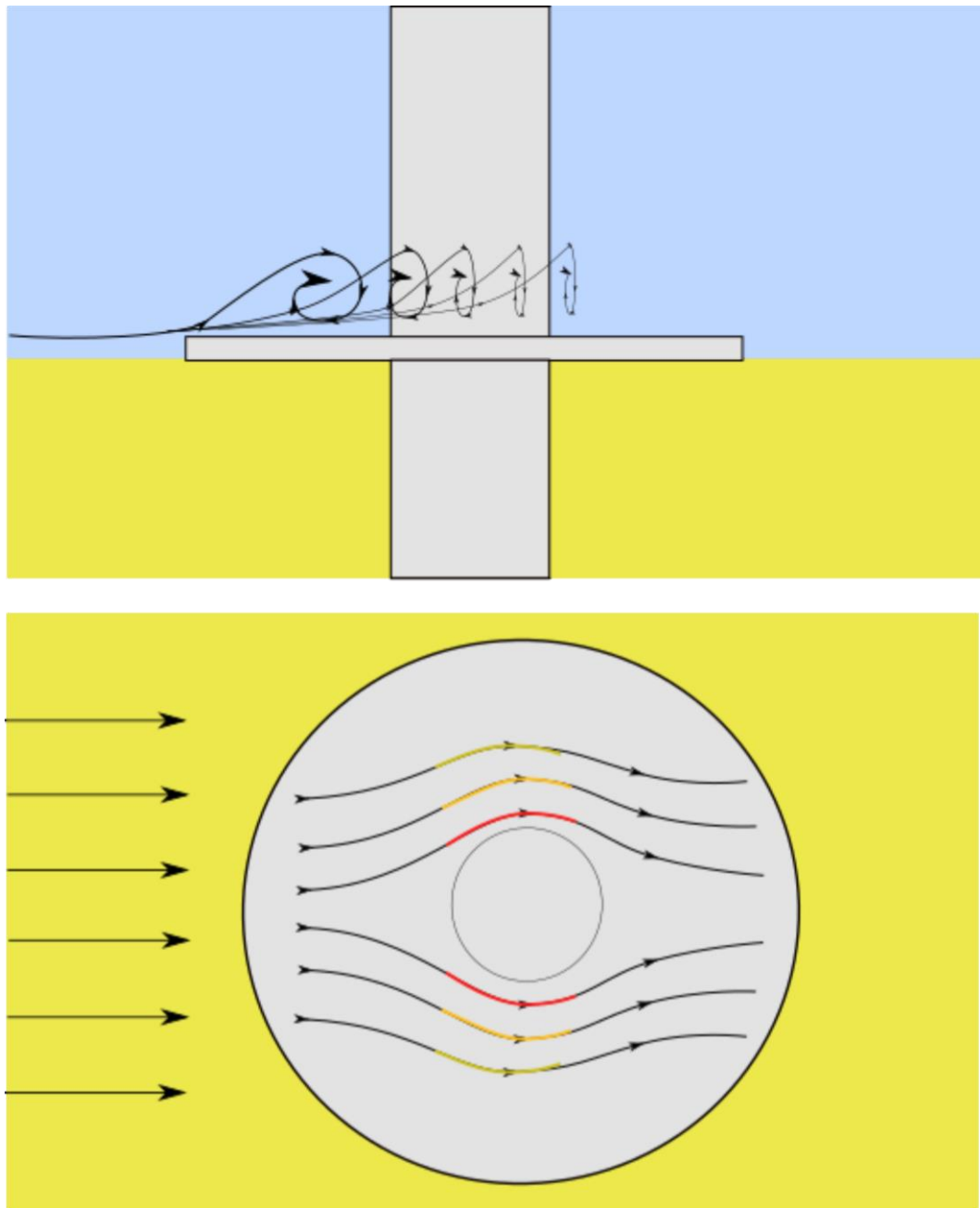


Figure 2-26 – Collar Protection against Horseshoe Vortices and Flow Acceleration

Existing literature on collar protection is comprehensive and includes the effect of collar position, shape, thickness, width and the effect of multiple collars. Garg et al. (2005) shows that the most influential of these factors are the collar width and position. Jahangirzadeh et al.(2014) and Garg et al.(2005) found that the most effective collar width is 3-3.5D. This can be related to the upstream separation point which increases with Reynolds number exponentially, with a maximum separation distance of approximately 1.2D from the pile centre (Sumer and Fredsøe, 2002). In addition, smaller collars remain beneficial as they significantly delay the scouring process, as found by Alabi (2006) with a collar of diameter 2D. However, the long-term benefits of this collar

size are minor. The vertical position of the collar is arguably more crucial than the width; as if the collar is undermined the collar can strengthen the vortex, and result in a scour depth greater than a cylinder with no collar at all; de Sonnevile et al.(2010) and Garg et al. (2005) found that this was true for a height of $0.5D$ from the bed. In contrast, Jahangirzadeh et al.(2014) found that placing the collar underneath the bed surface by a factor of $0.5D$ provided more scour protection than a collar adjacent to the bed surface; for widths of $2D$ to $3.5D$.

Gravity Bases

Gravity base foundations are made of steel or concrete and rely on gravity for stability; which is commonly ensured by filling the structure with ballast. Many offshore structures use gravity foundations including lighthouses, breakwaters, oil platforms and more recently wind turbines. Gravity-based wind turbine foundations differ in geometry; however, the base commonly features an upper cylindrical section leading down to a larger filled conical section with a cylindrical base and a collar, Figure 2-27. Despite these common elements, it is clear from the geometric relationships of the previously discussed structures that subtle changes in geometry can cause obvious changes in the erosion pattern and scour depth.

The initiation of scour underneath a gravity base foundation can lead to catastrophe. However, at present limited investigations have been made into scouring underneath a gravity base structure. This can potentially reveal what conditions are necessary for scour to propagate underneath or result in failure. Currently, the only related research is the amplification of horseshoe vortices under collars, but this only provides a small insight into the scouring underneath a structure.



From the left: Gravitas (Gravitas, 2014). Skanska Marine Projects and Grontmij (Skanska, 2014). Vici Ventus (Vici Ventus, 2014).

Figure 2-27 – Gravity Base Examples

Larsen and Frigaard (2005) investigate the scouring around a gravity base and three other foundations types with and without protection under current and wave conditions, Figure 2-28. The scouring without protection showed that the gravity base (C) scours the same as the suction bucket (D) under current only conditions, less than both the monopile (A) and concrete tripod (B). Under waves and current the gravity base scours slightly more than the suction bucket however still less than the tripod and monopile.

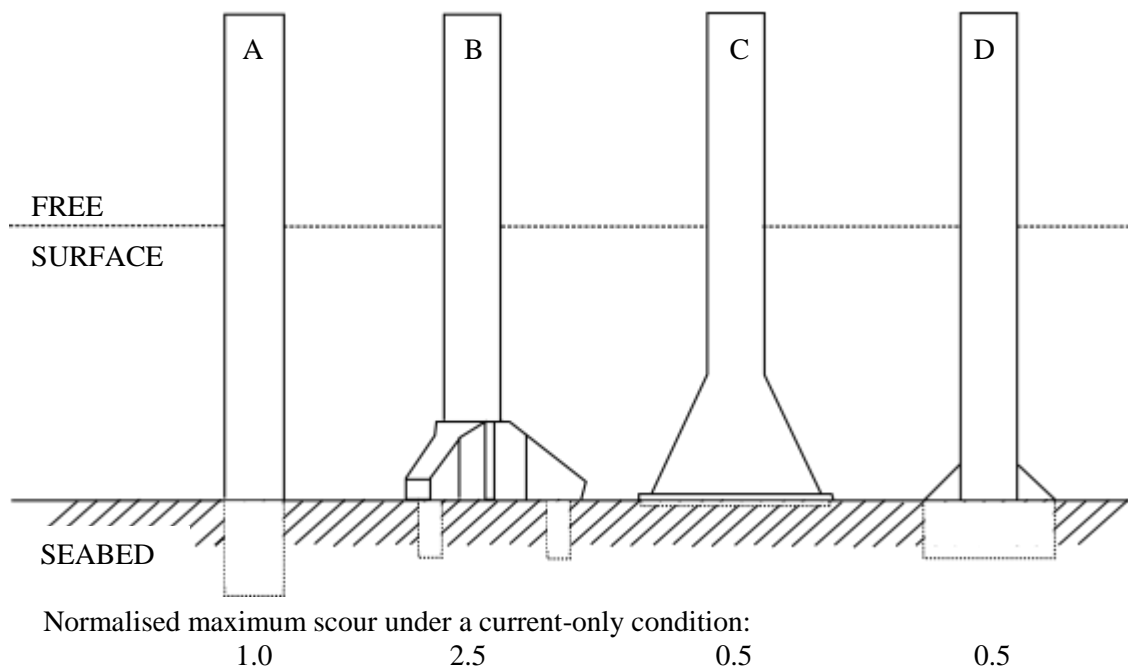


Figure 2-28 – Experimental scour depth around different foundations (Larsen and Frigaard, 2005)

Further insight into the scouring around a gravity base structure can be obtained using the initial scouring around similarly shaped suction caissons. However, these structures extend below the bed surface and therefore do not provide insight into the scour underneath.

Suction Caissons

A suction caisson is a large cylindrical, open bottomed base that is installed using the gravitational force upon its weight or with additional negative pressure applied to the cavity.

The geometry includes a large bottom cylindrical ‘bucket’ section and a smaller top cylindrical connecting section, with an intermediate section that varies in shape and size, Figure 2-29. They are considered as a gravity base because the weight of the sediment in the ‘bucket’ provides the stability; however, they are separated from traditional gravity bases due to the differences in scour caused by to the extension beneath the bed surface.

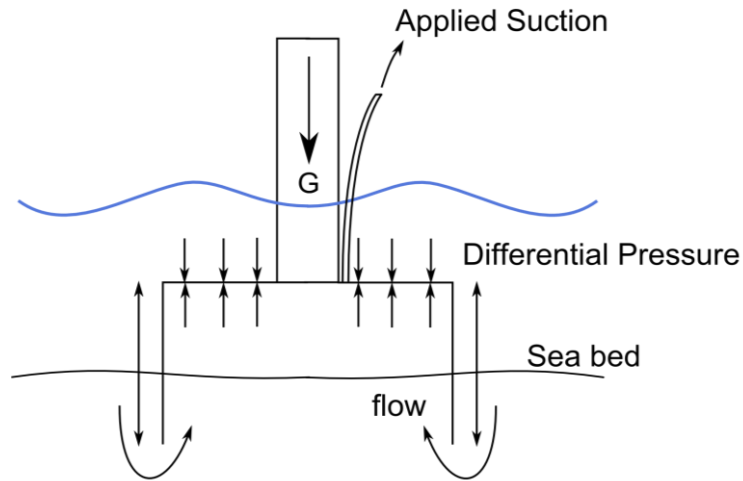


Figure 2-29 – Suction Caisson Diagram

Research on the scouring around caissons is limited, which is speculative because their use for offshore wind turbines is relatively new (Carbon Trust, 2014). It is apparent from Melville (2008) that the scour depth around a caisson structure is dependent on the foundation diameter and protrusion height from the bed surface. If the protrusion is submerged below the sand bed the scouring can be reduced, as the top of the protrusion provides protection. As the protrusion is raised towards the same level as the bed the scouring is reduced further, until an inflection point where the scouring starts to increase again. This increase continues as the protrusion passes the bed-level and continues until a maximum is reached, Figure 2-30.

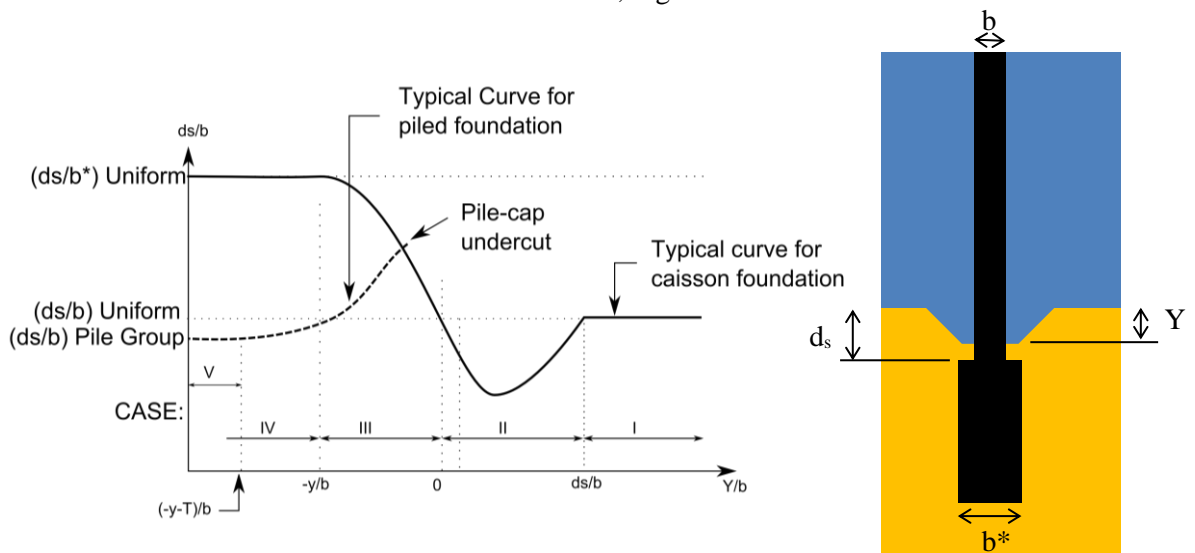


Figure 2-30 – Caisson Parameter Effect on Scour depth. Data: (Melville, 2008)

The mid-section between the two diameters is also shown to impact the scouring by Whitehouse (2004), whereby when the protrusion is level with the bed surface a conical interface is shown to scour more than a blunt, 'flat-topped' interface. This is related to previously described conical effects; as if the cone angle is increased the adverse pressure gradient and horseshoe vortex scour will also increase.

Tri-Piles

Tri-piles and tripods can be used with both suction bucket and pile driven designs. They are advantageous as scour is minimised compared to a monopile design and there is less preparation required before installation. In addition, the continually increasing turbine size is making tripod designs more practical, as they dismiss the need for increasing large hammers to drive the piles into the seabed (Zaaijer, 2003).

However, due to the size and additional complexity of these structures the construction and maintenance costs are increased (Van der Tempel et al., 2010) and there are additional transport issues.



Figure 2-31 – Tripod Foundation
(Subsea World News, 2014)



Figure 2-32 – Tri-pile Foundation (Brickwell, 2012)

An interesting study by Stahlmann and Schlurmann (2012) on scouring underneath tripod foundations shows that the scouring does not just occur around the three piles, but also underneath the central pillar.

Larsen and Frigaard (2005) investigate the scouring around a monopile, conical gravity base, conical suction bucket and tripod foundation. The unprotected tests ran with the four foundation types show that the scouring is worse around the tripod foundation for both current and waves conditions. This does not agree with the results of Zaaijer (2003) however it is evident when comparing the tripod designs between Stahlmann and Schlurmann (2012) and Larsen and Frigaard (2005) that differences in the central section can significantly increase the contractual scour underneath the structure.

Monopiles with slots

The investigation into piles with slots is relatively unique and is interesting from a hydrodynamic point of view, however, problematic from a structural strength perspective. Hakimzadeh et al. (2012) and Liang (2015) investigate the advantages of conical and cylindrical piles with slots in the centre and demonstrate the resulting scour reductions, due to the reduction of pressure gradients in front and behind, and the disruption and resultant stress reduction due to lee-wake vortex shedding and horseshoe vortices.

Monopiles with strakes

Strakes have been used on both large and small cylindrical structures to influence aerodynamics, for example on chimneys stacks and towers to reduce the lee-wake vortex shedding effects, as shown in Korkischko and Meneghini (2011). Their use within hydrodynamics is less common however Izadinia and Heidarpour (2012) test strakes and collars around monopiles in order to reduce scour. The results are encouraging and show that strakes can lead to a scour reduction of up to 50%. This is because in addition to reducing the lee-wake vortices the cable also disrupts the down-flow at the front that normally strengthens the horseshoe vortex.

2.3.2 Representation

Prediction Formulae

Prediction formula are only available for shapes with a uniform cross-section and provided by a number of authors, however, the dependant variables are consistent and can be split into four main groups;

- Flow; represented by fluid density, viscosity, velocity, and depth
- Sediment; represented by sediment diameter, critical velocity/shear stress, density, and distribution
- Pier (cross-sectional geometry); dependant on shape but only diameter for monopiles
- Time; represented by total and equilibrium time.

The relationships between each of these variables have been studied extensively to form equations for a number of features, as described in the following.

Maximum Scour Depth

Investigation into the maximum scour depth around cylinders is common and has led to a number of prediction formulae. These have been assessed several times by different sources; for example Gaudio et al. (2010) and Mohamed (2005). However, these studies amongst others discussed within, reveal the unsatisfactory nature of existing equations, and indicate that they should only be used as a guide (Graf and Altinakar, 1998). In addition to those reviewed in (Gaudio et al., 2010, Mohamed et al., 2005) others are available in (Melville and Chiew, 1999, Olsen and Kjellesvig, 1998)

Width, Length, and Area Formula

In addition to maximum scour depth formula, Khwairakpam et al. (2012) is one of the first to present prediction formulae for the width, length and area of the scour hole. However, despite a close agreement between measured and predicted values, the dataset used is limited and subsequently the validation is not thorough.

Equilibrium Scour Time Formula (Time Scale Formula)

The time taken to reach an equilibrium state is an important factor for both marine and alluvial scenarios. In offshore environments it is important to know the time constraints between the placement of a structure and its protection (Harris et al., 2010), as typically these activities are not successive. In the case of bridges, excessive scouring is one of the main causes of failure, and therefore establishing and then either compensating for or protecting against the maximum scour depth is critical (Guney et al., 2011). Despite the importance of equilibrium scour time there are a limited number of prediction formulas. Throughout publications the most commonly used is from (Sumer et al., 1992), which includes one for currents alone and another for waves alone, also see (Melville and Chiew, 1999) and (Peder Hyldal Sørensen and Bo Ibsen, 2013).

Scour Background Theory Summary

This chapter has explored the foundation theory necessary for the prevailing scour experiment and computational model. This has been discussed in three sections, the expected offshore flow conditions, the physics of erosion and the fluid dynamics around foundation structures.

The fluid dynamics around typical foundation structures comprise of three main mechanisms, the horseshoe vortex, flow acceleration and vortex shedding. The size, magnitude and frequency of these mechanisms are dependent on the fluid properties, sediment bed and pile geometry. These mechanisms drive the scour process that is initiated once the threshold bed shear stress is exceeded, resulting in sediment driven along the bed or up into the suspended load layer. The magnitude of the threshold value and volume of sediment removed is dependent on the flow velocity, properties of the sediment, geometry of the bed and direction of flow. Examples of scour development have shown that for a shape of uniform cross section the scour depth propagates exponentially resulting in an asymptotic value, for both live-bed and clear-water scenarios. The resultant scour rate and asymptotic depth is dependent on all discussed variables, due to the combination of flow mechanisms and sediment erosion.

Finally, the pile shape effect upon scour topology, development, and rate due to changes in flow mechanism are demonstrated, aiding later analysis of scour around unique geometries with non-uniform cross-sections.

Chapter 3 Gravity Base Foundation Experiment

Scour around a gravity base foundation was examined experimentally under a unidirectional current to provide a greater understanding of the scour topology around increasingly popular, yet alternate gravity-based offshore wind turbine foundations. In addition, even though it should be avoided in reality, it enabled a great insight into the scouring underneath such structures. Furthermore, because the experiment was in-house it is optimal for validating computational models as all of the required variables are known or can be ascertained.

3.1 Facility

The experiment was conducted at ‘The Deep’, Kingston upon Hull, in the Total Environment Simulator (TES), MCGOVER. The TES is 16 m long, 6 m wide and 1.6 m deep with glass walls on one side. The inlet and outlet are located either end of the flume and are connected by two parallel pumps each with a maximum flow rate of 500 l/s and sediment recirculation capability. The facility also includes an 8-paddle wave generator capable of producing waves up to 0.5 m high, (University of Hull, 2013), Figure 3-1- TES Facility, Hull.



Figure 3-1- TES Facility, Hull.

3.2 Setup

The experimental conditions are based on the North Sea, where the average water depth is 35m with a maximum spring tide current velocity of 2.2 m/s. This was simulated using a 1:100 scale, resulting in a water depth of 0.35m and flow rate of 0.22 m/s, using Froude number scaling. However, the scaling method was not applied to the sediment as this would increase the cohesive properties and change the sediment behaviour, as described by Whitehouse et al.(2006) in a similar scenario. Therefore, the sediment bed was composed of a sediment diameter of 0.15mm. The flume was set up with a horizontal bed surface that comprised of a central sediment section surrounded by a fixed-bed, Figure 3-2. The sediment section extended downstream by 8 m from the inlet at a constant width of 2.3 m. The depth of sediment depth was 0.1 m from the inlet to 4m downstream and 0.2 m local to the structure in order to capture the deeper scour.

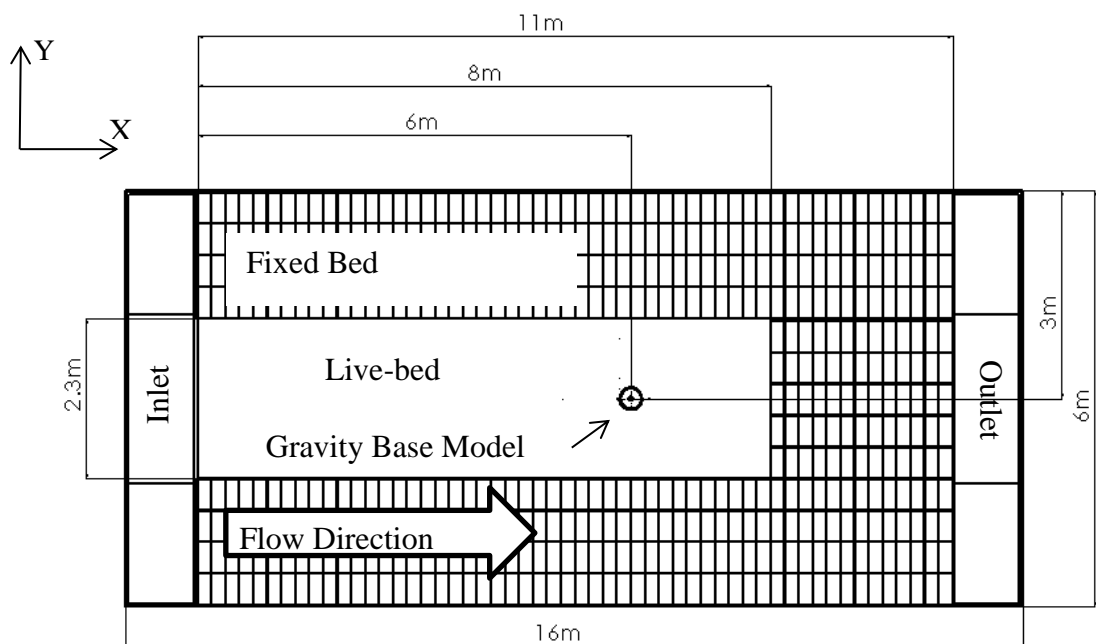


Figure 3-2 – Flume Setup

3.2.1 Gravity Base Foundation Model

The gravity base model was of steel construction and painted in order to ensure a smooth surface. The model is of 1:100 scale as can be seen in Figure 3-3. It was positioned 6 m downstream from the inlet, to allow the flow to develop before interacting with the structure and sufficient length downstream of the structure to capture any lee-wake vortex induced scour.

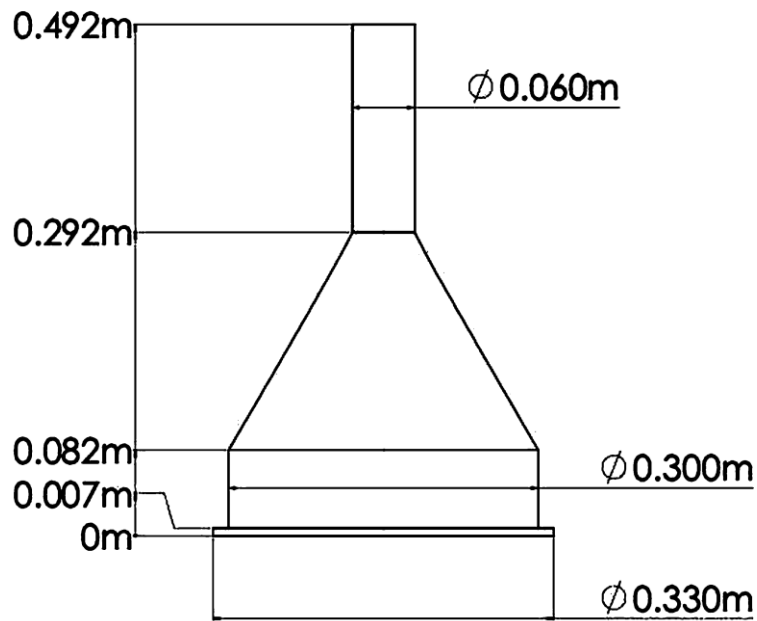


Figure 3-3 – Gravity Base Foundation Model

3.2.2 Measurement Equipment

Acoustic Doppler Velocimeters

Four Nortek 10Mhz Acoustic Doppler Velocimeters (ADV's) (Nortek AS, 2015) were employed to record instantaneous 3D velocity and turbulence values. The ADV's operate by analysing a small volume sample of sediment-laden fluid located 0.15 m below and therefore measurements were not possible within 0.15m of the free-surface. The probes are also capable of measuring the vertical distance to the bed surface, which was performed at each measurement location. The probes were mounted transversely on an overhead motorised carriage at $y = 0$ m, 0.15 m, 0.3 m and 0.87 m, enabling velocity measurements to be taken at any point around the structure.

3D Scanner

A 3D laser scanner (Leica-Geosystems ScanStation 2) was used to record the initial and final bed topology. Scans were taken with a resolution of 1 mm in close proximity to the structure and 2.5 mm elsewhere. Additional scan details are in the following 'Procedure' section.

3.3 Procedure

The flume was slowly filled with water to not disturb the sediment until a water level of 0.35 m was obtained; considering the change in depth once the pumps were started and the flow was induced. The pump speed was then gradually increased until a combined mass flow rate of 400 l/s was reached, resulting in an average flow velocity of 0.22 m/s.

Velocity measurements began after several minutes to allow time for the flow to stabilise. Readings were taken at 44 locations (Figure 3-4) at 10 different heights (0.05. This was achieved

by moving the ADV mount manually in the x-direction and electronically in the y-direction, before pausing to take a reading. All ADV data was taken in the first 1.5 hours of the experiment, prior to any major morphological changes. Each recording was made at 25 Hz for 130 s and post processed to obtain average velocities using computer software WinADV (Bureau of Reclamation, 2007). Filtering on these samples included removal of readings due to communication errors and phase-space threshold de-spiking (Goring and Vladimir, 2003). The developing bed topology was regularly monitored until no further scouring was visible. The experimental was ran for a total of 10 hours over three sessions, two of 1 hr 30 min and one of 7 hrs.

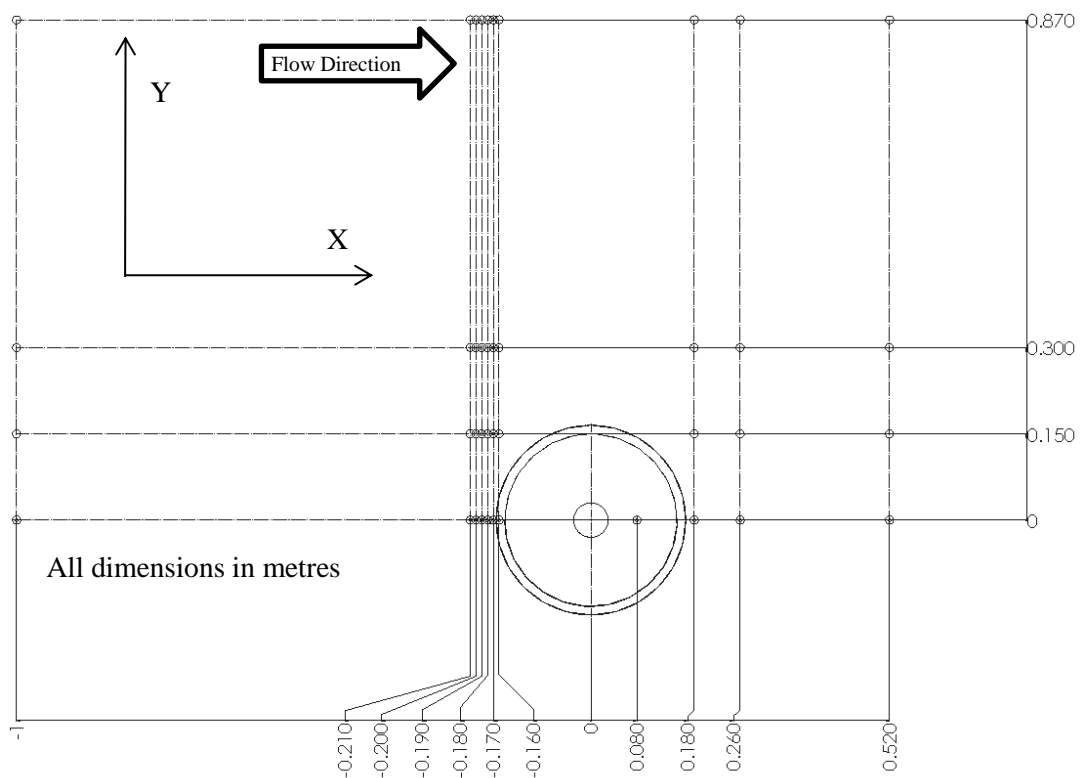


Figure 3-4 – Measurement Positions

The flow velocity was gradually decreased, and the flume was slowly drained in preparation for the final 3D scan. These were taken from three locations, upstream to the left and right and one centred downstream. Several fixed-target markers were employed so that the three scans could be aligned and merged afterwards in order to create a complete 3D representation. The scan data was processed by exporting the data from each scan using Leica Cyclone (Leica Geosystems, 2008) in a point cloud format, then aligned and merged in CloudCompare (Girardeau-Montaut, 2013) followed by cleaning in Meshlab (Cignoni et al., 2008) using distributed point sampling (Ranzuglia et al., 2012). In order to visualise the merged cloud it was converted into a mesh using MeshLab (Cignoni et al., 2008) and imported into CFD Software Star-CCM+ (CD Adapco, 2014).

3.4 Results

3.4.1 Hydrodynamics

This section analyses and identifies the main hydrodynamic features around the gravity-base model using the processed velocity and turbulence data. Each feature is discussed in order of position starting with the furthest upstream.

Upstream Velocity Distribution

The velocity profile, 1 m upstream from the pile is of logarithmic distribution, however, it is not fully developed. This is clear from Figure 3-5, which shows a more developed flow downstream from the pile.

Figure 3-6 shows that the velocity distribution 1 m upstream is not uniform and already features a reduction in velocity in the centre of the channel, due to the adverse pressure gradient caused by the pile. However, despite the difference in velocity profile, further analysis of the velocity profiles using the log law reveals no statistically significant change in roughness height (0.166 mm with a standard deviation of 0.04) or bed shear stress (0.185 Pa with a standard deviation of 0.006).

Figure 3-7 shows a more detailed view of the velocity decrease as the flow approaches the pile along the central plane $y = 0$. This shows that the lower half of the channel (< 0.15 m) shows a greater decrease in velocity than the top, because the cross-sectional area of the gravity base is greater at the base.

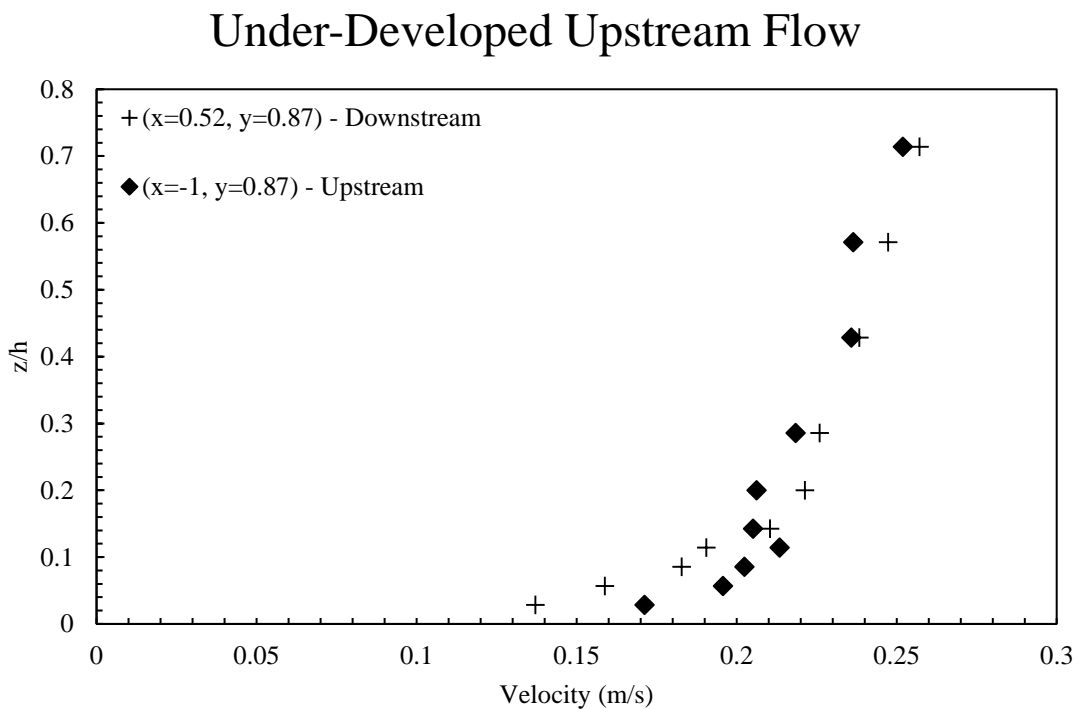


Figure 3-5 – Velocity Profiles showing under-developed upstream flow

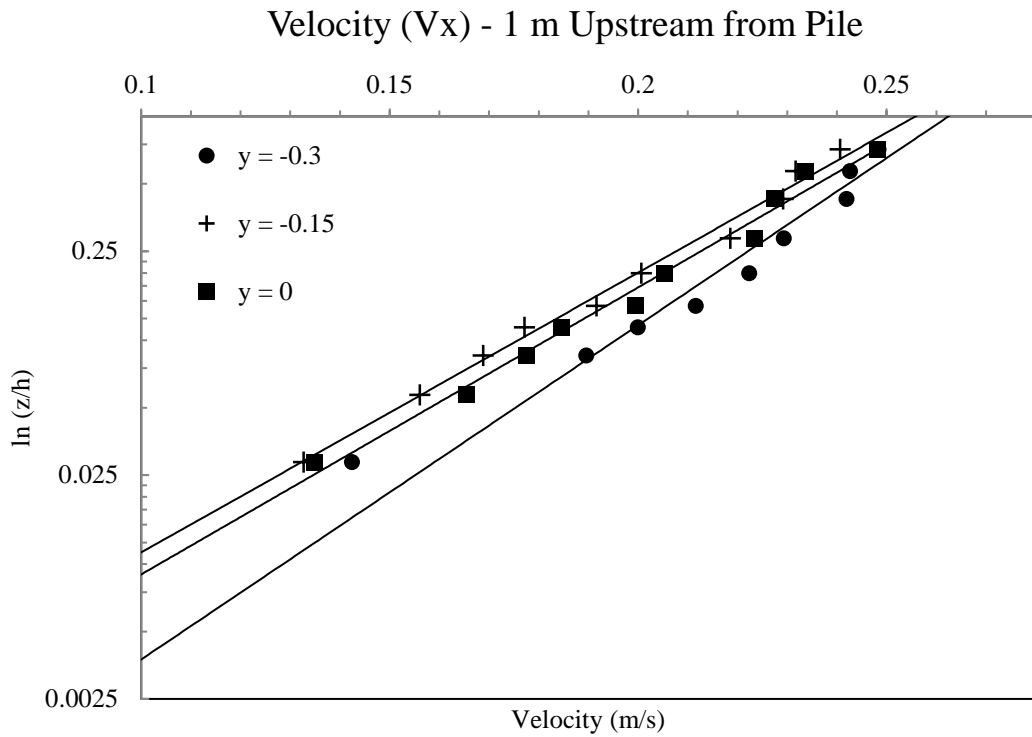


Figure 3-6 – Velocity (V_x) Reduction due to Obstruction, 1m Upstream.

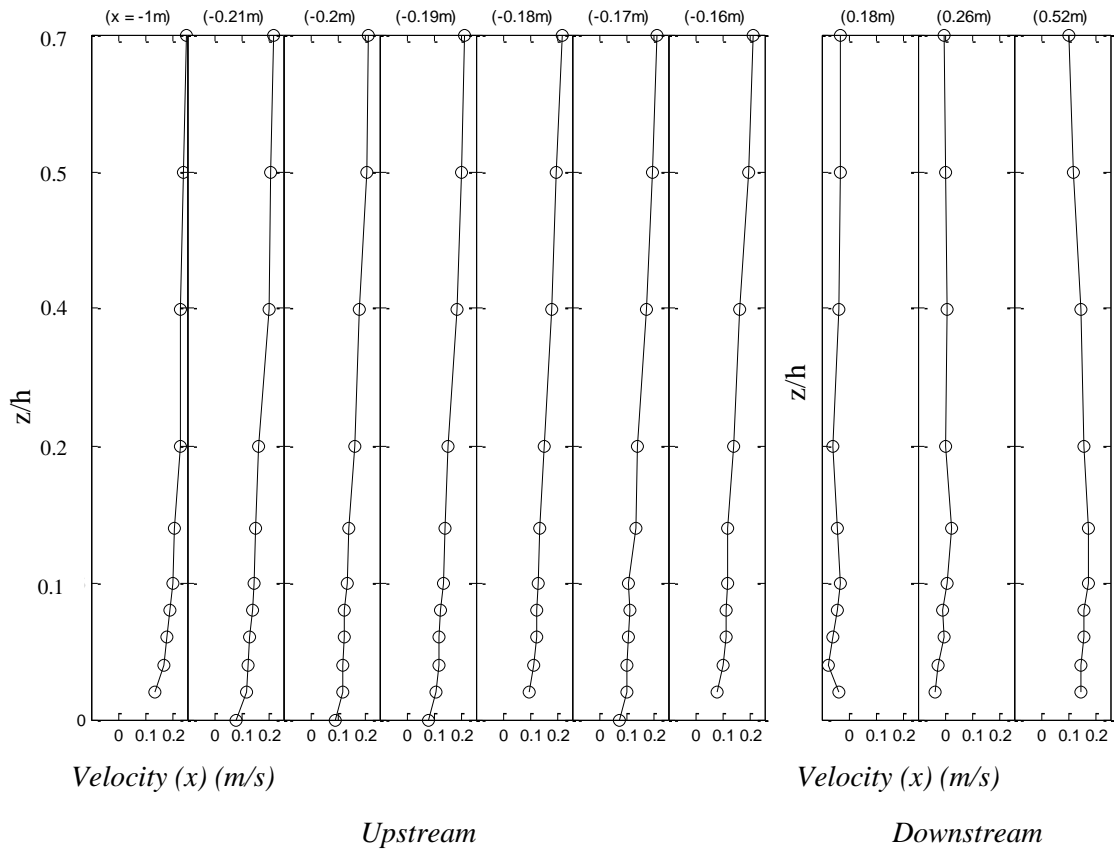


Figure 3-7 – Velocity Profiles along the Centreline

Horseshoe vortex

Figure 3-8 represents the vertical velocity components of the flow along the central plane at 9 heights from 0 to 0.25 m. In the lower section close to the pile down flow is present below $x = 0.05$ m, indicating the formation of a horseshoe vortex; following the dynamics that surround horseshoe vortices as discussed in Chapter 2. This is supported by the later formation of a small bank on the bed upstream of the horseshoe vortex position within the first hour, and the formation of a trench underneath the horseshoe vortex thereafter.

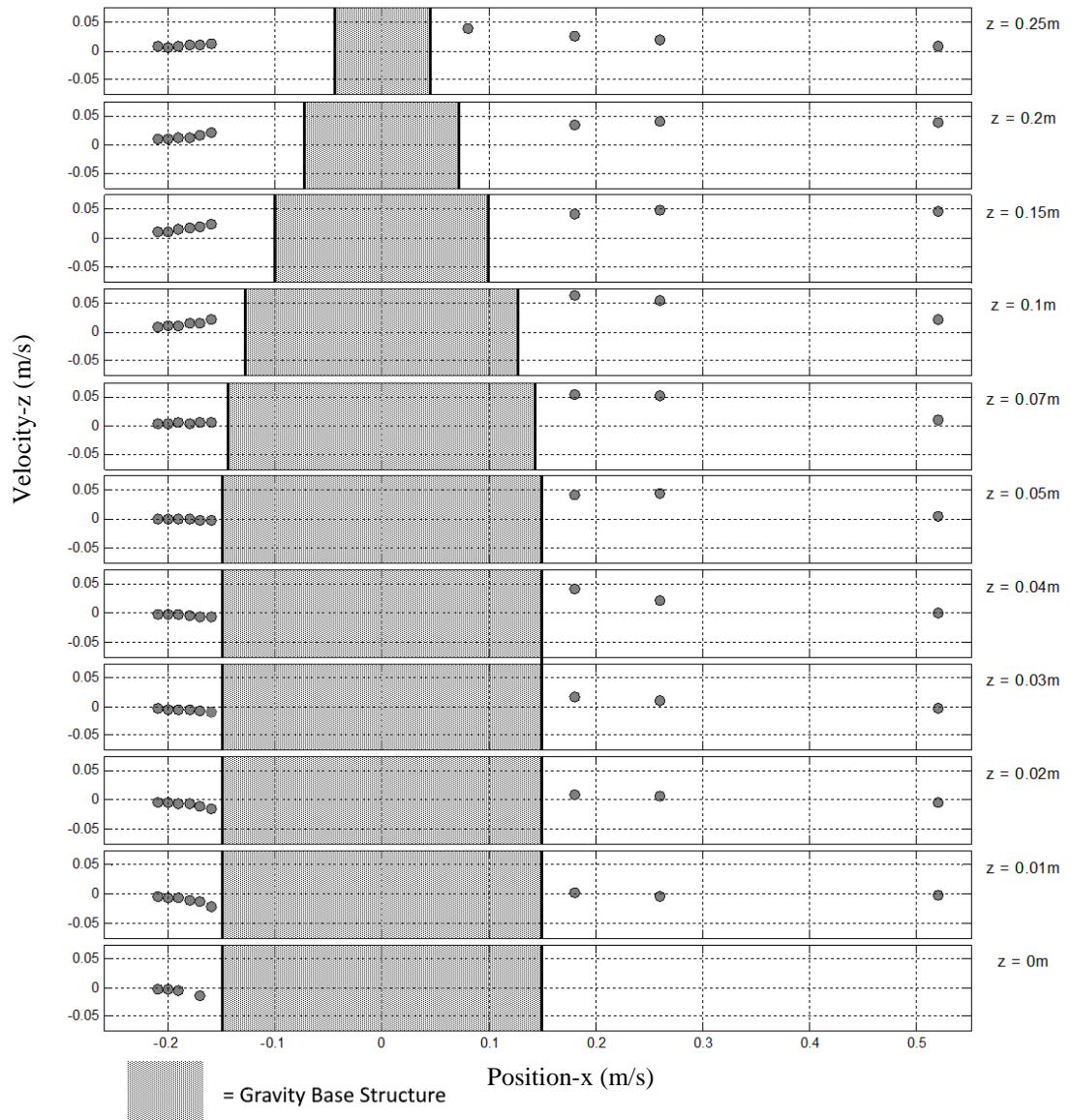


Figure 3-8 – Vertical Velocities surrounding Gravity Base Foundation

Flow Acceleration

Figure 3-9 shows three velocity profiles, two from the side of the pile and one from upstream for reference. A comparison of the three shows acceleration of flow around the pile with a maximum velocity of 28.5 m/s located in the lower half of the boundary layer.

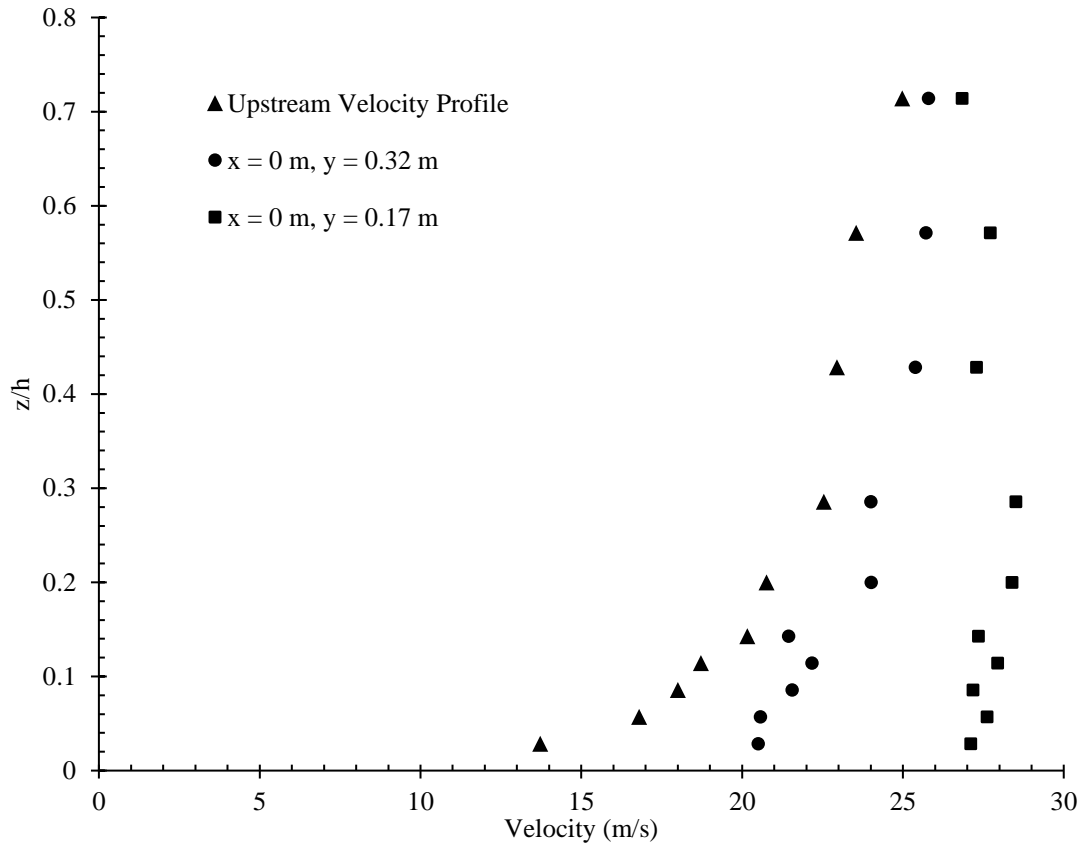


Figure 3-9 – Experimental Velocity Profile Development

Vortex Shedding

The cylindrical nature of the gravity base foundation makes it highly susceptible to vortex shedding. Estimated shedding frequencies are between 0.185 and 0.75 Hz based on a maximum and minimum diameter of 0.3 m and 0.06 m, and a Strouhal number of 0.2 (Strouhal, 1878). Velocity fluctuation maps from above and the side, Figure 3-10 and Figure 3-11, show high turbulence in typical areas of vortex shedding.

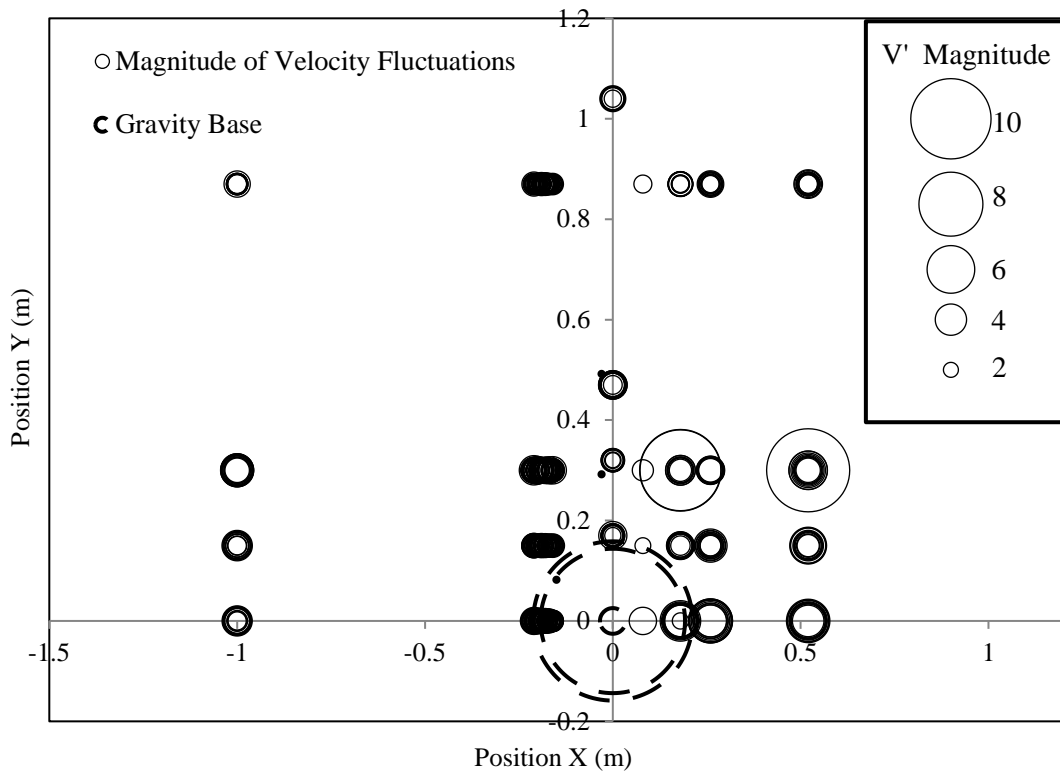


Figure 3-10 – RMS Local Velocity Magnitude Fluctuations (X-Y Plane)

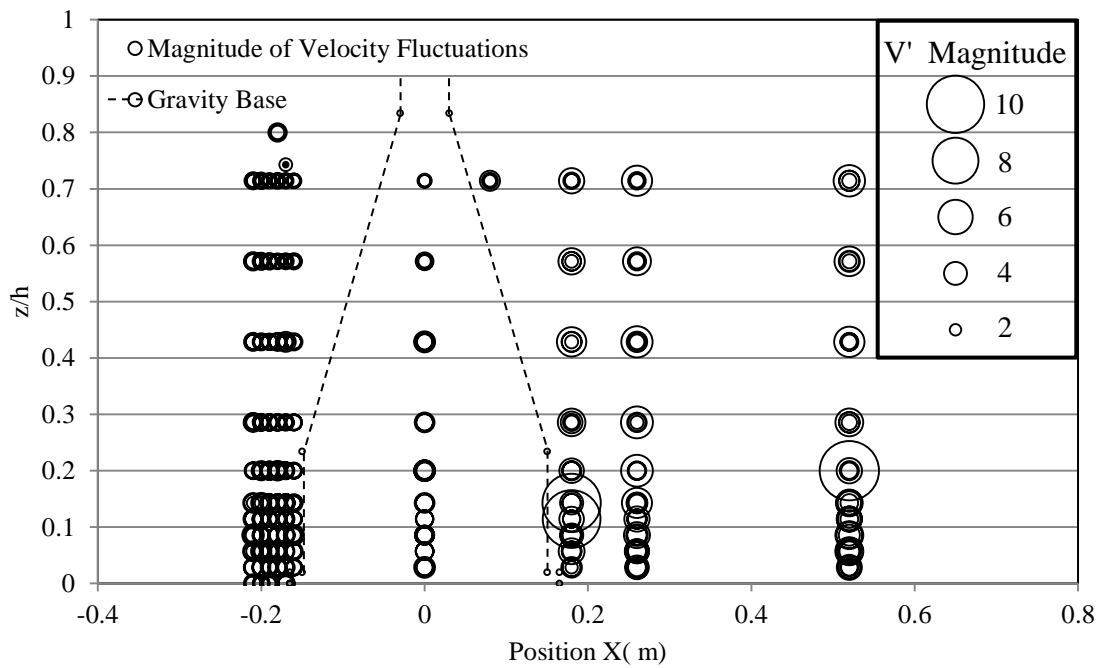


Figure 3-11 – RMS Local Velocity Magnitude Fluctuations (X-Z Plane)

Further Fourier analysis of the velocity data taken in this area revealed one significant frequency, at position 0.18 m, 0.3 m, 0.114 (x, y, z/h). The frequency amplitude graph for the velocity (x-direction) data taken at this point is shown in Figure 3-12. The peak frequency at 0.93 Hz is significantly greater than the shedding frequency (0.15 Hz) related to the adjacent 0.3 m diameter base and Strouhal number of 0.2. In conjunction with the wide position of the high-turbulence and therefore vortex shedding areas this is due to early detachment of the boundary layer.

The difference between the gravity base shape and the standard cylindrical shape that the Strouhal number is based upon is the reduction in diameter above, i.e. the conical shape. It is presumed that this reduces the boundary layer separation angle on the larger diameter because the separation on a smaller, concentric diameter occurs at a different time and position. It is unfortunate that frequencies could not be obtained in-line with the conical shape as it would have been extremely interesting to analyse the difference and therefore link between frequencies as the diameter changes.

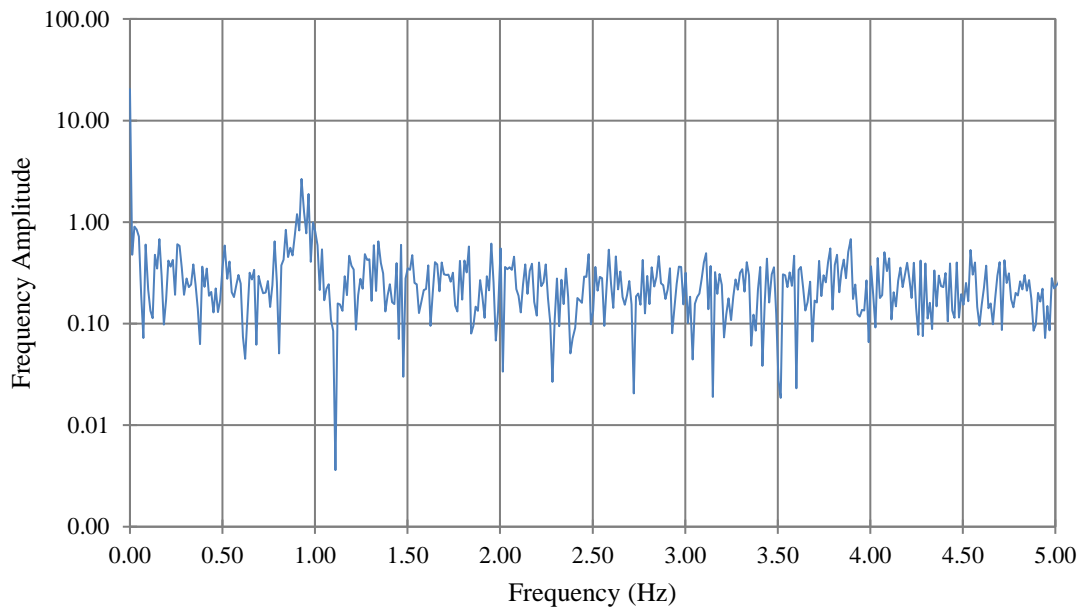


Figure 3-12 – FFT Analysis of Velocity (X-Dir) at x, y, z/h of 0.18 m, 0.3 m, 0.114.

3.4.2 Erosion

First Development: 0 – 2hrs

In the first hour, a small bank formed concentric and upstream of the pile, spanning approximately 30 degrees either side of the front, see Figure 3-13. The distance from the bank to the structure coincides with the size of the horseshoe vortex indicated by the horizontal velocity components shown previously in Figure 3-8. The formation of such a bank is rarely documented in marine morphology literature and is more common in Aeolian Morphology, where the bank is referred to as an ‘echo dune’ (Qian et al., 2011, Tsoar, 2001). This is formed by sediment deposition from the horseshoe vortex into an upstream stagnation point adjacent to the bed surface.

In addition to the echo dune, Tsoar (2001) illustrates the built-up of sediment behind the structure which is also present in the current experiment. This occurs in a ‘shadow’ zone under steady streaming conditions (Sumer and Fredsøe, 2002). This condition is explained in more detail later in this chapter.

Downstream of the structure pitting of the bed surface was visible in two straight lines leading away from the pile at 45 degrees. This continuously develops and is depicted more clearly in later images of the final topology.

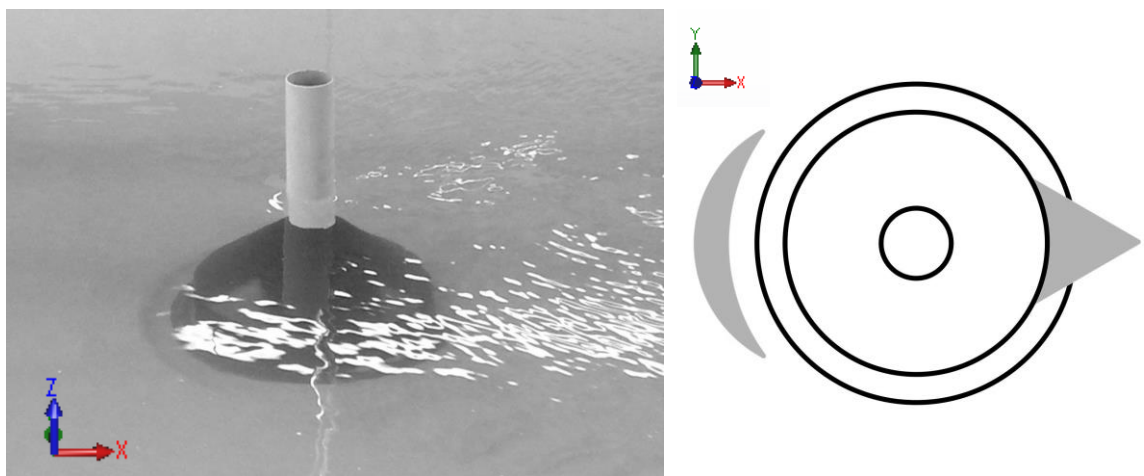


Figure 3-13 – Scour after 2 hrs

Second Development 2-3 hrs

The horseshoe vortex in front of the pile continued to erode the adjacent bed and a trench was visible after approximately 2 hours. Simultaneously, the bank that formed in front of the pile had washed away, Figure 3-14.

Furthermore, it is clear, however unexpected that there is very little scouring at the sides due to flow acceleration. This suggests that the skirt has provided protection against scouring due to flow acceleration at the sides.

The lee-side bank continued to increase in height, width and length and formed 'V' shape as seen below. The previously shallow pitting present downstream was more obvious after 2 hours following continued erosion, alongside the faint formation of parallel pitting inside of the original pitting.

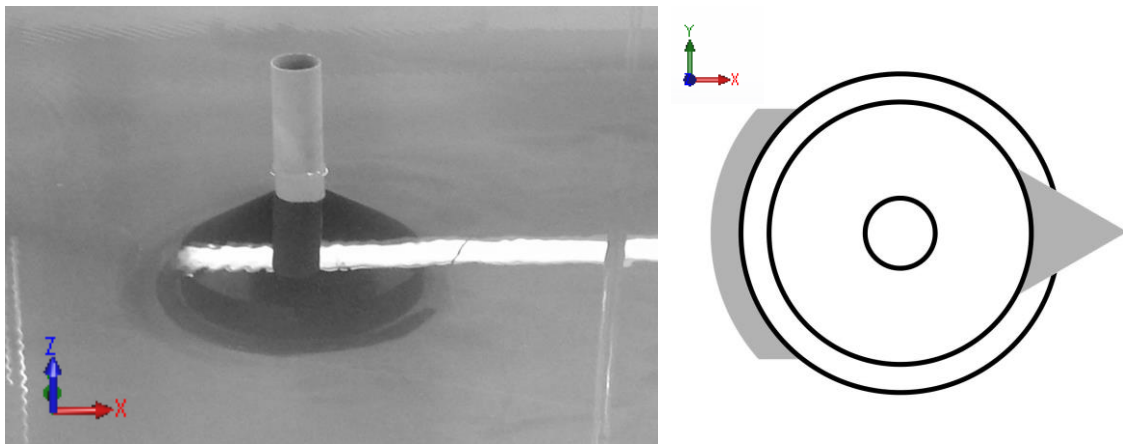


Figure 3-14 – Scour after 3 hrs 10 min

Third Development 3-7 hrs (Equilibrium Point)

The trench formed by the horseshoe vortex continued to erode and began to propagate underneath the structure. In addition to the main trench, a shallower secondary trench formed on top of the first with a larger radius. However, unlike the first trench, this trench was not concentric to the structure. As shown by Figure 3-15 both of the trenches dissipate at around 30 degrees, which again supports the fact that no scour developed as a result of flow acceleration.

Visual inspection of the scour around the pile showed no further development after 7 hours. However, it is clear from previous studies such as Melville and Chiew (1999) that clear-water scour takes a considerable amount of time to reach an equilibrium state and it is more likely that the scour is still developing, but at a rate which is difficult to identify over just a few hours. The scour that propagated underneath the structure could not be seen or detected. However, the

sediment around the structure will dissipate if the supporting sediment underneath is removed, and therefore further scour underneath is identifiable through morphological changes on the bed surface around the pile. Thus, it was concluded that the scouring underneath the pile has also reached a low scouring rate. To ensure that the scouring underneath and around the pile had reduced in speed significantly the experiment was ran for a further 3 hours.

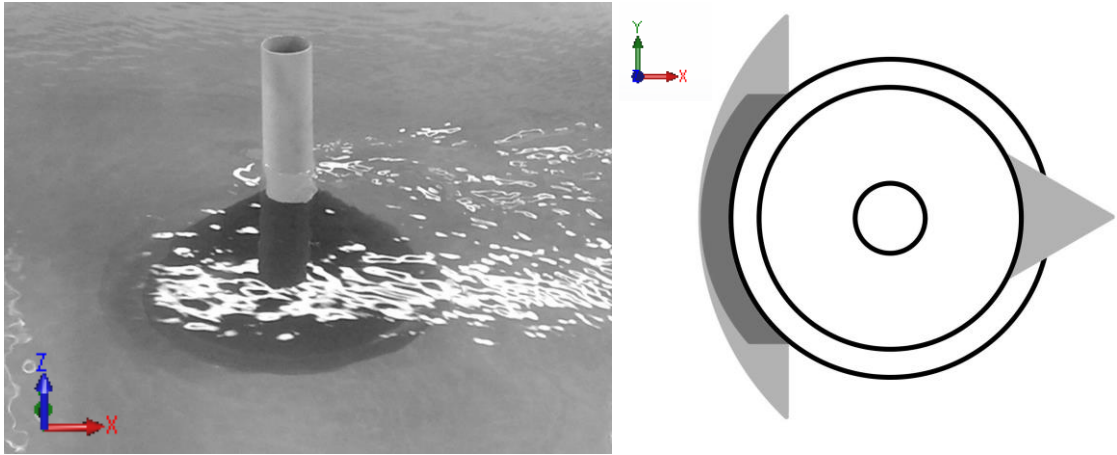


Figure 3-15 – Scour after 7 hrs

Final Topology

Upstream Bed

The sediment-bed depth upstream from the pile did not change significantly; however, bed forms developed as seen in Figure 3-16. As shown by Soulsby (1998) the shape of a bed form is dependent on the flow conditions, specifically the strength of the current or waves. The ‘current ripples’ shown have an average amplitude of 9 mm and are asymmetric and shaped like the teeth on a saw, which signifies that they are due to current forces that have caused the threshold of motion to be exceeded, but not by enough to remove the ripples completely. In addition, this is supported by the 2D upstream flat, bedform-less section of 2D in length where the velocity of the flow has decreased, Figure 3-17.



Figure 3-16 – Bed Formations

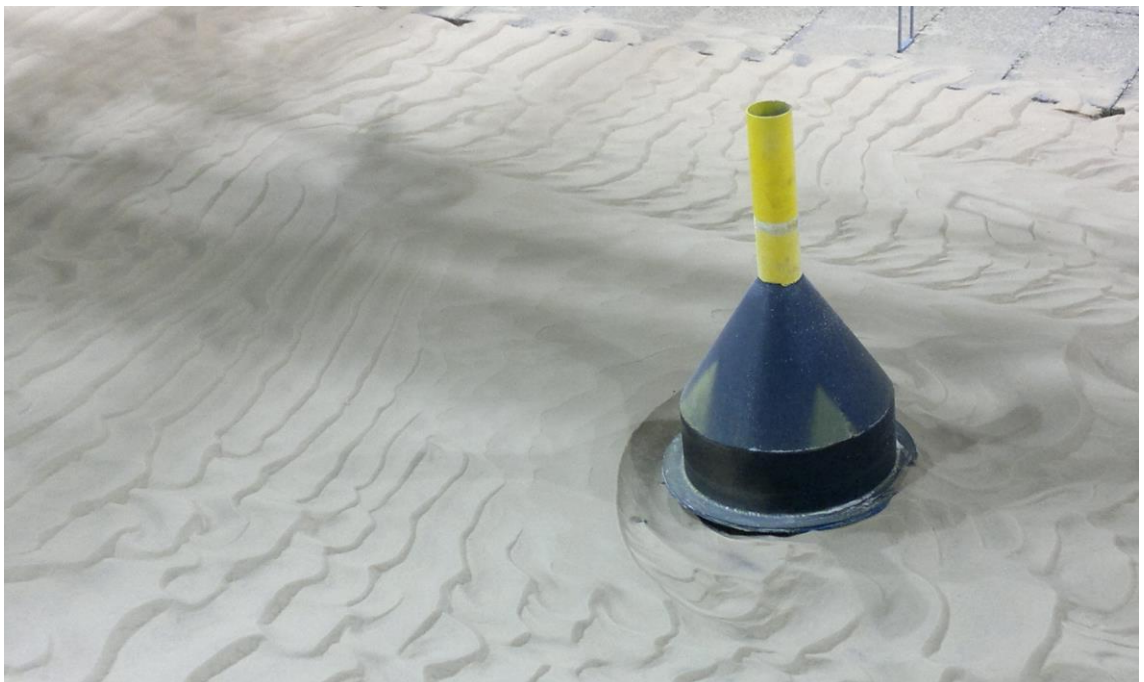


Figure 3-17 – Local Bed form changes

Local Scour

The trench that formed at the front of the pile extended underneath and scoured approximately one third of the sediment that supported the structure, in a crest formation, Figure 3-18. The trench is characterised by an upslope similar to the angle of repose and a downslope with a steeper angle, Figure 3-19. In addition, the trench gradually dissipates as it sweeps around the structure and ends at 45 degrees from the front. In conjunction with no scour at 45° during scour development, where accelerated flow velocities are greatest, it is concluded that the collar has protected against all scour due to flow acceleration around the structure.

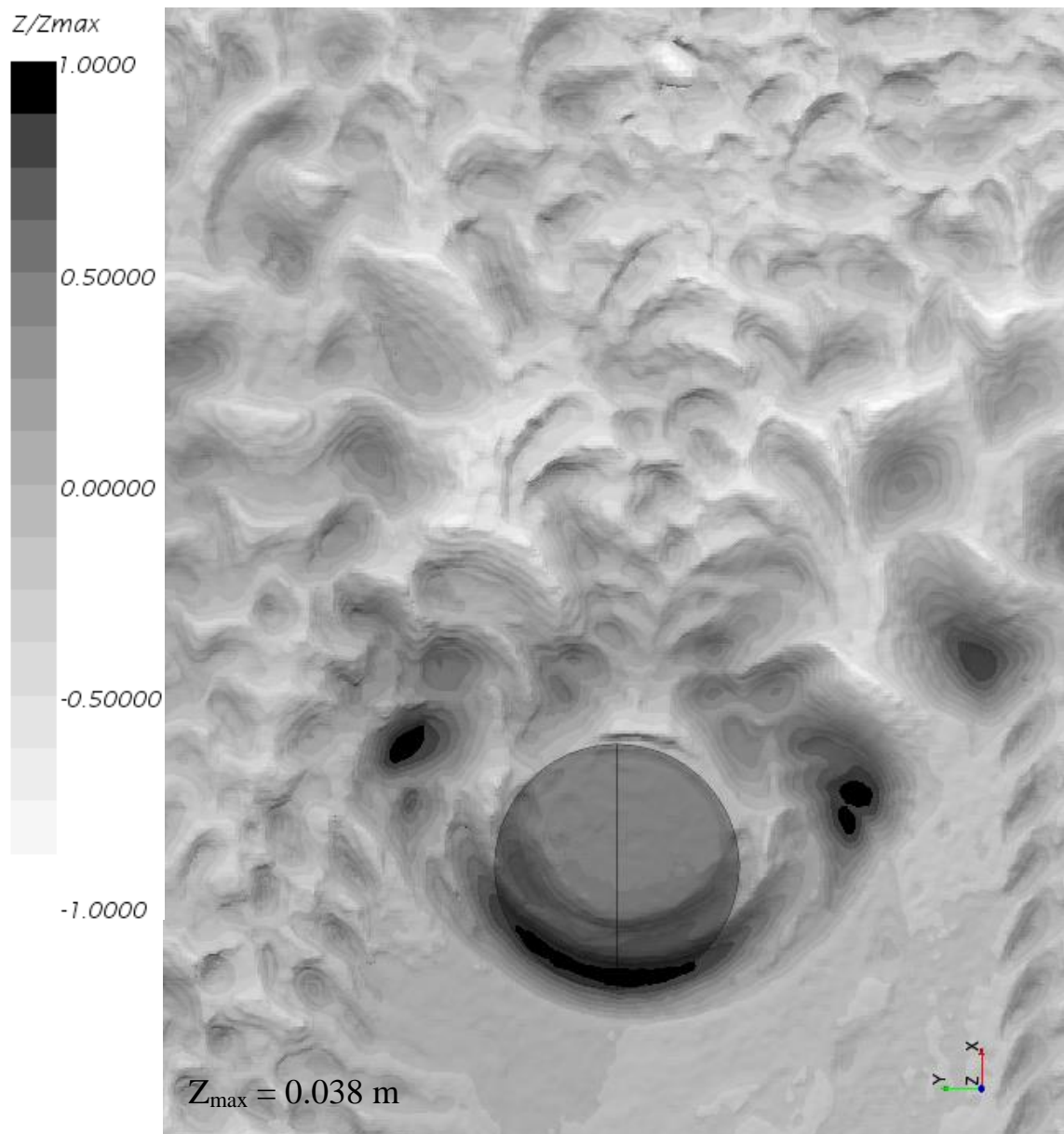


Figure 3-18 – Scour Depth Contours (Top View)

Within the trench is a step that suggests there are two mechanisms present. This is supported by the fact that one of the steps is not concentric to the pile, as the shallower step deviates away from the pile at the sides. This is because one step is due to a horseshoe vortex contained by the lip and the other is due to a horseshoe vortex and subsequent flow underneath the structure.

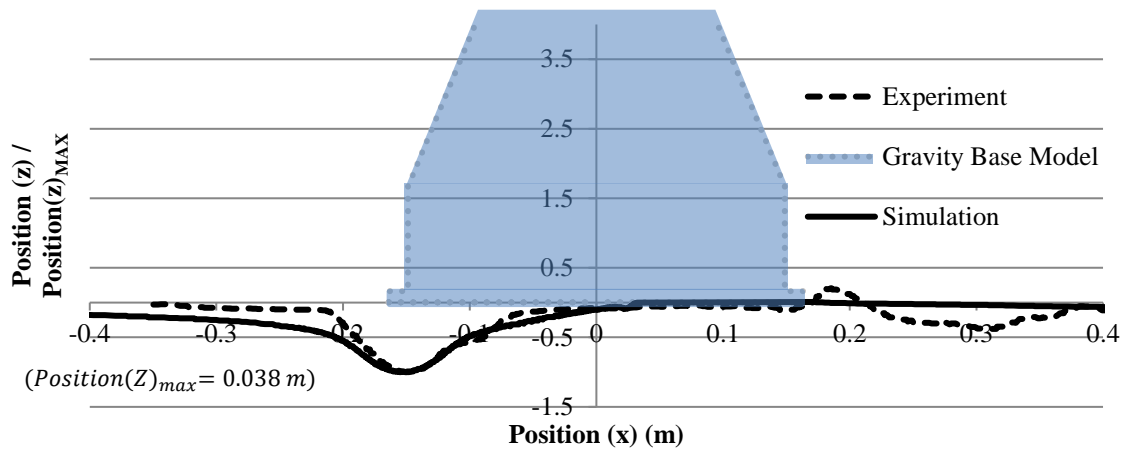


Figure 3-19 – Final Scour Depth along Centreline

The final deposition behind the structure extended onto the lip forming a ‘V’ shape behind the pile. The 3D scan data recorded a maximum height of 0.014 m on the lee-bank; however, the scan was made after the flume was drained which subsequently removed some of the sediment from the lee bank that included the highest point. This deposition occurs because there is a ‘shadow’ area behind the pile, which is protected from the flow by the pile and is not affected by high turbulence or vortex shedding.

Downstream Scour

The presented downstream pitting formed symmetrically in a straight-line leading away from the pile at a 45-degree angle, Figure 3-20. In addition, shallower pitting also occurred inside and parallel to the first. The main pitting varies in depth as the distance from the pile increases; beginning with a maximum depth similar to the trench.

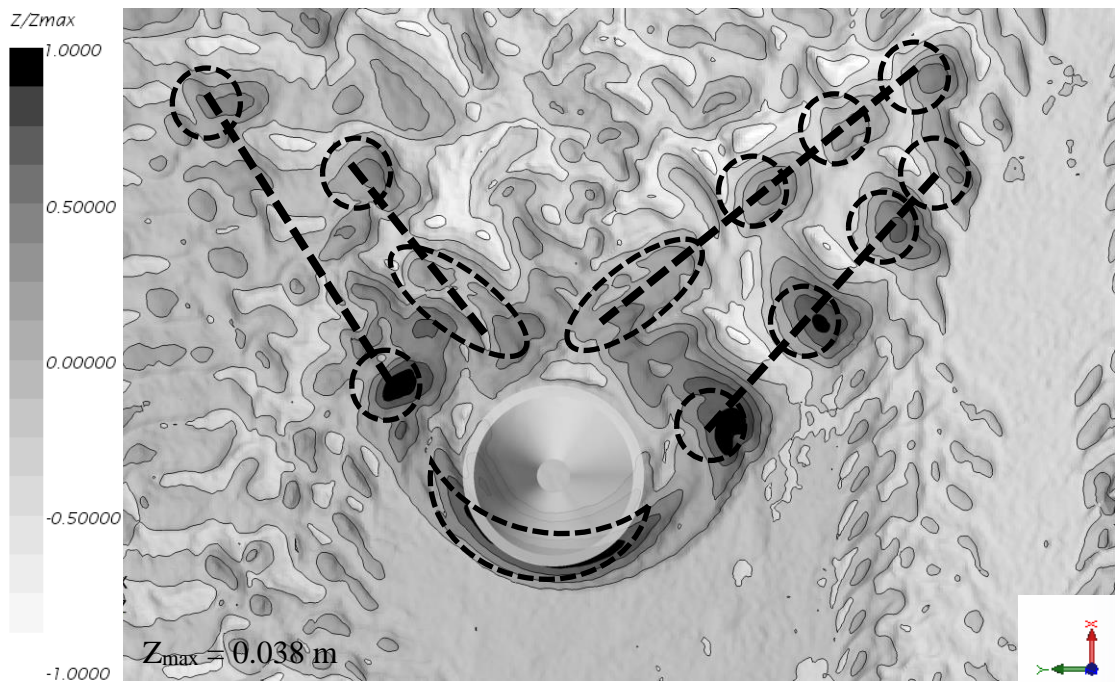


Figure 3-20 – Downstream Pitting

Typically, erosion that occurs downstream of bluff bodies is due to vortex shedding or distortions on the free surface; including the effect of waves. However, the present scouring characteristics do not agree with those typically found around a cylinder.

Under steady flow conditions vortex shedding travels in a straight path behind the structure due to the mean flow direction and increases in width as the Reynolds Number increases. However, the current scouring begins with an angle approaching 45 degrees resulting in an extremely wide path. This strongly suggests that the scouring is not due to vortex shedding under a steady current.

“Steady streaming” is where non-uniform oscillating motions result in vortex shedding due to features such as waves or sinusoidal flows. The subsequent vortices can vary significantly from those caused by steady flows, including symmetric, asymmetric, single, double and triple pair vortices (An et al., 2009).

Initially, oscillatory flow was not considered as the flow is assumed constant and the long period, shallow waves present were thought to be negligible. However, the detached scouring behind the cylinder is typical of vibration induced vortices, as shown in (Umeda, 2011), in addition the deposition of sand behind the structure is associated with steady streaming due to the ‘shadow’ zone found behind the pile (Sumer and Fredsøe, 2002). This suggests that, based on a literature search on scour around cylindrical structures, the pitting in the current experiment is due to non-uniform oscillating motion.

However, the gravity base model differs from a simple cylinder which can substantially change the resultant scouring. As a result, an extensive literature search of scouring around structures more similar to the gravity base model was conducted in order to find similar erosion topography.

(Alabi, 2006) was the only source that included similar topography formed by current-only conditions around a pile with a collar.

The results of Alabi (2006) show detached scouring in the form of pitting at a wide and sharp angle from the pile, matching the pitting in the current experiment. In addition, there is also a similar trench at the front and no scouring at the sides due to flow acceleration. Furthermore, very similar bed forms developed downstream of the pile.

Given these similarities there remains two possible explanations for the scour pattern; either both experiments include non-uniform oscillations which have been unrecognised, or the use of a collar under certain flow conditions results in this type of flow pattern.

The maximum scour depth obtained in the experiment was 0.038 m, which was located in both the trench and the pitting closest to the trench.

In addition, it should be noted that the intervals made during the experiment could affect results, which was unfortunately discovered after the experiment was ran. This is well documented by (Zanke et al., 2011), who shows that that if the flow is stopped the scouring at the front of a cylinder extends further upstream and reduces in depth. This is because the forces that were originally holding the sediment grains and therefore sediment bed in position are removed, allowing grains to slide down into the scoured trench.

Gravity Base Experiment Summary

The experiment provides insight into the unique scouring surrounding and underneath a gravity base structure. The capture of local velocity profiles and final scour topology are vital to computational verification, in order to compare accuracy and if necessary investigate discrepancies. In the later development chapter, this experiment is replicated and compared to simulation results.

Publications detailing the scour topology around gravity base foundations are rare and this experiment has unveiled unique scouring attributes including the two overlaid upstream trenches and in-line downstream pitting, both attributed to the lip around the structure. Additionally, it is shown that the lip provides significant scour protection due to the minimal scour typically surrounding 45°.

Chapter 4 Computational Fluid Dynamics

Computational fluid dynamics (CFD) is a highly versatile tool used for a variety of applications. Typically, CFD is linked to widely known applications such as car aerodynamics; however, it is used in more diverse applications including Sports Wear design (Pinnoji et al., 2008), jet engines (Zhang et al., 2012), washing machines (Jung et al., 2008) and food cooling (Xia and Sun, 2002).

CFD is built upon the fundamental Navier-Stokes equations that govern viscous fluids, by ensuring conservation of mass, momentum and energy. These equations often result in a complex calculation hence the use of computers in conjunction with techniques such as the commonly used finite volume method; as discussed in this chapter. Furthermore, the ‘full’ Navier-Stokes equations remain too complex to feasibly compute even on the todays computers, and are therefore commonly used in a reduced form to lower computational cost and time.

CFD first came to fruition in the 1960’s when computers became powerful enough to compute the governing fluid dynamic equations. However, at this point only inviscid, irrotational, linear problems could be solved.

Since the 1960’s computing potential and solve algorithms have improved significantly and costs have fell, enabling CFD to blossom. Use of the Reynolds Averaged Navier-Stokes (RANS) became common in 1972 following publications on RANS closure, including (Jones and Launder, 1972, Launder and Spaulding, 1972), allowing the computation of viscous flow, in addition to past achievements including rotational and non-linear flows.

RANS equations are still commonly used today, however typically in conjunction with models that improve efficiency or reduce the number or magnitude of downfalls. Aside from RANS other methods are available including LES (Large Eddy Simulation) and DES (Detached Eddy Simulation) that improve accuracy especially regarding turbulence capture however, RANS remains the better-suited choice in some cases, and sometimes the only option as many Multiphysics additions are only RANS compatible.

Model choice is commonly balanced between the required accuracy and the associated computational time and cost. In this chapter, the models and settings that allow various levels of accuracy and computational cost for single and multiphase models are explored, followed by a discussion outlining the appropriate choices for this specific study.

4.1 Turbulence Models

The common methods to resolve turbulence are Large Eddy Simulation (LES), Reynolds Averaged Navier Stokes (RANS) and the Reynolds Stress Model (RSM) with seven additional transport equations; however, others exist including hybrid models such as Detached Eddy Simulation (DES), but are not yet commonly included in all CFD software. In addition to each method, many turbulence models are available which are also software specific.

Reynolds Averaged Navier-Stokes (RANS)

The RANS approach is one of the simplest and least computationally expensive. It is based on Reynolds Decomposition, which is a technique that separates the mean and fluctuating parts of a system; in this case the mean and fluctuating velocity components. These fluctuating velocities represent the turbulence in a system and form the Reynolds Stresses (Ferziger and Peric, 2002).

To compute the Reynolds Stresses and close the time-averaged Reynolds Stress equations, several turbulence models are available. The more popular models are the k- ϵ , k- ω and SST model (Andersson, 2012).

The standard k- ϵ and k- ω models are very similar and require two additional transport equations. The main numerical difference between the two is how the length scale is calculated as the k- ϵ model uses the turbulent dissipation rate, ϵ , and the k- ω uses the turbulence frequency, ω .

The k- ϵ turbulence model (Launder and Spalding, 1974) is one of the most widely used and validated (Versteeg and Malalasekera, 1995). It is one of the most stable models, which converges well and has proven success in recirculating and confined flows. However, the standard model performs poorly in high strain flows (Versteeg and Malalasekera, 1995) and is commonly criticised for low performance in cases of large adverse pressure gradients. The k- ω turbulence model (Kolmogorov, 1991) offers improved accuracy over the k- ϵ model especially in cases of adverse pressure gradients and fast changes in boundary layer; however, the model is less stable.

The use of the standard k- ϵ and k- ω models is now less common, but they form the basis for improved and popular advanced versions that reduce inherent problems. Examples include the k- ϵ two-layer model (Rodi, 1991) which offers improved near-wall treatment for low Reynolds Number, turbulent flows. A second example is the k- ω SST model (Menter, 1993) which utilises the near-wall performance of the k- ϵ model and includes limits to prevent the overestimation of turbulence in stagnation areas. This model is also one of the most popular RANS models, especially for aerodynamic applications.

Another two models which have improved the k- ϵ model significantly are the Realizable and RNG models, which use two different methods to improve accuracy. The RNG model adopts a 'renormalisation group' method, whereby the small scales of motion are removed from the

governing equations and their effects are instead represented by larger scale motions and a modified viscosity term (Versteeg and Malalasekera, 1995). The modifications to the ϵ equation improves the accuracy of this model especially in high strain flow, improving upon a major limitation of the standard k- ϵ model. Similarly, the realizable model also significantly improves high-strain predictability. This is due to the models ‘realizability’, allowing certain constraints to be made that are consistent with the physics of turbulence.

Despite the difference in method sources report either an insignificant difference between the two or a small amount of evidence that the realizable models performs better. Firstly, SIMULIA, a widely used CFD code has stopped supporting the RNG model entirely, because as explained by a director at SIMULIA, they feel that the RNG model provides little or no advantage and they do not know why it would be selected over the Realizable model (Wasserman, 2016).

Secondly, Ansys Fluent documentation states “*initial studies have shown that the realizable model provides the best performance of all the k- ϵ model versions for several validations of separated flows and flows with complex secondary flow features*” (Ansys Fluent, 2014).

Therefore, due to the similarity or possible advantage, only the realizable model will be used for later testing.

A less common RANS model choice is the Reynolds Stress Transport Model that requires seven additional transport equations and offers the greatest accuracy of the RANS models; however, it requires significant computing power and time which is partially due to the additional equations, in addition to slower convergence.

Large Eddy Simulation (LES)

Turbulence may be represented as eddies that are superimposed on the mean flow, which are averaged out by the RANS model. The LES model works differently by resolving the larger eddies and modelling the smaller ones, however, the process of filtering the larger eddies subsequently removes the information from the smaller eddies. The removal of the smaller eddies and the interaction between the larger eddies causes sub-grid-stresses (SGS), which must be modelled using an SGS model. The filtering of larger eddies and the SGS model are key concepts of the LES model and a range of each are available, see (Chung, 2002) and (Versteeg and Malalasekera, 1995) for an overview of the models.

The LES model is significantly more accurate than RANS, as the time independent capture of large-eddies and ‘universal’ smaller eddies (Versteeg and Malalasekera, 1995) is far more accurate than all eddies that have been time averaged and represented by a mean flow velocity and subsequent fluctuations. However, LES is far more expensive regarding computational time and power (Chung, 2002). LES schemes are typically implemented using explicit time schemes (Zhiyin, 2015) and therefore require a Courant number less than unity to remain stable. Analysis and investigations into Implicit LES models (ILES) have increased in the last decade (Aspden et

al., 2008, Margolin, 2005, Grinstein et al., 2007) however the model remains problematic. Therefore, in respect to the current study, if a Courant number greater than one is required to make the solve time feasible LES is not an option.

Detached Eddy Simulation (DES)

The third mainstream model is Detached Eddy Simulation, which is a relatively new hybrid method that utilises both RANS and LES techniques. The RANS model is used for boundary layers and irrotational flow areas while the LES model is used for detached turbulent regions; but only when the grid is fine enough. This provides a compromise between the computationally expensive and high accuracy LES model, and the low accuracy, computationally efficient RANS model. The DES model still suffers from some of the problems associated with the individual RANS and LES models, and there are issues where the RANS and LES interface (Mockett, 2009); however, the model holds massive potential once these problems are resolved.

4.2 Discretization

The transport equations associated with each of these models are solved using the finite volume method, commonly used by both open source and commercial CFD software. The use of the finite volume method requires discretization of the fluid domain, of which the grid structures can be generalised into two categories, structured and unstructured.

Structured meshes comprise of hexahedral elements in a structured or block-structured configuration. The structured configuration includes orthogonal and non-orthogonal ‘body-fitted’ meshes where areas are refined through converging gridlines as shown. Block structured meshes consist of an orthogonal grid structure, where refinement is achieved by dividing cells so that the edge length is halved. This makes it significantly easier to mesh complex geometries and prevents the creation of excessive cells due to refinement propagation into unnecessary areas.

Unstructured meshes have no grid structure and are ideal for complex geometries. Unstructured meshes can contain several types of mesh elements to form hybrid meshes. In 3D cases, this typically consists of a core polyhedral or tetrahedral mesh with hexahedral cells at boundaries, allowing for better mesh resolution and therefore boundary layer prediction. In addition, polyhedral and tetrahedral cell types enable an extremely fast change in mesh resolution and therefore provide the most computationally efficient structures (Biwas and Strawn, 1997).

Polyhedral and tetrahedral cells have different accuracies, convergence rates, meshing times and memory requirements. The quantitative difference is dependent on the specific case however it is found that a polyhedral mesh is best with respect to accuracy and computational efficiency (Tu et al., 2007). This is confirmed in (Star-CCM+, 2012) which states that the accuracy of polyhedral cells is the same as 5-8 times the number of tetrahedral cells.

The size of each element or cell determines the spatial accuracy and therefore smaller elements are most effective in areas of interest or complex flow. The flow around a basic monopile is used as a baseline for this study and includes many of the flow mechanisms that also exist around other foundation shapes, namely; upstream separation, upstream horseshoe vortex, high acceleration and separation at the side of the pile and downstream areas of vortex shedding.

The correct capture of these mechanisms is of high importance as they are responsible for the greatest scour. The optimum element size in each of these areas is discussed at the end of this section, as it is intertwined with factors not introduced yet including turbulence models, wall functions and temporal resolution.

4.2.1 Discretization Error

Discretization or numerical error describes the difference between the exact solution of the partial differential equations and the numerical solution obtained with finite discretization in space and time. This difference can therefore be reduced by decreasing the size of the finite elements or time-step, however, is also dependent on element quality and the transition of element type or size.

The non-linear geometry of scoured domains typically increases discretization error as the reduction of cell size to accommodate complex voids often decreases cell quality. This however can be avoided using discretization error indicators, either prior or post calculation to trigger a remeshing event; these indicators are discussed in detail in (Roy, 2010).

The pre-timestep indicators are used directly after mesh generation, before any calculation or in the case of moving boundary simulations after re-meshing mid-simulation. These indicators are cell quality based including cell aspect ratio and skewness; such indicators are used in the developed scour model and are described in further detail in *Chapter 7 Scour Model Composition, Automation*. Furthermore, several codes now include iterative, quality based discretization, that reduces error and improves mesh quality; a procedure found in Openfoam's SnappyHexMesh (www.openfoam.com, 2016) and Star-CCM+ (Star-CCM+, 2014).

Post-calculation indicators include the previously discussed cell quality indicators, but also importantly numerical solution outputs, providing signs of numerical divergence. As it will become evident, these indicators are especially important in morphological deforming mesh simulations, as they can be used mid-simulation when there is perhaps no re-mesh but the mesh is changing, and cell quality is reducing.

4.3 Wall Treatment

The method used to compute the near wall flow is dependent on the near-wall mesh resolution and assessed using the wall- y^+ value;

$$y^+ = \frac{u^* y}{\nu}$$

Equation 16

The wall y^+ is referred to several times during this section in which the distance from the wall, y , is the height of the cell adjacent to the wall, u^* is the shear velocity and ν is viscosity.

The most accurate treatment is applied to low wall- y^+ values whereby the viscous sub-layer is resolved by the grid sufficiently, and the turbulence model is valid throughout the boundary layer, including the viscous sublayer. This model is best suited for wall- y^+ values of one or less however this requires a fine mesh resolution and is therefore computationally expensive.

The lowest accuracy treatment assumes the near-wall cell lies within the logarithmic region and is for high wall- y^+ values from 12 to 30 (or ~60 for two-layer models). This treatment uses wall functions that predict the near-wall flow using the empirical log-law (Equation 1, Chapter 2).

Turbulence models can also include automatic wall treatments called ‘All wall- y^+ ’ where either the low or high wall- y^+ treatments are automatically applied based on the near-wall conditions. This can also include a transitional wall- y^+ treatment between the low and high models when the cell centroid lies in the buffer layer; which is used for this study as accommodates the non-uniform flow velocity and structures local to a surface mounted pile.

In general, wall functions apply velocity and turbulence distributions as a function of wall distance. These functions are useful as they enable a significantly lower mesh resolution; however, their accuracy is limited, and they are sensitive to wall- y^+ values. In addition, they perform poorly in flows where the applied log-law is not valid such as separated, adverse pressure gradient, re-attaching and stagnating flows.

An additional model called the ‘Advanced Two-Layer Wall Treatment’ is available for RANS $k-\varepsilon$ and $k-\omega$ models to improve their poor near-wall prediction at low Reynolds Numbers (Versteeg and Malalasekera, 1995). This model essentially splits the boundary layer calculation into two, predicting both the viscous sublayer and the remaining boundary layer. This model significantly improves near-wall predictions using the RANS $k-\varepsilon$ and $k-\omega$ models and is therefore a popular choice.

4.4 Temporal Resolution

Time stepping methods are split into two categories, implicit and explicit. These are discussed in the following using the Courant Number (or Courant-Friedrichs-Lewy number), Equation 17.

$$CFL = \frac{u\Delta t}{\Delta x}$$

Equation 17

This is a ratio of the distance travelled by the fluid in one timestep (velocity, u , times time, Δt) compared to the distance required to flow through a cell, Δx .

The explicit, forward difference method computes the state of a system during time step $t+1$, using the state of a system, Y , at the previous time step, see Equation 18 (Bui, 2010).

$$Y_{k+1} = Y_k + f(t_k, Y_k)\Delta t$$

Equation 18

Explicit schemes are simpler and less computationally expensive in time and memory compared to implicit methods. However, explicit methods have poor stability and a requirement for CFL numbers below unity. Due to these characteristics, they are best used when time accuracy is paramount.

Implicit schemes use backwards differencing whereby the future state of the system is attained by solving an equation which contains the current and future state of the system, Equation 19 (Bui, 2010).

$$Y_{k+1} = Y_k + f(t_k, Y_{k+1})\Delta t$$

Equation 19

Due to the backwards differencing formulation, 1st order and 2nd order versions in time can be used, improving time accuracy.

Implicit methods take longer to solve than explicit when compared using the same time step and are more computationally expensive. However, the longer solve times can be significantly reduced by utilising the stability of the implicit method with large CFL numbers (Bui, 2010).

Due to the timescales typically encountered in scour simulations, in combination with structure size, flow velocity and resultant mesh resolution, retaining a CFL less than unity can result in lengthy, and often unfeasible physical solve times.

However, allowing a CFL larger than one will reduce accuracy, and potentially the capture of flow features altogether. If the implicit method is adopted and a CFL greater than unity is accepted, the time step is next determined by the flow mechanisms; vortex shedding and related

fluctuations in flow acceleration, and the horseshoe vortex. These allow for a significantly greater time step; for example, using the details from the first development case (velocity = 0.247 m/s, diameter = 0.2 m and total Scour Time = 72,000 s) it can be demonstrated that the time step can be increased by a factor of 10 whilst accurately capturing the vortex shedding;

Ensuring a CFL < 1:

$$\text{Approximate } u_{\max} = 2u_{\infty} = 0.494 \text{ m/s,}$$

$$\Delta x = 0.0087 \text{ m (Course grid of 72 elements per 360 degrees around the pile diameter)}$$

$$\begin{aligned} CFL = 1 &= \frac{u\Delta t}{\Delta x} = \frac{0.494\Delta t}{0.0087}, \therefore \Delta t = 0.017\text{s} \\ &= 4.2 \times 10^6 \text{ timesteps} \end{aligned}$$

Ensuring the accurate capture of vortex shedding:

$$\text{Shedding Frequency: } St(0.2) = \frac{fL}{v}, \therefore f = 0.25 \text{ Hz,}$$

Minimum time step accuracy of 1/30 x shedding period:

$$= \frac{1}{0.25\text{Hz} \times 30} = \Delta t = 0.133 \text{ s}$$

$$\begin{aligned} \text{Therefore, total time steps} &= \frac{72,000\text{s}}{0.133\text{s}} \\ &= 5.5 \times 10^5 \text{ timesteps} \end{aligned}$$

The time accuracy required to accurately capture the horseshoe vortex is dependent on the turbulence model, because as is shown in the later *Monopile Investigation* only the LES model captures transient horseshoe vortex/vortices. Therefore, depending on the level of accepted accuracy/simplification the horseshoe vortex may not limit the time step size at all.

In addition to the flow mechanisms other simulations aspects can determine the time step, including the bed deformation rate and resultant bed geometry. These aspects are also case sensitive as depend upon the erosion rate, cell size and transient topology in combination with the specific mesh. For many of the morphological single phase simulations within this study the time step is limited by the rate of topological development, as investigated and discussed in *Chapter 7, Single Phase Model, Case 1 – Preliminary Scouring around a Simple Monopile*. However, the two-phase simulations remain limited by the CFL, as otherwise secondary sediment phase volume is lost, as discovered in the *Two Phase* section within *Chapter 7*.

4.5 Morphing Methodology

The topological development of scour around offshore marine structures requires a 3D simulation, for which there are two methods to represent the eroding bed-surface (Liang et al., 2005); the mesh deformation method (Boundary Conforming Mesh) or the Curvilinear immersed boundary method (CURVIB) (a non-conforming boundary mesh). These methods displace the bed surface to replicate scouring using control points defined by the cell nodes or independent control points

on the bed. The displacement at each point is defined using a velocity or typically displacement distance based on the calculated local scour.

The CURVIB method is similar to the FAVOR method (Fractional-Area-Volume-Obstacle-Representation) (Hirt, 1993) entailing a fixed background mesh and a sliding baffle interface separating solid and fluid regions. The interface is able to both deform and slide up and down the background mesh, removing the need to re-mesh.

The deforming mesh method (or conforming boundary mesh) moves the bed-boundary by stretching the fluid domain, therefore not requiring a solid volume or sliding boundary. However, this does make re-meshing compulsory to retain good mesh quality and avoid numerical error. Within the software used for this study the deforming mesh method is available, which accommodates the bed-deformation by stretching cells throughout the whole domain. This firstly minimises the likelihood of poor quality cells and secondly helps reduce the stretching of the cells layers adjacent to the bed surface; minimising the impact of boundary layer computation and therefore the wall shear stress. This is advantageous over other models that limit the stretching, for example by only stretching the first few cells on the bed surface or below a certain height.

4.6 Multiphase Flow

The introduction of a secondary sediment phase requires additional modelling decisions as there are several secondary phase numerical modelling and phase interaction methods available. Similar to the single-phase modelling choices, the multiphase options also range in accuracy and application and are discussed in the following section.

4.6.1 Dispersed Phases

Dispersed phases can include solids, liquids or gases and are spread out within a larger primary phase, for example bubbles in a bath or sand in water. The following dispersed phase methods allow for many additional phases, for example, a range of sediment particle sizes in a scour simulation. These models range significantly in accuracy, starting with the homogeneous Eulerian or passive scalar model.

The homogenous Eulerian model is solved using the general transport equation however assumes there is zero relative velocity between phases and therefore is only applicable to driven flows where the drag forces dominate the gravity or buoyancy forces; and therefore dispersed particulates can only be used for very small particle sizes (< 0.1 mm) (Wörner, 2003). Thus, this model is ideal for dispersed phases which have minor effect on the primary flow, for example rising smoke or tracer dye in a fluid. This method is the most computationally efficient; however, is also one of the least accurate.

The (heterogeneous) Eulerian multiphase method is often referred to as a ‘two-fluid model’, whereby the additional phase is treated as another continuum (Alhajraf and Rubini, 2000) that interacts with the primary phase. Each phase uses the same pressure; however, conservation of mass, momentum and energy apply. This significantly improves the accuracy compared to the homogeneous model and therefore enables both single and two-way coupling between phases, promoting increased accuracy. These interaction models are also applicable to other methods and discussed in more detail at the end of this section.

In contrast to the preceding Lagrangian method, the computational expense of the Eulerian model is relatively low and independent to the volume of additional phase present.

The Lagrangian method is a particle-tracking model, and groups particles in order to reduce computational expense. Particles are tracked by computing their trajectories as they travel through the computational domain independent to cell locations (Brennen, 2005); unlike the Eulerian methodology. The Lagrangian model offers one and two-way coupling, and interaction models beyond what is available with the Eulerian approach including atomisation, break-up and collision, however; due to the premise of this study only the collision model is considered further. It is generally perceived that the Lagrangian approach is more accurate and computationally expensive than Eulerian. However, this depends heavily on the case-in-hand as with dispersed solid particles there is evidence to suggest that the Lagrangian method does not offer significant accuracy over the Eulerian (Nijdam et al., 2003, Vié et al., 2014). Also, depending on the particle loading Lagrangian compute times are not always greater (Zhang and Chen, 2007).

The final possibility, DEM (discrete element method) (see (Bićanić, 2004)), is an extension to the Lagrangian method that calculates the trajectory of each particle individually, without groupings. The accuracy in respect to the coupling and additional force models is the same as the Lagrangian method, however this model can explicitly account for particle-particle interaction. This is the most advantageous feature of this model and is the only one that provides this, however, as a result it is also the most computationally expensive.

4.6.2 Dispersed Flow Phase Interaction Models

The previously discussed numerical schemes require additional models to accurately capture both interphase and alternate phase interactions. These models allow for the interchange of conserved quantities; improving the calculation of forces such as lift and drag or enabling interphase interactions such as particle collision. The following section provides a brief overview of the models available that apply to this study.

The interaction between continuous and dispersed phases is crucial as it drives the transport of sediment and is computed using interaction models, including those for computing lift, drag and turbulent dispersion.

The drag force upon a single object is quantified using a drag coefficient. For a single object under simplified conditions, for example a sphere in laminar flow, the drag coefficient is calculated using the size of the sphere, the relative velocity (between object and flow) and the fluid density. The exact relationship between these variables has been researched extensively, famously by Stokes (1851), followed by many others studies for different shaped grains and wider datasets, as described in (Hölzer and Sommerfeld, 2008).

In addition to particle shape and speed, the surface roughness, deviation in shape and size, distribution of surrounding particles and fluid turbulence all impact the drag upon each particle. The Eulerian and Lagrangian methodologies do not however track individual particles, which is computationally expensive and the approach used by the DEM method. Therefore, empirically based models are used to calculate the change in drag on volumes of particles accounting for turbulence (using a drag correction exponent) and distribution (for example the Richardson Zaki drag correction factor (Richardson and Zaki, 1997)). Models are typically application-specific due to their empirical derivation and the present study requires a model applicable to solid particle, high concentration flows due to the expected high concentration bed load transport. The major parameters affecting lift of a particle are relative velocity between the particle and fluid, shear rate of the fluid and particle rotation speed. However, typically, the drag forces significantly outweigh the lift forces upon a sediment particle which explains why commercial CFD software offer a sparse range of lift coefficient models in comparison to drag models.

The turbulent dispersion model redistributes the dispersed phase based on the turbulence levels. The magnitude of this effect can be set using a constant, however it is common to use a turbulent Prandtl number (Weinan and Vanden-Eijnden, 2001); in which different formulations exist. The resultant coefficient, either constant or derived using the turbulent Prandtl number can have considerable effect upon the flow, ranging from essentially no effect to extreme redistribution of the discrete phase. The methods available for computing the turbulent Prandtl number reduce any user error; however, even these require input. To conclude, the turbulent dispersion force is necessary to simulate a correct sediment concentration on the bed surface and throughout the water column, however similar to other models it can be tuned to meet the required result.

In a typical scour scenario, the interaction between dispersed phases is negligible as sediment loading is low resulting in little interaction. However, if the interaction is necessary either the Lagrangian or the DEM models are required. The Lagrangian model offers a collision model that uses restitution coefficients to compute momentum exchange. In addition, this model also allows for friction effects upon contact if the dispersed phase consists of solid particles.

4.7 Summary

4.7.1 Model Validation and Verification

The methods discussed range significantly in required resource, accuracy and stability, which are all important factors when defining a computational fluid dynamic model. Finalising a decision between the three is determined by the requirements, which as a recap from the introduction are to firstly investigate the flow around alternate offshore structures, followed by the resultant scouring, and then finally using the obtained knowledge and developed model, explore the potential geometric improvements to reduce the scour.

The approaches discussed in this chapter are interlinked but from a top-level, the first objective to investigate the flow, requires a model that can capture the mechanisms responsible for scouring. This validation of the model is reflected back upon when making computational and empirical component decisions, within the following chapters. The accuracy (how close the prediction is to reality) of this model must be high enough to allow a correct understanding of these mechanisms and importantly result in wall shear stresses that drive a realistic scour development. The predicted scour development concerns both the second and third objective, to understand the scour development and utilise it to explore scour mitigation. Similar to the flow, the accuracy of the development must be high enough to allow correct topology development, which therefore drives an accurate normalised topology more than the absolute depth. However, it must be made clear that this statement does not allow absolute values to be overly inaccurate, as this would lead to inaccurate normalised topology, which does not satisfy the outlined objectives. Furthermore, this verification of the model's performance is presented and discussed in Chapter 7 - Scour Model Development.

4.7.2 Turbulence Models

It is clear that computational accuracy is inversely proportional to time and numerical robustness, given the expense and gain of the different turbulence models. To summarise the common models, the first two-equation RANS models ($k-\omega$ and $k-\epsilon$) offer the greatest robustness and solve time but the lowest accuracy. The other Reynolds based model, the RSM, offers a very high level of accuracy; however, it stumbles across the same convergence problems as the two equation RANS models and has extremely high computational time and power costs; which are not always warranted (Ansys Fluent, 2014). For increased accuracy, a model with a different turbulence capture approach must be used, such as the LES model. This model uses a different methodology to RANS providing a significantly better resolution of the turbulent structures, however, is computationally more expensive than RANS and less robust. The only other main method, which combines RANS and LES is the DES model, which is less common and not as well founded. This provides the accuracy of an LES simulation with a lower expense of computational time and power; however, it still contains problems.

The mainstream models have very different attributes and the final choice should be determined by the expected flow and required accuracy, due to the relationship between numerical precision, robustness and time, and importantly model validation and verification. In conjunction, the long timescales associated with scour may also help determine the model choice as one method to compensate for the long timescales and therefore solve times is to use large time steps, resulting in large Courant numbers which are known to cause divergence in LES and therefore DES models.

Existing literature shows that RANS is the most common turbulence model used for scour modelling with a slow progression towards DES, (Khosronejad et al., 2012). Despite having the lowest accuracy RANS has been shown to replicate experimental results accurately, see (Azhari et al., 2010, Zhao et al., 2010, Khosronejad et al., 2013, Tulumilli et al., 2010). However, the loss of accuracy compared to LES and RSM models is undeniable; a comparison can be found in (Rodi, 1997). The differences are greatest in areas where the RANS model struggles including highly swirling flows and adverse pressure gradients. Unfortunately, these features are innate in both horseshoe vortices and lee-wake vortices. Alternatively, a greater accuracy can be obtained with the LES and DES models, however, given the long time scales their use is unfeasible. This is firstly because they are more computationally expensive, and secondly unlike the RANS model, this cannot be negated by using a large time step due to numerical divergence.

This discrepancy between poor accurate yet successful results using the RANS model is discussed further in the literature review and explored further in 0, whereby results using the different turbulence modelling methods are directly compared.

4.7.3 Multiphase Factors

The Eulerian and Lagrangian methods are most applicable to this study as the remaining passive scalar method is not accurate enough and the DEM is computationally too expensive. The decision between Lagrangian and Eulerian is dependent on the accuracy required, because as discussed previously the computational cost between the two can be minimal. On reflection of the objectives, if it is found that the Eulerian model can be used to accurately predict the deposition and transport of sediment, and therefore the correct concentration profiles then it can be used for further scour testing. In order to explore this possibility, existing scour models with a Eulerian sediment phase are reviewed in the next chapter.

The available multiphase interaction models for the Eulerian and Lagrangian methods are the same except the Lagrangian collision model. The lift, drag and turbulent dispersion models are key and others are available but not critical. The key models each contain different methods of computation that typically require values generated from flow parameters, however, all also contain user-defined coefficients that allow for model tuning and therefore a considerable variation in results. To retain consistency and accuracy, it is advisable to set all coefficients that are defined using flow parameters before tuning, with user-defined constants.

4.7.4 Mesh

If scour is simulated using a deforming mesh, complex bed geometries are formed, which are best represented using an unstructured mesh. However, if the cut-cell or CURVIB method is used the deformations do not affect the global mesh and it is better to use a structured mesh.

High mesh resolution is crucial in areas of high importance, such as the horseshoe vortex. The flow in such areas is best predicted without wall functions due to their downfall in complex flow. In order to capture the rich dynamics of the HSV a fine mesh is necessary, defined by either a minimum number of cells across the vortex using a mesh independence study or a cell size corresponding to a specific turbulent length scale. Alternatively, if fluctuating mechanisms are of interest the time step can be set to a fraction of the fluctuation wavelength, and then the cell size can be determined using a maximum CFL of one.

In areas of lower importance, the mesh resolution can be sacrificed for solve time. This is applicable in areas far from a pile, where only a developing or fully developed boundary layer is present. Here, the flow does not have to be fully resolved as wall functions can predict the flow sufficiently. The wall functions perform best using a hexahedral block-structured mesh adjacent to the bed surface with a minimum of three layers. In the present CFD software, Star-CCM+, this is achieved using the ‘trimmer’ mesh or ‘Prism Layers’ which are applied alongside an alternate core-mesh. The specific details of the structured-wall and adjacent core-mesh are investigated within using mesh independence studies, as they are dependent on the flow conditions of each case.

CFD Background Summary

This chapter provides analysis of the options available when setting up a CFD simulation, tailored to the capture of long-term scouring around foundation structures. This includes the main areas of discretization, turbulence models and wall treatment, time resolution, deforming mesh methods and multiphase flow options. The final section of this chapter discusses each section in turn, assessing the best combination of settings for the scenarios simulated in later chapters. The more precise details of each section, for example cell size and time step, is dependent on the specific simulation conditions and therefore assessed alongside each specific simulation in later chapters.

Chapter 5 Scour Model Literature Review

5.1 Morphological Models

A vast number of scour models are evident in scour investigation publications, with each constructed differently due to user preference or tailored to the application. However, there are common aspects, such as the number of phases which is used to group models in the following review. Furthermore, because of the model variation, only representative three, two and single-phase models are discussed, based upon typical model structure, elements, and successful analyses. This review therefore aims to provide an overview of the mainstream (three-dimensional) scour models, in order to aid decisions regarding the different modelling options.

5.1.1 Three Phase

Warner et al. (2008) presents a model developed within ROMS (Regional Ocean Modelling System), a generic open sourced framework designed for offshore physical modelling. The RANS equations are used to solve multiple-sediment, water and air phases in a Eulerian manner; including an ‘unlimited number’ of sediment classes, which is unique within this type of transport model. Interaction between the Eulerian fluid and sediment phases is one-way coupled, and advection and diffusion control the sediment phases with adjustment for vertical settling. Also, sediment concentration affects upon the fluid are accounted for by increasing the fluid density, based on the sediment concentration. The sediment bed and fluid sections are built up with layers, which is important as enables layers of different bed compositions, a unique aspect of this model. The free-surface was captured using a method similar to the VOF method, called ‘cell flux blocking’. A wave module is also applied and forms an integral part of the model.

The erosion of sediment from the bed surface is calculated using empirical formulae for bed load transport, specifically ‘Peter- Meyer and Muller’ (Meyer-Peter and Muller, 1948) and ‘Soulsby and Damgaard’ (Soulsby and Damgaard, 2005) to account for wave effects. In this model, the sediment bed is moved in increments of active layer thickness, whereby if the concentration in the layer become too large the active-layer moves up, and if too little it moves down. The thickness of the active layer is controlled based on the equation proposed by (Harris and Wiberg, 1997), which uses a factor of the average grain diameter plus a factor of the excess shear stress, as shown in Equation 20, where k_1 and k_2 are empirical constants of 0.007 and 6.

$$z_a = \max[k_1(\tau - \tau_c)\rho_0, 0] + k_2D_{50}$$

Equation 20

The concentration in the active layer is dependent upon the falling suspended load, new bedload due to the empirical formula, bed load from upstream and the exiting bed load. This is then used to displace the sediment bed using the approach similar to the CURVIB method, which is commonly used in many sediment transport models.

This model concentrates on primarily the wave-bed interaction and the evolution of complex sediment beds. It is applied to four test cases, demonstrating a developing concentration profile, migrating sediment trench, wave-coupled erosion and the evolution of a complex sediment-bed composition over a wide coastal area. The results from all cases are encouraging as agree well with experimental data.

Three-phase models are uncommon, however, not as rare as models which enable ‘unlimited’ sediment classes and multi-layered bed-composition. The structure of this model is perhaps the most complex of those available, however, still follows the general form of empirically based sediment transport models; with empirical bed load formula, adjustment for slope, and a conservation of sediment adjacent to the bed.

This type of geophysical fluid dynamic (GFD) model is primarily used for large-scale studies such as marinas and coastal areas. As a result, such cases are typically computed two-dimensional due to the required compute resource. Furthermore, due to the typical use of these models the contained fluid dynamic solvers often struggle with small scales of space and time (Tang and Keen, 2011).

A three-phase model has also been demonstrated within DELFT3D-FLOW by Lesser et al., (2004), using similar cases to Warner et al. (2008). The method to control the suspended load and bed load are very similar to Warner et al. (2008) however the empirical formulae used for bed load, slope effects and suspended load differ, as use formulae by Van Rijn et al., (2001), Bangold (1966) and Ikeda (1982). A feature included in this model is a morphological acceleration factor (otherwise referred to as MORFAC), which is used to speed up the simulation by multiplying the bed displacements by a constant. This is tested in two cases; the morphological changes over a coastal area and the erosion of a hump. Interestingly, the influence of the acceleration factor was negligible in the case of an eroding mound, but not in a coastal erosion case; likely due to the inclusion of tidal cycles.

A point of note within this model is the user-defined constants that are added to several of the empirical formulas for tuning the model. These accommodate for the inaccuracy of empirical formula, which is not always approached in sediment transport models despite the potentially significant impact. As empirical formulae are used within the model prescribed in this study, they are firstly assessed using external sources, prior to testing against experimental data.

5.1.2 Two Phase

Two-phase models that neglect a free-surface avoid calculating the fluid-air interface and any additional erosion due to waves, reducing computational cost. Jahangirzadeh et al. (2014) investigates the scouring impact of collars around cylinders through experiments and numerical simulations. The numerical model is two-phase using the RANS turbulence model, built within

SSIIM 2.0. Similar to the previously discussed model, bedload and suspended load is predicted using formulas proposed by Van Rijn (1987).

The grid for the numerical model was chosen after a mesh resolution study, and the model was tuned to match the experimental data by testing different empirical formula and roughness heights. The report shows extremely good agreement to experiments, although it surprisingly does not appear to suffer from the common error associated with horseshoe vortex prediction using the RANS turbulence model.

The previously mentioned tuning is typical in sediment transport models and in addition to empirical formula and roughness height, other factors are used for tuning including adaption lengths, bed load coefficients and diffusion coefficients.

5.1.3 Single Phase

Single phase models that do not compute a secondary sediment phase typically predict the sediment concentration above the bedload using empirical formula, or in some cases neglect it entirely. This reduces computational cost however also reduces the accuracy, especially in live-bed scenarios.

Zhao et al. (2010) presents a single-phase model, however the sediment concentration in the bedload layer is tracked in order to compute the bed movement using a variant of the Exner equation. The Exner equation in simplistic terms is a mass conservation equation governing cells adjacent to the bed, which is balanced by moving the cells on the bed surface. The model is used to investigate the scouring effect around piles of different shapes and angles of attack. The results are promising but there are discrepancies between numerical and experimental results, by a maximum of 50% in equilibrium scour time and 10% in equilibrium scour depth.

A factor which contributes to this underestimation is the previously mentioned poor prediction of the horseshoe vortex using the RANS turbulence model, which is also stated in other literature. The scour differences between LES and RANS is demonstrated in (Khosronejad et al., 2013), which includes a comparison of the scour around groups of rocks. The topological results depict the averaging effect in the RANS simulations, showing both smooth scour holes and areas of deposition. It is also shown that the LES prediction is closer to experimental results in areas of erosion and deposition. The difference in equilibrium scour depth and deposition height between LES and RANS ranges from 5% to 20%. The difference in equilibrium scour between time is also affected, as both models under predict the equilibrium depth, with RANS performing worse. To conclude, despite the discrepancies both models predicted the morphological changes well in terms of morphological displacement and time. Interestingly, this model obtains reasonable results whilst neglecting suspended load.

The discussed single-models have all included a form of sediment conservation on the bed surface, however, more simplistic models have been used with reasonable results. (Tulimilli et al.(2010) investigates the scour underneath bridge structure during flooding. In this model, the bed deformation is calculated from only the calculated bed flux using empirical bed load formula, which avoids considering the existing bed load, or retaining a specific bed load-layer height. Despite this simple approach, the model performed reasonably well, showing a scour pattern similar to the experimental with a difference in maximum scour depth of only 10%.

5.1.4 Literature Review Discussion

Many sediment transport models follow a specific structure of which the numerical method used to compute the fluid flow is typically RANS, however, it has been made clear that if a higher accuracy is required LES is necessary; to capture the turbulent structures that are otherwise time-averaged by RANS leading to the possible removal of important flow dynamics. The successful outcome of the discussed RANS based scour models suggests that the achievable accuracy is sufficient for the current work, in order to successfully predict scouring, however, in order to understand the differences further three simulations using RANS, RSM and LES are analysed and compared in the next chapter.

Methods used to close the turbulence equations vary, along with the use of wall functions and other methods to compute the bed shear stress, especially when waves are included. A factor entwined with wall functions and bed shear is the bed roughness, which is typically a multiplication of the grain diameter and usually tuned to suit the model. Within this study, 2.5 x grain diameter is used to represent the bed roughness, unless during model development significant differences are found between experimental and simulation velocity profiles and resultant wall shear stress, at which point it will be used to tune the model.

A sediment phase is critical in live bed scenarios as this is the most accurate method to compute the transportation and deposition of sediment. This phase is generally represented using the Eulerian approach due to the expense of other methods. This phase is controlled at a minimum using advection and diffusion, and a function to account for increased concentration effects; however, there are many other interaction models available. If a sediment phase is not modelled it is common to predict the sediment concentration above the bed load layer using empirical formula, or neglect it completely; as seen in (Khosronejad et al., 2013).

In order to validate the model, based on the initial objectives and considering the initially stated simplifications, the scour and therefore removal of sediment, only requires a single-phase model. This is because a single phase model is capable of accurately capturing the removal of sediment in a clear water environment, based on the results of Khosronejad et al. (2013) and the principle that the empirical bedload formulae will remain valid if there is no upstream bedload or suspended load sediment, that would otherwise impact the removal rate.

However, it is apparent that for some circumstances a secondary phase is unavoidable, for example when the upstream flow has a high sediment concentration. For these circumstances, the proven capability of the Eulerian model in the discussed literature is used to support the construct of a two-phase model. This undergoes simple testing in a pseudo-2D channel and trench in Chapter 7.

The required empirical formulae have been shown to range considerably, with the most commonly used bedload formula sourced from publications by Van Rijn, and critical shear stress derived from the work of Shields. However, in order to investigate further and choose the formulae for this study they are tested in the first development case (Chapter 7).

The movement of the sediment bed to simulate erosion or deposition is typically achieved using one of two methods; a deforming mesh or the ‘cut-cell’ or CURVIB approach, discussed in the section ‘Morphing Methodology’. This is controlled by conserving a specific amount of sediment within the bed load layer and balancing it with the movement of the bed surface, which is popularly achieved using Exner equation. Within the tested software, Star-CCM+, only the deforming mesh method is available and therefore the CURVIB approach is not explored in this study.

An Alternative Approach

The most accurate method to model sediment erosion would be to avoid the use of empirical formula and rely more upon dynamical equations, furthermore, for single particles as opposed to volume fractions of a cell, however, this is extremely computationally expensive.

Zhao and Fernando (2007) follows this approach and presents a two-phase (fluid and sediment) Eulerian model, which does not rely on empirical erosion formula. Instead, ‘dynamical equations’ are used to compute the movement of sediment on the bed. Despite the clear advantages of this method, it is not customary practice as it is computationally expensive, hence the two-dimensional approach. Irrespective of the fact this study cannot be represented two-dimensionally, the problems that were faced using this method were overcome and good agreement was achieved for the scouring underneath a pipe, however not for a secondary mine-burial simulation but it appears other factors may have been responsible. This is potentially the route sediment transport models will follow once advancements in computing have made it more feasible, and stands as an interesting future prospect.

Literature Review Summary

This chapter has presented the most common methods used to model scour, categorised by three, two and single-phase models. The success, structure and application of each method has been discussed followed by an assessment of the commonalities, in addition to the features that are most beneficial to this study. Following this review and the previous chapter on CFD options,

some modelling options have still not been defined as their outcome is unclear, therefore, one of the main undetermined factors, the turbulence model, is investigated more in the next chapter.

Chapter 6 Hydrodynamics of Foundation Structures

This chapter investigates the fixed-bed, single phase and two-phase aspects supporting the prevailing morphological simulations. The flow around a cylinder is firstly simulated using RANS, RSM and LES models to examine the magnitude of the previously discussed RANS model downfalls. This investigation concentrates on the horseshoe vortex and flow acceleration around the pile due to the significant scour impact.

The resultant scouring around many structures has been compared and analysed in existing research, however, there are limited studies that have compared the initial bed-stresses around a large variety of geometries, both complex and simple. Therefore, the second section examines the single-phase flow around a range of both existing and new foundation structures, providing an insight into the initial scouring around complex structures prior to further analysis using transient scour simulations.

6.1 Monopile Investigation

Chapter 5 Scour Model Literature Review, revealed that RANS turbulence models have been effective in a number of scour simulations; however, this is contrary to the fact that RANS models do not accurately capture flow-mechanisms that are key to scouring, in comparison to LES.

This contradiction is investigated by analysing the quantitative difference in flow and wall shear stress around a bed mounted pile using the mainstream turbulence methods covering a range of accuracies, namely RANS Realizable Advanced $k-\varepsilon$ (Versteeg and Malalasekera, 1995) with two-layer all wall- y^+ formulation, Reynolds Stress Model (or second-order closure model (Versteeg and Malalasekera, 1995)) using the Quadratic Pressure Strain Model and the LES model with the WALE Subgrid Scale model. This enables a far greater understanding of any discrepancies that may occur in the validation stage and further RANS generated results. The specific models were chosen as they represent the highest accuracy versions of each method.

In order to meet the stated objectives, the captured flow must be representative, meaning that the flow must enable the identification of key features and result in wall shear stresses that form realistic and accurate scour topology. Furthermore, the level of accuracy must allow identification of changes in scour given changes in geometry, therefore permitting scour reducing measures.

For the three models 1st order time and 2nd order spacial accuracy was used. As stated in 0, the use of 2nd order time accuracy provides more accurate results, however, is not possible with the final scour model due to instability issues and therefore testing using the higher order time accuracy would be valueless even at this early stage.

All simulations were run implicitly with a time step corresponding to a maximum Courant number of one throughout the whole domain. In order to ensure convergence of each timestep several

convergence criteria are used. For all three simulations the standard deviation of the sum of wall shear stresses on the bed must be below 0.005 over the last 5 iterations and the standard deviation of the volume averaged velocity over the whole domain must be below 3×10^{-5} over the last 5 iterations. These values were chosen based on the standard deviation after a large number of initial iterations were ran for each timestep and the residual velocity values were below 0.001.

Additionally, a minimum and maximum number of iterations were set to 10 and 25 respectively. This was based on the initial convergence speed when using an excessively large number of iterations (100) and once velocity residuals reached below 0.001.

The flow parameters, geometry and mesh are identical for all three cases. The flow and geometry are chosen as they result in a Reynolds Number that will form an unsteady horseshoe vortex system, matching the flow regime typically found offshore:

- Reynolds number: 18,400
- Pile diameter: 0.08 m
- Depth: 0.5 m
- Grain diameter: 0.00038 m

Therefore, the separation point for these conditions is approximately 1D upstream from the front of the pile; separation distance diagram in (Sumer and Fredsøe, 2002). Additionally, an unsteady horseshoe vortex system is expected based on the data in (Huang et al., 2014), see Figure 2-13.

Boundaries

The main areas of study in this investigation are the horseshoe vortex and flow acceleration around the cylinder, excluding the downstream vortex shedding. Due to the symmetrical nature of the features of interest, the horseshoe vortex and flow acceleration, it is permissible to model only half the cylinder, as shown in Figure 6-1.

The inlet is positioned 25D downstream and set with velocity and turbulence conditions that replicate a fully developed flow profile. This is defined using a preliminary simulation with identical roughness height, water depth and mean velocity within an infinitely long channel and no pile (due to the continual circulation of velocity and turbulence values from the outlet to the inlet). This same method was successfully used by Khan (2014).

The top, side and central symmetry plane were applied with a zero gradient, slip-condition with a distance of 5D between the side wall and central symmetry plane. The bed surface is applied with the same 0.00095 m roughness height as the preliminary simulation and lastly, the outlet boundary is positioned 25D downstream.

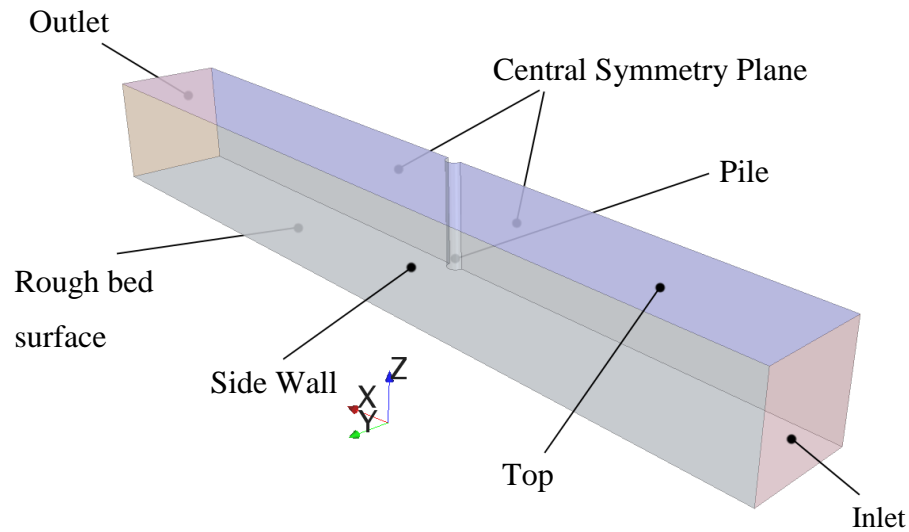


Figure 6-1 – Geometry Setup

Mesh

The flow far from the structure is relatively simple and thus can be predicted using wall functions; therefore, the wall $y^+ \left(\frac{u_* y}{\nu} \right)$ was maintained between 1 and 30 using a constant first cell height. The minimum resolution for the mesh above the first-layer was determined based on attaining a smooth logarithmic velocity profile. This was achieved using seven structured-layers on the bed with increasing thickness covering approximately 5% of the depth, with large polyhedral cells above.

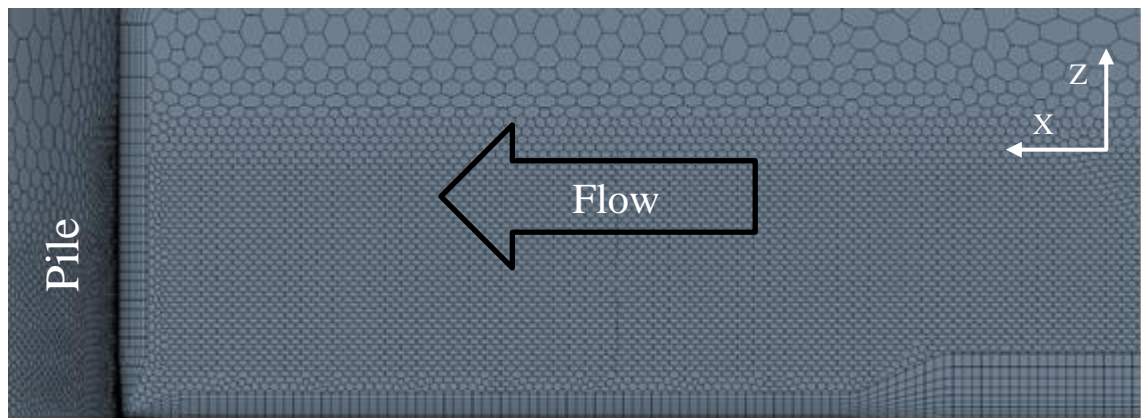


Figure 6-2 – Mesh Refinement

The local mesh contains two refinement volumes, one to capture the flow separation and horseshoe vortex and another to capture the down flow into the horseshoe vortex and flow around the upper part of the structure.

The lower mesh was determined by changing the size of the refinement volume and the cell size within, whilst monitoring the maximum and average shear stress around the front of the pile. These values converged with a control height of $0.25 D$ and cell size of 0.003 m , (Figure 6-2); following testing of over 20 combinations of size and volume.

A radius of $2D$ was chosen based on the maximum expected separation point, guided by (Sumer and Fredsøe, 2002). It was ensured that the wall- y^+ remained less than one to avoid wall functions by reducing the first structured layer thickness. A total of ten layers were used in order to utilise the higher-accuracy quad cells to predict the correct separation point and horseshoe vortices. The mesh above this was again refined using a convergence study to ensure that the down flow influencing the HSV is captured correctly, resulting in a cell size of 0.005 m.

6.1.1 Results

Horseshoe Vortex

The LES model predicted an unsteady horseshoe vortex system, featuring horseshoe vortices that constantly alter in size and position. The results were recorded over 9000 time steps to visualise the system. Two horseshoe vortices, one small and one large were always present at the foot of the pile and smaller and less stable vortices were present upstream; which are continuously generated and then travel downstream to eventually merge with the larger vortex at the front of the pile.

The horseshoe vortex systems produced with the RANS and RSM models are significantly different, featuring steady systems of fewer vortices. Figure 6-3 displays this using the q -criterion (Q) along the symmetry plane, representing the local balance between shear strain rate and vorticity magnitude. A vortex is identified when the vorticity is greater than the rate of strain, resulting in $Q > 0$ (Holmén, 2012). This specific method is chosen as it is capable of indicating and vortices (Ghasempour et al., 2011). The comparison demonstrates the swirling flow capability of each turbulence method in the expected order of LES, RSM and RANS. Additionally, the poor RANS predictive capabilities of swirling flows are demonstrated by the velocity streamlines. The streamlines begin at an upstream distance of 0.14 m, in a vertical alignment with a spacing of 0.75 mm.

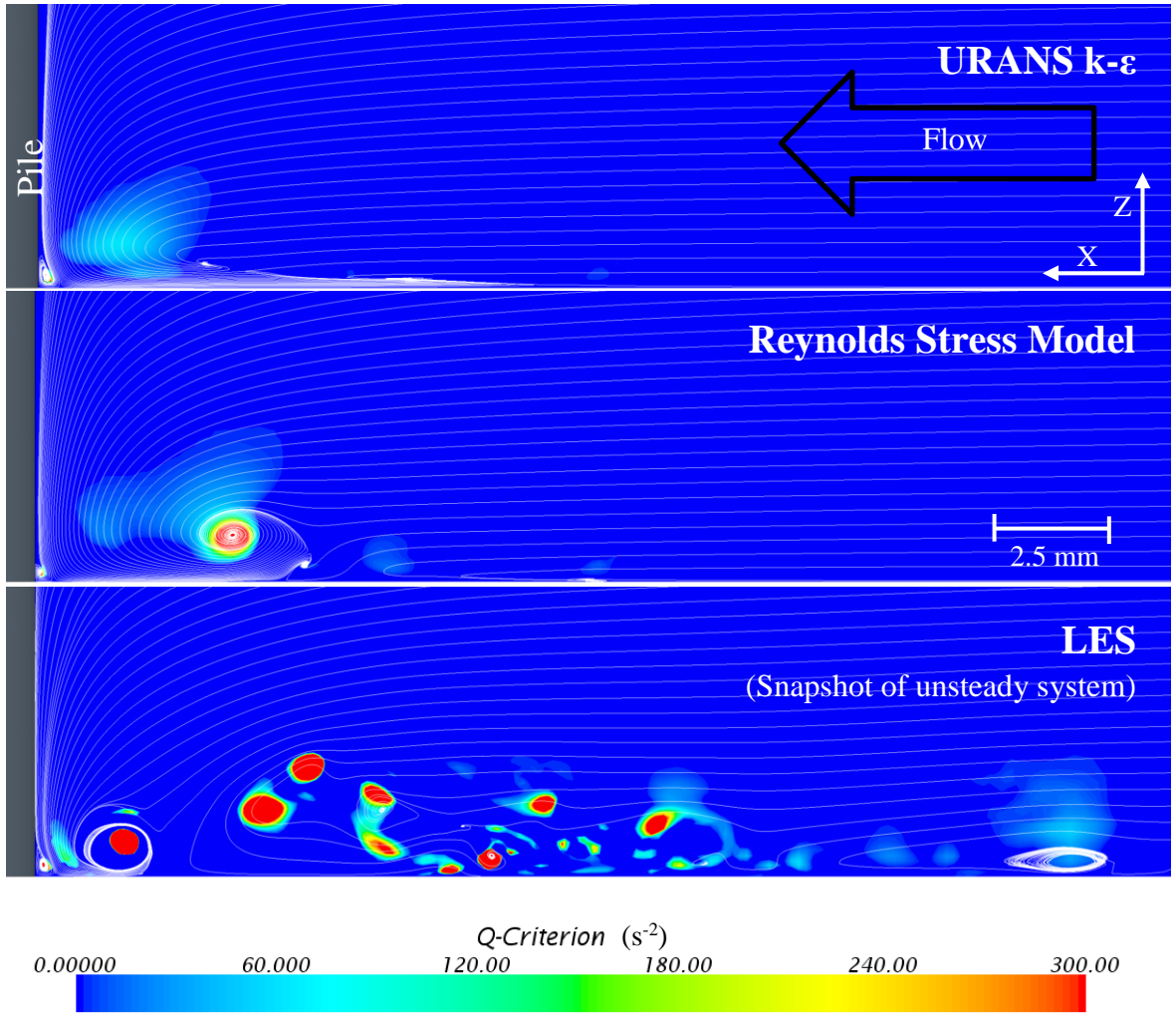


Figure 6-3 – Turbulence Model Comparison, Q Criterion

Upstream Boundary-layer Separation

The areas of flow reversal indicating flow separation are highlighted in blue in Figure 6-4. The RSM and RANS models have similar areas of flow reversal starting at an upstream distance of 0.095 m (1.2 D) from the pile centre similar to the predicted 0.08 m (1 D). However, the LES model displays a different flow reversal area that begins earlier than RANS and RSM at 0.17 m (2.1D) but similar to the RANS and RSM predictions the height of flow reversal only starts to increase at approximately 0.1 m.

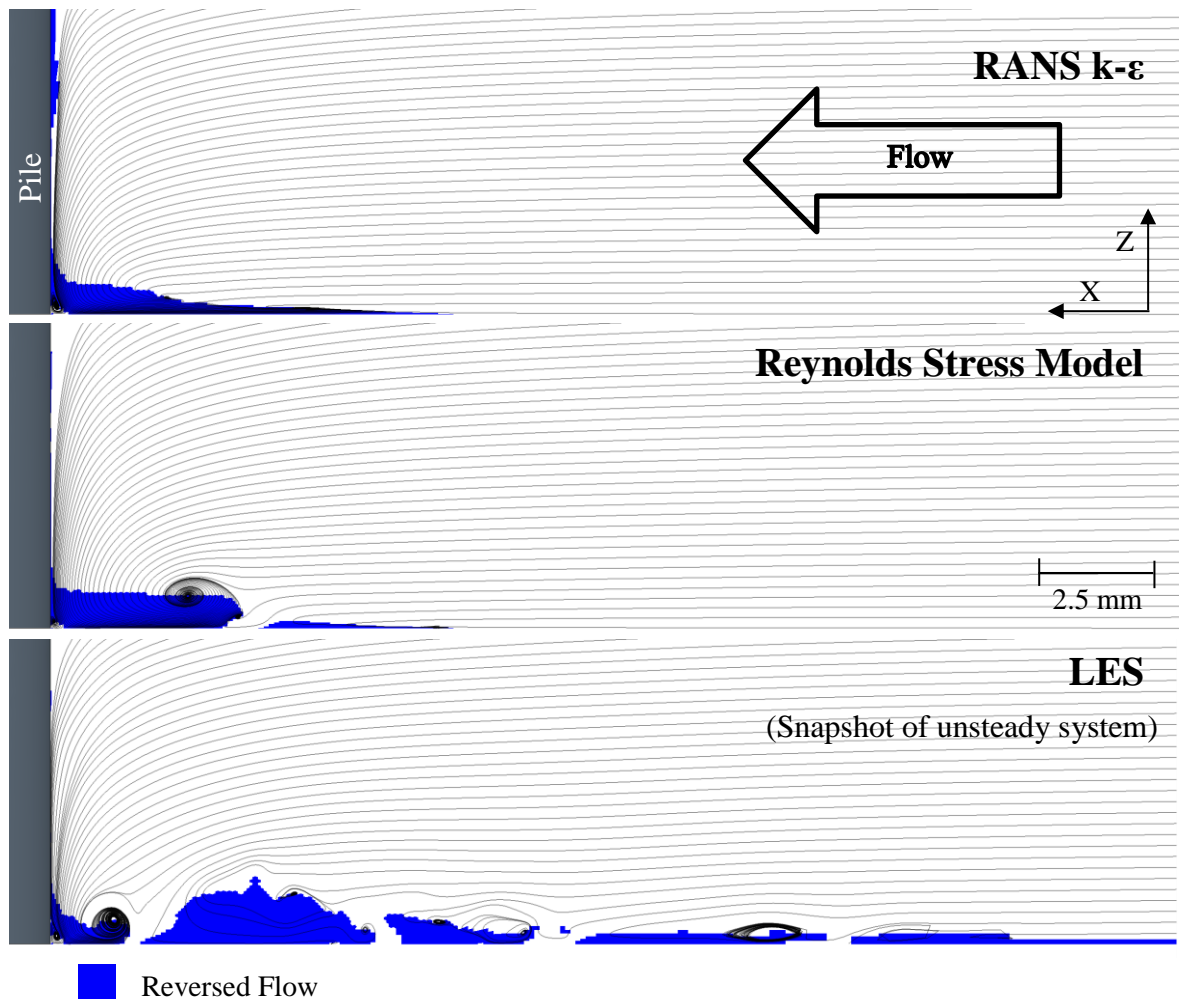


Figure 6-4 – Turbulence Model Comparison, Reversed Flow

Wall Shear Stress

The resultant wall shear stress maps for the three models are shown in Figure 6-6, accompanied by Figure 6-5 that illustrates the maximum wall shear around the pile within 2D; note that due to the fluctuating result of the LES simulation the both upper and lower extreme values are displayed.

All models display the highest wall shear around 57 degrees from the front at a stress of 0.9 Pa. The RANS and RSM models both feature wall shear stresses that dissipate away from this point

in all directions; however, the LES model results in strands of high stress concentric to the pile due to fluctuating horseshoe vortices.

Maximum Stress within 0.16 m (2D)

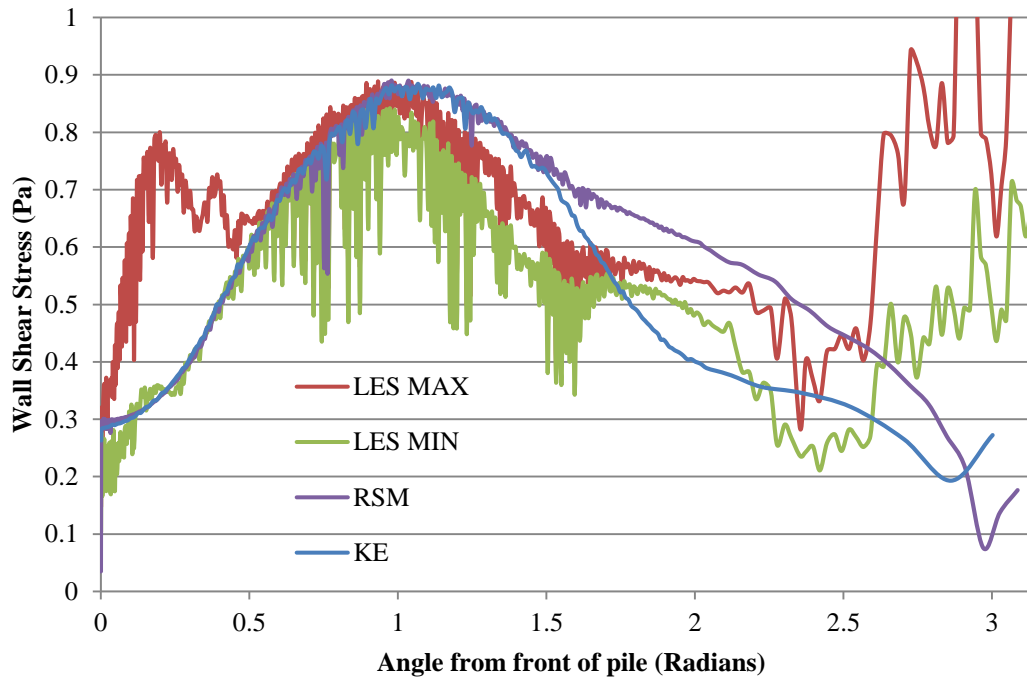


Figure 6-5 – Turbulence Model Comparison, Surrounding Max. Wall Shear

The greatest difference between the models is the shear stress at the front, which aligns with the differences in horseshoe vortex systems. The LES model fluctuates significantly at the front due to the unsteady horseshoe vortex system, as seen from the range in values in Figure 6-5. Depending on the time, the maximum wall shear stresses can be as low as the other two turbulence models or as high as the wall shear stress at 57 degrees. These high shear fluctuations at the front are the features that RANS models are criticised for missing, and can be key to correctly predicting scour.

To quantitatively compare the curves in Figure 6-5, the correlation coefficients (r^2) between each are provided in Table 6-1. This data again indicates the similarity between the RSM, KE and LES minimum values, and the large difference to the LES maximum values.

	KE	RSM	LES MIN	LES MAX
KE	1	0.874	0.680	0.266
RSM	0.874	1	0.669	0.162
LES MIN	0.680	0.669	1	0.241
LES MAX	0.266	0.162	0.241	1

Table 6-1 – R-Squared Correlation of the maximum stress points around the Pile

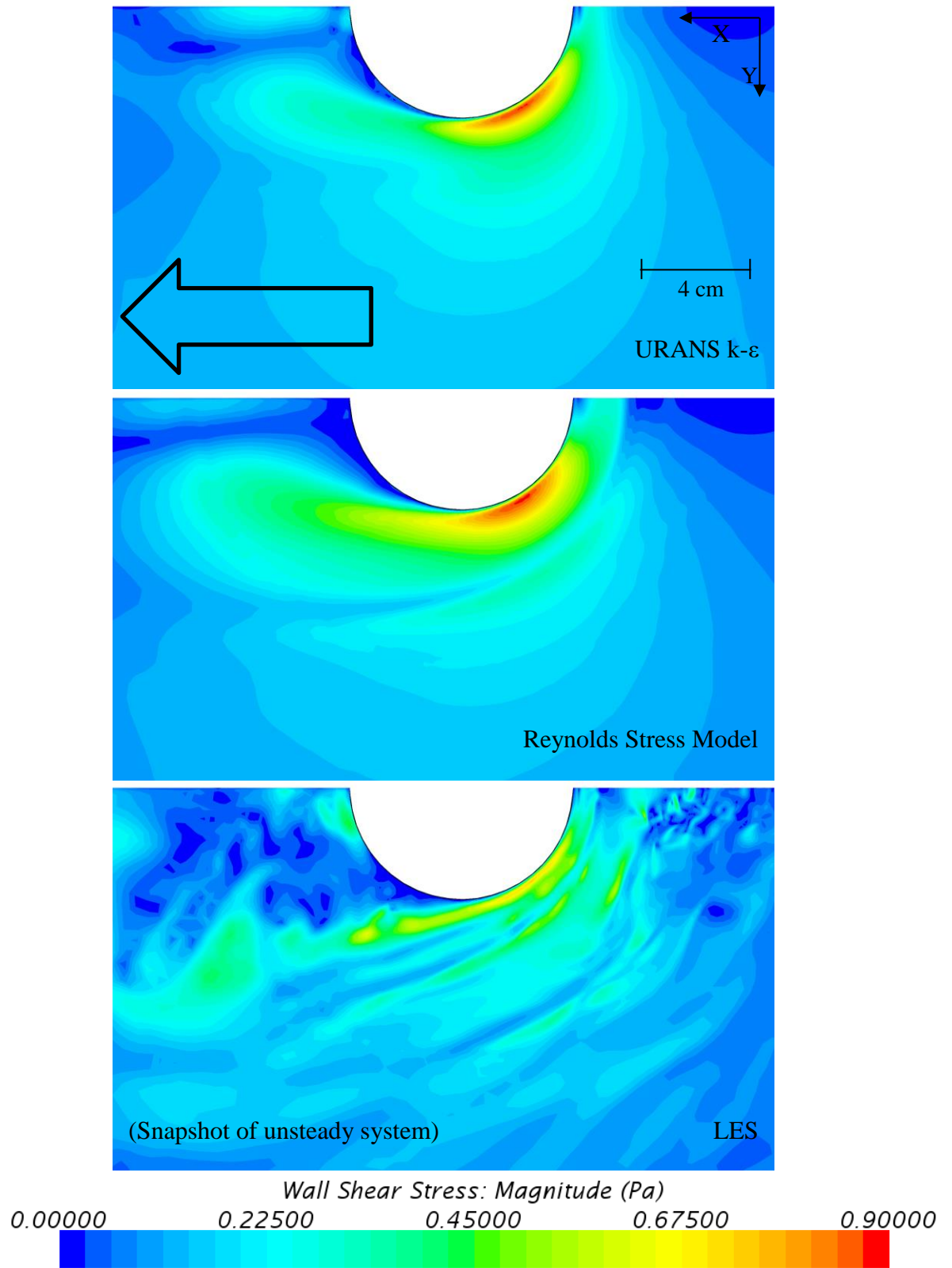


Figure 6-6 – Turbulence Model Comparison, Wall Shear Stress

This brief investigation unveils the magnitude of the accuracy lost when using either the RANS or RSM model in comparison to LES. The most significant differences are in the upstream horseshoe vortex area evident from the differences in streamlines, q -criterion and importantly the wall shear stress.

The impact upon scouring is largely dependent on the flow variables, as they determine the magnitude, location and frequency of the high wall shear stresses due to the horseshoe vortices. In a worst-case scenario, the high stresses would be stagnant in position and remain high, fluctuating frequently. This would be poorly predicted with the RANS and RSM models as they fail to replicate the same high stresses at the front of the pile. Alternatively, if the high stresses occur infrequently moving over a large area the scouring effect can be considered negligible; closing the gap between LES and RANS predictions.

The outlined thesis objectives require identifiable flow features in order to analyse the flow around structures and accurate shear stresses (with emphasis on normalised shear stress maps) in order to correctly predict and analyse scour and look for mitigation methods. This chapter and the previous Chapter 5 have provided a valuable insight into both of these factors (the flow mechanisms and shear stresses) which aids the decision into which turbulence model to use.

In respect to the flow mechanisms this study has shown that although the strength and detail of features that are hard to predict with RANS are lost, for example the horseshoe vortex with high swirl and strain, flow mechanisms are still identifiable, for example with the streamlines and areas of reversed flow. The RANS k - ϵ and Reynolds stress model correctly displayed the mean flow features, however lost the finer detailed flow mechanisms captured using the LES model. Based on the capture of flow features alone it would appear there is a huge discrepancy between LES and RANS that would lead to entirely different shear stresses and therefore scour, however this study and previously described literature show otherwise. This study shows that although the wall shear stresses are clearly more time-averaged with the RANS model, the surrounding mean shear stresses are not indifferent enough to cause a significant change in scour. The largest difference is due to the large averaging effect that causes a loss in detail, as shown by the shear stress maps in this study and also the scour in (Khosronejad et al., 2013) however, because the effects are experienced over a lengthy period of time, there is a minor difference in absolute scour depth (5-20% in (Khosronejad et al., 2013)).

The ability to capture the correct shear stresses and significantly reduce computational resource using high Courant numbers supports the use of the RANS model. Therefore, from this point forward the RANS model is used which includes steady-state non-deforming simulations, due to their later use in transient deforming simulations.

However, it should be noted that if it becomes imperative that highest flow accuracy is required, then the model can be quickly and easily changed to use LES due to the advantages of using a commercial package.

Monopile Investigation Summary

This investigation has allowed for a quantitative view of the wall shear stresses produced around a pile with different turbulence models. The greatest difference is in the horseshoe vortex region, where LES is significantly different to the other two models. However, there is still clear evidence of the horseshoe vortex and the resultant, time averaged wall shear stresses are extremely close. As the RANS model is able to capture the flow mechanics and the resultant shear stress are extremely close to the more accurate LES model, in conjunction with the ability to use large courant number with the RANS model, it is to be used for all further scouring simulations.

6.2 Alternate Pile Shape Investigation

This section acts as a preliminary investigation into the scouring around complex foundation geometries. New and existing designs are investigated under steady state, non-scouring conditions; utilising the fact that flat-bed shear stresses indicate the initial scour topology due to the strong relationship to erosion rate as shown by the excess shear stress based bedload equations. This allows a large number of geometries to be investigated as requires approximately 1% of the time necessary for transient scour simulations.

As portrayed by this thesis a large number of offshore pile designs now exist. This investigation concentrates on two of the main types, monopiles and suction caissons. Variations of these types are tested neglecting any free-surface effects, permissible using a significant water depth (40m) and a comparatively small pile diameter (5m) and the boundary layer height; developed from a velocity profile of mean velocity 0.6 m/s over a bed composed of sediment with a mean diameter of 0.4 mm.

6.2.1 Monopile Optimisation

The most common monopile scour prevention devices are disc-shaped collars, which have been investigated exhaustively including the effects of multiple collars, spacing, position and diameter. Alternate and innovative prevention methods such as vegetation, monopiles with slots (Hakimzadeh et al., 2012, Nohani et al., 2015, Heidarnejad et al., 2010) or strakes (Korkischko & Meneghini, 2011) pose practical problems, however remain scarcely investigated despite evidence of positive impact.

Vegetation is a known scour preventative including artificial seaweed and reeds, however; its application to an offshore pile scenario is rare. The computation of such a scenario is unfortunately extremely complex given the intricate, flexible geometry and the unavoidable need for very accurate discretization and deposition model. Investigation into slots has shown scour reductions up to 24%, as shown by (Hakimzadeh et al., 2012, Heidarnejad et al., 2010, Nohani et al., 2015). These sources test a large majority of the potential slot configurations and this study therefore concentrates primarily on strakes. As discussed in Chapter 2 strakes have historically been used to impact aerodynamics, however their testing and use in hydrodynamic applications is rare.

Strake Testing

Izadinia and Heidarpour (2012) investigated the scouring effect of strakes by utilising pre-existing cables, demonstrating a scour reduction up to 50%. To obtain a greater understanding of the hydrodynamic changes caused by strakes the following study investigates the sensitivity of strake geometry upon bed shear stress (Figure 6-7). The sensitivity analysis starts with the design parameters shown in Table 6-2; which are then changed and simulated in turn, resulting in 26 simulations.

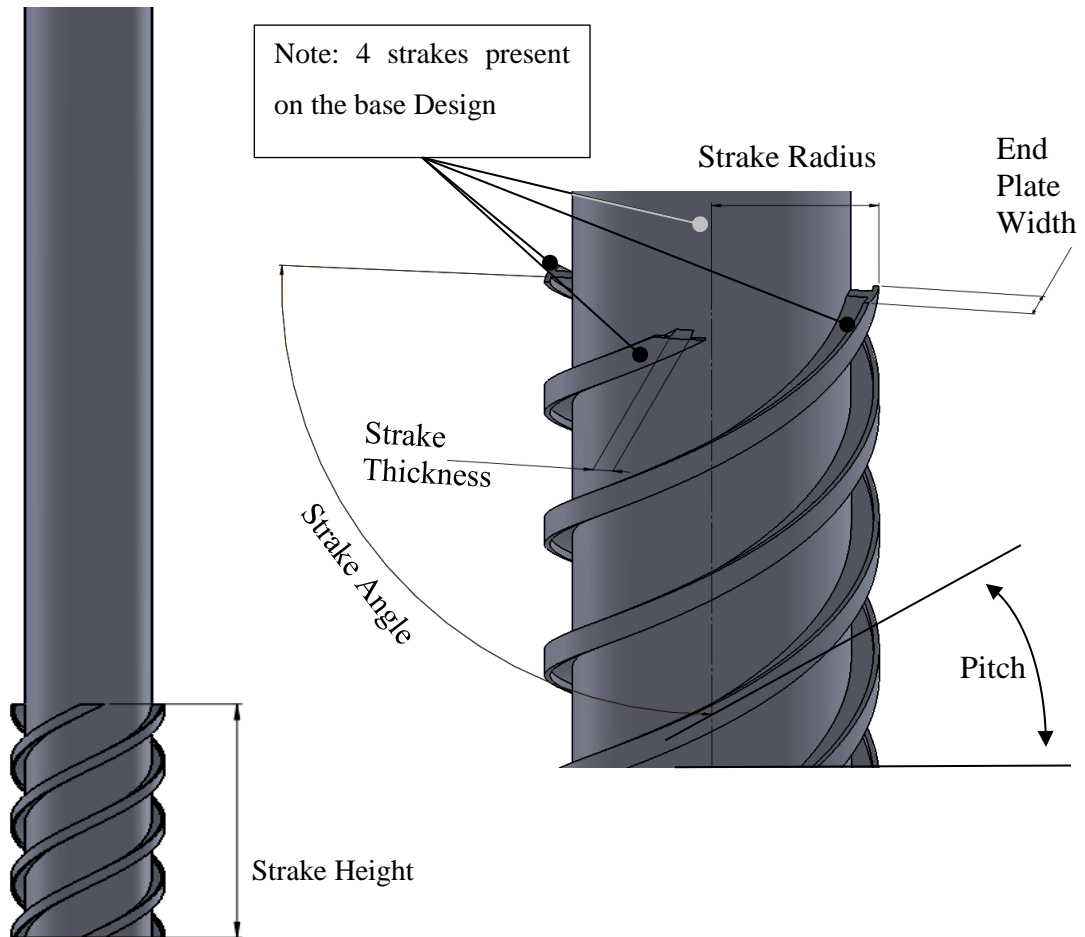


Figure 6-7 – Strake Parameterisation

	Base Design	Min	Max
Number of Strakes	4	0	12
Pitch (m)	10	10	45
Strake Radius (m)	3	3	8
Thickness (m)	0.2	0.2	0.6
End Plate Width (m)	0	0	2
Strake Height (m)	1	1	40
Strake Angle (°)	0	0	60
Start Position (°)	0	0	60

Table 6-2 – Strake Base Design Parameters

Simulation Setup

Physics

The single liquid phase is calculated using the steady-state RANS equations, closed with the K- ϵ turbulence model alongside additional two-layer, all wall- y^+ formulation (see Chapter 4, Turbulence Models).

Boundary Conditions

The fluid domain surrounding the strake structure extended 30D upstream, 40D downstream and 20D either side of the pile, with a depth of 8D, as shown by Figure 6-8. Due to the unsymmetrical nature of strakes symmetry could not be applied, unlike the previous simulation. The velocity and turbulence values at the inlet represent a fully developed flow profile generated using a preliminary simulation, with a mean velocity of 0.6 m/s and grain diameter of 0.2 mm.

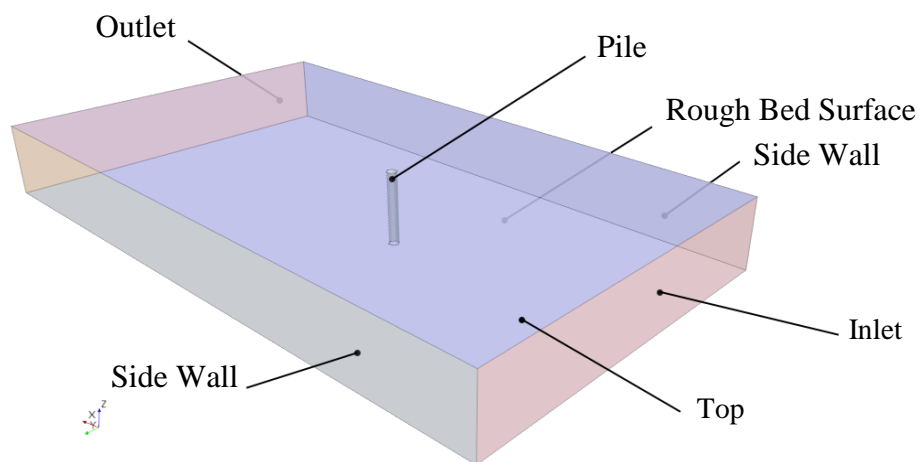


Figure 6-8 – Strake Testing Domain

Mesh

The domain is discretized with core polyhedral and orthogonal cells on the bed and pile surfaces. Refinement incorporates two cylindrical volumetric controls, the first encapsulating the horseshoe vortex and extending beyond the strakes (Figure 6-9); modified depending on strake permutation. The second specifies a larger cell size than the first, extending above the first volume capturing the down flow. This control extends to double the pile diameter, unless wider strakes are present whereby 1.2 times the strake diameter is used. The prism layers were defined by applying 6 layers with a stretch factor of 1.5, keeping the first layer greater than the roughness height whilst maintaining a wall $y^+ < 30$ close to the pile. Outside of this region the overall prism layer thickness was increased and first layer decreased, to accommodate for the increased speed and boundary layer thickness. The height of the first layer remained greater than the roughness height, whilst keeping the wall y^+ as low as possible and retaining good aspect ratio cells.

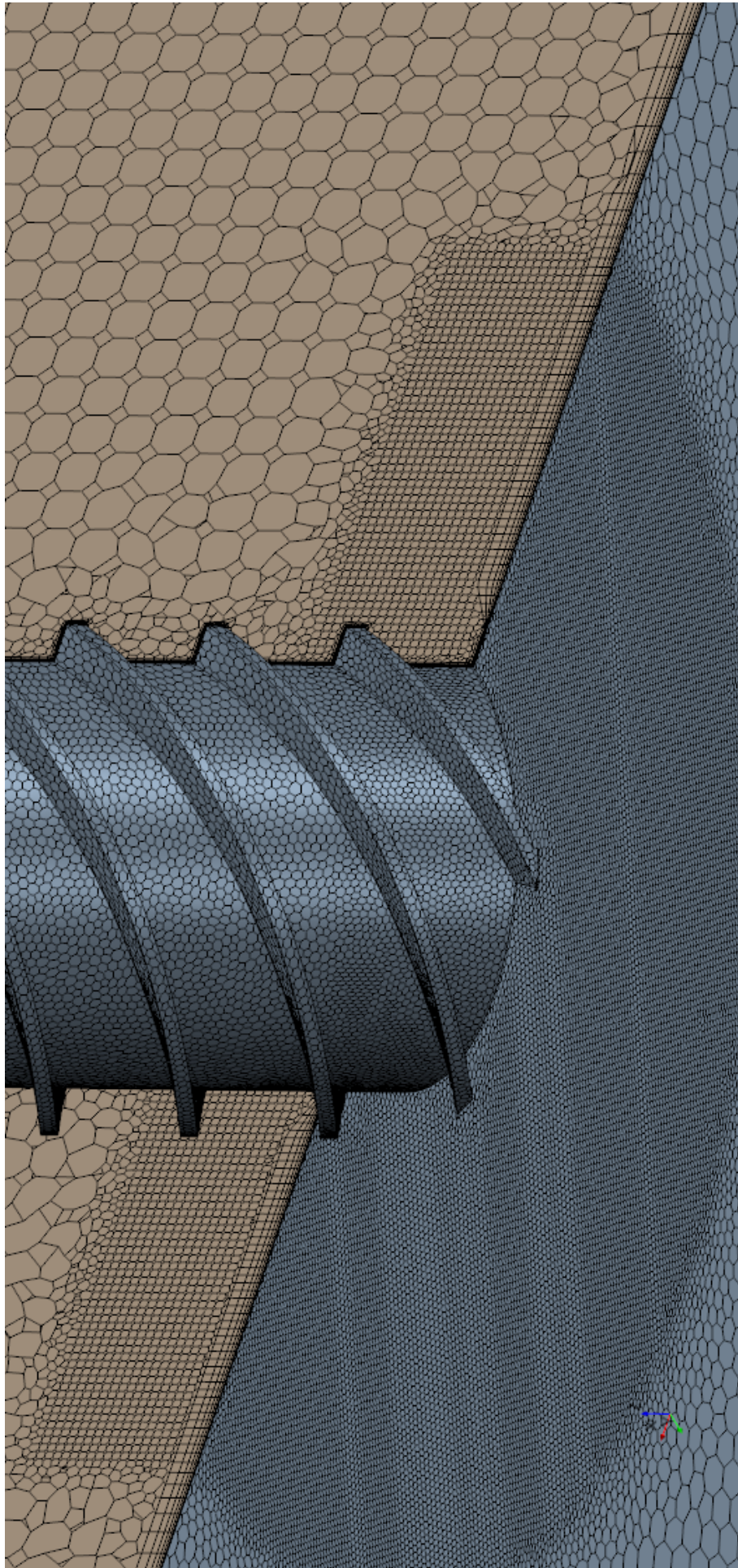


Figure 6-9 – Strake Testing Mesh – Base Design

Results

In order to assess the effect of each permutation the maximum normalised and surface average normalised wall shear stress within a 10m and 20m radius referred to as local and global shear stress are recorded.

The modification of each parameter reveals a trend in both maximum and surface average stresses, and it is important to understand the reasoning behind these especially the changes that lower the stresses. Therefore, the following assess these changes and when necessary further investigates the resultant changes in flow.

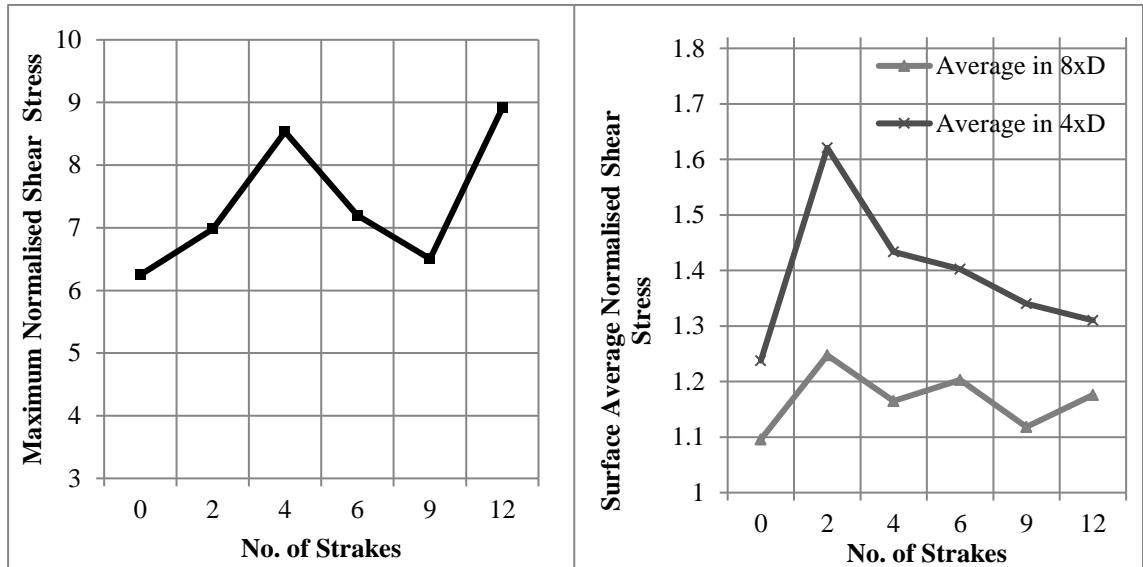


Figure 6-11 – Number of Strakes Impact

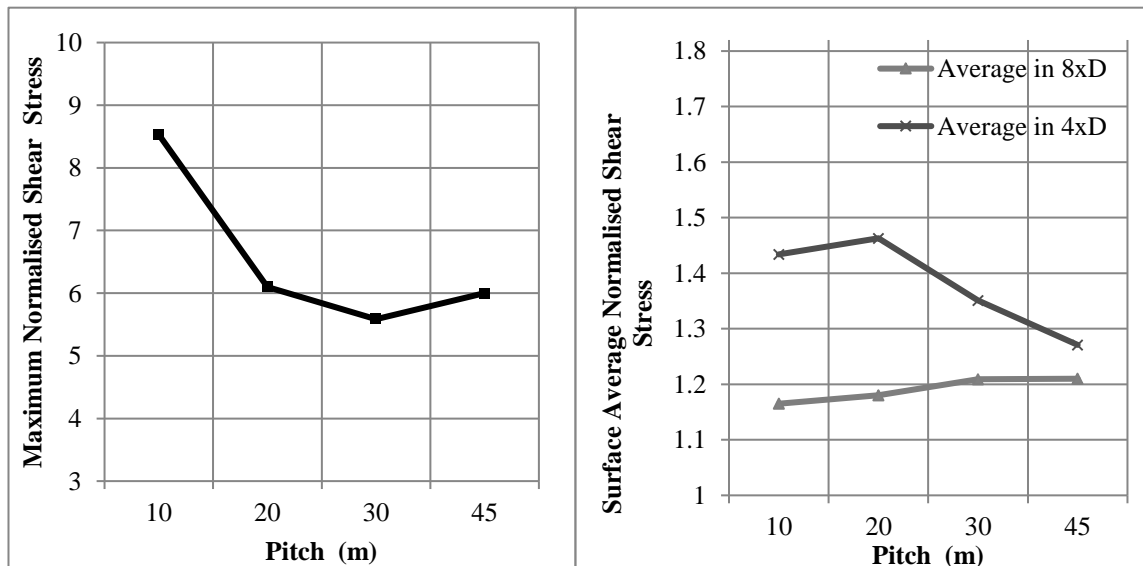


Figure 6-10 – Strake Pitch Impact

Beginning with the most prominent features, the introduction of strakes initially increases the shear stress, followed by a decrease as the number of strakes is increased further, evident from both local and global shear stress, Figure 6-11. The increase in maximum shear stress from 0 to 4 strakes is discovered to be due to the position of individual strakes, as shown by the change in

rotation as discussed shortly. The proceeding decrease from 4 strakes to 9 is explained by the blockage caused by the additional strakes; which reduces the flow speed and therefore the high shear due to strake corners. The last, and final increase is due to the close proximity of the strakes, providing a flow ‘guide’ from the front around to the bed surface, duplicating the effect evident in Figure 6-17.

Figure 6-10 shows that increasing the pitch raises the average global shear stress but lowers the maximum and local average. A reduction in pitch makes the pile more streamlined allowing the flow to remain attached. However, causes the shear stress resulting from strake corners to increase, therefore raising the local shear stress. This is evident from the contour plots in Figure 6-12, illustrating the bed shear stress and velocity at a z/h of 0.0025.

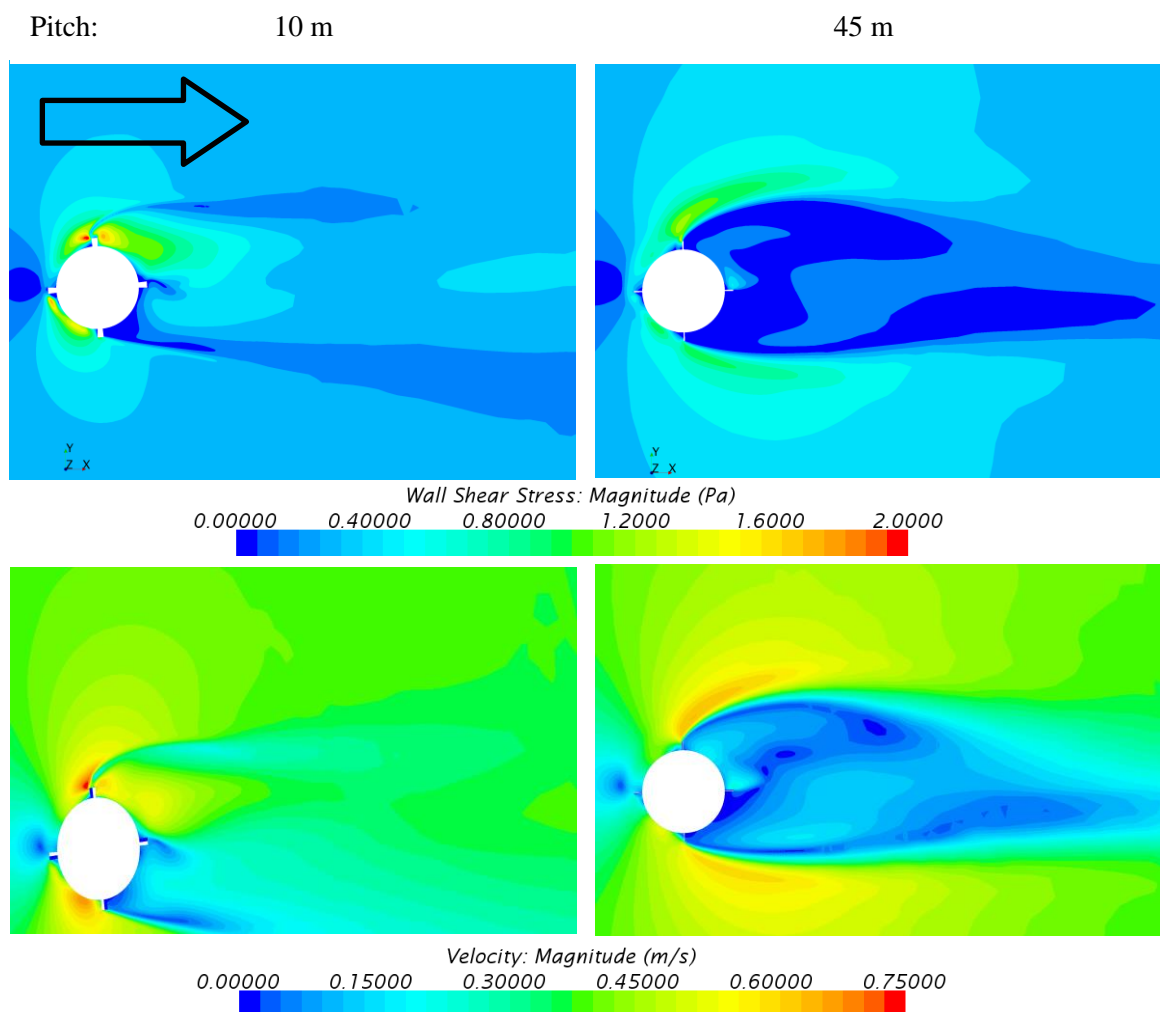


Figure 6-12 – Velocity Magnitude Contour Plots, 10m and 45m pitch

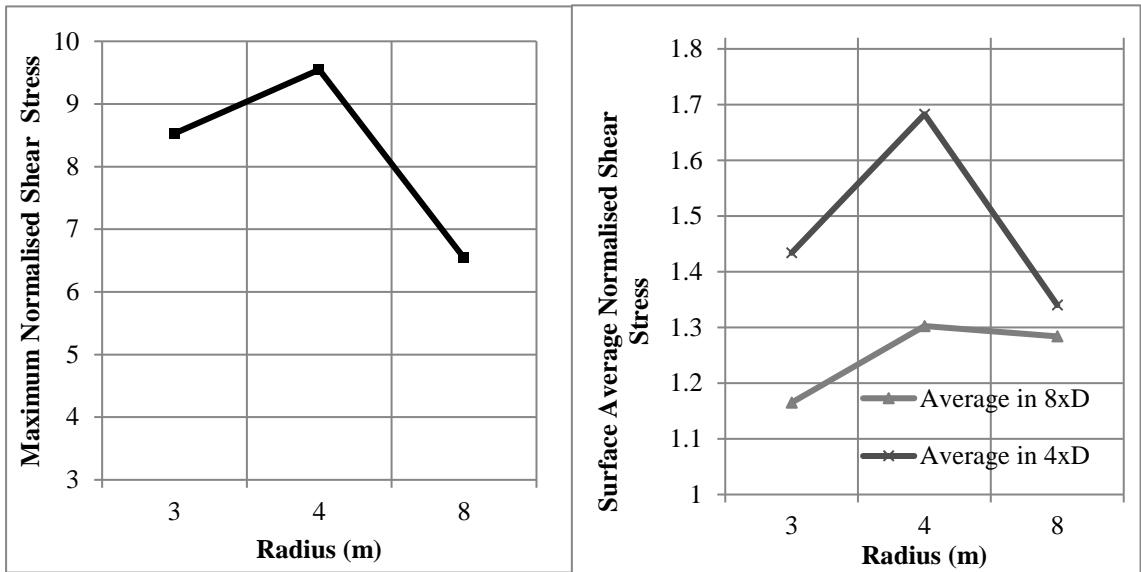


Figure 6-13 – Strake Radius Impact

An increase in strake radius initially increases the average shear followed by a continual fall, Figure 6-13. Analysis of shear stress contour plots reveals that the initial rise is due to the shear stresses produced at the edge of the upstream strake. This reduces as the strake radius is increased further as the end of the strake breaks out of the front stagnation area. Additionally, as width is increased the shear stresses produced by the end of the strake on the converging side (Figure 6-14) decreases significantly, as it breaks out of the high velocity area.

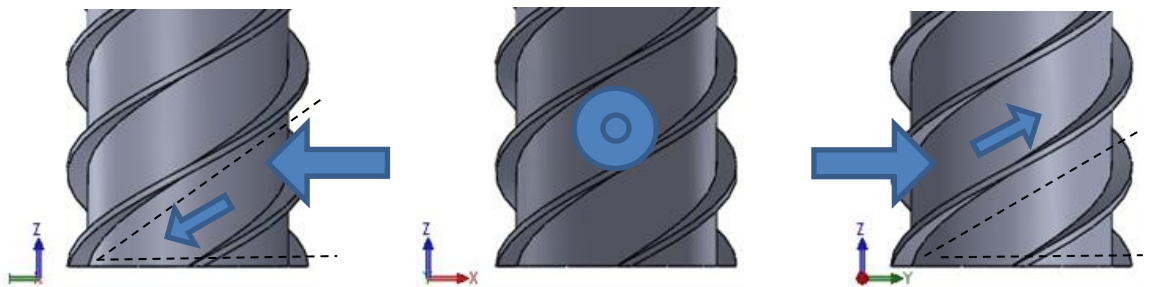


Figure 6-14 – Strake Geometry Converging and Diverging Sides

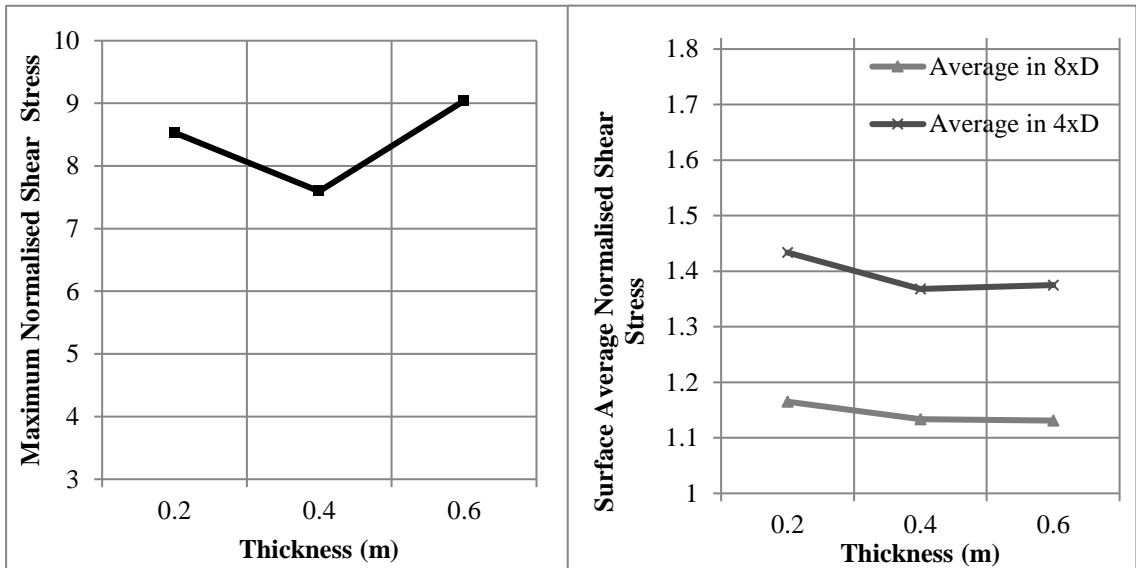


Figure 6-15 – Impact of Strake Thickness

A change in strake thickness displayed a negligible change in average shear stress. Furthermore, the fluctuation in maximum shear stress is minor compared to other design changes and is explained by the small changes in mesh as thickness is changed, Figure 6-15.

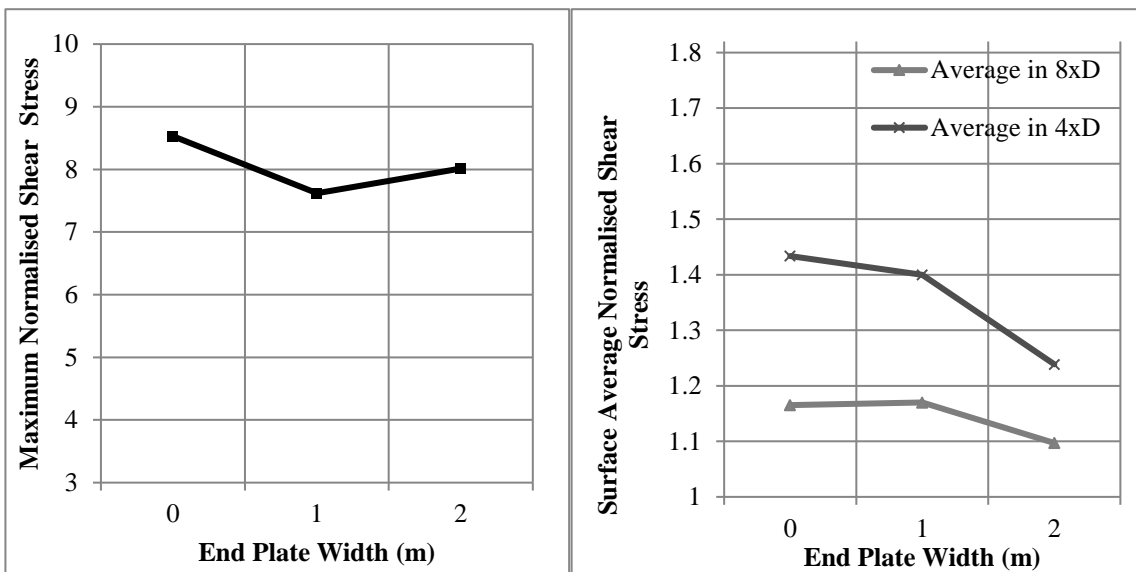


Figure 6-16 – End Plate Width Impact.

The results show that the average shear stress decreases as end plate size is increased, Figure 6-16. The analysis reveals that larger plates deter the flow from following the strakes, Figure 6-17, avoiding previously high stresses, Figure 6-18. On the converging side, there is a similar amount of stress due to vortices, however lower stresses downstream, Figure 6-18.

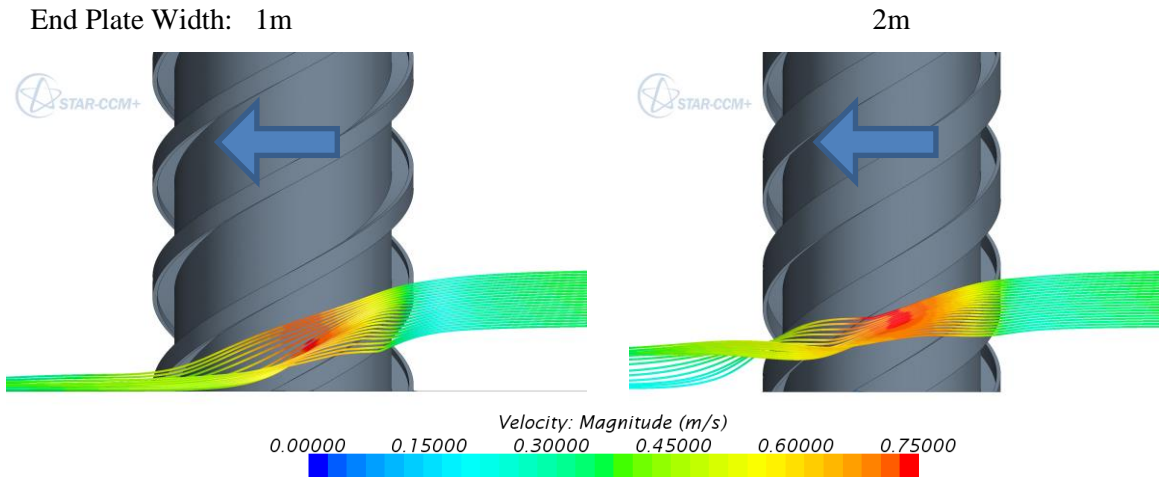


Figure 6-17 - Strakes – Larger End Plate Flow Attachment

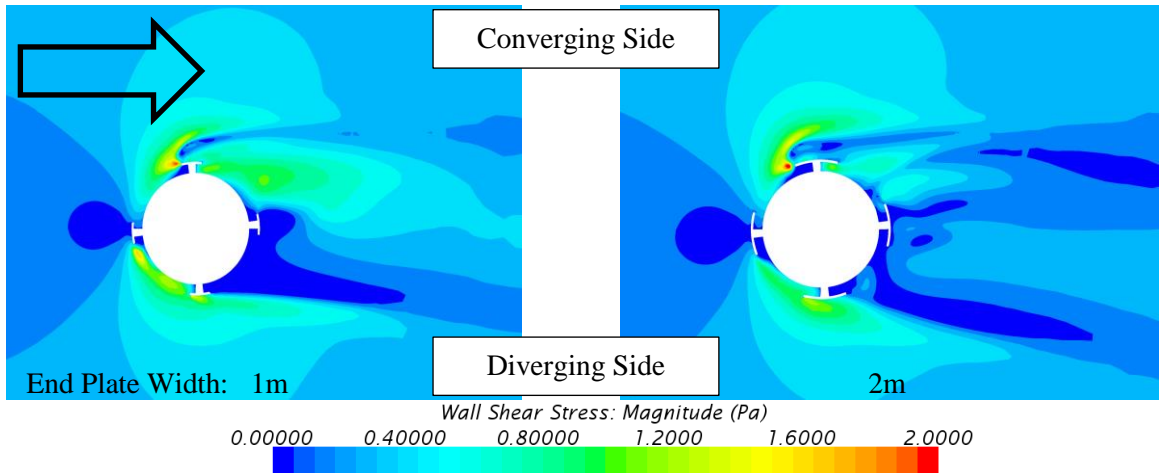


Figure 6-18 - End Plate Width Effect on Wall Shear Stress

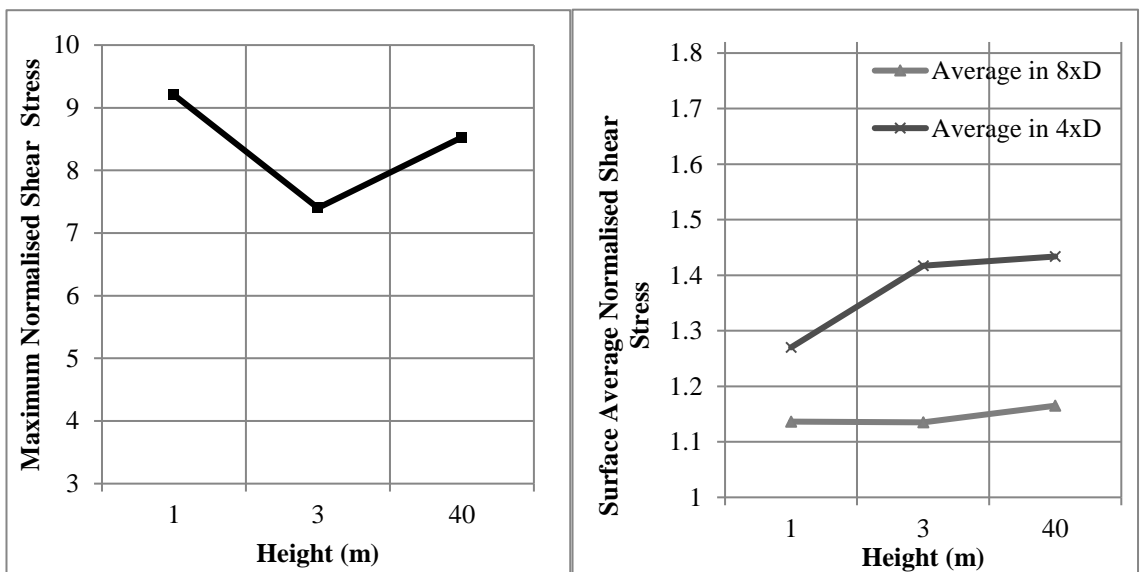


Figure 6-19 – Strake Height Impact

A reduction in strake height lowers the average shear stresses; simply because this reduces the blockage factor on both sides. In addition, there is a reduction in flow velocity behind the structure, evident from a reduction in downstream shear stress in bed contour plots.

A strake angle smaller than 90 degrees essentially creates a conical spiral, as shown by the section-cut in Figure 6-20. This was expected to divert more flow away from the bed surface; however, both shear stress contour plots and average shear stress show no considerable change, Figure 6-20.

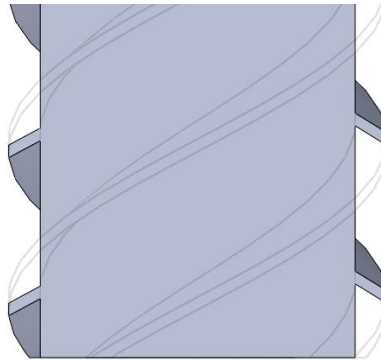


Figure 6-21 – Strake Geometry Conical Effect

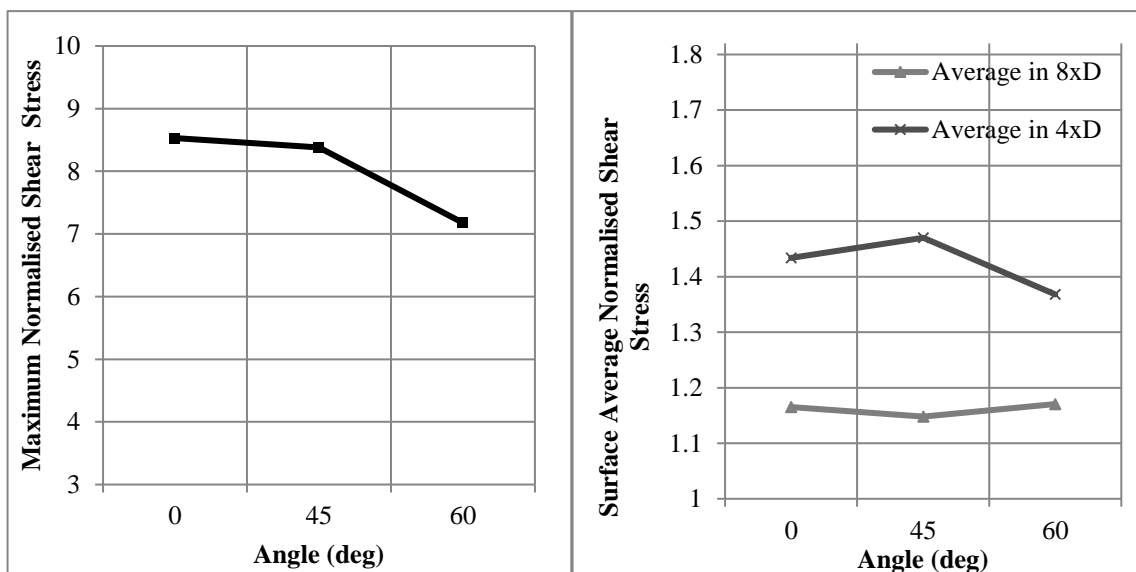


Figure 6-20 – Strake Angle Impact

As mentioned earlier adjusting the structures angle of attack highlights the effect of strake position, as shown by Figure 6-23 which illustrates that the shear stress on the end of strakes is highest when placed in the area of highest velocity, at 45-90 degrees, Figure 6-22. Additionally, high shear stresses are produced when the strake is parallel to the flow direction; however, as

highlighted by the effect of strake radius, this is only valid if the strake does not protrude the stagnation region.

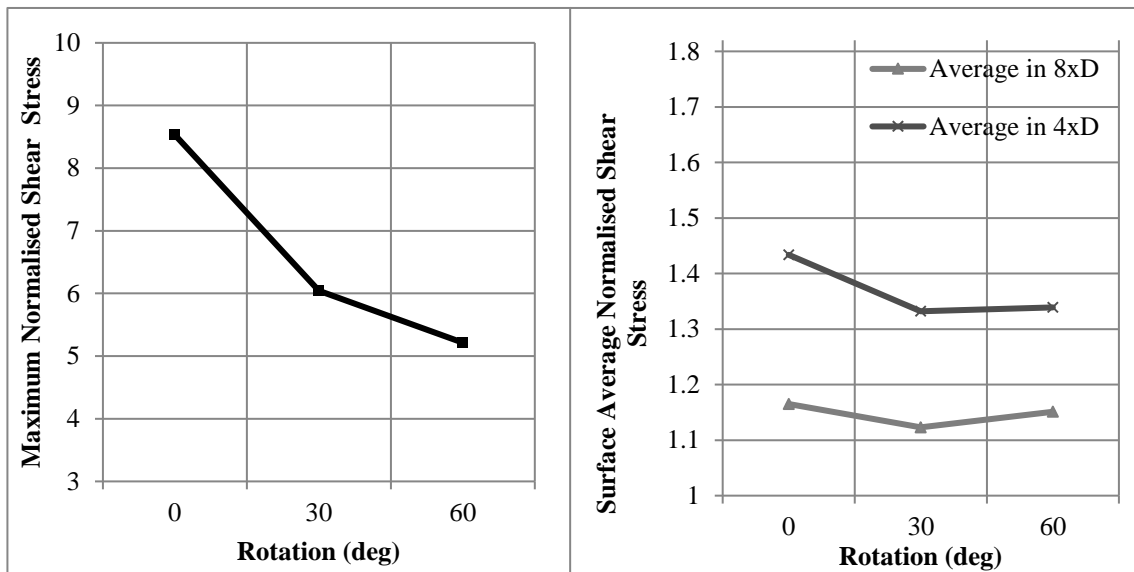


Figure 6-22 – Strake Rotation Angle

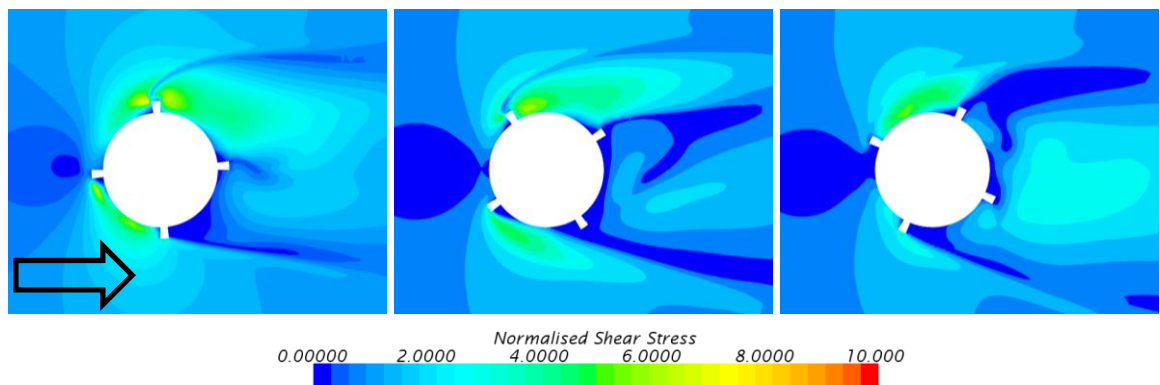


Figure 6-23 – Changing Strake AOA

The tested permutations have revealed the factors that lower average wall shear stress when changed individually, but none have resulted in a local or global shear stress lower than a monopile. Testing a greater range of each variable may result in an improved design, however this also makes the design less practical. As an alternative, the factors of greatest influence are combined with the aim of reducing the shear stress below that of a monopile.

The strake design, Table 6-3, Figure 6-24, was developed by maximising the positively impacting parameters, namely;

- Increasing number of strakes
- Increase pitch (although this raises the global shear stress)
- Increase strake radius (there is a lower threshold value)
- Increase end plate width
- Reduce strake height (which also improves the practical and numerical efficiency)

The resultant design improved the global shear stress by 23% compared to a monopile and 28% compared to the original strake design. The local (20m diameter) shear stress is not used as a measure as is the same diameter as the strakes and therefore does not account for the surrounding shear stress. Additionally, the maximum shear stress was reduced by 12.5%, Figure 6-25.

No. of strakes	Pitch (m)	Strake Radius (m)	Thickness (m)	End Plate Width (m)	Strake Height (m)	Strake Angle (deg.)	Start position (deg.)
8	25	10	0.2	2	3	0	0

Table 6-3 – Optimal Strake Design Parameters

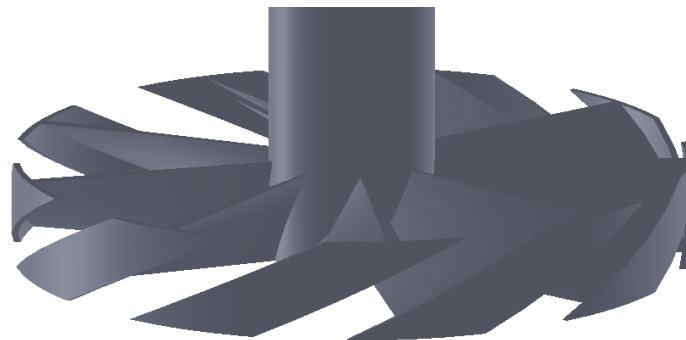


Figure 6-24 – Optimal Strake Geometry

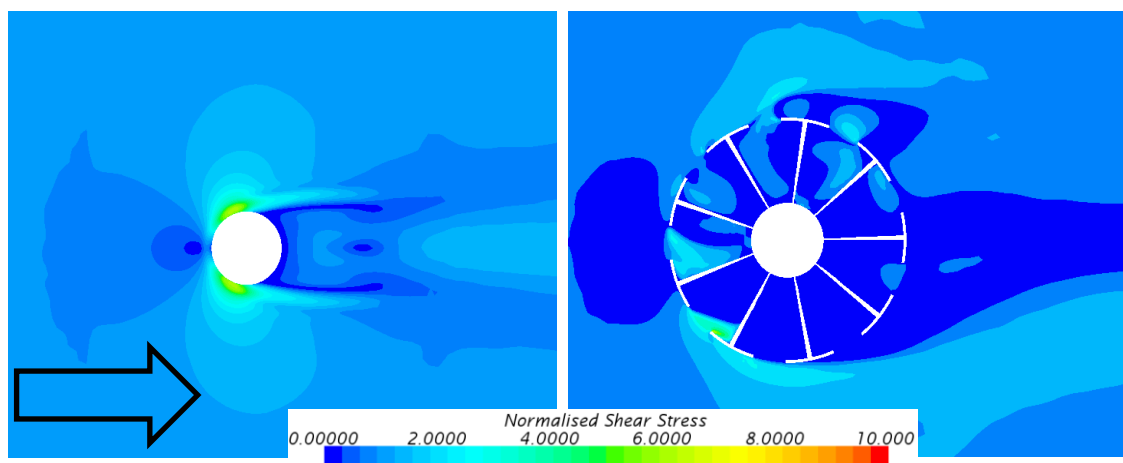


Figure 6-25 – Optimal Strake Geometry Shear Stress Comparison

In addition, 20 other combinations of the six advantageous factors (pg. 114) were simulated to ensure that no combination of parameters had a negative impact; however, all provided higher shear stress values.

The final design is significantly different from the initial base design and how strakes are commonly recognised. This is because the strakes upon the final design do not cover a large proportion of the pile, as the strakes far from the bed surface do not help to reduce the bed shear

stresses. The design operates as a unidirectional barrier from the upstream flow and due to its large radius reduces the wall shear stress at the outer edges. In addition, the average shear stress is lowered by 23% compared to a cylinder alone with few areas of heightened shear stress.

The final iterations of design have shown to provide reductions in shear stress, however, the design itself is not practical due to its large, complex structure and the difficulties that would incur during installation. Furthermore, if when scouring begins it is found that it naturally erodes underneath the structure, it will be difficult to ensure its presence below the seabed.

Monopile Optimisation Summary

A reduction of the maximum and surface averaged values around a monopile have been investigated using strakes, as they have been shown to be beneficial yet remain scarcely researched. Initially, a sensitivity analysis was performed investigating 8 geometric strake variables, enabling a better understanding of the impact of strakes and the most influential parameters. These parameters were then combined to target a design which minimised the shear stresses the most compared to a monopile alone, resulting in a reduction in maximum by 12.5%, and global average by 23%. However, due to the practical issues regarding the design this structure will not be used for further scour simulations.

6.2.2 Suction Caisson Optimisation

As discussed in *Scour around Alternate Shapes* in Chapter 2, in comparison to the simple monopile research on the scouring around suction caissons is relatively limited and they are a comparatively new design of offshore turbine foundation. The following analysis has two functions, firstly, it supports the objective to investigate the flow around these alternate structures. Secondly, it allows a preliminary insight into the potential scour reduction given changes in geometry and therefore supports the later and further investigation into the scour around suction caissons.

Mid-Section Testing

This section investigates the effect of the diagonal section between the suction caisson ‘bucket’ and monopile top. The geometry of the support between the two surfaces is explored with the aim of minimising both the average and maximum bed shear stress, reducing the scour volume and maximum depth.

The structural integrity of the structure is not explicitly accounted for; however, existing suction caisson designs are used as a guide. Furthermore, the design changes are driven by fluid dynamics and do not restrict further and significant structural improvements of negligible effect on the fluid dynamics; for example, if changing the number of supporting struts from 8 to 4, the thickness of each strut can be increased to improve the structural strength with minimal effect upon the flow.

Early suction bucket designs predominately include a conical mid-section however more recent designs including the ‘Universal Foundation’ (Nielsen, 2013 , Fredolsen-Energy, 2015) use struts. The following section specifically investigates the effect of strut design and the influence of design features, closely following those on the ‘Universal Foundation’.

The domain size and boundary conditions are the same as the previous monopile investigation, except with half the width and a central symmetry plane due to the symmetrical nature, Figure 6-26.

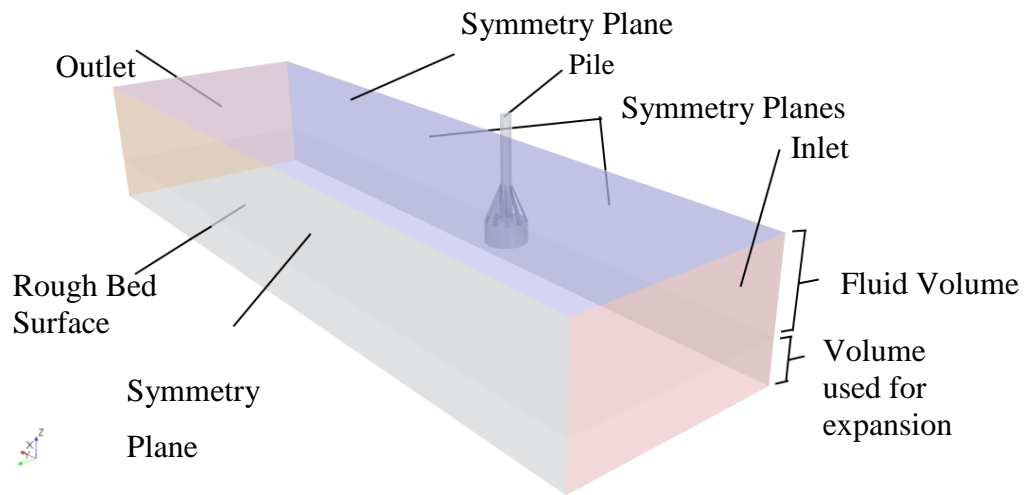


Figure 6-26 – Suction Caisson Testing Domain

Initially, design extremes are tested to provide guidance in for the form of a cone and suction caisson without a centre section, Figure 6-27.

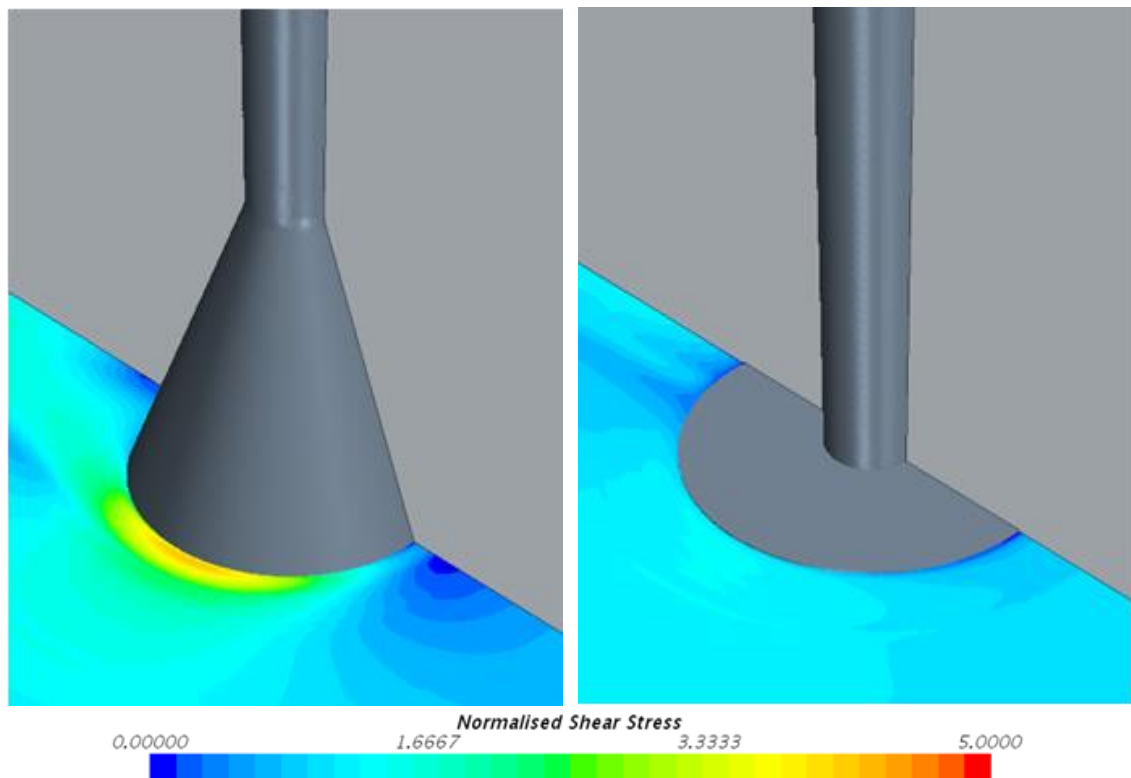


Figure 6-27 – Suction Bucket Base Designs

Suction Bucket Mid Section	τ/τ_{∞}		
	Maximum	Surface Average	
		20m Radius	40m Radius
Cone	4.25	1.33	1.15
No Mid Support	1.31	1.034	1.05

Table 6-4 - Suction Bucket Results for Base Designs

The two geometries represent two extremes of mid-section shape, resulting in the normalised average shear stresses shown in Table 6-4. The colour codes scaled are continued throughout this chapter and indicate the normalised shear stress variable; maximum, local and global average (with all normalised values being a ratio to values taken from free-stream undisturbed areas). The difference in 22% within the 20m radius is attributed to the reduction in blockage and the transfer of high shear from the bed in case (a) to the top of the caisson in (b). It is clear that case (b) is the best design in terms of low shear stresses however due to the hollow caisson base additional support is necessary between the two surfaces.

The number of struts, hole size and end plate width are investigated to gain an understanding of their effects and guide further scour simulations.

Single Rib Configuration

Prior to structures with multiple ribs, a short investigation was completed into the effect of single rib parameters. The investigation explores the effect of a single strut at varied angles of attack, Figure 6-28, comprising of 176 simulations formulated using the parameters in Table 6-5.

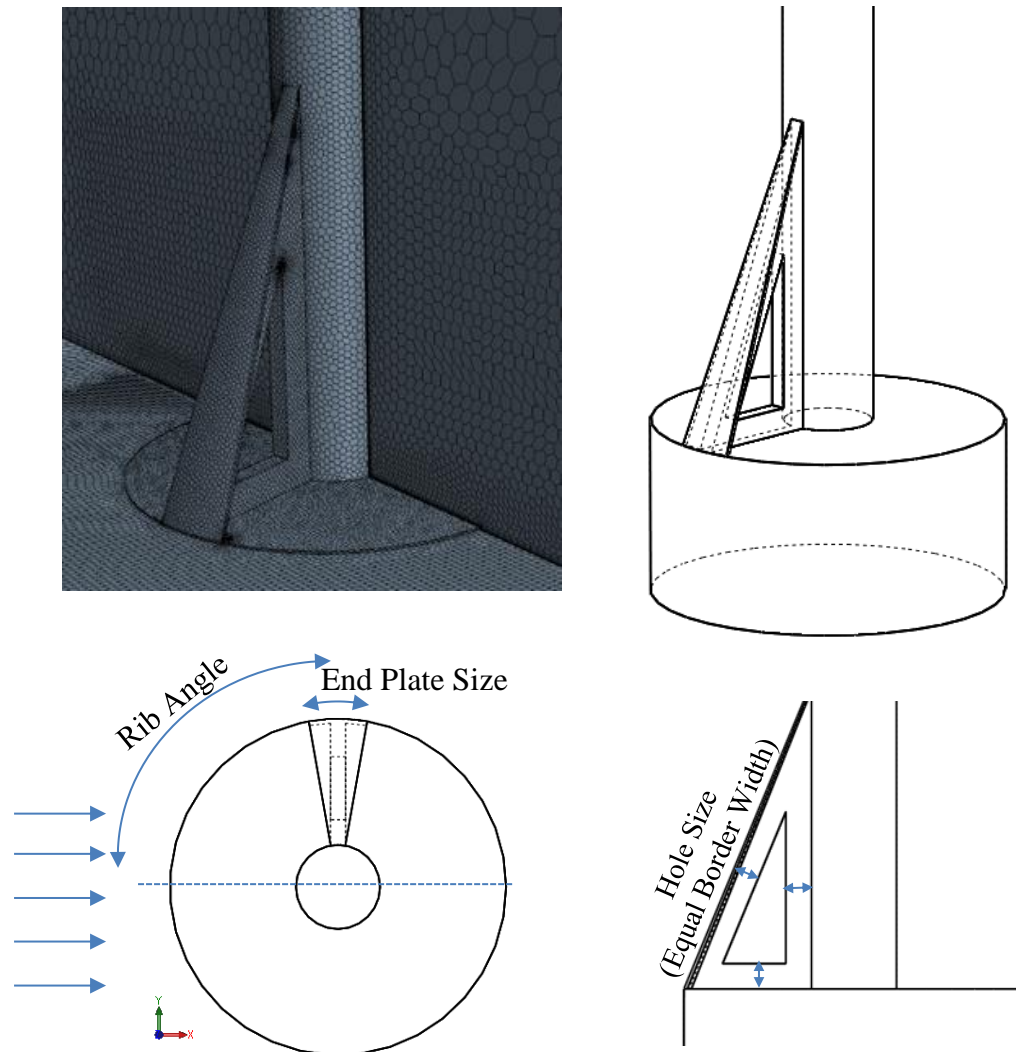


Figure 6-28 – Single Rib Geometry

Parameter	Test Values
Angle (deg)	15, 30, 45, ..., 165
Hole Size (%)	0, 10, 25, 45, 70
End Plate Width (°)	0, 10, 20, 25

Table 6-5 – Single Rib Design Parameters

Each design is analysed using the normalised bed shear stresses, specifically the maximum and surface averages within a radius of $4D$ and $8D$ (D being the upper pile radius of 5 m), referred to as local and global. The results show a correlation between all designs with a maximum value between $0-90^\circ$; matching the maximum shear stress point around a simple cylinder. In the

following section, the maximum and surface average values are examined individually, focusing on trends and identifying the optimal parameter range to reduce the shear stress. This knowledge is then used to analyse the effect of multi rib structures more effectively.

The maximum normalised shear stress begins between 1.4 and 3.6 when the rib is at 15°, followed by an increase and peak between 45° and 90° finishing with a continual fall to a value between 1.25 and 3 at 165°. The largest variation between results is in the region of 45-90°, coincidentally where the maximum occurs for all design permutations. Additionally, it is shown from a summarised version of these results that the angle of maximum shear stress increases as plate width or hole size is increased, Figure 6-30 and Figure 6-30.

		Plate Width (deg)			
		0	10	20	25
Rib Position (deg)	15	2.39	2.50	2.78	2.88
	30	2.63	2.71	2.64	2.69
	45	2.96	3.48	2.70	2.64
	60	3.08	3.59	3.57	3.40
	75	3.30	3.55	3.76	4.04
	90	2.90	3.38	3.69	4.08
	105	2.78	2.90	2.96	2.97
	120	2.51	2.30	2.32	2.41
	135	2.08	1.94	2.13	2.41
	150	1.89	2.03	2.58	2.71
	165	1.34	1.76	2.47	2.36

Figure 6-30 – Single Rib – Hole Size Averaged Value

		Hole Size			
		0.00%	10.15%	23.89%	68.81%
Rib Position (deg)	15	3.08	2.71	2.40	2.37
	30	2.81	2.73	2.74	2.39
	45	2.84	3.23	3.45	2.26
	60	3.24	3.39	4.62	2.38
	75	3.38	3.17	4.14	3.96
	90	3.20	2.99	3.31	4.54
	105	2.77	2.76	2.99	3.09
	120	2.46	2.36	2.50	2.22
	135	2.23	2.22	2.19	1.92
	150	2.18	2.19	2.91	1.92
	165	2.14	2.25	2.07	1.47

Figure 6-30 – Single Rib – Plate Width Averaged Values

Extraction of the maximum value for each design across all angles reveals a clear trend, as shown by Table 6-6. This demonstrates that for a greater plate width the maximum can be decreased by reducing either the hole size, or with the larger hole sizes the plate width.

		Plate Width (deg)			
		0	10	20	25
Hole Size	0.0%	3.69	3.38	3.28	3.32
	10.2%	3.06	4.03	3.88	3.65
	23.9%	3.77	5.00	5.27	5.49
	68.8%	3.48	4.35	4.84	6.15

Table 6-6 – Maximum Single Rib Value Per Design

The maximum value from 15-165° for each design permutation is useful when assessing the worst-case scenario. However, the average is more applicable given the typically unknown angle of attack and likelihood of multiple ribs. Table 6-6 shows that in general, the average can be lowered by reducing the hole size or decreasing the plate width, replicating the previous trend in maximum, Table 6-7.

		Plate Width (deg)			
		0	10	20	25
Hole Size	0.00%	2.88	2.73	2.70	2.72
	10.15%	2.49	2.68	2.85	2.89
	23.89%	2.63	3.04	3.17	3.28
	68.81%	2.14	2.51	2.77	2.96

Table 6-7 – Average Single Rib Value over all angles

However, all average values for a hole size of 69% in Table 6-7 feature a significant drop in local shear stress. This is because of the pressure relief due to the larger hole avoids flow diversion around the outside of the structure, Figure 6-31.

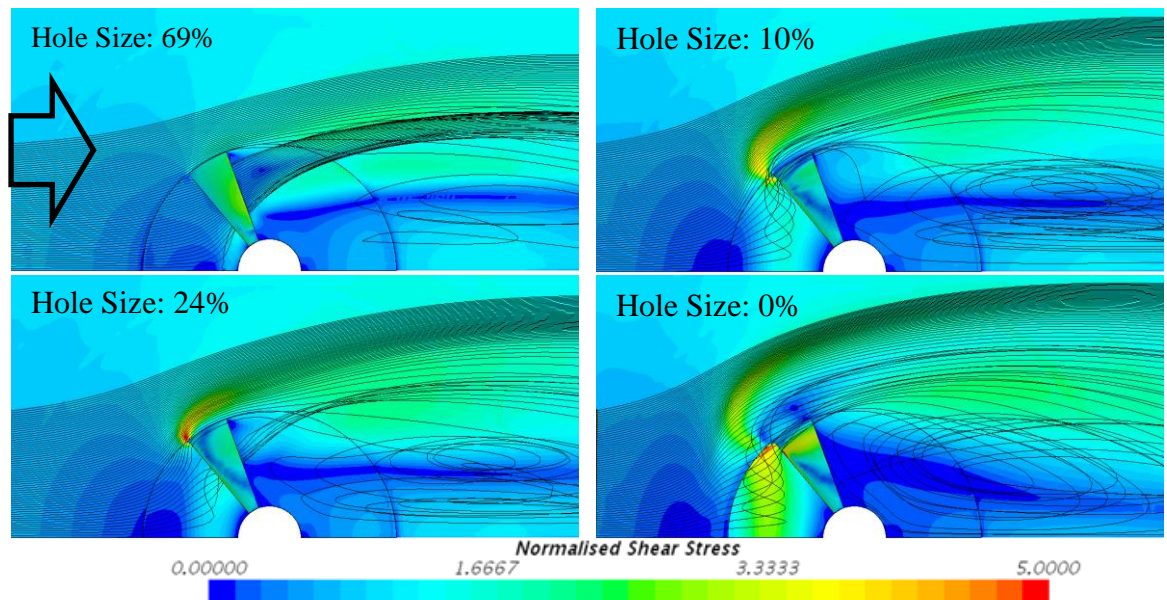


Figure 6-31 – Single Rib Hole Size Effect

The surface average shear stress peaks when the rib is positioned between 0 and 60° with minor variation between designs, which is no surprise as this is typically the area of highest shear stresses. The global surface average decreases from 60° with a minimum at 165°, however, locally the minimum occurs at 120° followed by a gradual increase.

The optimal design is assessed according to the surface average values between 15 – 165°, Table 6-8.

Maximum from 15° to 360°

Local Surface Average					Global Surface Average						
		Plate Width (deg)						Plate Width (deg)			
		0	5	10	12.5			0	5	10	12.5
Hole Size	0.00%	1.348	1.372	1.389	1.378	Hole Size	0.00%	1.193	1.173	1.178	1.174
	10.15%	1.237	1.256	1.235	1.244		10.15%	1.137	1.150	1.148	1.142
	23.89%	1.270	1.270	1.262	1.276		23.89%	1.144	1.160	1.141	1.147
	68.81%	1.141	1.148	1.187	1.222		68.81%	1.098	1.102	1.112	1.128

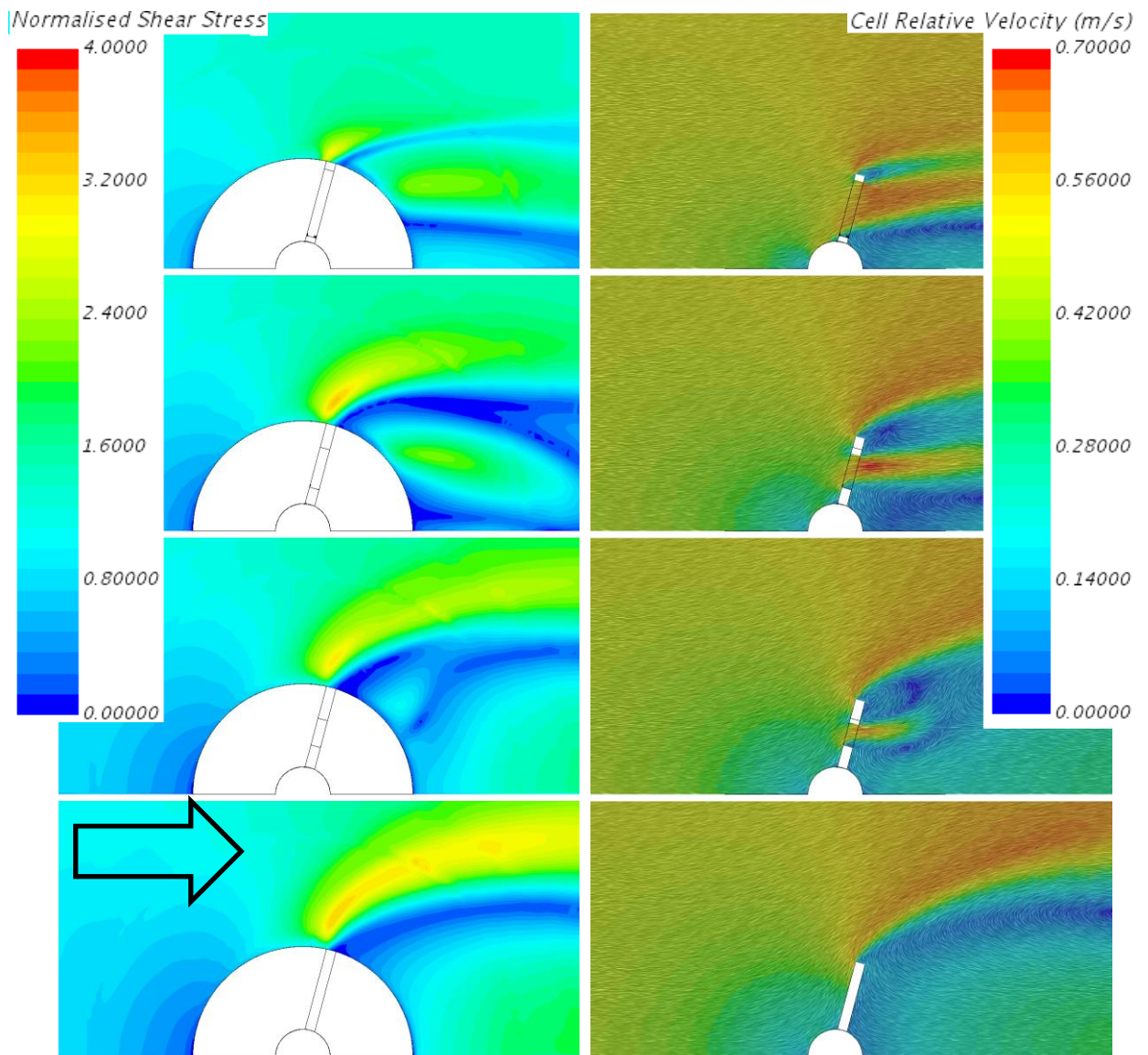
Average from 15° to 360°

Local Surface Average					Global Surface Average						
		Plate Width (deg)						Plate Width (deg)			
		0	5	10	12.5			0	5	10	12.5
Hole Size	0.00%	1.087	1.068	1.060	1.062	Hole Size	0.00%	1.126	1.121	1.121	1.122
	10.15%	1.023	1.013	1.023	1.032		10.15%	1.093	1.086	1.086	1.090
	23.89%	1.061	1.068	1.076	1.081		23.89%	1.073	1.073	1.074	1.082
	68.81%	1.070	1.074	1.088	1.094		68.81%	1.064	1.063	1.070	1.072

Table 6-8 – Single Rib Surface Average Values

The global maximum and average values increase as hole size is reduced, directly correlating to the change in blockage. This trend is evident for the majority of angles and importantly those susceptible of the highest stresses. The plate width has minimal effect on these values because the greatest shear stresses occur at 90°, where the plate chord is parallel to the flow.

The local maximum surface average values follow a similar trend, with the exception of a hole size of 10%. This is because in addition to the beneficial blockage reduction, the small hole size restricts the downstream length, and raises the height of accelerated flow; therefore, increasing the distance to the bed surface, as illustrated in Figure 6-32.



Rib at 105°. No end plate. Hole 0% - 69%. Vector plane at z = 3m.

Figure 6-32 – Single Rib – Hole Size Effect on Accelerated Flow and Blockage

The single-rib results show that in general, the hole size has a greater impact on the surface average values than the plate width; however, each has an equal effect upon the maximum values, Figure 6-33. Additionally, these figures show that the impact is dependent on the angle, which reaches a peak for the maximum at 90° and surface average at 105°.

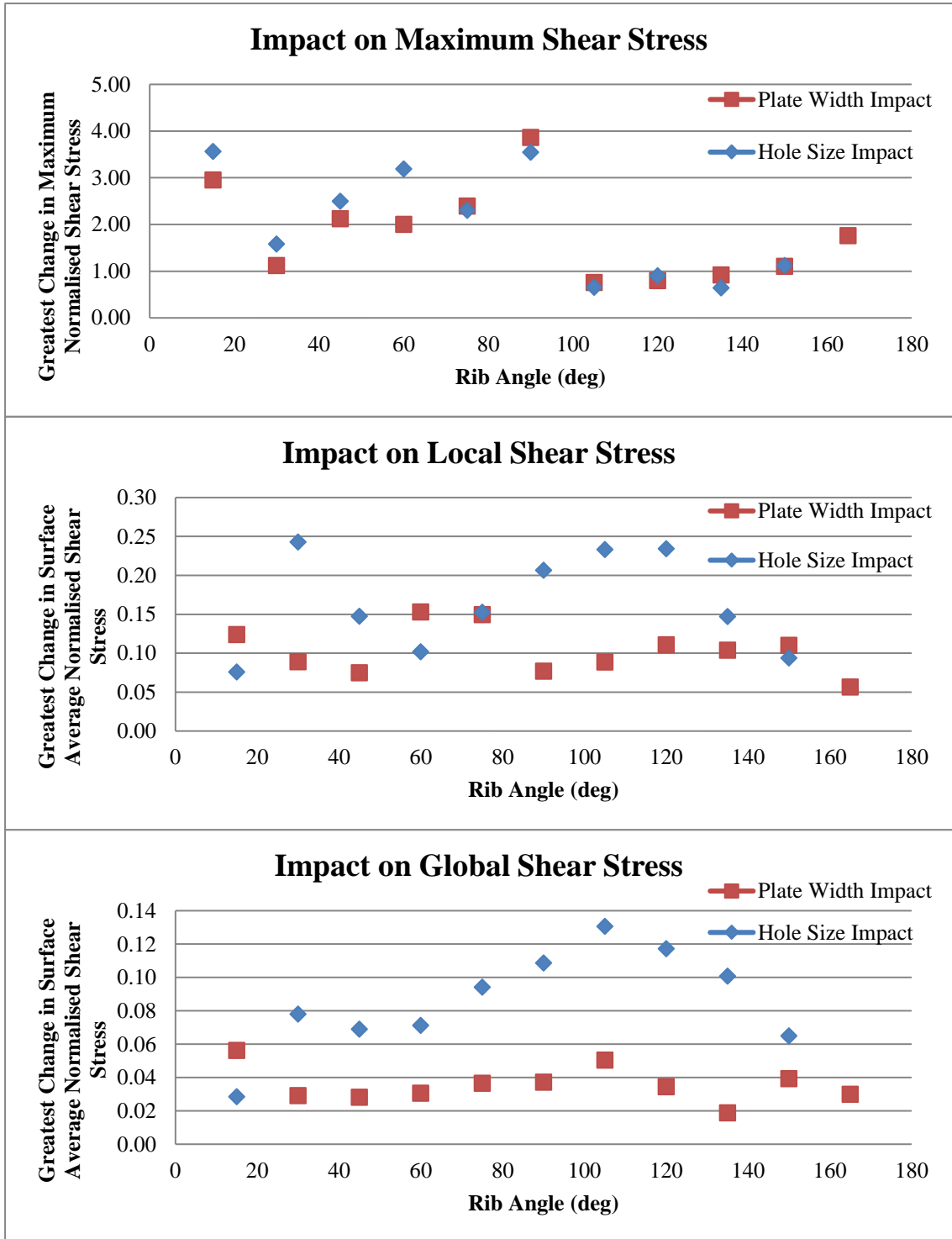


Figure 6-33 – Single Rib - Hole Size Effect on Accelerated Flow and Blockage

This supporting investigation of single rib design changes upon the shear stress, at varied angles of attack has presented important trends that help analyse multi rib structures. To conclude, the greatest maximum and surface average values occur in the first 90° when the drag on the structure is of a maximum. The maximum shear stress is always located at the edge of the end plate (or rib if no end plate) and is produced by the volume of flow passing the corner due to the flow escaping around the outside of the rib, in addition to the flow passing the outside of the structure.

If the blockage ratio is reduced by increasing the hole size the surface average shear stress reduces, however this also increases the maximum as raises the speed of flow passing the outer corner of the rib. The maximum stress is impacted equally for the tested range by end plate and hole size. However, the average shear stress is less sensitive to the change in end plate size. Based on this information the introduction of multiple ribs at arbitrary angles of attack will increase the blockage factor and form multiple high shear stress points. Furthermore, the maximum shear will likely decrease in response to the reduced flow upon each rib and decrease the fluid speed past the structure.

Multiple Rib Configuration

The introduction of multiple ribs changes the flow surrounding each individual rib and therefore the proceeding tests repeat the changes in hole and plate size however with a varied number of ribs, Table 6-9. A repetition of test parameters may initially be view as unnecessary, however, the preliminary single rib study provides foundation knowledge for the proceeding study and therefore aids the understanding of the complex fluid dynamics.

Variable	Test Values
Number of ribs	3, 4, 6, 10.
Hole Size (%)	0, 10, 25, 45, 70
End Plate Size (°)	0, 25, 15, 20, 25
Alternate orientation (°)	60 (for three ribs) 45 (for four ribs)

Table 6-9 – Multi-Rib Design Parameters

The same range of plate width and hole size was used as previous alongside a change in the number of ribs; 3, 4, 6 and 10. In addition, due to the effect of rib angle, alternate orientations are used for 3 and 4 ribs to provide a comparison to the worst-case scenario when a rib is placed in the region of highest shear stress, 0-90°.

A comparison of the multi rib structures to the previous single rib structures is shown in Figure 6-34. These data points are generated by comparing each design iteration for 3, 4, 6 and 10 ribs against the worst single rib result for the matching rib angles, removing the sensitivity of the multi-rib structure angle of attack. For example, the 6-rib structure has ribs at angles of 30°, 90° and 150° and therefore is compared to single ribs at the same angles.

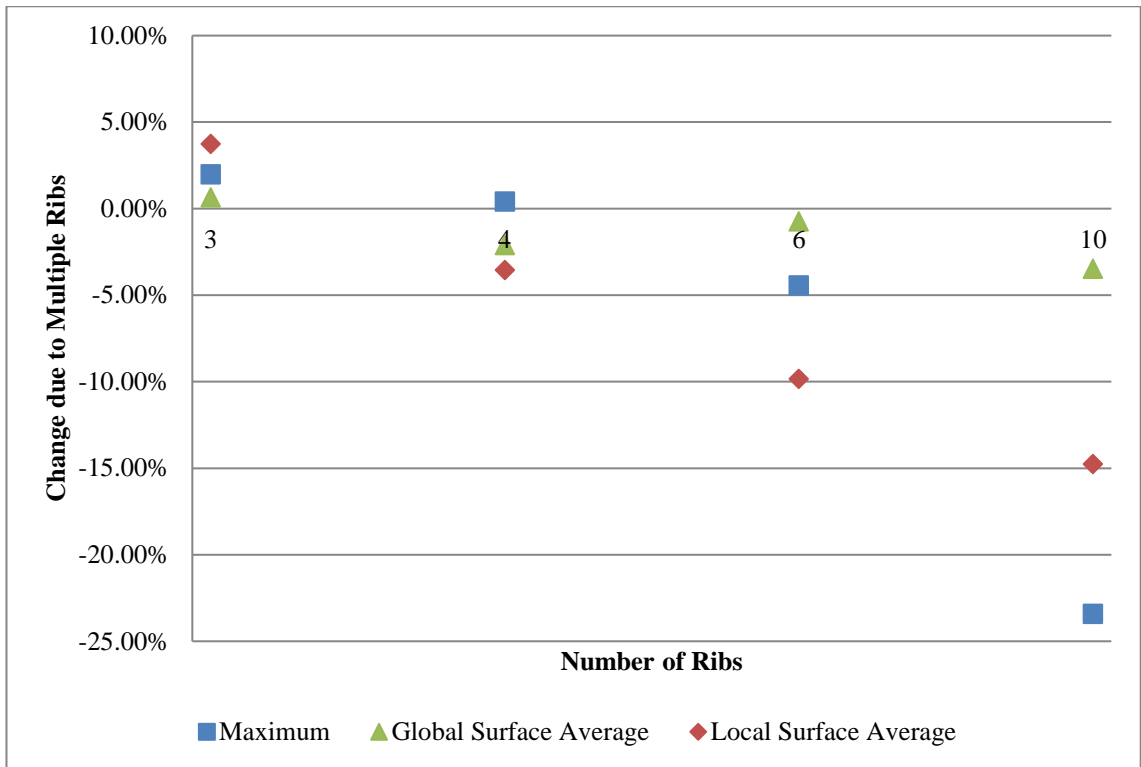


Figure 6-34 – Impact of Multiple Ribs

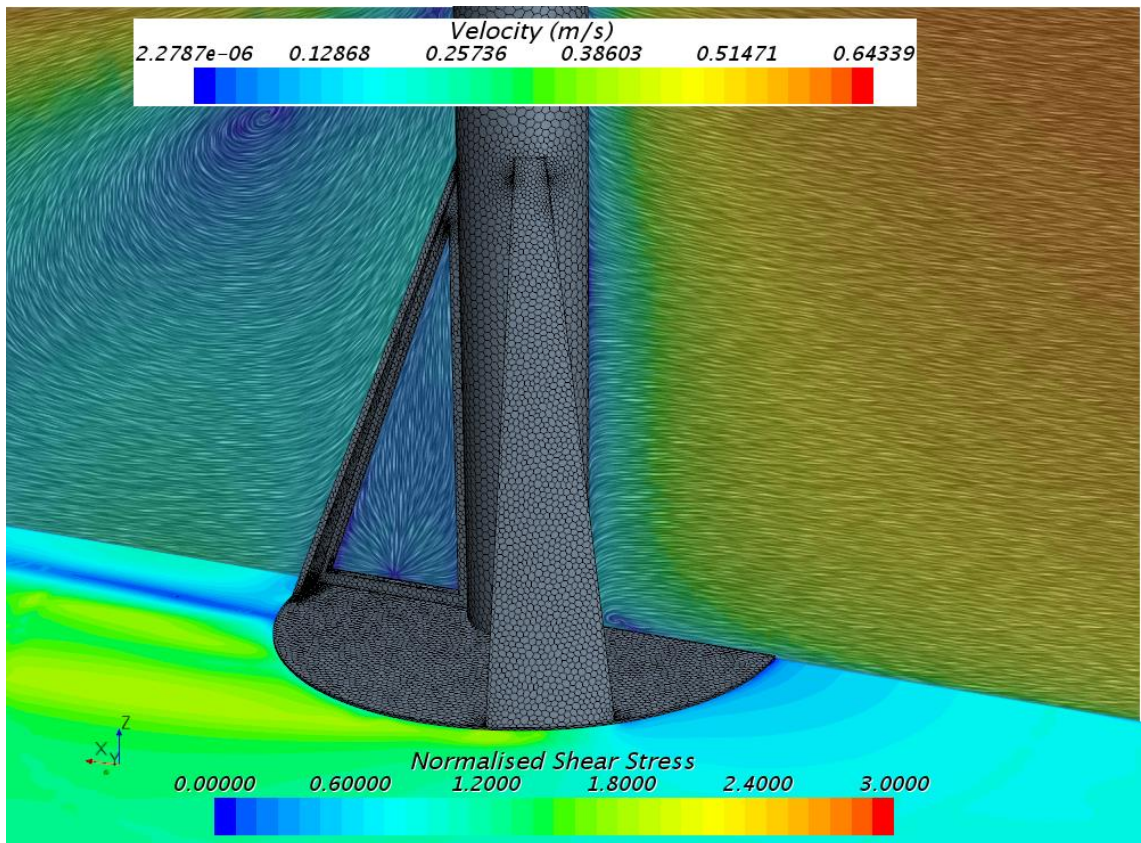


Figure 6-35 – Low Blockage Factor Design

Figure 6-34 shows that the local maximum and surface average values improve as the number of ribs increase. The global surface average values show a comparatively consistent improvement of ~3%. In addition to these advantages, an increased number of ribs also reduces the sensitivity

to structure rotation. In response to the clear advantages of more ribs a select number of simulations with 14 and 18 ribs were ran, where it was found that an inflection point exists because the structure starts to replicate a solid cone causing high maximum and surface average values.

The optimal hole size and plate width is assessed using the average of the maximum and surface average values across all rib multiples, Figure 6-36. This reveals that when accounting for all three variables the design with the lowest blockage factor (hole 69%, no plate) is optimal, Figure 6-35.

Furthermore, it is apparent that within the design parameters if additional structural support is necessary is it beneficial to increase plate width over hole size. These trends better represent structures with six or more struts, as structures with less number of struts are more sensitive to angle. Additionally, because the flow is reduced more rapidly with less struts, the shear stresses are more dependent on the strut geometry.

		Maximum Normalised Shear Stress				
		Plate Width (deg)				
		0	10	15	20	25
Hole Size	0.0%	3.49	3.14	3.39	3.32	3.14
	10.2%	2.79	3.11	3.54	3.30	3.20
	23.9%	3.47	4.19	4.19	3.96	3.67
	43.5%	3.22	4.04	3.68	3.37	3.40
	68.8%	2.65	3.09	3.48	3.15	3.21

		Surface Averaged Normalised Shear Stress (4D)				
		Plate Width (deg)				
		0	10	15	20	25
Hole Size	0.0%	1.17	1.15	1.19	1.19	1.19
	10.2%	1.02	1.05	1.07	1.09	1.09
	23.9%	1.05	1.09	1.06	1.06	1.05
	43.5%	1.02	1.06	1.06	1.07	1.08
	68.8%	1.02	1.07	1.11	1.11	1.10

		Surface Averaged Normalised Shear Stress (8D)				
		Plate Width (deg)				
		0	10	15	20	25
Hole Size	0.0%	1.17	1.16	1.16	1.16	1.15
	10.2%	1.11	1.12	1.12	1.12	1.12
	23.9%	1.10	1.11	1.09	1.10	1.09
	43.5%	1.07	1.08	1.08	1.08	1.09
	68.8%	1.04	1.06	1.08	1.08	1.08

Figure 6-36 – Average values across all Multi-rib structures

Suction Caisson Optimisation Summary

Increasing the number of ribs decreases the maximum and surface average shear stresses. However, there is a point of inflection when the design starts deviating towards a cone geometry.

On average, decreasing the hole size increases surface average shear stress values, directly related to the increased blockage. The maximum shear stress peaks at a median hole size of 24%, with lowest values at a hole size of 0 and 70%. This is due to accelerated flow which extends onto the bed surface behind, whereas with the smaller and larger hole the flow is more restricted or not forced through a converging hole at all.

The end plate size has minimal effect upon maximum and surface average wall shear stress values in comparison to the hole size, especially with six or more struts.

This study has provided insight into the effect of suction bucket geometry on initial scour. It has been stated that the maximum shear stress represents the highest initial scour rate and surface average values reflect the initial sediment volume removal rate. This statement is investigated further using scour-inclusive suction bucket simulations after the following chapters surrounding the scour model's validation and development.

Steady-State Investigation Summary

This chapter has investigated the reduction of maximum and surface average bed shear stresses around a monopile and suction caisson foundation. The monopile investigation included a sensitivity analysis which enabled the identification of the most influential factors and generation of an optimal design.

The suction caisson analysis entailed a design of experiments (DOE) used to investigate the effect of a singular rib and multiple ribs around the middle section of a caisson foundations. This provided a detailed insight into the geometric effects upon the bed shear stresses enabling a reduction in simulations in Chapter 8 which further investigates the scouring around suction caissons using the developed morphological model.

Chapter 7 Scour Model Development

This section presents the development and testing of the morphological model, for single and two-phase flows. The proceeding section revisits the methods and formulae required within such a model and analysis and testing of the most suitable, followed by the implementation of the model.

The final two sections seek verification of the models scouring accuracy using external experimental data. The single-phase model is quantitatively compared to two monopile experiments, the in-house gravity-base experiment and qualitatively to a caisson structure of varied bed-protrusion heights.

The two-phase model is initially compared without any bed-deformation to sediment concentration profiles along a straight channel and across a trench; enabling a better understanding of the two-phase aspects and validation without morphology. The bed-deformation is then enabled, and the trench scenario is re-run for a significant amount of time and compared to experimental results.

7.1 Scour Model Composition

This section concludes the main model elements that are discussed in the literature review and smaller model details that are not yet addressed.

7.1.1 Fluid Phases

The literature review revealed that turbulence and multiphase models of a higher order accuracy are uncommon and only used when crucial, due to the increase in computational expense.

The primary objective of this study is to investigate the impact of geometry upon scouring and therefore a single-phase model is deemed sufficient. Furthermore, the contained single phase model does not include a suspended sediment prediction unlike several published scour models, because in the area of greatest interest around the pile the complexity of flow makes any suspended load prediction invalid.

An exception to the single-phase model is when there is heavy upstream sediment loading, requiring a two-phase model, which is also investigated in this chapter. This model adopts the Eulerian multiphase method alongside several phase interaction models.

7.1.2 Empirical Formula

As stated in Chapter 2, the bedload formulae of Van Rijn (1991) (Equation 12) and Peter-Meyer-Muller (1948) (Equation 13) are selected based on their proven success and simple formulation. These formulae are both tested in the first case in addition to necessary critical shear stress formulae.

The available critical shear stress formulae range significantly and have shown to deviate in critical shear as much as 50%. Several have been tested by (Camenen and Larroudé, 2003) and each favours a specific parameter range, however their accuracy is still poor. As a result, two empirical critical shear stress formula are also tested alongside the two bedload formula in the first case in order to provide further insight and aid a decision. The equation used to move cells due to erosion is as follows;

$$\frac{\Delta z}{\Delta t} = -\left(\frac{1}{1-\gamma}\right)q_b$$

Equation 21

Whereby, Δz is the change in vertical height, Δt is the timestep, q_b is the bedload transport mass and γ is the bed porosity. Equation 21 is derived from the original Exner equation, (Paola and Voller, 2005), however for this single-phase model the divergence term is removed as it is assumed that all eroded sediment is removed from the bedload layer.

7.1.3 Slope Effects

Van Rijn et al. (2006) assesses common slope effect formulae that account for changes in incipient motion and sediment load. It is shown that the recent formulae of Dey (2001) shows good agreement with experimental values; however, this is based on a one-directional flow. An alternate formula is used for this model that accounts for any flow and bed slope direction, Equation 22, as demonstrated in (Khosronejad et al., 2011, Roulund et al., 2005).

$$\tau_{cr,\alpha} = \tau_{cr} \left[\cos \beta \left(1 - \frac{\sin^2 \alpha \tan^2 \beta}{\tan^2 \phi} - \frac{\cos \alpha \sin \beta}{\tan \phi} \right) \right]$$

Equation 22

Whereby $\tau_{cr,\alpha}$ is the critical shear stress on a slope, τ_{cr} is the critical shear stress on a near flat bed, β is the angle of steepest decent from horizontal, α is the angle between the steepest slope and the velocity vector and ϕ is the angle of repose.

Figure 7-1 shows a graphical representation of Equation 22, illustrating the increased and decreased effects upon the critical shear stress. Within this model, maximum decrease in critical shear stress is limited to 99%, in order to avoid numerical error.

Additionally, when steep slopes are formed in areas of low shear stress a sand slide mechanism is used to avoid the creation of unnaturally steep slopes, whereby the bed is deformed to account for the sliding and with the two-phase model sediment mass is released. This sand slide model applies a deformation distance as a function of the distance necessary to return it to the angle of repose, Equation 23, based upon the method implemented by Liang et al. (2005).

$$\Delta z = -0.5 \sqrt{A} \tan(\beta - \phi) \cdot \varphi$$

Equation 23

The variable φ is a function of the cells vertical position resulting in values between 0-1 to ensure that higher position cells are adjusted first, avoiding the creation of unnatural holes.

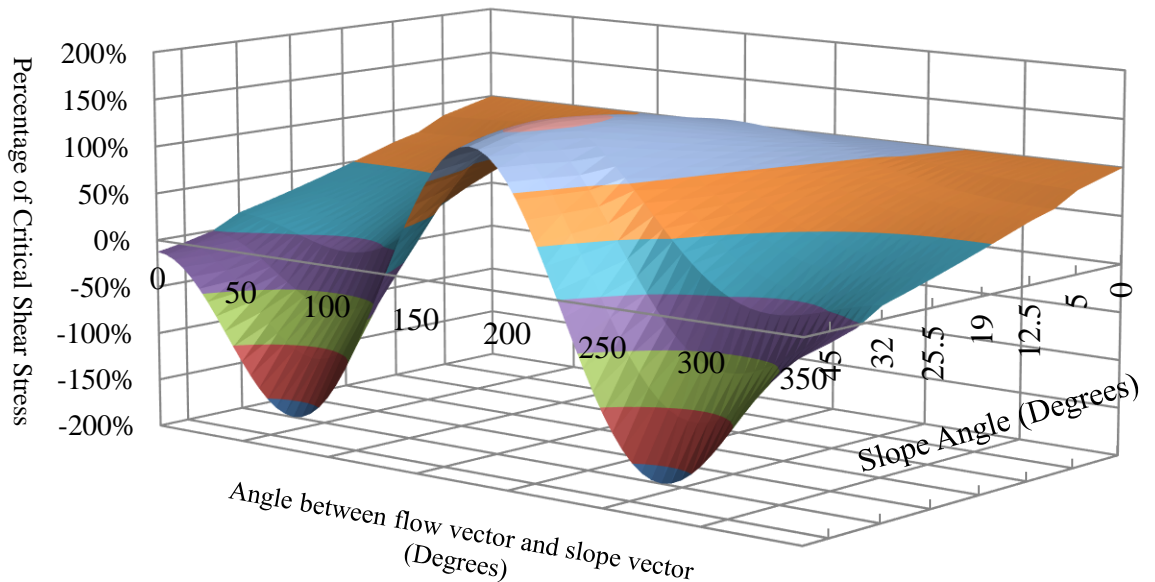


Figure 7-1 – Angle of Repose Model Characteristics

7.1.4 Deposition Formula

The two-phase model adopts the Eulerian multiphase method due to its efficiency and effective use in other studies. This model simulates erosion and deposition by lowering or raising cells on the bed surface alongside an equal amount of sediment mass flux.

The two-phase model is built upon the single-phase model with an additional secondary phase, and bed morphology that switches from erosion to deposition when the volume fraction of sediment in a cell exceeds 20%. The deposition height is 80% of a cells volume fraction of sediment over 20%;

$$\Delta z = \frac{(((\alpha_s) - 0.2)0.8V)}{A} \left(\frac{1}{1 - \gamma} \right)$$

Equation 24 – Deposition Formula

The method of accounting for deposition once a specific sediment volume fraction is commonly in simulations adopting the CURVIB morphing method, such as (Alhajraf and Rubini, 2000). The reason that only 80% of the sediment above 20% is considered is that this avoids fluctuation between erosion and deposition, and high and low sediment volume fractions; therefore, improving numerical stability.

As previously mentioned the two-phase model includes a positive or negative sediment mass flux on the bed surface equating to a respective amount of erosion or deposition. This is formulated using the displacement distance of each node, namely;

$$\dot{m}_s = \Delta z \cdot A \cdot \rho_s \cdot \Delta t \cdot (1 - \gamma)$$

Equation 25 – Mass Flow to Displacement Formula

7.1.5 Implementation

The equations that are used to displace the cells on the bed surface are handled by a simplistic decision tree which can be implemented into software in a number of ways, Figure 7-2. This study was demonstrated in commercial CFD software Star-CCM+ (CD Adapco, 2014) in which they are applied using inter-software ‘field-functions’.

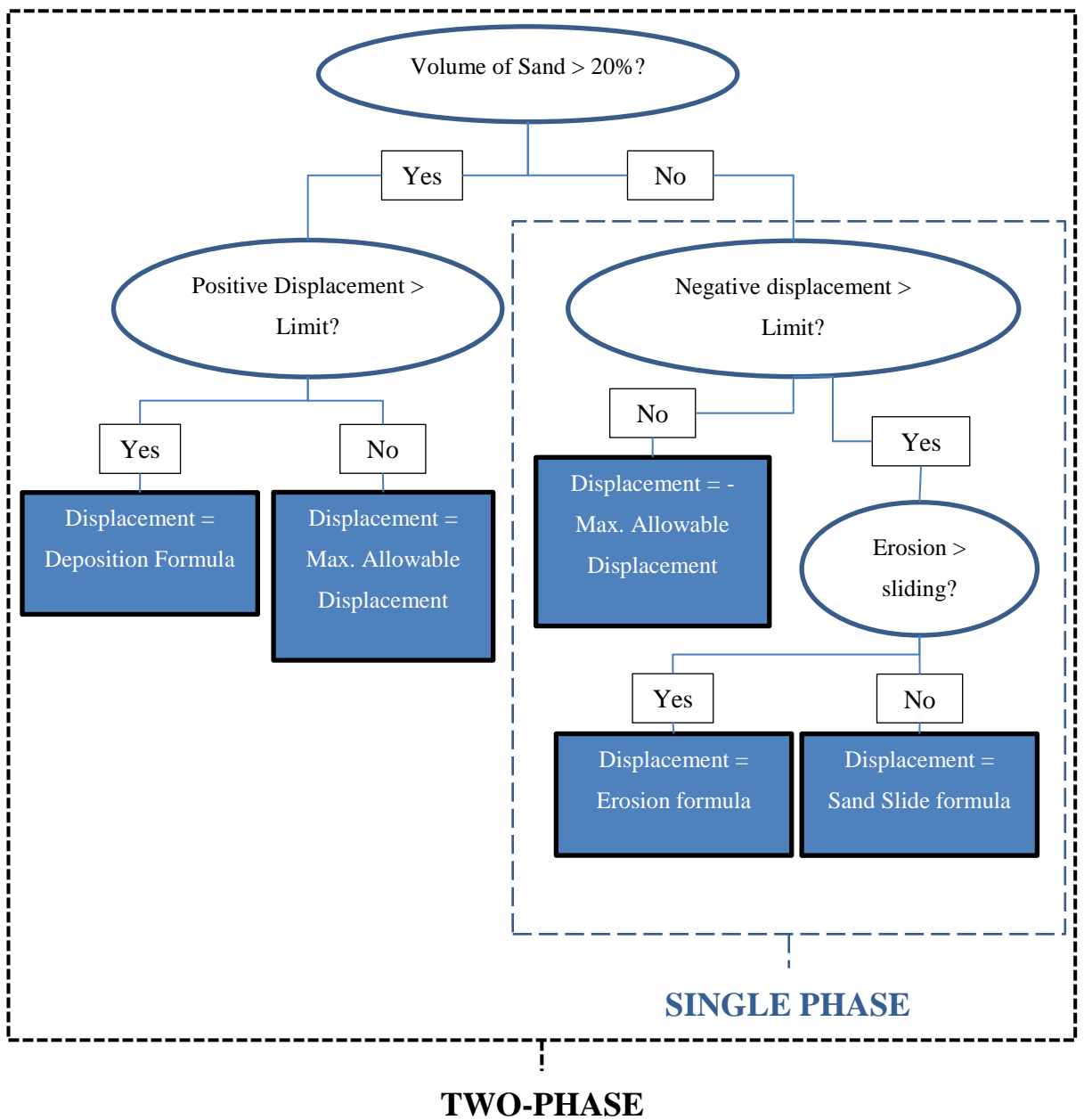


Figure 7-2 – Simplified Flow diagram of the single and two-phase model

The equations and coding that drive the bed morphology are relatively universal and can be used within, or alongside most CFD codes. However, in addition to this implementation challenges were faced as a result of modelling choices, beginning with the remeshing procedure.

7.1.6 Re-meshing

Due to the use of a deforming mesh that vertically stretches and compresses the whole domain it is necessary to re-mesh when significant bed deformation had occurred in order to retain a good quality mesh. This requires a re-meshing procedure, as to re-mesh whilst retaining the deformed bed-surface requires export of the deformed bed-surface, import as an initial surface and then a re-mesh. However, this re-meshing procedure creates several other problems resulting in a complex meshing procedure, as shown by Figure 7-3. A second hurdle is the warping of geometry

after several re-meshes, which is remedied by extending the initial surface below the bed surface, inspired by the CURVIB method as shown by a loop of steps 8-5-6-7-8.

In order to extract the volume of interest created by the initial surfaces they are stitched together creating a surface mesh on the volume of interest only. This process is also able to fill holes which are created when for example a non-deforming surface such as the pile is stretched radially by the morphing bed-surface, that when re-meshed is replaced by the original pile geometry creating a hole between the two.

The holes between fixed and deforming surfaces are more pronounced when the scouring occurs underneath a structure. These are still to be filled however the resultant surface is unnatural as a surface is created between the two closest points. Therefore, it is necessary to apply a preliminary extraction of the geometry without symmetry, of the volume of interest underneath the structure to produce a more natural surface. Then, the bed-surface from the preliminary extraction can be used for the main wrapper, shown by steps 1-4 in Figure 7-3; the complete re-meshing process is shown by steps 1-8.

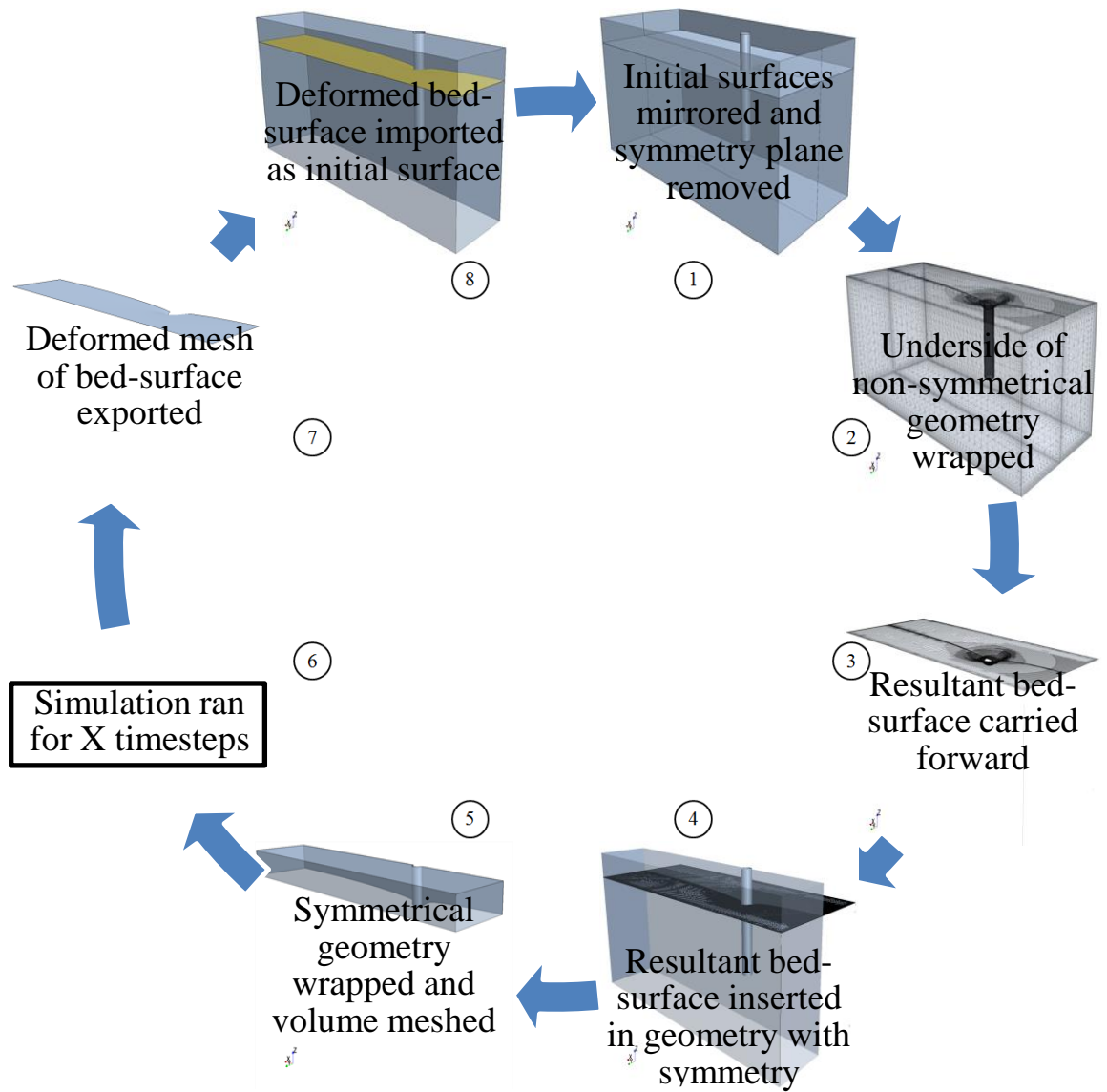


Figure 7-3 – Meshing procedure for complex structures

7.1.7 Automation

The re-meshing procedure was automated using a Java macro allowing the simulation to run autonomously. Initially, meshing was triggered at a constant time step frequency; however, this was modified as meshing can take a considerable time and the necessary meshing frequency changes with flow conditions, time step, mesh and scour development. In addition, problems occurred between meshing intervals that resulted in numerical divergence that stopped the simulation completely or caused unnatural deformations that were then present for the remainder of the solve.

These problems were reduced by invoking mesh quality and numerical convergence checks after every time step and relaying the values back to the macro, allowing a premature re-mesh if the values exceed defined thresholds.

The thresholds prevent errors after re-meshing using zero volume and area indicators, which identify possible numerical divergence using high wall shear and cell validity monitors and indicate the formation of poor quality cells using cell aspect ratio, cell quality and cell skewness monitors, Table 7-1. The contained values were set by monitoring the properties of the cells that causes divergence in early development cases.

Monitor	Min	Max
Face Validity	0.7	-
Wall y^+	-	200
Aspect Ratio	0.01	-
Cell Quality	0.01	-
Cell Skewness	-	90
Wall Shear Stress	-	70

Table 7-1 – Simulation Monitor Values

The face validity is an area weighted measure of the normal values on the faces of a cell compared to the position of its centroid. Perfect face validity means the normal is facing exactly outwards, see Figure 7-4.

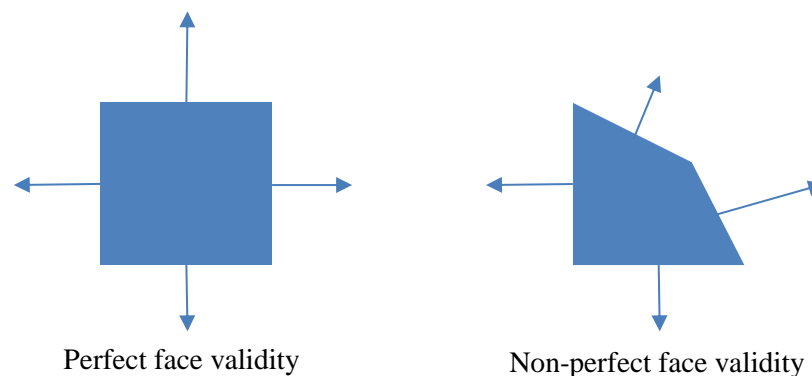


Figure 7-4 – Face Validity Example

Wall y^+ has previously been discussed, see Equation 16, and aspect ratio is a comparison of a cells width, height and depth. Cell quality assesses a cell based on both distribution of surrounding centroids and the orientation of cell faces. When using the RANS model the cell quality can drop extremely low without causing numerical divergence, hence the low threshold value, however, the likelihood of divergence increases exponentially approaching 0, and is a useful trigger for re-meshing. Finally, the cell skewness is simply the angle between two neighbouring centroids, and vector created by one of the centroids and the centred face centroid, see Figure 7-5.

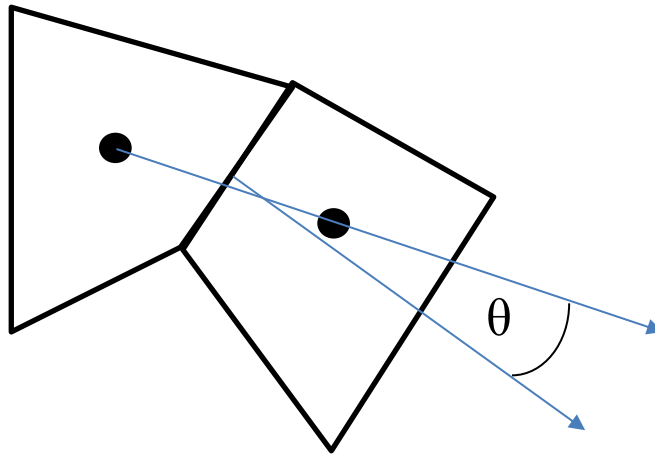


Figure 7-5 – Cell Skewness Diagram

Numerical Stability

It has been stated how the deposition formula was modified to improve numerical stability, however issues still arose whilst iterating as the converging wall shear stress values effected the erosion rate, which in turn changed the sediment flux. Therefore, a table is used to store the deformation values after each time step, which is then used to provide constant erosion values for all iterations during the proceeding time step as opposed to values fluctuating with the driving wall shear stress. This also removed an issue which occurred with the passive scalars, discussed in the following chapter.

Scour Model Composition Summary

This section has defined the different elements of the scour model following the stated choices in earlier chapters. This included the number of fluid phases, morphological method and required equations. The remaining decisions, such as mesh resolution and time step are dependent on the flow conditions and therefore discussed in each individual case.

7.2 Single Phase Model

This section comprises of four cases to verify the required accuracy and ensure confidence in the scour model. The first two cases are around a simple monopile, with different flow parameters from various sources. The third simulates the experiment in Chapter 3 and the final case is around a suction caisson, and combines 10 scour simulations to match a well-documented trend.

Case 1 – Preliminary Scouring around a Simple Monopile

Preliminary Testing

The first case is compared to an experiment outlined in Link et al. (2008), the key parameters are given in Table 7-2. This case is chosen for two main reasons, firstly it offers periodic bed topography that enables both the absolute depth and normalised developing topology to be compared. Secondly, it provides one of the simplest scenarios, clear water scouring around a simple monopile, which is important for initial testing as increases the chances of understanding erroneous or unusual results. As this is the first case, it is used to test and decide aspects of the model, specifically including the empirical formulae, and detect and rectify any potential problems; all of which are discussed at the end of this case.

Area	Parameter	Value
Flume:	Width:	2 m
	Length:	26 m
Working Section:	Width:	2 m
	Length	4 m
Pile	Diameter:	0.2 m
	Position from Inlet:	16 m
Sediment	Diameter	0.00026 m
	Depth	0.5 m
Flow	Average Velocity	0.247 m/s
	Depth	0.3 m
	Dimensionless Shear Stress	0.95
Time	Experimental	72000 s (0.83 days)
Maximum Scour Depth	Experimental (@ 72000s)	0.126 m

Table 7-2 – Case 1 Parameters

Setup

Prior to the transient scour simulation, several tests were conducted to examine the necessary mesh resolution and domain size. The original experiment consists of an upstream distance of 16 m, which is not necessary for the computational model as additional upstream distance can be accounted for by the computational inlet condition. This process was carried out after the mesh convergence study, and is therefore also discussed afterwards.

Mesh

The variables of interest in the convergence study are the maximum and average wall shear stresses local to the pile, in addition to the developing velocity profiles approaching the pile. The convergence study was conducted in stages starting with the upstream prism layers, core cell size and cell size on the bed surface. Due to the combination of different sizes over 15 mesh combinations were tested. The cell size close to the pile was then refined in two sections identical to the methodology used in the steady state simulations; one for the horseshoe vortex and flow acceleration and another for the decelerating and downwards flow above; this entailed 10 different mesh size combinations.

In addition, a second, courser mesh was tested in order to explore its overall effect on the scour topology, as using a mesh 1/5th of the size (which reduced further as scour developed due to the accuracy capture of the scour hole) reduced the maximum and average shear stress values by only 10%, however improved the solve speed considerably. The fine and course mesh are shown in Figure 7-6.

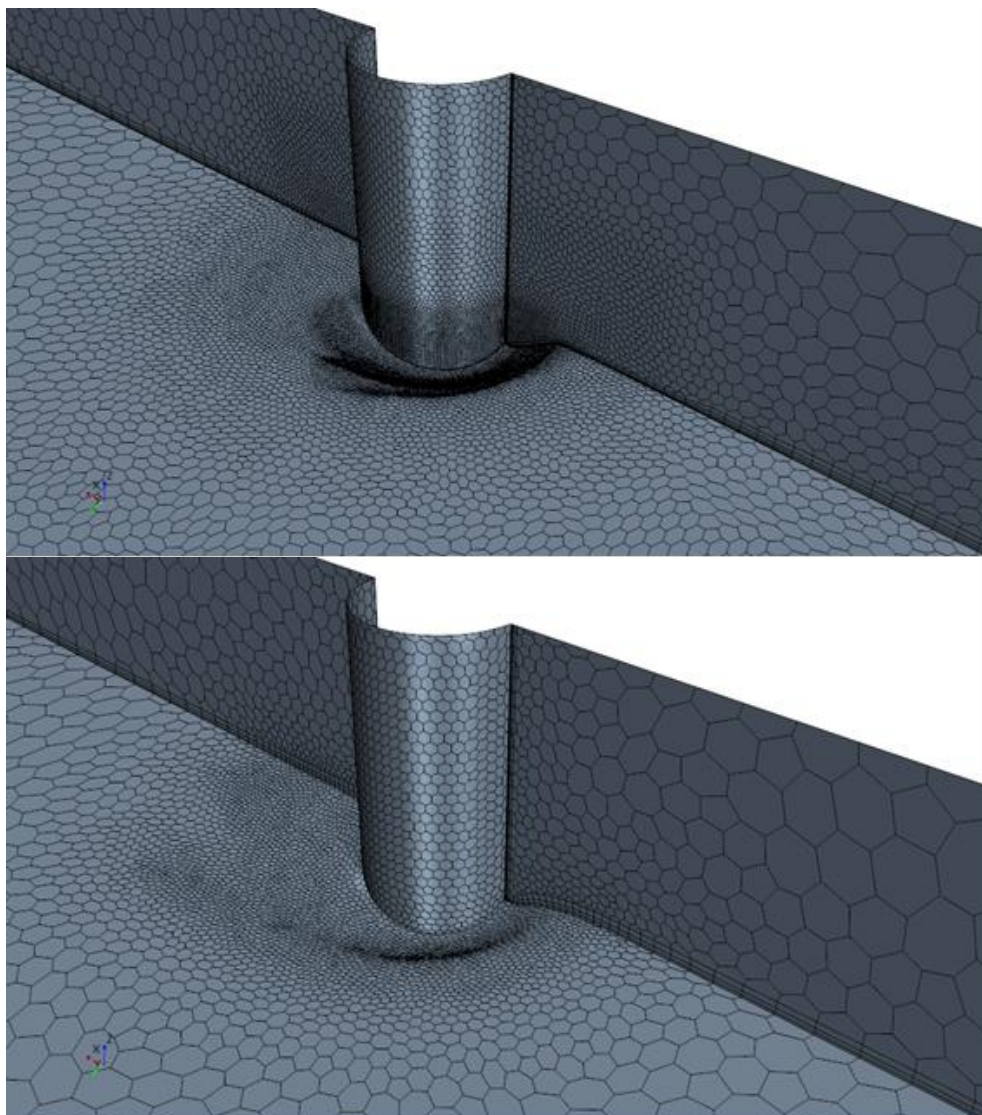


Figure 7-6 – Converged and Course Mesh

Domain Size

Following the mesh convergence, the flow variables from the full 16 m simulation were extracted at 2m intervals and used as inlet conditions for several simulations of reduced upstream length. This process revealed the upstream bed length can be reduced to 2 m without affecting the wall shear stresses around the pile or approaching velocity profiles, two sets of these results are shown in Figure 7-7. The downstream length was also reduced but with no effect on the shear stresses, however, as flow complexity increases as scour develops, a length of 2 m was chosen. The width of the symmetrical section remained unchanged at 1 m due to the sensitivity of the blockage factor at low width-to-pile-diameter ratios, the final domain is shown in Figure 7-8.

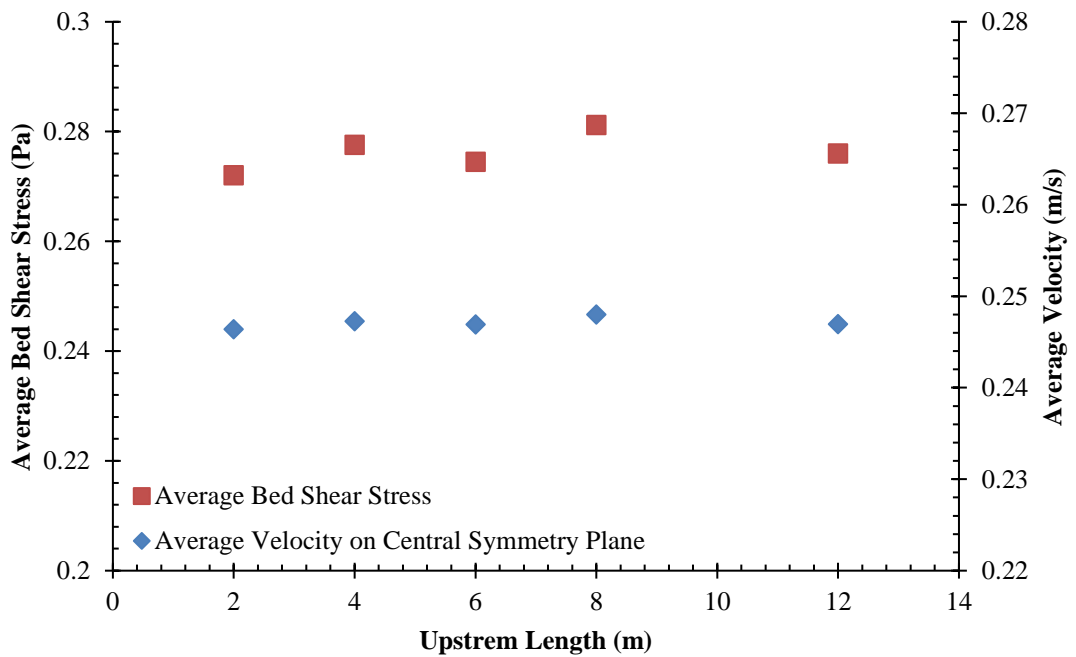


Figure 7-7 – Monitored values when testing the required upstream domain size

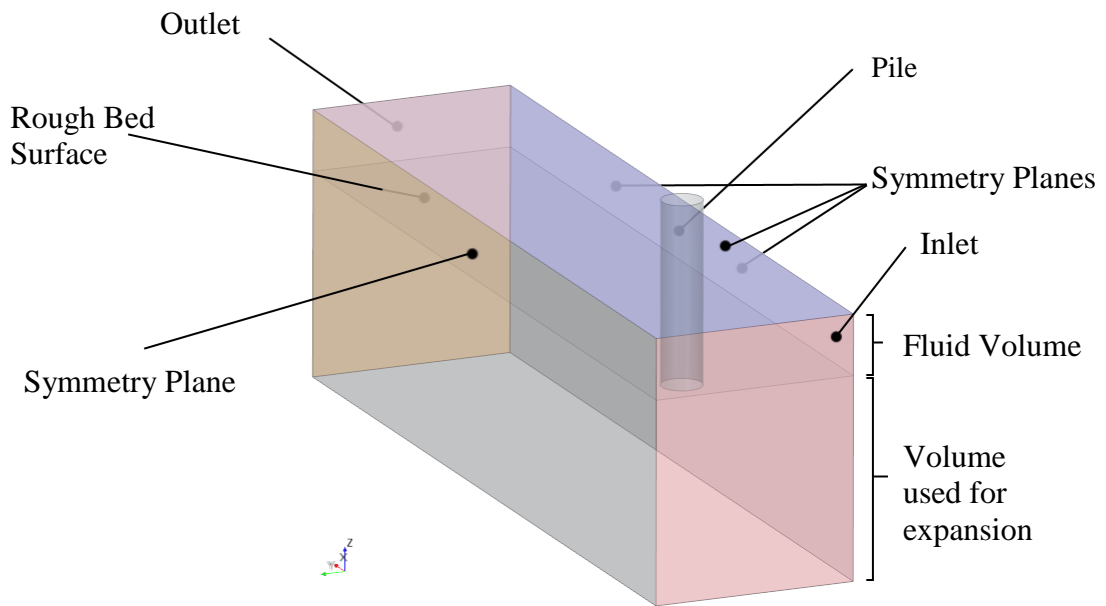


Figure 7-8 –Case 1 Boundary Conditions

Time step

As previously discussed, the time step required to capture vortex shedding is unrealistic given the long scour timescales and therefore requirement for large courant numbers. For example, using this case, the predicted vortex shedding frequency is 0.25 Hz (based on a Strouhal Number of 0.2) and a minimum recommended 30 timesteps per wavelength results in a time step of 0.13s. Therefore, a total 5.5×10^5 time steps are required for the 20 hours. As RANS is used at least 10 iterations will be required for each time step each taking an average of 0.6 s (taken from the actual simulation), leading to 38 days required to solve the simulation. However, alternatively the use of large courant numbers with a time step of 1.5 s results in a solve time of 3.3 days, a reduction of 90%.

The two remaining scour mechanisms, the horseshoe vortex and flow acceleration are time step insensitive when generated using the RANS model as discovered in 0, *Monopile Investigation*. Therefore, none of the primary scour mechanisms determine the time step in this scenario and it is instead governed by numerical divergence due to high courant numbers or a high mesh deformation rate.

The relationship between scour rate and time step was investigated during this case, which revealed that numerical error could be avoided by limiting the deformation distance of the adjacent cell height per time step. Additionally, if the time step were adjusted so that the maximum deformation height is below this limit the resultant courant numbers did not cause numerical error. These initial simulations were also used to define numerical divergence and mesh quality indicator thresholds for the automatic re-meshing procedure.

Empirical Formula

This case was used to test two excess shear stress formulas, Guo and Shields-Brownlie (Equation 6 & Equation 7), and two bed load formulas, Peter-Meyer-Muller and Van Rijn (Equation 13 & Equation 12) of which the results are shown in Figure 7-9.

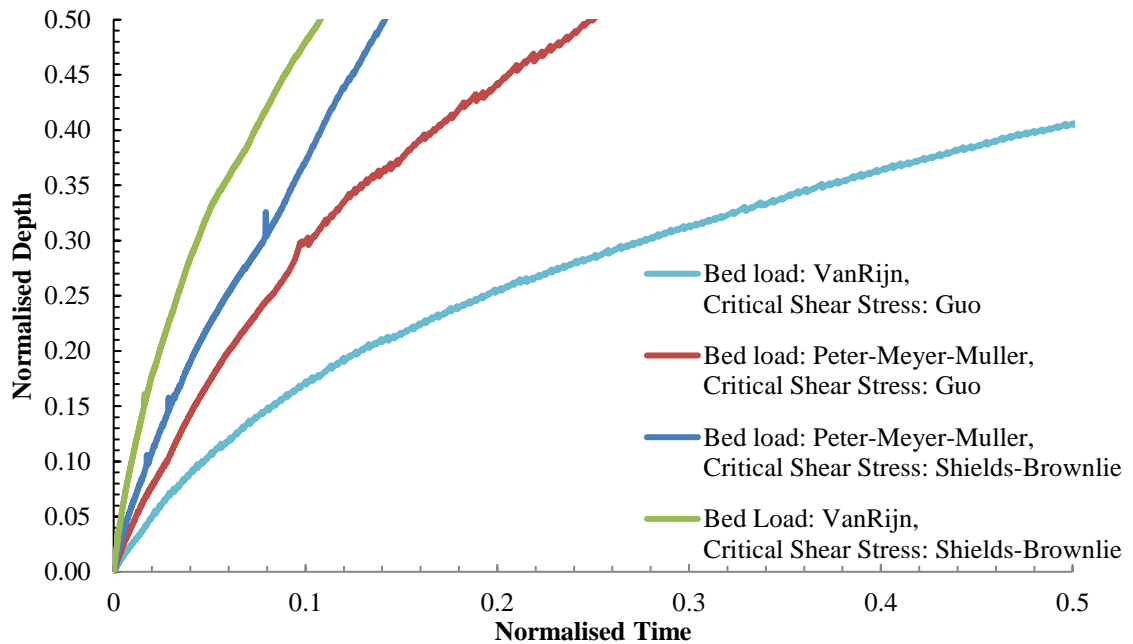


Figure 7-9 – Case 1 Empirical Formula Testing Results

The structure of these equations results in an asymptotic equilibrium value determined by the critical shear stress formula and propagation of maximum scour depth determined by the bed load formula. These facts in conjunction with the results demonstrate the significant difference in empirical formula; namely that the Guo (2002) formula has a lower critical shear stress and the Van Rijn formula is more sensitive to the critical shear stress value. In this case, the critical shear stress formula of Brownlie and bed load formula of Van Rijn are closer to the experimental values. Due to this fact and the successful use of these formulas, they are used for all future simulations.

Results

The final results are shown in Figure 7-10, alongside the results for a courser mesh. The correlation between simulation and experiment is good for the first 3 hours of simulated physical time with an error of 25%, 8% and 6% against the first three experimental data points. The slow convergence towards experimental values in the first three hours leads to a matched result at 3.6 hours. The correlation from this point onwards degrades because as shown by Figure 7-11 the simulated scour gradient reduces at a slower rate; resulting in a final simulation scour depth 30% greater.

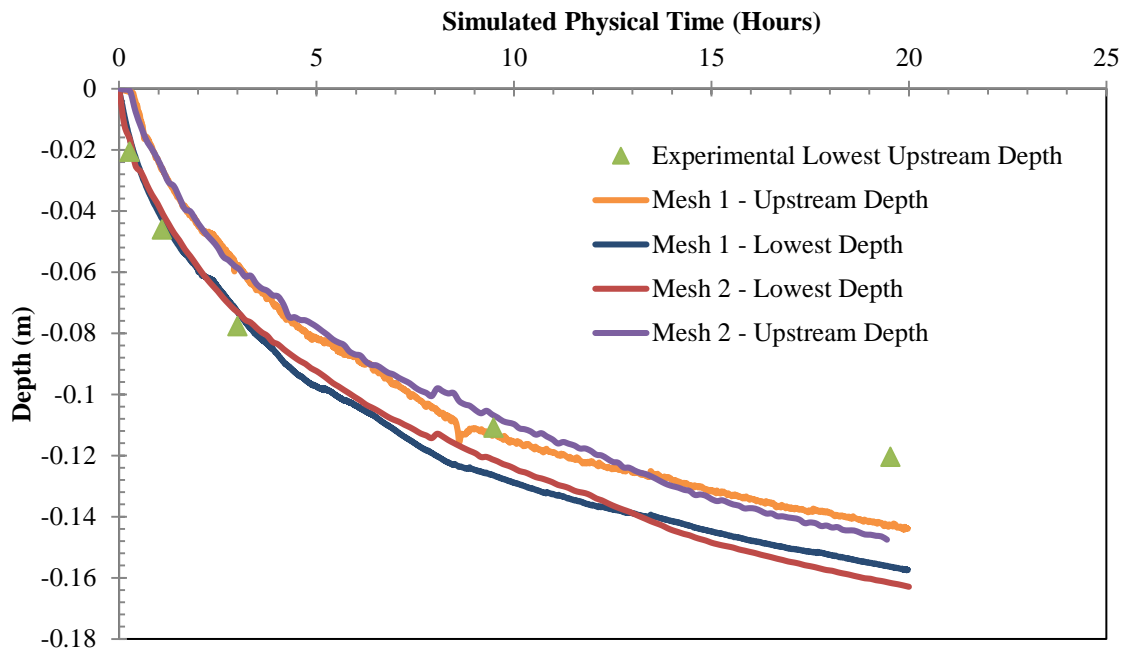


Figure 7-10 – Case 1 Lowest Point Development Mesh Comparison

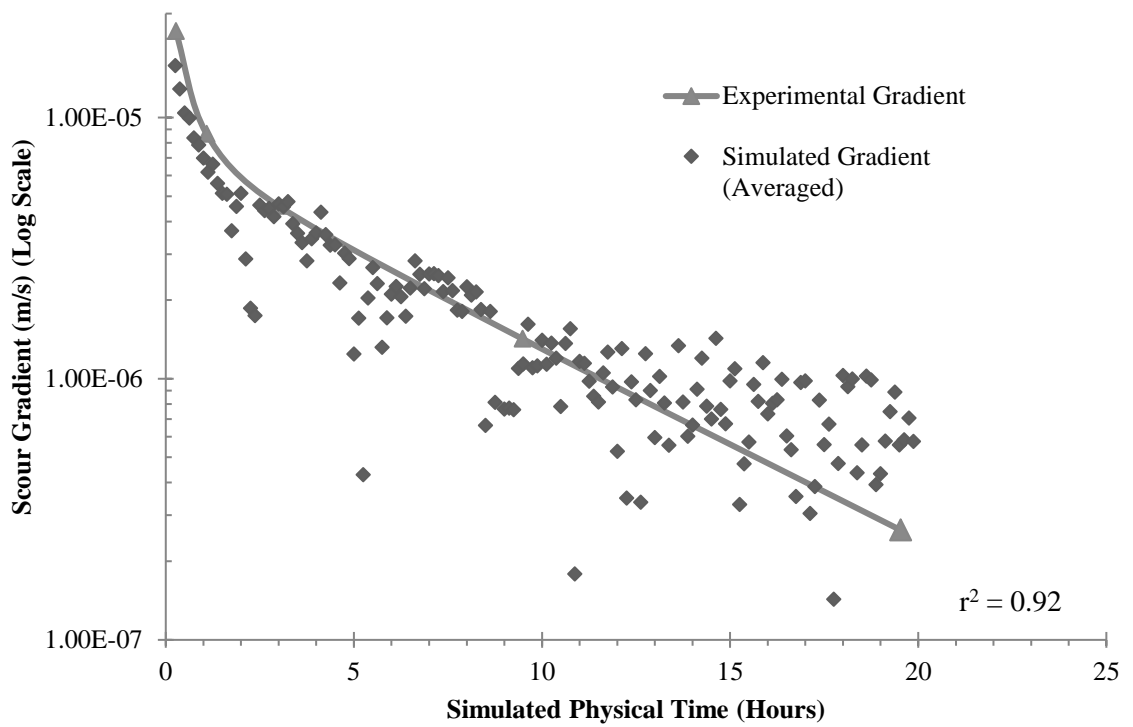


Figure 7-11 – Case 1 Scour Gradient Comparison

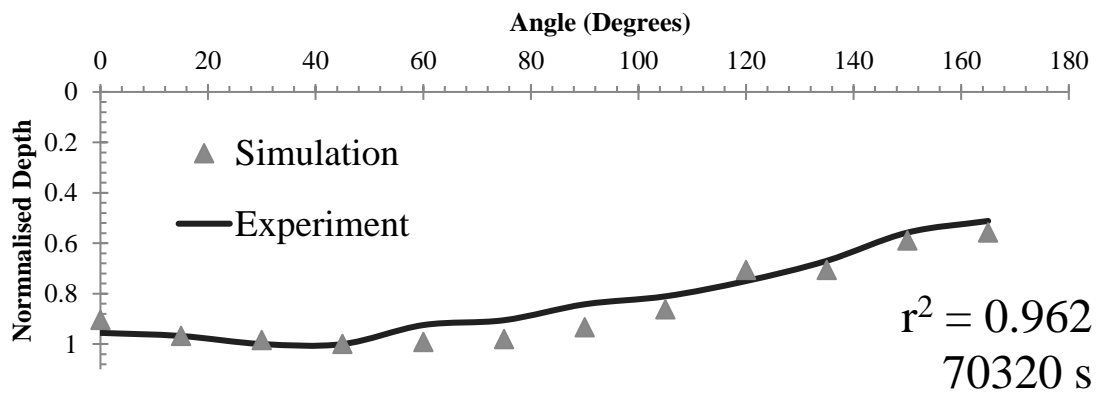
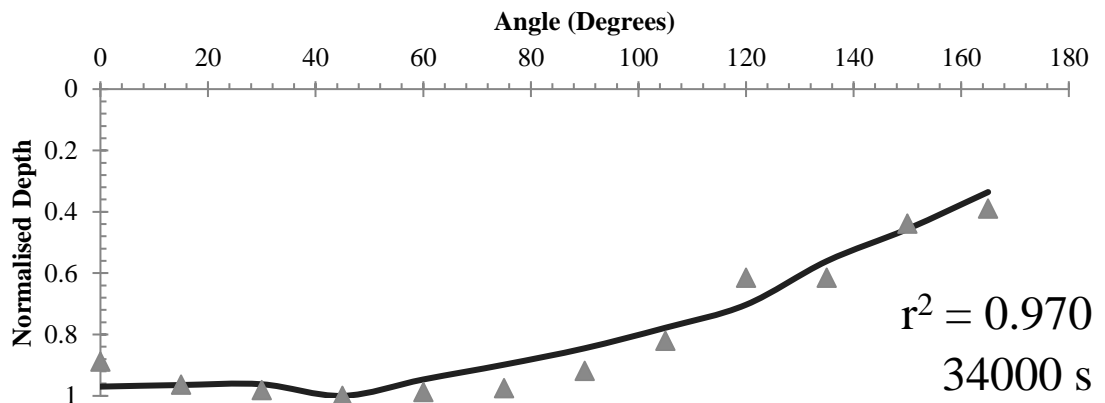
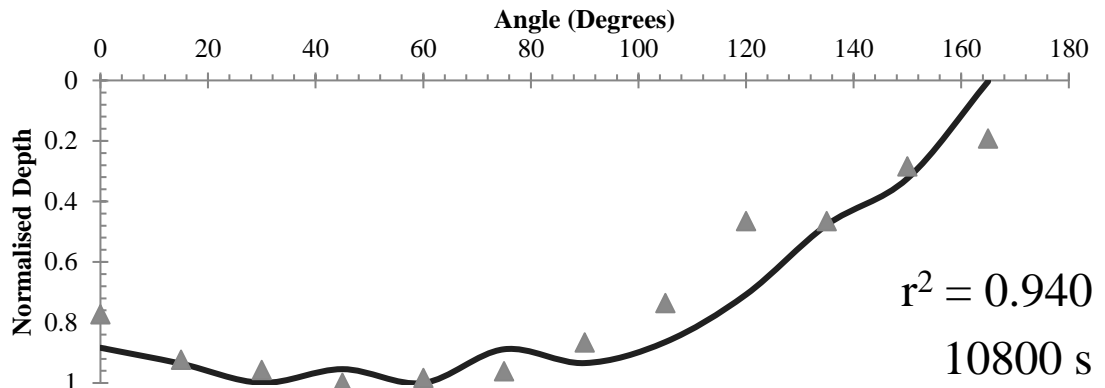
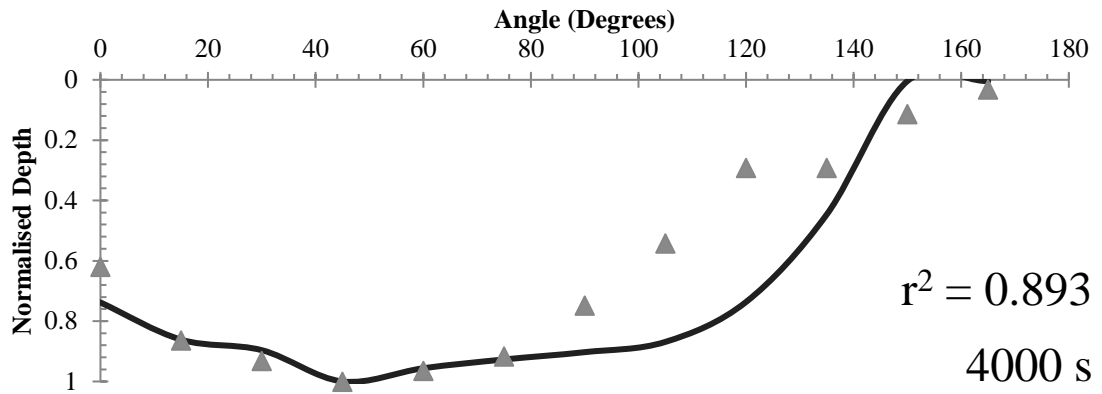


Figure 7-12 - Case 1 Developing Radial Topology

A comparison of the normalised maximum depth in each radial plane, between simulation and experiment for 4 time points is shown by Figure 7-12. This shows that the normalised topologies are more precise than the absolute difference, using the displayed r^2 values.

The absolute scour depth is the greatest inconsistency in this case, specifically beyond 3 hours. As discussed this is a result of the scour gradient decreasing too slowly leading to a final scour depth difference of 30%. This discrepancy could be due to a number of reasons, which have been split into three categories; mismatching simulation-experimental setup and empirical and fluid dynamic error.

The differences between experiment and simulation include simplifications due to the empirical formula used such as the single grain size and density. Additionally, the free surface is neglected which at a small h/D value is predicted to cause an over prediction. Roulund et al. (2005) simulated the same conditions and uses a reduced water depth of only 20 cm to represent the height of the bed boundary layer due to the free surface, and reports that if a 25cm boundary layer was used scour would increase by 10%.

The experiment features a concrete block bed-surface stretching from the inlet to 2m upstream from the pile. This was suspected to be a partial cause of the increased scour depth and a steady-state simulation of the whole channel with a concrete block section represented by a greater roughness height was ran. However, the difference in velocity profile or wall shear stress around the pile was negligible.

The potential error of the empirical formula, firstly the critical shear stress is evident from the variation in formula shown by Dey (1999) and Rashid (2010) with up to 15 times difference. The bedload formulas can also result in extreme differences as shown by (Camenen and Larroudé, 2003). These extreme differences are often the result of variables at the limit or outside the limits of the formulas intended use, however, significant differences remain, as shown by the tests ran at the start of this case.

The potential fluid dynamic errors include firstly the HSV as previously discussed, however the detailed experimental results show that the normalised topologies align, specifically the scour depth between the front and side of the pile. The prediction of the high shear stresses at the side driving the maximum scour depth are assumed accurate due to the mesh convergence study and previous comparison to LES, however there is the possibility that the changes in topology result in a lower accuracy.

Case 2 – Detailed Scouring around a Simple Monopile

A second monopile case was compared to provide confidence in the model by excluding fluid dynamic error due to experiment-simulation mismatch; using a greater h/D ratio and a provided experimental velocity profile. The case is sourced from Alabi (2006) and the key variables are shown in Table 7-3.

Area	Parameter	Value
Flume:	Width:	1.22
	Length:	20
Working Section:	Width:	1.22
	Length:	12.43
Pile	Diameter:	115 mm
	Position from Inlet:	7 m
Sediment	Diameter:	0.00053 mm
	Depth:	0.16 m
Flow	Average Velocity:	0.249 m/s
	Depth:	230 mm
	Dimensionless Shear Stress:	0.4
Time	Experimental	285000 s (3.3 days)
Maximum Scour Depth	Experimental (@ 285000 s)	0.140 m

Table 7-3– Case 2 Parameters

The domain size, mesh and time step used for this case were defined using same procedure as Case 1, resulting in the domain shown in Figure 7-13. Furthermore, due to the outcome of the formulae testing in Case 1 the Brownlie critical shear stress and Van Rijn bed load formula are employed.

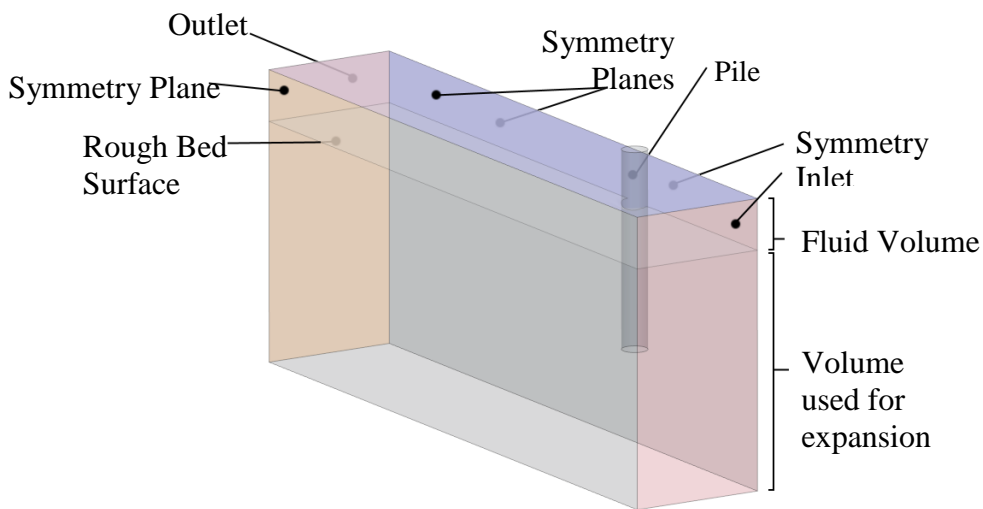


Figure 7-13 – Case 2 Fluid Domain

Results

A comparison of the developing lowest bed position revealed a constant absolute difference between simulation and experiment of 33%, with the simulation underpredicting. However, the normalised results as shown in Figure 7-14 are extremely similar with an r^2 correlation of 0.976. Furthermore, this provides a better understanding of the discrepancies as there are limited sources of error that remain constant throughout the scour stages.

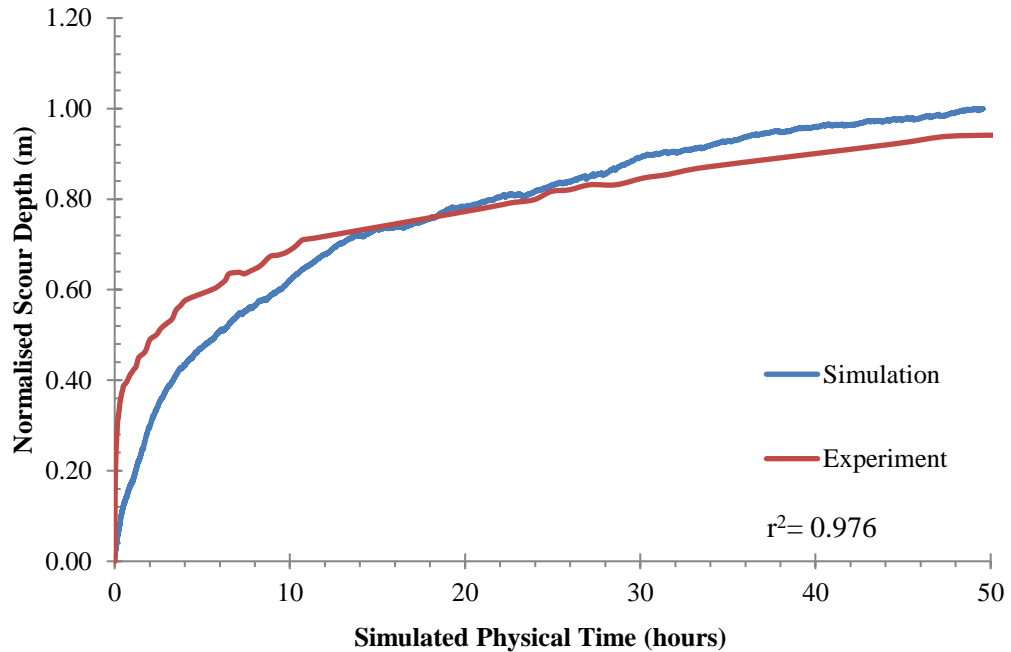


Figure 7-14 – Case 2 Scour Development Results

Analysis of all variables concludes that the source of error is the critical shear stress; due to the previously stated inherent error or incorrect inner variables such as grain size and density. The bed load formula, the other source of empirical error is unlikely as this determines the trend, which as seen in Figure 7-14 is correct.

The predicted fluid dynamics are dismissed as such errors will not remain constant as topology develops. The remaining possibilities are the velocity profile and free surface effects; however, the velocity profile was extracted from the experimental results and neglect of the free-surface causes over prediction. The similarity of a normalised trend for this case improves model confidence however it is clear from Case 1 and 2 that errors remain.

Case 3 – Scouring around a Gravity Base Foundation

Testing the model using the in-house experimental detailed in *Chapter 3 Gravity Base Foundation Experiment* introduced complexity due to the foundation geometry, shallow water depth and underside scouring. However, it is advantageous to have access to all setup variables and a wide scope of flow and topological data as eliminates areas of potential error highlighted in the previous cases.

A preliminary steady-state simulation revealed that use of the experimental velocity profile as an inlet condition resulted in an extremely under-developed flow near to the pile, due to the evolution from a velocity profile with free surface effects, to one without. Therefore, the inlet velocity profile was computationally generated with a fully-developed no-free-surface conditions.

The simulation required a significant amount of re-meshing time triggered by the frequent creation of poor quality elements underneath the structure; due to the sharp corner between the bottom of the foundation and the void underneath.

The simulated scour at each hour is shown in Figure 7-15, followed by the development of maximum scour depth in Figure 7-16. The simulated scour begins at the sides of the structure spanning from -5 to $+90^\circ$ with the maximum depth at 45° . At 2 hours the resultant small sweeping trench extends radially from the lip of the gravity base by a maximum of 0.063 m in addition to a small amount of scouring underneath the structure.

As shown by Figure 7-15 the scour depth rate is greatest during the first three hours, followed by a gradual decrease in rate. Between 3 and 4 hours, the trench extends to the front of the structure forming a trench spanning -90 to $+90$ degrees and continues to grow over the remaining 7 hours in depth and radially, extending outwards from the structure and also underneath. However; the trench does not expand around the back of the structure, primarily due to the upsloping bed resisting erosion.

The underside scouring does not begin experimentally before 3 hours and the early simulation underside scour is attributed to the single-phase simulation not capturing the build-up of sediment underneath the structure.

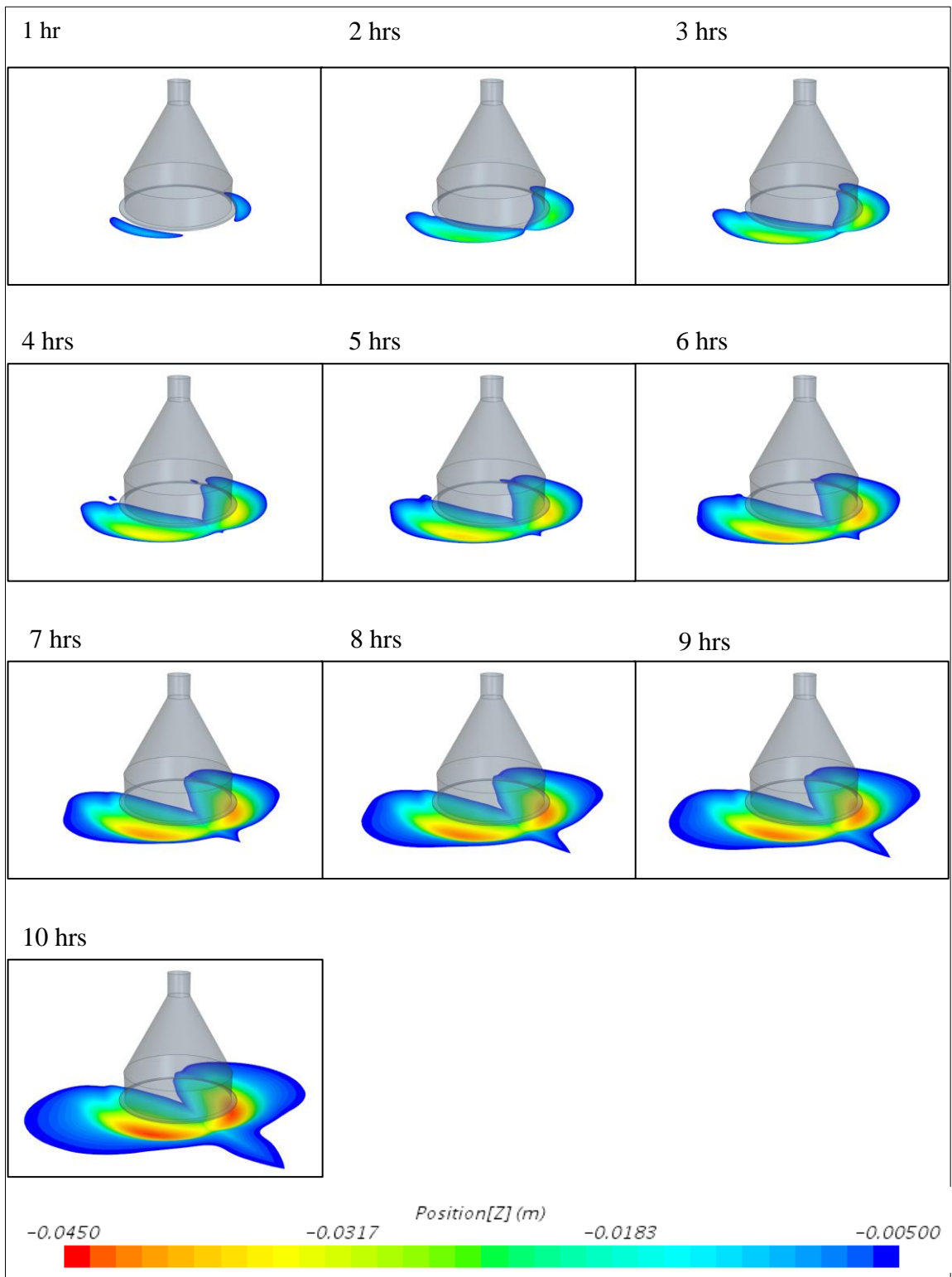


Figure 7-15 – Case 3 Hourly Scour

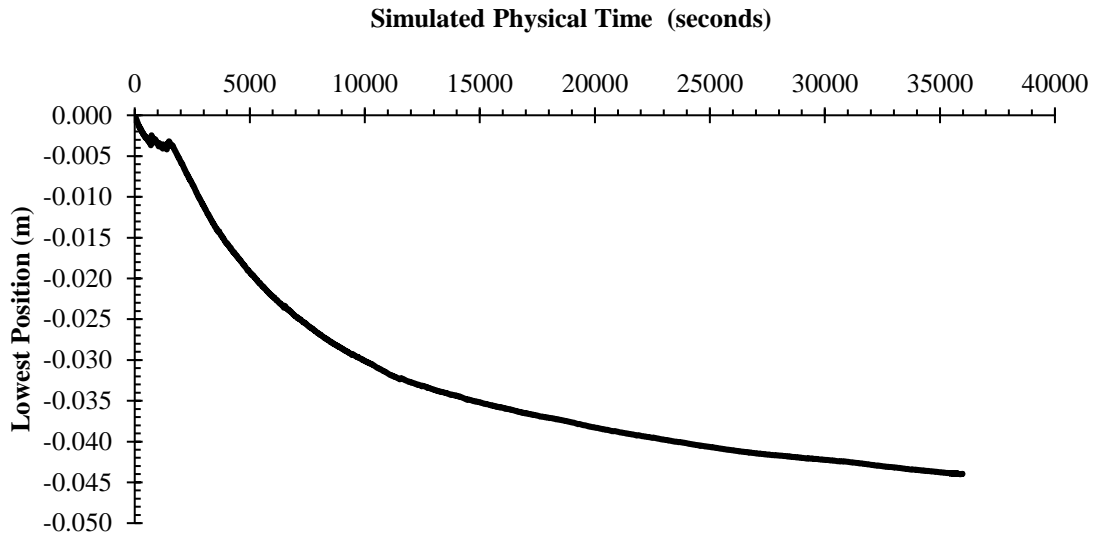


Figure 7-16 – Case 3 Scour Development

The final normalised topology is shown in Figure 7-18 alongside the experimental result. The trench formed in the experiment remains constant in maximum depth from the front spanning around to 45° with a maximum depth of 0.038 m. The simulated trench does not follow this result and increases from the front to a maximum depth of 0.042 m, also at 45°. This discrepancy is likely a result of poor horseshoe vortex prediction in combination with no initial sediment build-up at the front of the structure.

The final topology does not feature downstream pitting or a disturbed bed outside the main scour area. This is primarily because the large time step and RANS solver time-average and therefore smooth the results. Additionally, the repetitive re-meshing also smooths the bed surface.

The bed topology along the symmetry plane shown in Figure 7-17 provides a clearer view of the trench and simulated topology similar to the experimental result. Additionally, the up and downstream slopes of the trench are the same as the experimental result.

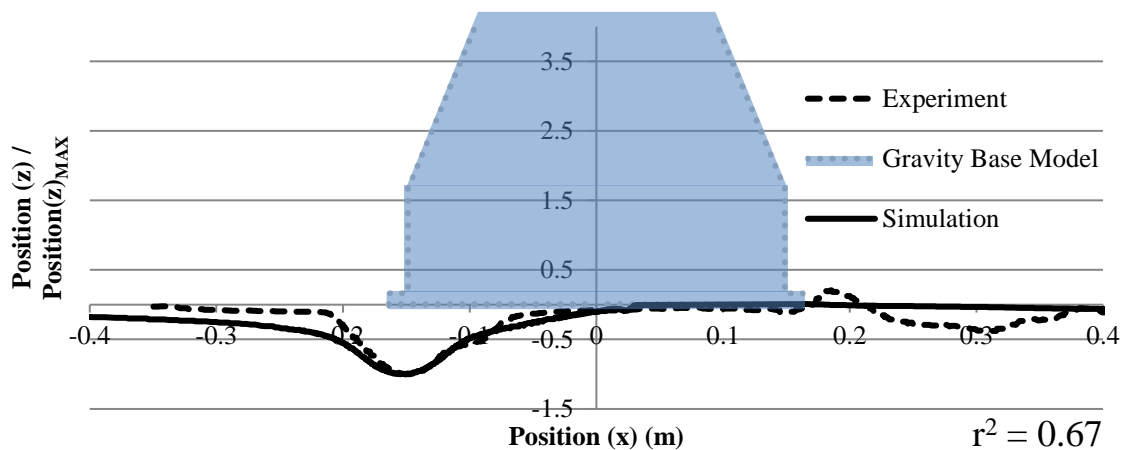


Figure 7-17 – Case 3 Normalised Topology Along Symmetry Plane

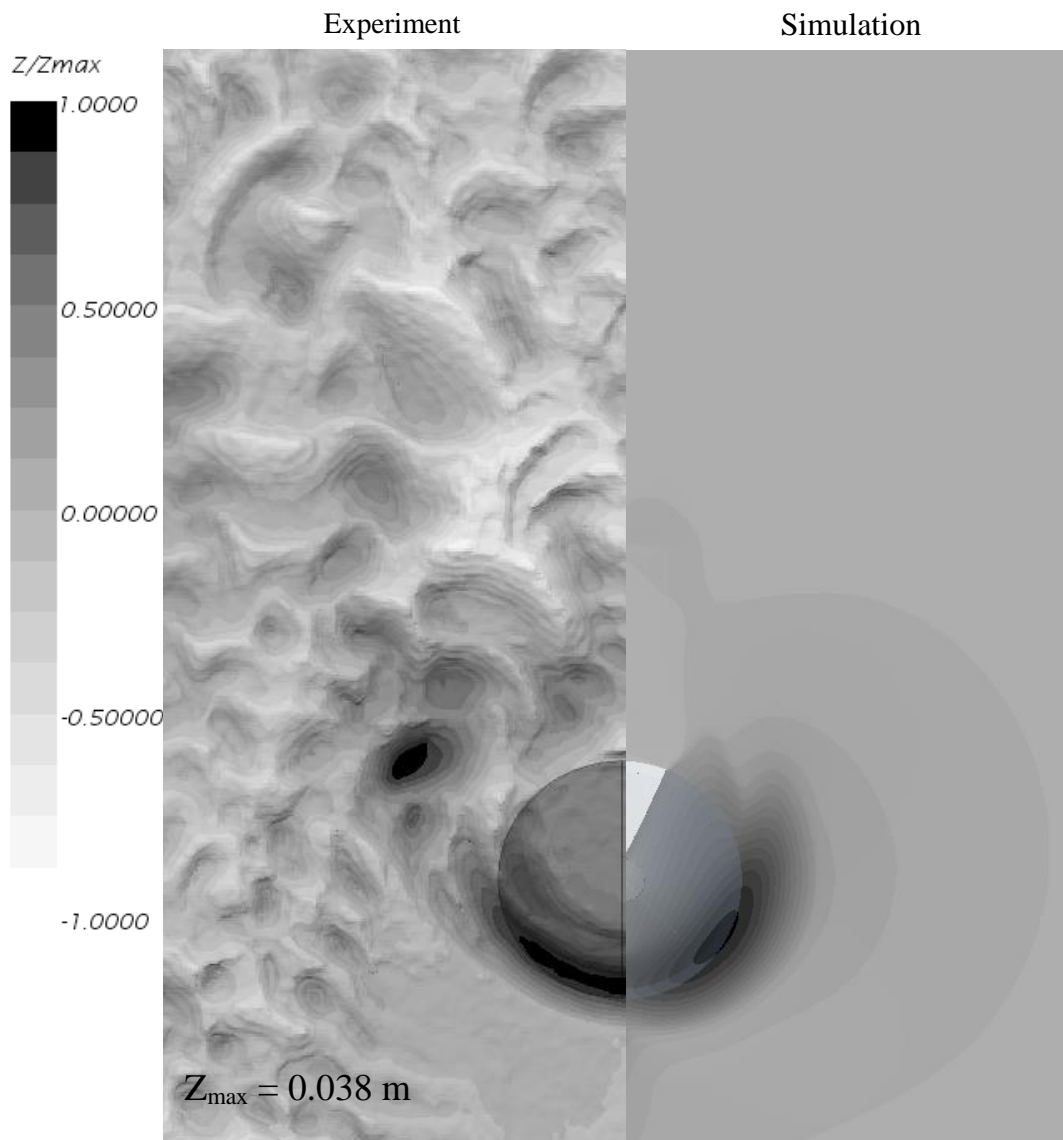


Figure 7-18 – Normalised Scour Topology

The simulation of an in-house experiment has enabled a thorough investigation compared to previous cases due to additional experimental data, allowing the identification of the discrepancies and similarities.

The simulation scour began at the sides of the spread to the front and expanded radially (positively and negatively) as well as downwards, as opposed to the experiment where scour began at the front propagating around the structure and outwards, prior to scouring underneath. This discrepancy is attributed to the single-phase not capturing any deposition and poor horseshoe vortex prediction. However, the trench forms in the same place with a similar maximum depth (especially when compared to previous results).

As issue that is not evident from the results in the effect of the mesh ‘wrapping’ that enables underside scouring. This feature, as briefly mentioned, resulted in the frequent creation of poor

quality cells and numerical errors; that were resolved by re-meshing. Furthermore, these problems resulted in a significant, unreasonable amount of additional time.

In addition to simulation stability and time, the wrapper is sensitive to mesh settings and the speed of underside scour propagation can be influenced by these settings. Therefore, this is the only underside-scouring simulation in this thesis due to the unfortunate additional research required prior to further use.

However, these results have contributed to the verification of the model and confidence in its accuracy, but questions remain regarding the source of previous issues, hence the nature of the proceeding case.

Case 4 – Scouring around a Suction Caisson at Multiple Elevations

Previous cases hold a poor accuracy of absolute maximum scour depth for reasons previous discussed; categorised into mismatching simulation-experimental setup, empirical and fluid dynamic error. In order to eliminate the mismatching setup, fluid dynamic error and improve confidence in the empirical formula this test case compares the differences between several simulations under user-defined conditions to match a well-documented trend. This trend as demonstrated by (Melville, 2008) is the effect of suction caisson base protrusion height on scour depth.

Clear water conditions are generated using a mean velocity of 0.5 m/s with a 40m water depth over a sediment bed comprised of grain diameter 0.0008m. This results in a water depth greater than the boundary layer height; eliminating error due to free-surface effects. For all tests the boundary conditions, boundary distances and sediment properties remain constant. The two extremes of suction caisson position are shown in Figure 7-19.

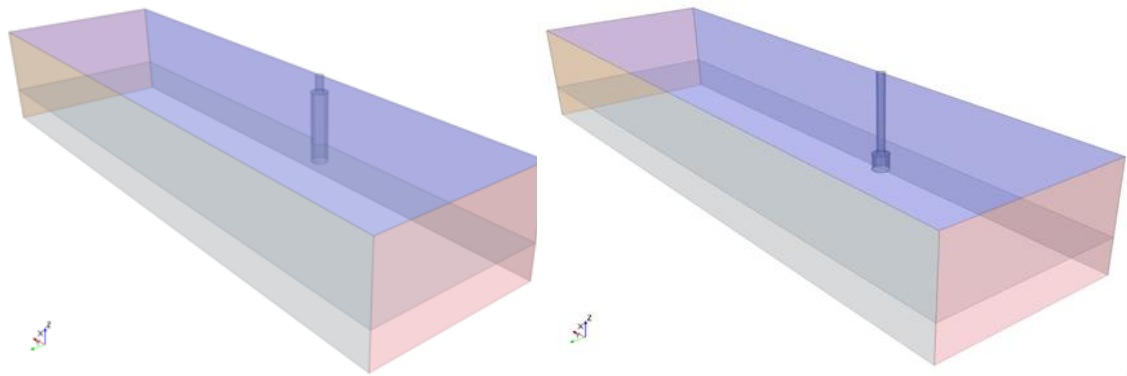


Figure 7-19 – Suction Caisson Position Extremes

The caisson base and pile diameter are 10m and 5m respectively. The test extremities are essentially monopiles (of 5m and 10m) which are estimated to reach equilibrium after 120 and 240 days using the equation in (Melville and Chiew, 1999). The two extremes are ran for 5% of this time resulting in 60-70% of the maximum depth (Melville and Chiew, 1999); allowing for the trend to be recognised. The full predicted time is not necessary as it is the difference in scour development and not the equilibrium scour depth that is of interest.

In order to equally weight the changing geometry, those simulations with a pile-cap elevation between $(-)/y/b$ and 0 with a 10m diameter structure at the bed surface are run for 12 days matching the 10 m monopile. The simulations between 0 and $(+)/y/b$ are ran for a minimum of 6 days, or extended to 12 days if scouring continues to propagate below the caisson top. The results are shown in Figure 7-20 and Figure 7-21 - Pile-Cap Elevation Final Topology and display the developmental maximum scour depth and final topology.

Results

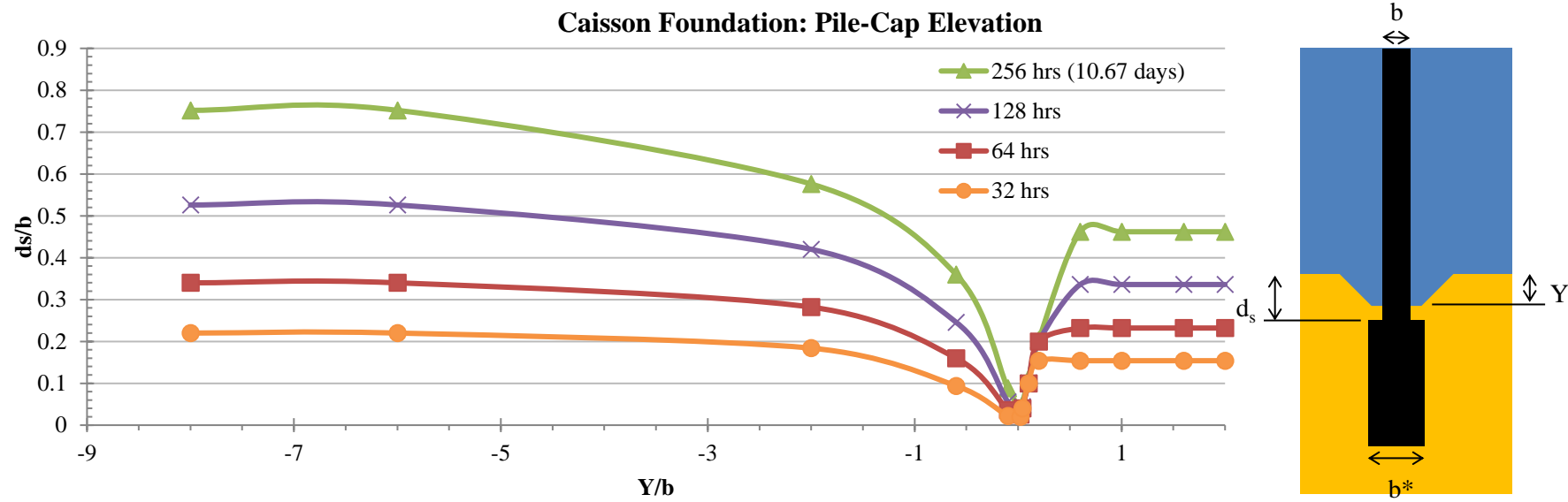


Figure 7-20 – Pile-Cap Elevation Scour Development

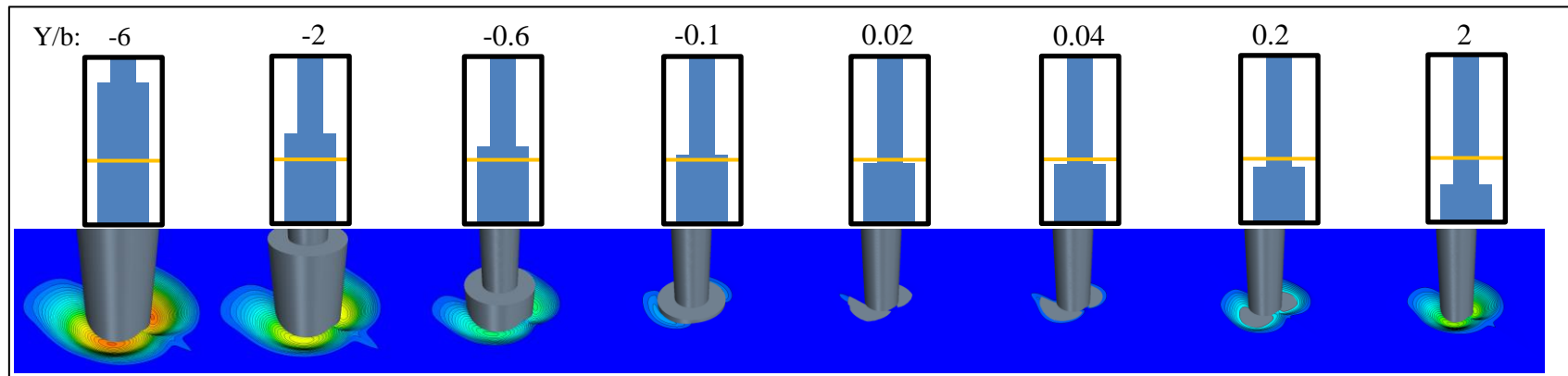


Figure 7-21 - Pile-Cap Elevation Final Topology

The scour depth at 265 hours in Figure 7-20 matches the target trend shown in (Melville, 2008); illustrated in the previous Figure 2-30 (Page 51). It was stated that simulation results are not ran until true equilibrium and instead will be ran for a set percentage of the predicted equilibrium time; which for the 10 m and 5 m monopile should result in a 50% difference in maximum scour depth. Comparison of the results show that for the whole scour period the maximum depth at the 10 m monopile is double that at the 5 m for half the scour period, with a maximum deviation of 6%.

The reduction in scour depth from $y/b = -8$ to 0 is due to the reduction in down flow and therefore strength of the resultant HSV and flow acceleration. The scour depth reduces exponentially against cap elevation, which is also shown by similar studies around complex pier configurations such as (Moreno et al., 2015).

The lowest point shown in Figure 7-20 is within the positive region of y/b and is repeated by simulation results however the magnitude of the trough is significantly less due to the low τ/τ_∞ of 0.65, as shown alongside two peripheral simulations with higher ratios, Figure 7-22.

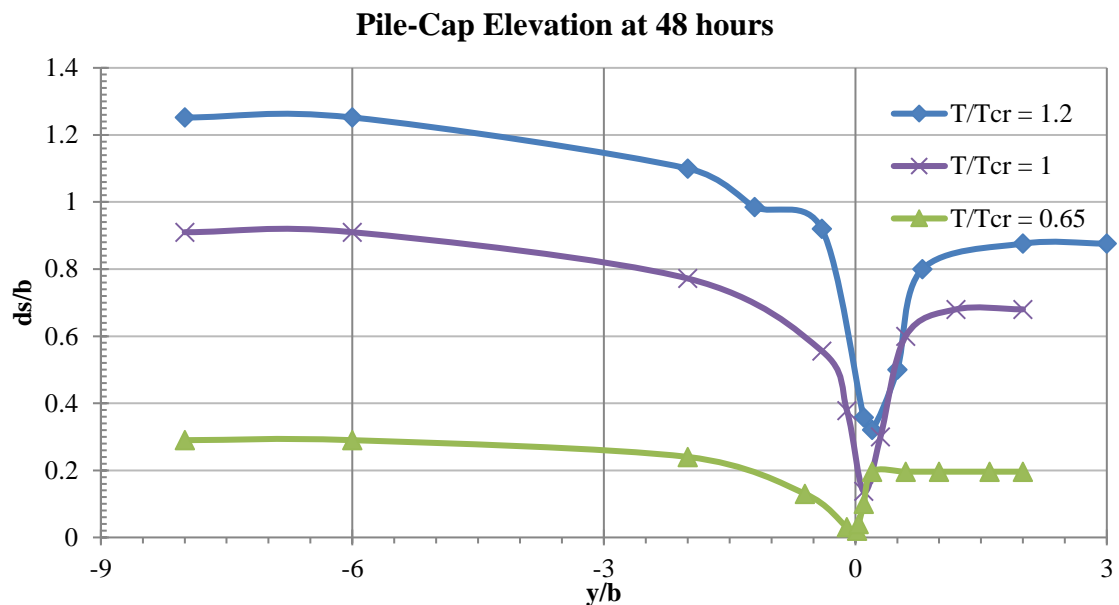


Figure 7-22 – Excess Shear Stress effect on Suction Caisson Scour Depth

The developing scour topology in the range $0 > y/b > 0.5$ deviates and it was discovered that when the caisson top is shallow scour starts at the back, as opposed to a deeper caisson base whereby the scour passes at the side, Figure 7-23. This is because with the deeper caisson base the typical scour topology is initially formed with a downstream-up sloping bed that reduces the scour behind the structure. This is however not the case with the shallower caisson base as the depth is not sufficient for the incline to form and therefore the trailing high-velocity results in shear stresses that exceed the critical threshold.

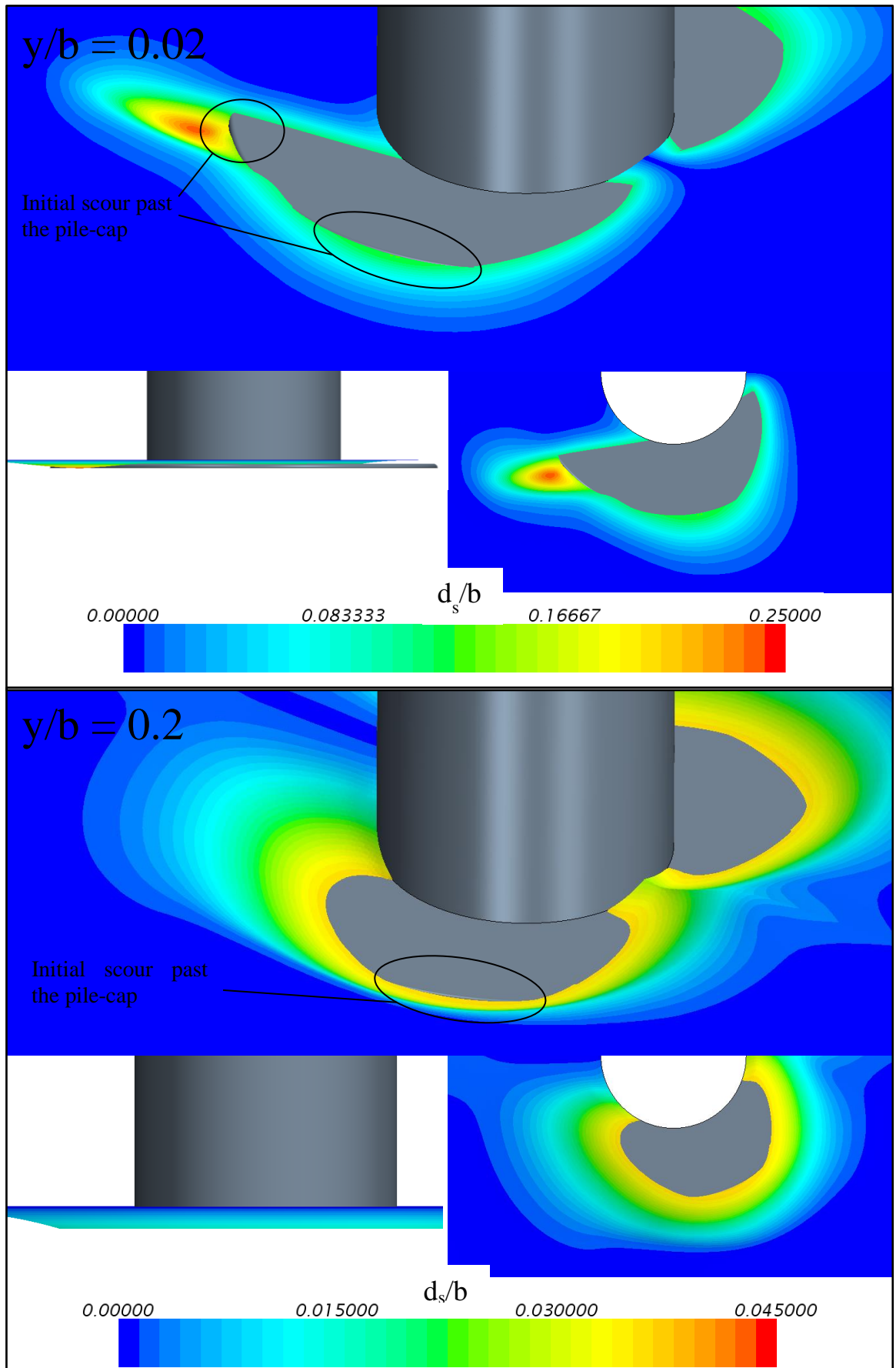


Figure 7-23 – Deviating Scour Topology with Pile-Cap Depth

The results have shown that the scour model can be successfully used to compare scour results. Furthermore, the results imply that the previous case errors in absolute depth are primarily due to poor representation of the experimental properties; through simplifications within empirical formula and simulation setup (e.g. free surface effects and underdeveloped velocity profiles).

Single Phase Model Summary

The four presented cases have proven that the single-phase model can provide the accuracy to meet the outlined objectives, given the high accuracy of normalised scour topology development, as evidenced by the high r^2 values. This is in addition to the trend in scour depth produced in Case 4; however, the limitations of the model have also been highlighted including shallow flows and scour underneath structures; evident from the issues faced with Case 3 – Scouring around a Gravity Base Foundation.

The first case was used to test, demonstrate, and reiterate the variation in empirical critical shear stress and bedload formulas. Furthermore, this testing enabled a clearer understanding of the discrepancies between experimental and simulated results in all other cases.

Case 2 aimed to minimise the discrepancies and was successful, through an increased boundary layer height to water depth ratio and an experimental inlet profile. However, error remained hence the requirement for testing against the in-house experiment (Case 3 – Scouring around a Gravity Base Foundation) and the well documented trend in Case 4 – Scouring around a Suction Caisson at Multiple Elevations. The final two cases showed the full capability of the model (single phase aspect) despite the dependency on varied empirical formulas.

7.3 Two Phase Model

This section compares simulation results to two cases, firstly testing the concentration profiles without any morphology for a straight channel and a trench. The second part utilises the trench case further by allowing for morphology and comparing the bed topology after a 10-hour period.

Scouring along a Straight Uniform Channel

(Van Rijn, 1981) details an experiment that captures the developing sediment concentration profile over a sediment bed with no upstream sediment load along a simple channel, Figure 7-24. This is used to test, tune and validate the two-phase model with no deformation.

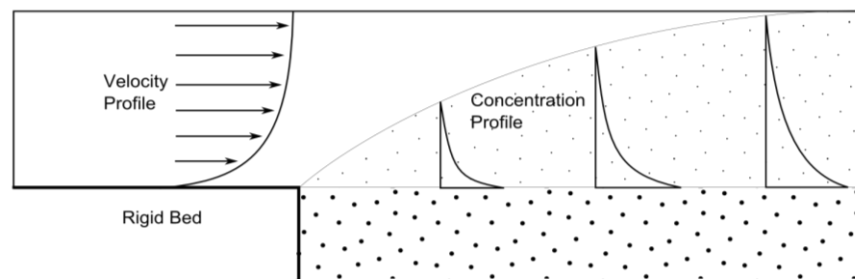


Figure 7-24 – Simulation Setup

Setup

This is conducted in a pseudo-2D simulation, because although the Eulerian multiphase model can be used two-dimensionally the deforming boundary cannot.

The results in (Van Rijn, 1981) include 10 m of sediment concentration results, however, due to the effect of the outlet the sediment bed in the simulation extended 25 m. All morphology on the sediment bed was suspended, however, both positive and negative mass flux remains. Prior to the sediment bed is a rigid section which extends 5 m from the inlet, Figure 7-25, with an experimentally matched depth of 0.25 m. The domain width was 0.147 m based on the mesh required longitudinally, the acceptable cell aspect ratio, and a reduction in velocity profile and sediment distribution validity when less than 4 cells represented the width. The simulation includes a fully developed profile with an average velocity of 0.67 at the inlet, developed with a bed roughness height relating to the grain size on the later sediment bed, 0.00023 m.

An important area within two phase models is the modelling of the secondary (particulate) phase and the interaction between phases; enabling the effects of lift, drag and turbulence. These interactions and the associated parameters can have a significant impact and are tested and examined using this case and discussed alongside the concluding result, as shown in Figure 7-26.

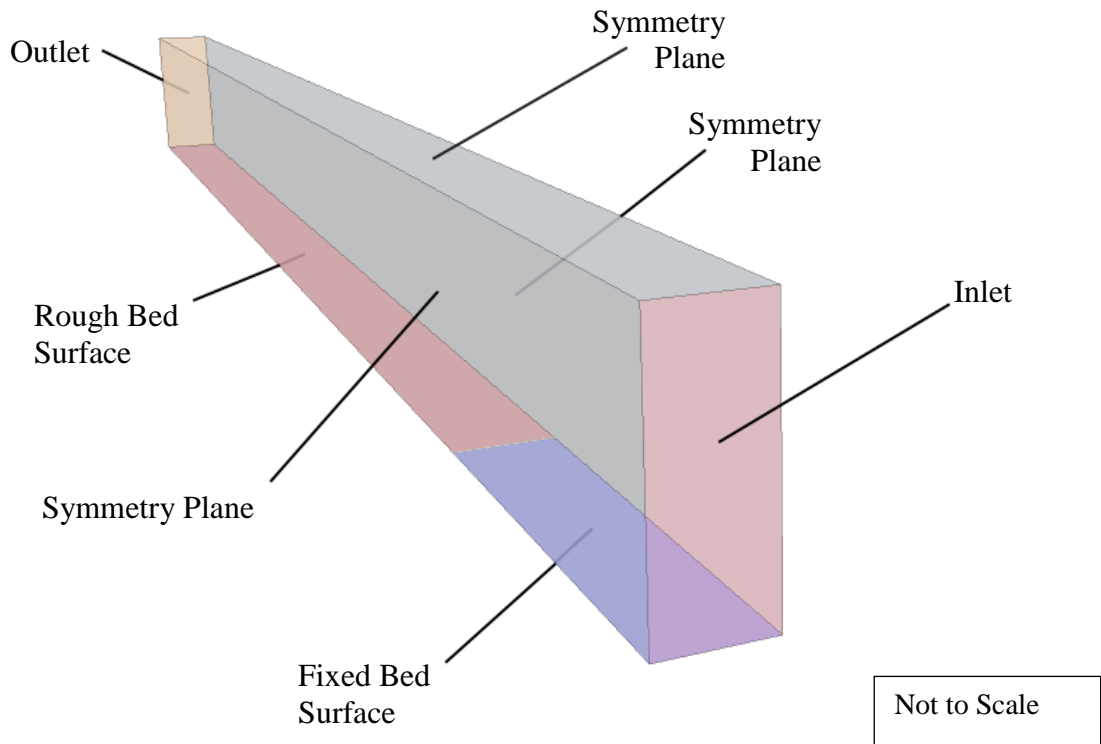


Figure 7-25 – Straight Uniform Channel Domain

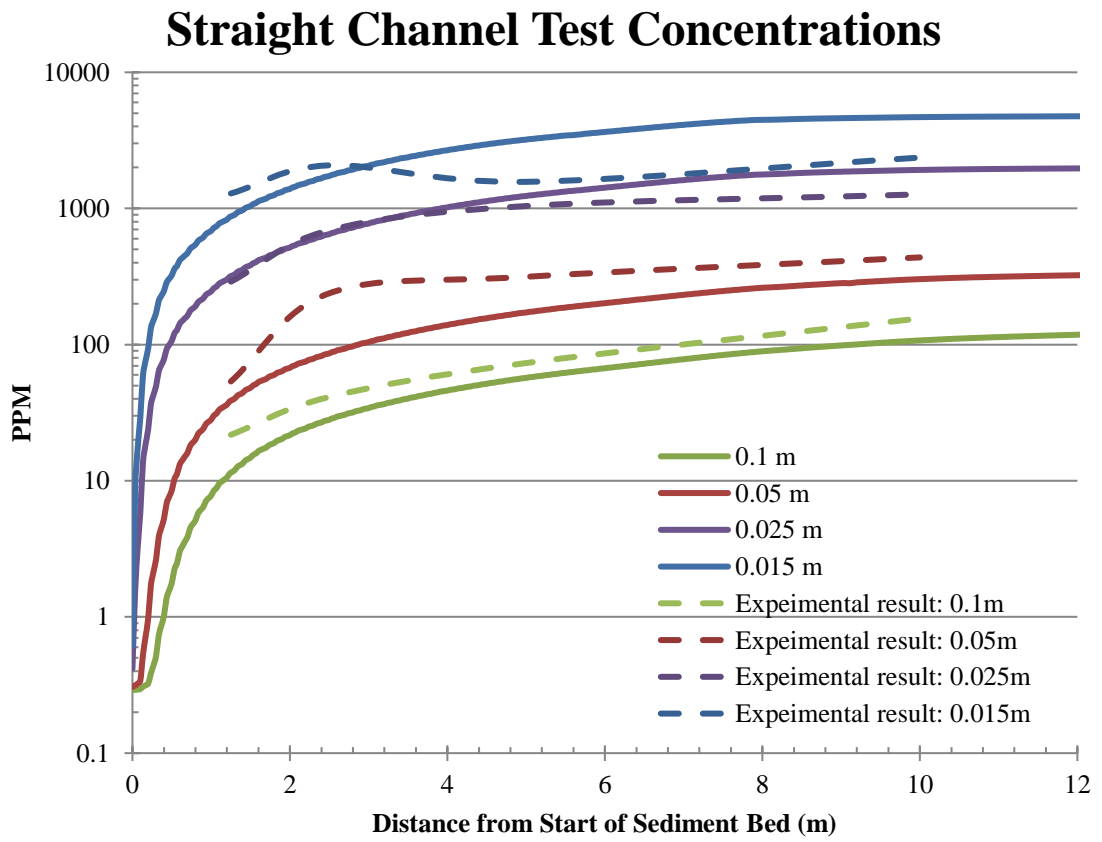


Figure 7-26 – Sectional Concentration Results

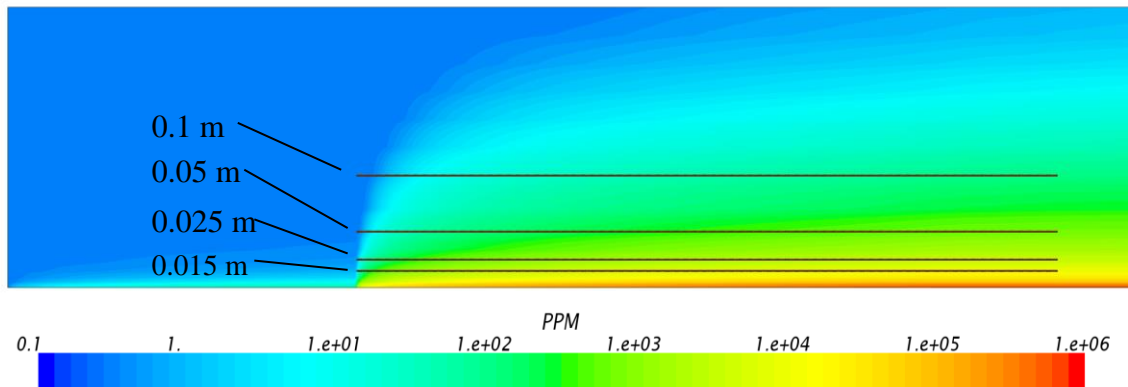


Figure 7-27 – Continuous Concentration Results

Figure 7-26 provides the sediment concentration at four heights within the lower half of the water column, as shown in Figure 7-27. Experimentally the concentration increases rapidly in the first 3 m followed by a slower, decreasing gradient that does not reach an equilibrium state before the end of the experimental results at 10 m. The simulated concentration matches this trend with a greater spread; however, the result is extremely sensitive to interaction model parameters, as discussed in the following.

The dispersion of sediment throughout the water column in the present case is primarily due to turbulence. The level of turbulent dispersion is commonly defined using the turbulent Prandtl number, signifying the ratio of momentum diffusivity over the volume fraction diffusivity due to continuous phase velocity fluctuations. This can be defined as a constant or calculated using a model, with each producing a different sediment concentration trend that can be further modified using inner parameters.

Overall, the existence of parameters for model tuning at several stages permits a wide range of results. Several are guided by flow or sediment conditions/properties however still allow for large variation in results and therefore potential error.

The results were produced using the particle induced turbulence model proposed by Tchen (Hinze, 1959) with correction parameters $C_{Production} = 0.5$, $C_{Dissipation} = 1.44$, Prandtl No. = 1 and $C_{Crossing_Trajectory} = 1.8$, with a tuned dispersion force constant.

Secondary to the dispersion model is the drag model, specifically the correction method that accounts for changes in volume fraction. This essentially controls the speed of settling after sediment has been dispersed up into the water column and therefore in this case influences the concentration gradient after the initial rapid increase. The drag correction is less sensitive to the contained user-defined values than the turbulent dispersion, regardless of correction method and therefore less susceptible to error.

The remaining lift and virtual mass and length scale choice also influence the concentration; however, the impact is comparatively less, and the parameters are better defined.

This case demonstrates that the computational model can replicate experimental concentration results. However, in cases where the concentration profile is heavily dependent on turbulent dispersion forces the result is very sensitive to dispersion method and parameters.

This case has unveiled the sensitive nature of the two-phase model, especially the dispersion parameters. This type of case where the erosion is immediate following approaching zero concentration due to an excess shear stress exceeding 10 is rare. Therefore, the proceeding case replicates a more common scenario of a flow with a pre-existing sediment concentration across a trench.

Scouring along a trench – Mass Transfer with no Morphology

Delft Hydraulics Laboratory (1980) provides experimental concentration and velocity profiles of flow across a sediment trench with upstream sediment supply, Figure 7-28. The total length of the domain is 8m, with a central trench that resides 0.15 below the start and end bed depth of 0.39m; the full simulation domain is shown in Figure 7-29. Converse to the previous case there is upstream sediment supply, lower τ/τ_{cr} ratio and mobile sediment bed throughout; therefore, reducing the concentration sensitivity to turbulent dispersion parameters. The experimental conditions are shown in Table 7-4.

Variable	Value
Inlet total load	0.04 kg/m ²
Mean flow velocity	0.51 m/s
Depth at inlet	0.39 m
Sediment Density	2650 kg/m ³
D ₅₀	0.00160 m

Table 7-4 – Experimental Conditions for Two-Phase Trench Case

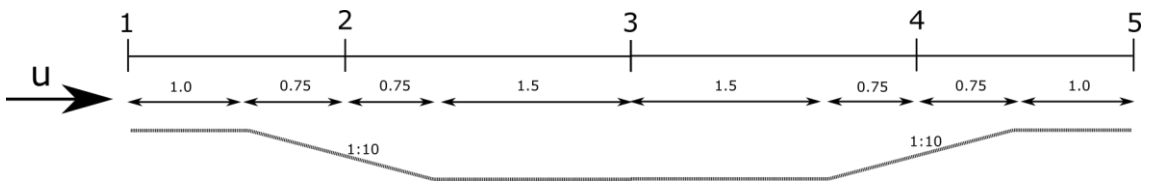


Figure 7-28 – Trench Setup

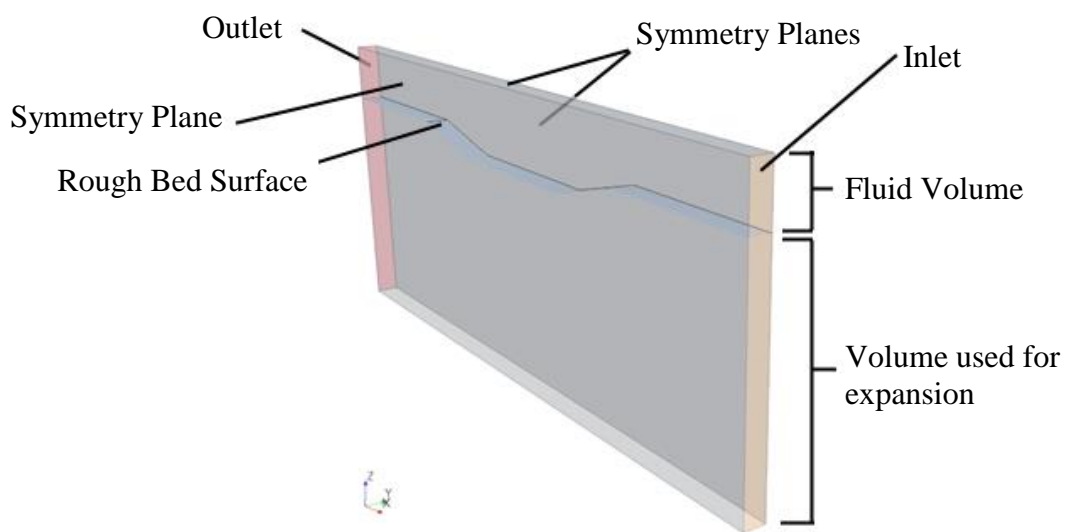


Figure 7-29 – Trench Simulation Domain

A fully developed assumption is made regarding the velocity and sediment concentration at the inlet, applied at position 1. The concentration profiles at points marked 2-5 in Figure 7-28 are shown in Figure 7-30 against experimental results. The concentration profiles stabilised and were extracted after 30 seconds which aligns with the time necessary for the flow to travel from inlet to outlet.

The alignment between simulation and experimental concentration varies with the only common difference being the free-surface effect in profiles 4 and 5. Comparison with the logarithmic scale in Figure 7-30 shows a similar trend however the absolute values especially approaching the bed surface are significantly greater. These results reveal the sensitivity of the volume fraction at which the erosion switches to deposition, that changes the amount of sediment build-up on the bed surface and therefore the sediment gradient above due to the turbulent dispersion. However, due to the sediment concentration at the inlet the concentration profiles (resulting from initial concentration and additional from erosion) were less sensitive than the profiles in the previous case.

Additionally, the time step sensitivity was found to influence the sediment deposition upon the bed surface, whereby if the courant number exceeded one deposition reduced significantly. Therefore, it was ensured that the courant number remained below one for this case and the following two-phase case with morphology.

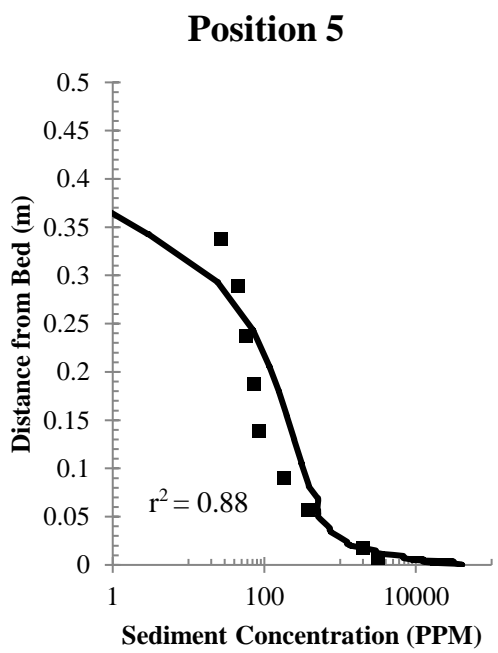
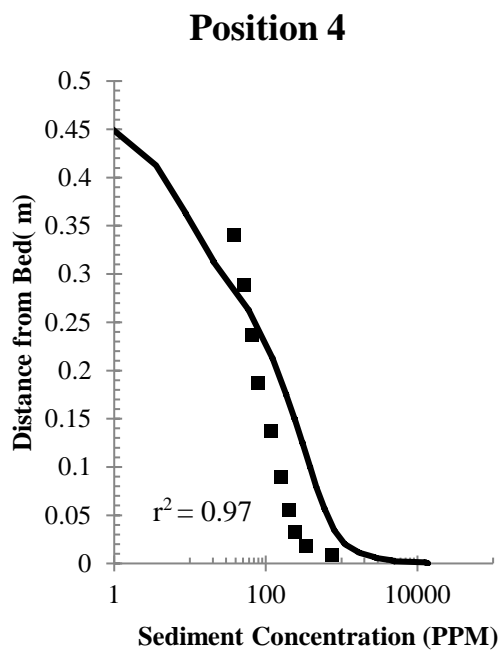
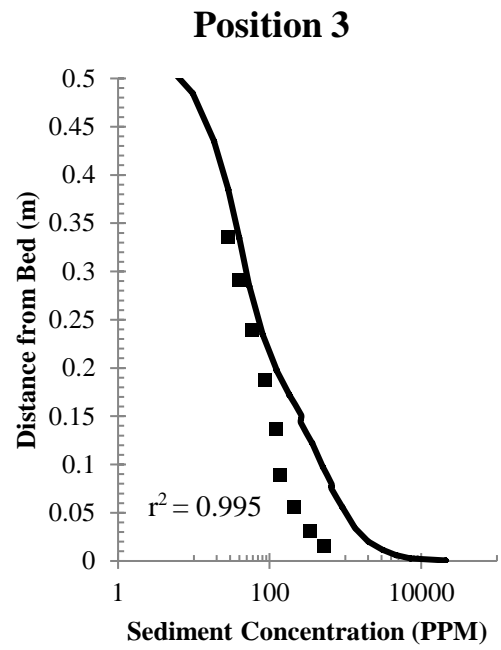
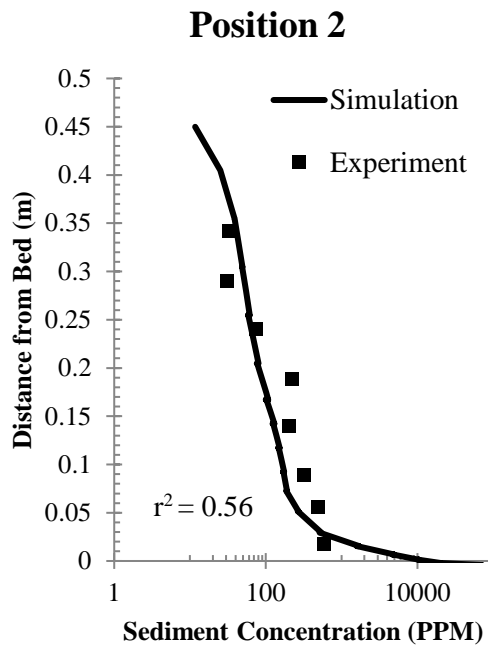


Figure 7-30 – Concentration Profiles along a Trench

Scouring along a Trench – Mass Transfer and Morphology

In continuation of the previous case the same trench is simulated with bed morphology activated and compared against the morphological results in (Delft Hydraulics Laboratory, 1980). The experimental results comprise of bed position for the length of the trench after 7.5 and 15 hours.

The simulation setup uses the same sediment and interphase parameters as the previous case and retains a maximum courant number of one throughout to retain volume fraction accuracy. This however resulted in an extremely long simulation time, especially given the already extended time due to the secondary phase and its interaction; resulting in approximately 2.5x the time necessary for a single phase morphological simulation. Consequently, only 6 hours were simulated as this took 750 hours to run (~32 days), the results are shown in Figure 7-31.

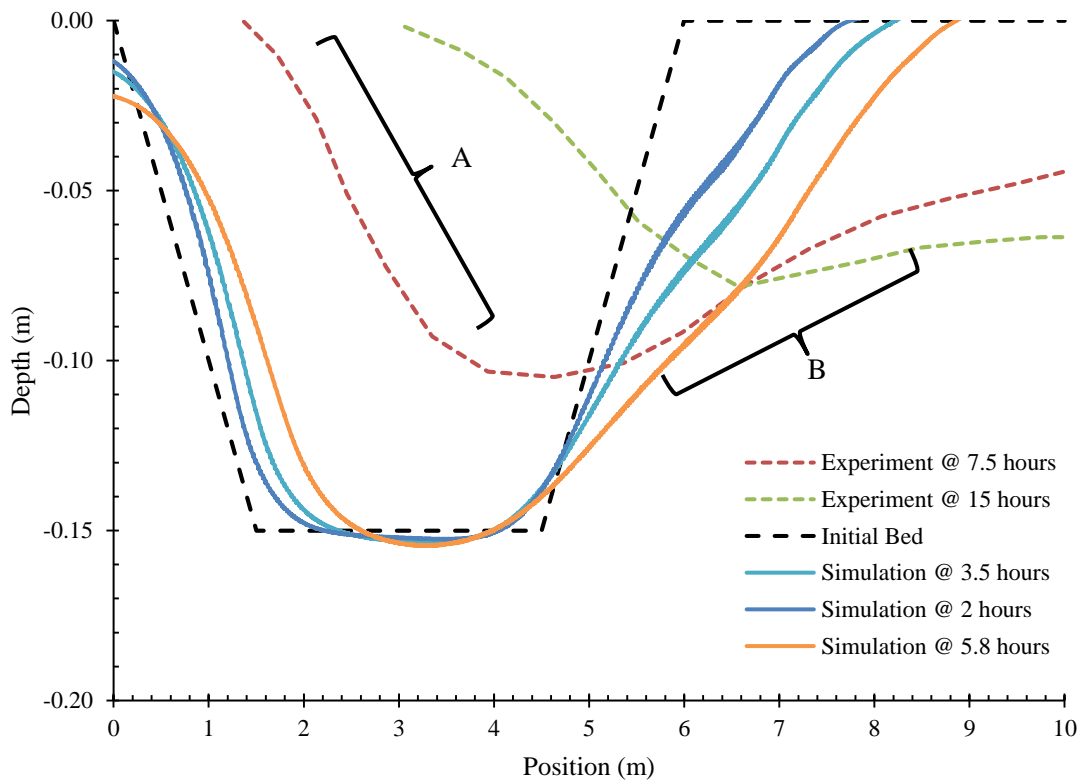


Figure 7-31 – Two-Phase Morphological Results

It is clear the simulation results significantly under predict, which based on the linear progression of section A, which is largely driven by deposition, by a maximum of 80%. The section of bed at 'B' further downstream appears to have undergone more erosion than deposition, but the level that erosion has been under predicted is not quantifiable due to the pivoting between erosion and deposition at $x = 6.5$.

The under-prediction of erosion has been discussed previously in full and the under prediction here is due to the same sources of error. The deposition in combination with morphology is likely to have under predicted due to the sensitivity of the phase interaction model parameters discussed

in the previous case. Additionally, the slow morphological rate per time-step may have also contributed as the maximum bed displacement at 6 hours was -7×10^{-7} m per timestep, which is approaching the numerical accuracy of the software.

On a positive note, the erosion and deposition occur in the correct places and the model was able to run continuously for weeks without numerical error, proving that the fundamentals of the model are correct allowing for further research into the two-phase model. This will likely however require improved computing resources due to the considerable time taken for this case.

Two-Phase Model Summary

The three contained cases have demonstrated the potential, yet sensitive and high computational expense of the two-phase model.

The first case simulated the erosion of sediment along a straight channel after a fixed bed section. This resulted in a high mass flow rate and sediment dispersion, which highlighted the sensitivity of sediment suspension time and distance travelled to the drag and turbulence dispersion parameters.

The second case simulated the sediment flux and dispersion along a trench (with no morphology) to replicate equilibrium sediment distribution profiles at 4 stages. The free-surface error evident in previous simulations created discrepancies at the free surface, but the larger issue was the difference in concentration close to the bed. This was due to the sediment concentration on the bed surface being extremely sensitive to first cell height (adjacent to the bed) and the transition volume whereby sediment is 'transferred' to the bed, and vice versa. Furthermore, the simulation was shown to be sensitive to time step, as it was evident that if the courant number exceeded one sediment flux was drastically reduced, therefore reducing deposition.

The final case adds morphology to the second case, simulating the migration of the trench. The fundamental aspects of the two-phase model resulted in erosion, deposition and therefore migration in the correct areas, however, the rate of migration was significantly slower than the experiment and therefore the final topology did not match.

Chapter 8 Morphological Investigation

8.1 Suction Caissons

The prerequisite suction caisson investigation in Chapter 6 unveiled trends between suction bucket geometry and initial shear stresses, and therefore initial scour topology. The steady state aspect allowed for many design iterations providing direction and reducing the necessary sample of scour simulations within this chapter.

This chapter simulates the scouring around a sample of the previously tested geometries allowing the hypothesised link between initial shear stresses and developing scour topology to be tested. This is followed by an analysis of the scour development which evidences clear relationships between the geometry and the developing scour topology. These relationships provide knowledge that enable scour to be reduced based on specific changes in geometry, to a level that allows reductions to be made at distinct stages of the development process; therefore, satisfying the second and third objective of this thesis; to analyse the scour around these structures and apply the knowledge learnt to explore scour mitigation methods.

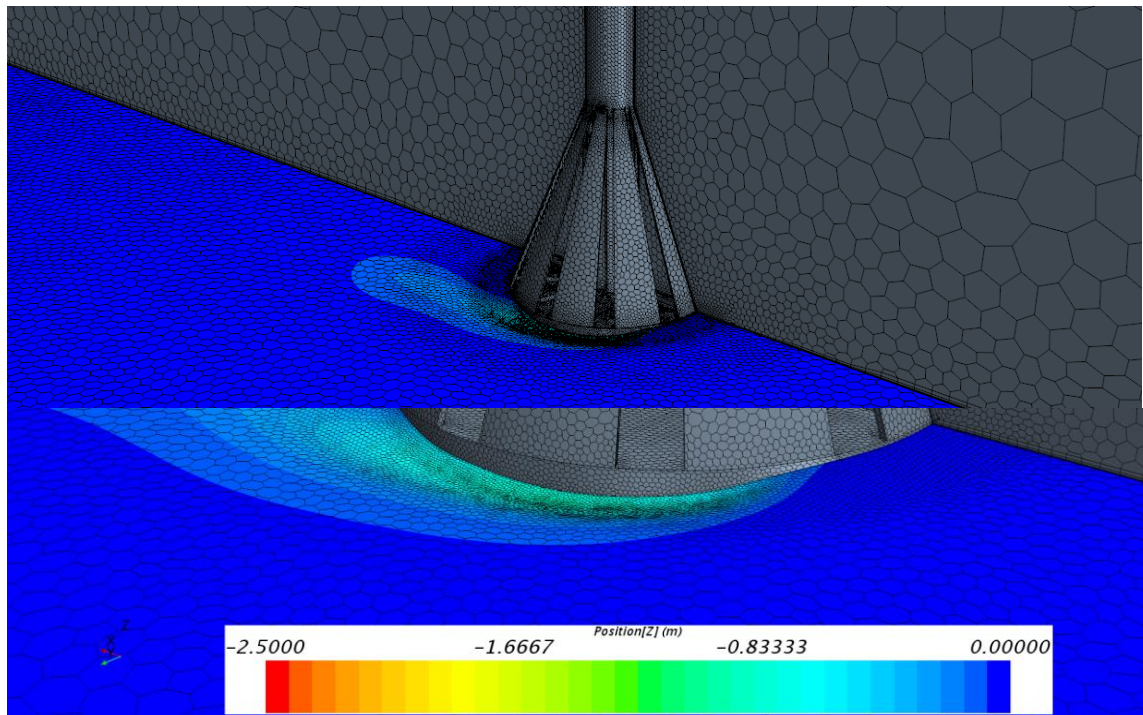


Figure 8-1 – Continued mesh resolution as scour progresses

The previous study (Chapter 6) highlighted that structures with a greater number of struts perform better and therefore this scour investigation simulates the erosion around seven 10-strut designs and a conical mid-section as reference. All designs were ran for a physical simulation time of 17 days allowing time for the scour to reduce in rate. The domain and boundary conditions are the same as those used for the steady state suction caisson simulation in Chapter 6. The mesh

resolution is also carried over from the steady state simulations, and continues at the same resolution as scour progresses, see Figure 8-1.

8.1.1 Results

The steady state shear stress results were compared against the initial scour gradient (rate of maximum scour depth over the first 30 minutes), and final scour depth, gradient and volume removed (after the final 17 days). The results were equated using correlation coefficients as shown in Table 8-1.

r ² values		Scour Results			
		Initial Gradient	Final Depth	Final Gradient	Final Volume
Steady State Results	Local Shear Stress	0.326	0.480	0.442	0.777
	Global Shear Stress	0.805	0.896	0.898	0.830
	Maximum Shear Stress	0.418	0.549	0.895	0.889

Table 8-1 – Correlation between Initial Shear Stresses and Scour Results

The correlations in Table 8-1 all exceed 30% which is expected due to the known link between shear stress and erosion, however, there also exists particularly high correlations greater than 80%. These strong relationships indicate that certain initial shear stress parameters can be used to predict the comparative scour difference between designs. Interestingly, the initial global shear stress correlates the highest to all scour results which aligns with part of the earlier hypothesis linking the global shear stress to scour volume. However, the hypothesised link between maximum shear stress and initial scour gradient is significantly outweighed by the average global shear stress. This misconception and the 90% correlation to global shear stress is attributed to the fact that maximum depth is not the result of a singular high stress point alone, but instead a concentrated area represented by the maximum, local and global shear stress.

The development of maximum scour depth and volume removed in Figure 8-2 and Figure 8-3 unveils additional unexpected relationships. Following the labelling and parameters used in Chapter 6, ‘H’ denotes the size of the hole in each rib as a percentage and ‘P’ denotes the angular width of each end plate. The results show that the ranking of the volume removed remains consistent for the entire process; however, the development of maximum depth is different for each and as a result the rankings change over time.

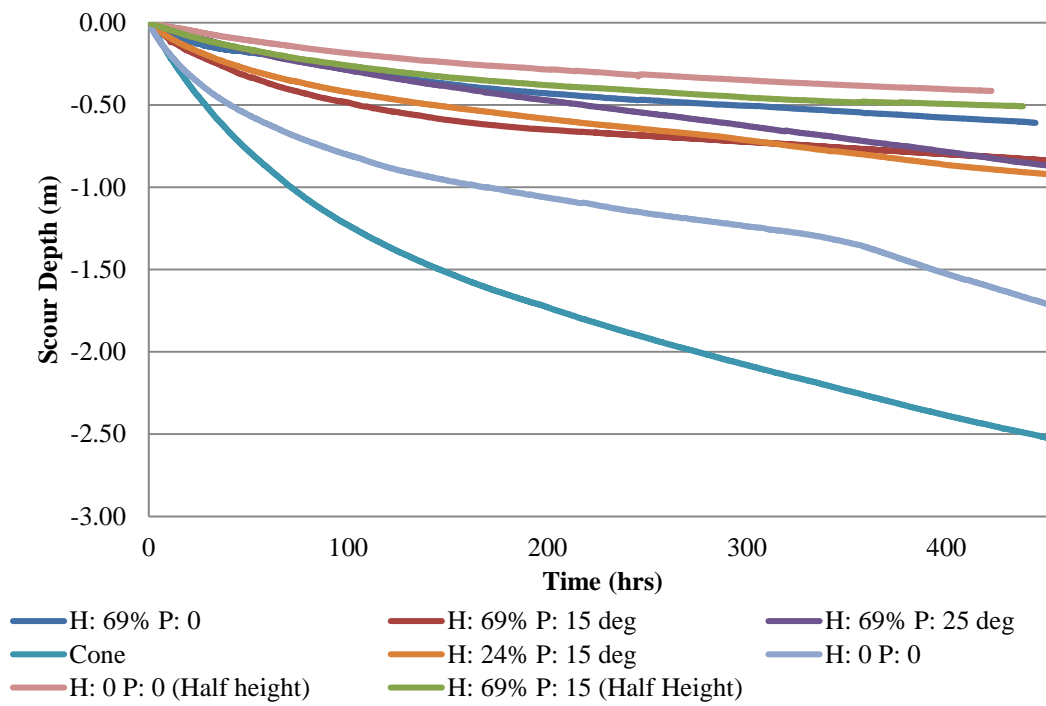


Figure 8-2 – Suction Bucket Scouring – Maximum Depth

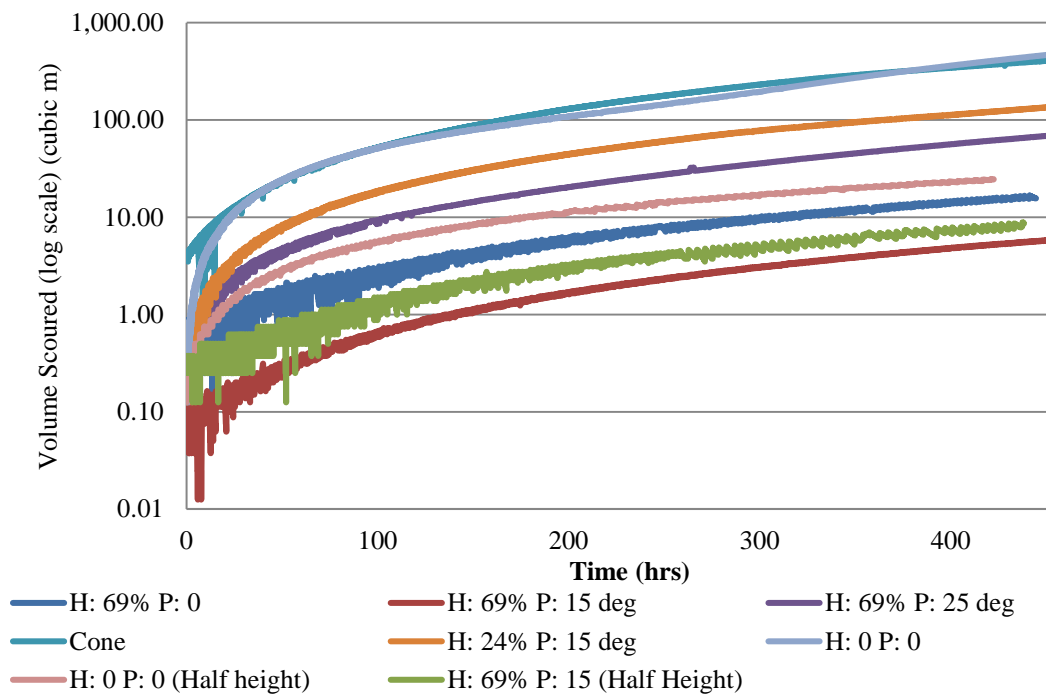


Figure 8-3 - Suction Bucket Scouring – Scour Volume

The development of maximum depth reveals further knowledge as larger end plate widths result in higher scour depth gradients, which differs from the negligible effect the plate size had on the initial shear stress.

The maximum scour depths in Figure 8-2 show how some designs cause the scour rate to decrease faster than others. Designs (H:69% P:0) and (H:69% P:25 deg) show that the increase

in size, or existence of the end plate encourages higher shear stresses for a longer period of time, attributed to the influence plates have on the accelerated flow around the structure.

A comparison of the scour development of designs (H: 69% P: 15 deg) and (H: 24% P: 15 deg) shows that a greater hole size increases the initial scour rate; however, this rate also reduces earlier than the smaller hole size resulting in a shallower final scour depth. This faster initial scour is due to the faster flow (due to decreased blockage) past the end of the rib which causes the shear stress due to the edge to increase. However, as the scour develops, and the bed level drops this effect reduces. Whereas, with the smaller hole size the blockage is greater and therefore the upstream pressure forces more flow around the base. This effect is also evident from scour contour plots, Figure 8-4, that show the scour radius and extension downstream correspond to the structures blockage.

These results demonstrate how the suction bucket mid-section geometry can significantly impact the scour depth and volume removed. In general, it is shown that a greater hole size and reduced plate width reduces scour; which was evident from the shear stress studies. However, the scour results have shown that if the scour duration is known the maximum depth can be reduced further is the link between duration, feature and resultant scour rate is known; e.g. high maximum shear due to the end of a rib has a shorter effect than the accelerated flow due to increased blockage or increased plate width.

This analysis has been completed for one flow condition and a specific geometry size, however demonstrates that the design of these complex geometry structures can be tuned to reduce the scour based on short, medium and long terms, by making specific, small design changes. The effect of this type of geometric change is important for suction caisson design and stands as unique research into scour mitigation methods around suction caissons.

Furthermore, the results prove that predictions based on simplified geometries are not sufficient, for example based on the blockage ratio alone; due to the significant impact of relatively small design features. This fact alone, proves that this relatively simple model is able to unveil potential scour mitigation methods.

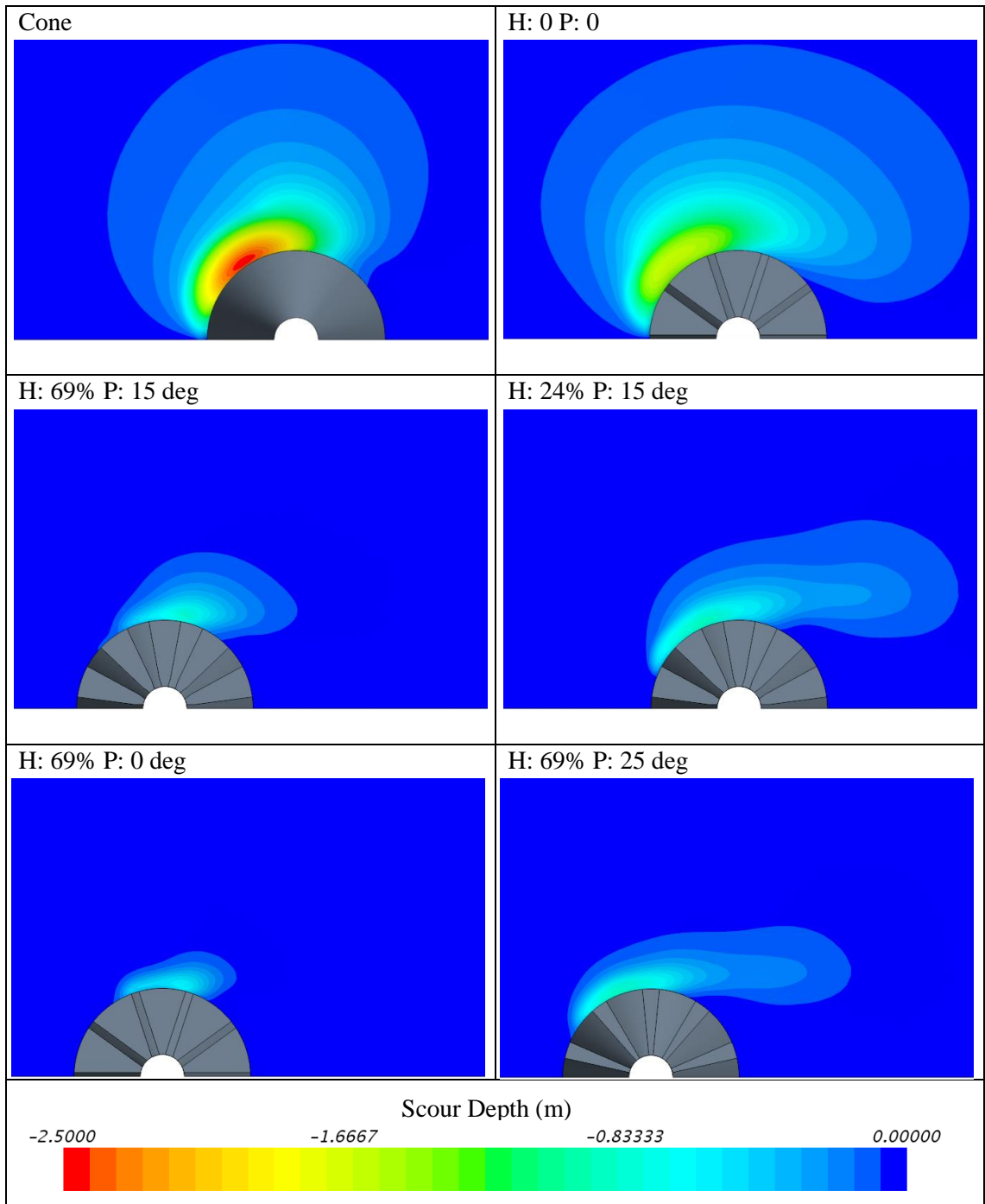


Figure 8-4 – Final Scour Contours

Morphological Investigation Summary

This chapter has utilised the developed morphological model to further the steady-state investigation in Chapter 6. Eight suction caissons of varied mid-section design were chosen based on their initial shear stress results, and the scour over 17 days was simulated around each, whilst recording the changes in maximum scour depth and volume of sediment removed.

The results enabled the hypothesised links between initial shear stress and scour development to be concluded; which showed the strongest link is between the initial average shear stress within a radius of 40m (4 x the radius of the structures base) and the final scour depth, gradient and volume removed. This is in addition to a strong link between the maximum initial shear stress, and the final scour gradient and volume.

The development of the maximum depth and volume also displayed scour transitions, whereby sections of different scouring rates could be identified; furthermore, these were able to be linked back to specific geometric features therefore providing a link between design features and their influence upon the scour process. These influencing factors are crucial to understand the potential scour and therefore mitigation around these structures, as described in more detail in the concluding chapter.

Chapter 9 Conclusion

The awareness of the importance of renewable energy continues to grow globally, matched by increased renewable energy generation (European Environment Agency, 2016) and cleaner methods of energy usage, e.g. electric cars. Therefore, the importance of studies such as this have also increased, as enable an increase in efficiency and a reduction in environmental impact when installing renewable energy devices.

This thesis has enabled the capture of flow and scour around alternate offshore wind turbine foundations, using a simplified scour model that has been developed within commercial CFD software. The specific focus towards suction caissons has unveiled new knowledge on the geometric dependency of the flow and scour development. Furthermore, the relationship between the scour and geometry has uncovered new knowledge on the link between geometry features and their impact of specific stages of scour development. These contributions are more specific than what the original objectives entail however this path was formed by the positive outcomes of the preliminary steady-state suction caisson investigation. From a practical standpoint, this knowledge has enormous potential benefits as unlocks new routes of scour mitigation when designing suction caissons.

This has all been possible due to the development of scour model, implemented in existing CFD software. The approach is different to many existing models due to the use of a single-phase model in a detailed 3D domain, within commercial CFD software. The simplified approach was adopted as the development proved that a single-phase model was sufficient to satisfy the objectives to explore the flow, scour and mitigation methods around alternate offshore wind turbine foundations. There are also many advantages to using a commercial CFD software, especially when exploring new concepts, including pre-implemented and up-to-date features and models, accessibility and usability.

The thesis consists of three main topics, the review of the required geophysical, fluid dynamic and computational elements, the combination of these elements to form the model and the analysis work carried out (both with and without scour, experimental and computational). The prerequisite topics were all discussed from a general stand point prior to focus on the specific and applicable aspects needed to form the scour model.

The geophysical fundamentals are complex and intertwined, and simplifications are necessary to make scour predictions regardless of scale or complexity. The primary simplifications of this study are the phases captured, bed representation and method to predict sediment flux. The most influential of these is the sediment flux prediction, which can range in simplification and accuracy. Due to the outlined objectives and existing literature it was decided to predict the scouring using an excess shear stress bedload formula, which therefore also required a critical

shear stress formula. This method presented several challenges, as the conditions used to formulate these equations and their simplicity makes their accuracy extremely sensitive to both flow and environmental conditions; including the presence and magnitude of waves and currents, the representation of and actual sediment properties, and the resultant sediment concentration gradient. As a result, formulae were initially short-listed and then tested using the developed model. A secondary aspect, in conjunction with the required formulae which impacts the computational model is the representation and prediction of sediment within the fluid domain, i.e. the capture of discrete sediment particles. The literature review took focus to this aspect, looking at the success when different numbers of phases were used, however, it was at this point decided and then later proved during model development that a single-phase would still enable the objectives to be met, and importantly enable scientific contributions. However, the choice of sediment representation and prediction methods often require tuning, which became more apparent when investigating the two-phase model (for heavy concentration flows where the sediment deposition prediction is unavoidable). These tuning parameters are contained in most empirical formulae and also in the computational model, to control factors such as roughness, discrete phase dispersion, drag and slope effects. In respect to single-phase model, which was developed significantly more in this study, the only model tuning that took place was the choice of empirical formulae, of both critical shear stress and bedload transport. All other possible parameters were left as advised by the latest developers or publishers of the respective formulae or algorithm.

The computational aspects are somewhat similar as simplifications are always required due to the complexity of flow, indefinitely when turbulent. Within CFD modelling there are a number of aspects that can be simplified, including the number of phases, turbulence model, discretization and temporal resolution. The choice of turbulence model was given particular attention in this study, especially because although RANS turbulence modelling is not the most accurate it has proven to give accurate results, and has the huge benefit of being stable when used with large timesteps – which is extremely important when trying to capture the mean flow dynamics and simulate days of scour. Furthermore, it was found for the tested cases that RANS was accurate enough to capture the change in scour given modifications to geometry, and therefore was used for all of the scour simulations.

The geophysical formulae were implemented within the CFD software through internally written variables, which enabled the displacement of the bed surface based on shear stresses, bed slope and flow direction (and additionally adjacent sand concentration for the small research into the two-phase model). The movement of the bed surface was enabled using an inbuilt surface deformation algorithm based on the conforming boundary mesh method, which essentially stretches/compresses the domain in the vertical direction when the surface is moves. Due to this fact, and the incurred change in cell quality, increased chance of divergence and decreased

accuracy, an external java macro was written to control the software. This java macro monitored key quality and divergence indicators that when triggered ran a remeshing algorithm, specifically designed for this study.

The development of the model, including verification of its capabilities was carried out in progressive stages. The first two recorded cases were used to test the short-listed empirical formulae, mesh resolution and resultant accuracy of the model to experimental results – specifically the developing topological profile. This was carried out by simulating the scour around a monopile in a channel. In addition, the results enabled identification of model's limitations and areas of error.

The monopile results were accurate and the third case duplicated the unique experiment that captures the flow around and underneath and gravity base foundation; detailed in Chapter 3. Despite the huge increase in geometric complexity, the normalised results were extremely close to experimental, with an r^2 of 0.67 when analysing the scour profile down the centreline.

The final development case included the simulation of 8 suction caissons with different base-protrusion heights. The aim of this case was to match a well-documented trend in scour, as the protrusion height is changed from negative to positive. These results were also successful, and permitted the use of the model to investigate suction caissons further, following a preliminary steady-state suction caisson study.

To provide a brief recap, the preliminary study used 176 steady-state simulations to analyse the resultant change in shear stress and flow given changes in suction caisson mid-section geometry. This allowed an insight into the geometry impact on scour, using the link between initial shear stress and scour rate, providing direction and a reduction in scour simulations. The suction caisson scour simulations are reported and analysed in Chapter 8, concentrating on the transient change in maximum scour depth and volume removed from 8 of the geometries tested earlier in Chapter 6. The results are extremely insightful as enable the identification of different periods of maximum scour-depth rate due to specific, relatively minor changes in geometry. This level of detail between the geometry of suction caissons and scour progression is unique, and supports further study into scenario specific scour results, with bi-directional flow which can be ran using the contained model.

From a practical perspective the large potential impact seen from altering the structure of the mid-section is huge. Based on the contained results the maximum scour depth and volume removed can be reduced by up to 50%. The tested scenario was not based on conditions at a specific location, and was only tested with one simplified flow speed, however, due to the impact the changes had on the fluid dynamics, improvements are possible at a range of flow speeds and conditions, but the magnitude may change. From a wider perspective, this research also raises the

awareness of the potential scour reduction given relatively small changes in design, especially when concerning geometries similar to the contained suction caisson.

9.1 Future Work

The successful development, validation and implementation of the single-phase model provides a foundation for its further use, extended development, or implementation in other CFD software.

Following the points raised in the conclusion the suction caisson analysis can be modified to predict the scour in the intended environment, using more specific suction caisson geometry; i.e. the required base and monopile section diameter and the protrusion height. This type of application would also directly benefit from the mid-section feature related effects uncovered in this study.

Alternatively, the existing model can be applied to a range of geometries, including other offshore wind turbine foundations, bridge and platform foundations, anchors, subsea stations, sea defences and other static structures; with the only exception being those structures that are subjected to scouring underneath, due to the issues met with the gravity base simulation.

Both the single and two-phase models are capable of investigating the scour around a wide variety of single and multiple structures creating a vast array of investigative uses. However, the considerable number of possible uses can be expanded, through further development of the model.

Extended development could include the addition of a free-surface enabling the capture of its influence upon the velocity profile, concentration profile in the two-phase model, the addition of waves and/or the capture of scour around shoreline situated structures. Such developments would extend the possible use of the model significantly, allowing the simulation of shallow waters and waves both inland and offshore. Furthermore, depending on the CFD software used to implement the model, the addition of an air phase would be relatively simple.

Development of the two-phase model, in addition to the free-surface, would be targeted at reduction of its computational expense, enabling feasible development and investigative use of its full-3D potential. The foundations for a 3D model are already evident from the pseudo-2D validation cases, and 3D simulations were trialled but due to the computational expense useful simulation durations could not be obtained.

To summarise, this thesis has delivered a method for developing a scour model within commercial CFD code, therefore enabling the use of pre-existing models and features, and potentially easing its usability and accessibility. The model's capability and potential has been demonstrated concentrating on suction caissons, however, due to its flexibility, the potential future use and discoveries are broad and exciting.

References

- ACHENBACH, E. 1968. Distribution of local pressure and skin friction around a circular cylinder in cross-flow up to $Re=5 \times 10^6$. *J. Fluid Mech*, 34, 625-639.
- ACKERS, P. & WHITE, W. R. 1973. *Sediment Transport: A New Approach and Analysis*, Hydraulics Research Station.
- ALABI, P. D. 2006. *Time Development Of Local Scour At A Bridge Pier Fitted With A Collar*. University of Saskatchewan.
- ALFADHI, I., YANG, S. Q. & SIVAKUMAR, M. 2012. Does the critical Shields stress for sediment transport depend on channel-bed slope? . Engineers Australia.
- ALHAJRAF, S. & RUBINI, P. 2000. *Numerical simulation of drifting sand*. PhD, Cranfield University.
- AMOUDRY, L. 2008. A Review on Coastal Sediment Transport Modelling. Proudman Oceanographic Laboratory.
- AN, H., CHENG, L. & ZHAO, M. 2009. Steady streaming around a circular cylinder in an oscillatory flow. *Ocean Engineering*, 36, 1089-1097.
- ANDERSSON, B. 2012. *Computational fluid dynamics for engineers*, Cambridge; New York, Cambridge University Press.
- ANSYS FLUENT 2014. Fluent Tutorial Guide. Release 15. *Chapter 4: Turbulence | 4.9 Reynolds Stress Model (RSM)*.
- ASPDEN, A., NIKIFORAKIS, N., DALZIEL, S. & BELL, J. 2008. Analysis of Implicit LES Methods.
- AZHARI, A., SAGHRAVANI, S., F. & MOHAMMADNEZHAD, B., A. 2010. 3D Numerical Modelling Of Local Scour Around The Cylindrical Bridge Piers. *XVIII International Conference on Water Resources*.
- BAILARD, J. A. 1981. An energetics total load sediment transport model for a plane sloping beach. *Journal of Geophysical Research: Oceans*, 86, 10938-10954.
- BAKER, C. J. 1979. The laminar horseshoe vortex. *Journal of Fluid Mechanics*, 95, 347-367.
- BANGOLD, R. A. 1966. An Approach to the Sediment Transport Problem From General Physics.
- BEHESHTI, A. A. & ATAIE-ASHTIANI, B. 2008. Analysis of threshold and incipient conditions for sediment movement. *Coastal Engineering*, 55, 423-430.
- BIWAS, R. & STRAWN, R. 1997. Tetrahedral and hexahedral mesh adaptation for CFD problems.
- BIĆANIĆ, N. 2004. Discrete Element Methods. *Encyclopedia of Computational Mechanics*. John Wiley & Sons, Ltd.
- BRENNEN, C. E. 2005. *Fundamentals of Multiphase Flow*, Cambridge, Cambridge University Press.
- BRETHOUR, J. & BURNHAM, J. 2010. Modeling sediment erosion and deposition with the FLOW-3D sedimentation & scour model. *Flow Science Technical Note*.
- BRICKWELL, D. 2012. Risks and Challenges Deep Offshore. BARD Group.
- BUI, T. 2010. Explicit and Implicit Methods In Solving Differential Equations. University of Connecticut.
- BUREAU OF RECLAMATION 2007. WinADV32. 2.028 ed.
- CAMENEN, B., BAYRAM, A. & LARSON, M. 2006. Equivalent Roughness Height for Plane Bed under Steady Flow. *Journal of Hydraulic Engineering*.
- CAMENEN, B. & LARROUDE, P. 2000. Numerical comparison of sediment transport formulae. *Marine Sandwre Dynamics*.
- CAMENEN, B. & LARSON, M. 2005. A general formula for non-cohesive bed load sediment transport. *Estuarine, Coastal and Shelf Science*, 63, 249-260.
- CAMENEN, B. T. & LARROUDÉ, P. 2003. Comparison of sediment transport formulae for the coastal environment. *Coastal Engineering*, 48, 111-132.
- CARBON TRUST. 2014. £6.5m trial of new low cost offshore wind foundation to commence this summer.
- CD ADAPCO 2014. Star-CCM+ 9.06.009.

- CHENG, C., SONG, Z.-Y., WANG, Y.-G. & ZHANG, J.-S. 2013. Parameterized expressions for an improved Rouse equation. *International Journal of Sediment Research*, 28, 523-534.
- CHENG, N.-S. 2007. Power-law index for velocity profiles in open channel flows. *Advances in Water Resources*, 30, 1775-1784.
- CHIEW, Y. M. 1984. *Local Scour at Bridge Piers*. PhD - Civil Engineering, The University of Auckland.
- CHUNG, T. J. 2002. *Computational Fluid Dynamics*, Cambridge University Press.
- CIGNONI, P., CALLIERI, M., CORSINI, M., DELLEPIANE, M., GANOVELLI, F. & RANZUGLIA, G. 2008. MeshLab: an Open-Source Mesh Processing Tool. *Eurographics Italian Chapter Conference*.
- CUI, H. 2011. *Estimation of Velocity Distribution and Suspended Sediment Discharge in Open Channels using Entropy*. Texas A&M University.
- DAS, S., DAS, R. & MAZUMDAR, A. 2013. Circulation characteristics of horseshoe vortex in scour region around circular piers. *Water Science and Engineering*, 6, 59-77.
- DE SONNEVILLE, B., RUDOLPH, D. & RAAIJMAKERS, T. 2010. Scour Reduction by Collars around Offshore Monopiles. *Scour and Erosion*. American Society of Civil Engineers.
- DELFT HYDRAULICS LABORATORY 1980. Computational of Siltation in Dredged Trenches.
- DEY, S. 1999. Sediment threshold. *Applied Mathematical Modelling*, 23, 399-417.
- DEY, S. 2001. Experimental study on incipient motion of sediment particles on generalized sloping fluvial beds. *Int. Journal of Sediment Research*, 16.
- DEY, S. 2003. Threshold of sediment motion on combined transverse and longitudinal sloping beds. *Journal of Hydraulic Research*, 41, 405-415.
- DEY, S. & RAIKAR, R. V. 2007. Characteristics of Horseshoe Vortex in Developing Scour Holes at Piers. *J. Hydraul. Eng.*, 4, 399-413.
- DIAB, R. M. A. E. A. 2011. *Experimental Investigation on Scouring around Piers of different Shape and Alignment in Gravel*, Darmstadt, Deutschland, TU Darmstadt.
- DIXEN, M., SUMER, B. M. & FREDSDØE, J. 2013. Numerical and experimental investigation of flow and scour around a half-buried sphere. *Coastal Engineering*, 73, 84-105.
- DYER, K. R. 1986. Coastal and estuarine sediment dynamics. *Geological Journal*, 22, 169-169.
- EAA 2009. Europe's onshore and offshore wind energy potential.
- EINSTEIN, H. 1948. The bed-load function for sediment transportation in open channel flows. *U.S. Department of Agriculture*.
- EINSTEIN, H. A. 1950. *The Bed-load Function for Sediment Transportation in Open Channel Flows*, U.S. Department of Agriculture.
- EL-GHORAB, E. A. S. 2013. Reduction of scour around bridge piers using a modified method for vortex reduction. *Alexandria Engineering Journal*, 52, 467-478.
- ESCAURIAZA, C. & SOTIROPOULOS, F. 2011. Reynolds Number Effects on the Coherent Dynamics of the Turbulent Horseshoe Vortex System. *Flow, Turbulence and Combustion*, 86, 231-262.
- ETTEMA, R. 1980. *Scour at Bridge Piers*. PhD Thesis, University of Auckland.
- EUROPEAN COMMISSION 2013. Renewable energy progress report.
- EUROPEAN COMMISSION 2015. Renewable energy progress report.
- EUROPEAN ENVIRONMENT AGENCY 2016. Energy in Europe 2016.
- EWEA 2004. WIND POWER TECHNOLOGY; OPERATION, COMMERCIAL DEVELOPMENTS, WIND PROJECTS, GRID DISTRIBUTION.
- EWEA 2011. Pure Power - Wind energy targets for 2020 and 2030.
- EWEA 2013. Deep Water - The next step for offshore wind energy. European Wind Energy Association.
- EWEA 2014. The European offshore wind industry - key trends and statistics 2013. European Wind Energy Association.
- EWEA 2016. Wind in Power, 2015 European Statistics.
- FEDERAL HIGHWAY ADMINISTRATION 2009. Bridge Scour and Stream Instability Countermeasures: Experience, Selection, and Design Guidance-Third Edition.

- FERZIGER, J. H. & PERIC, M. 2002. Computational Methods for Fluid Dynamics.
- FREDOLSEN-ENERGY. 2015. *Fredolsen-Energy - Technology* [Online]. Available: fredolsen-energy.com [Accessed].
- FRIEDMAN, S. P. & ROBINSON, D. A. 2002. Particle shape characterization using angle of repose measurements for predicting the effective permittivity and electrical conductivity of saturated granular media. *Water Resources Research*, 38, 18-1-18-11.
- GARG, V., SETIA, B. & VERMA, D. V. S. 2005. REDUCTION OF SCOUR AROUND A BRIDGE PIER BY MULTIPLE COLLAR PLATES. *ISH Journal of Hydraulic Engineering*, 11, 66-80.
- GAUDIO, R., GRIMALDI, C., TARAROJNORUZ, F. & CALOMINO, F. 2010. COMPARISON OF FORMULAE FOR THE PREDICTION OF SCOUR DEPTH AT PIERS.
- GE POWER AND WATER 2013. World's Most Efficient High Output Wind Turbine
- GHASEMPOUR, F., ANDERSSON, R., KEVLAHAN, N. & ANDERSSON, B. 2011. Multidimensional turbulence spectra - identifying properties of turbulent structures. *European Turbulence Conference*.
- GIRARDEAU-MONTAUT, D. 2013. CloudCompare. 2.6.0 ed.
- GORING, D. & VLADIMIR, I. 2003. Closure to "Depiking Acoustic Doppler Velocimeter Data". *Journal of Hydraulic Engineering*, 129, 487-488.
- GRAF, W. H. & ALTINAKAR, M. S. 1998. *Fluvial Hydraulics*, John Wiley and Sons Ltd.
- GRAF, W. H. & YULISTIYANTO, B. 1998. Experiments on flow around a cylinder; the velocity and vorticity fields. *Journal of Hydraulic Research*, 36, 637-654.
- GRAVITAS. 2014. *GravitasOffshore* [Online]. www.gravitasoffshore.com. [Accessed].
- GRINSTEIN, F., MARGOLIN, L. & RIDER, W. 2007. *Implicit Large Eddy Simulation*, Cambridge University Press.
- GUNEY, M. S., AKSOY, A. O. & BOMBAR, G. 2011. Experimental Study of Local Scour Versus Time Around Circular Bridge Pier. *6th International Advanced Technologies Symposium*.
- GUO, J. 2002. Hunter Rouse and Shields Diagram. *Advanced in Hydraulics and Water Engineering*.
- HAKIMZADEH, H., MEHRZAD, R. & AZARI, N. 2012. Experimental Investigation of the Effects of Slotted Conical Shaped Piers on Scour Process due to Steady Flow *ICSE6*. Paris.
- HARRIS, C. K. & WIBERG, P. L. 1997. Approaches to quantifying long-term continental shelf sediment transport with an example from the Northern California STRESS mid-shelf site. *Continental Shelf Research*, 17, 1389-1418.
- HARRIS, J. M., WHITEHOUSE, R. J. S. & BENSON, T. 2010. The time evolution of scour around offshore structures. *Proceedings of the ICE - Maritime Engineering* [Online], 163. Available: <http://www.icevirtuallibrary.com/content/article/10.1680/maen.2010.163.1.3>.
- HEIDARNEJAD, M., HAFAI BAJESTAN, M. & MASJEDI, A. 2010. The Effect of Slots on Scouring Around Piers in Different Positions of 180-Degrees Bends. *World Applied Sciences Journal* 8.
- HINZE, J. O. 1959. *Turbulence*. McGraw-Hill.
- HIRT, C. W. 1993. Volume-fraction techniques: powerful tools for wind engineering. *Journal of Wind Engineering and Industrial Aerodynamics*, 46, 327-338.
- HOLMÉN, V. 2012. *Methods for Vortex Identification*. Lund University.
- HSU, T.-J., JENKINS, J. T. & LIU, P. L. F. 2004. On two-phase sediment transport: sheet flow of massive particles. *Proceedings of the Royal Society of London. Series A: Mathematical, Physical and Engineering Sciences*, 460, 2223-2250.
- HUANG, R. F., HSU, C. M. & LIN, W. C. 2014. Flow characteristics around juncture of a circular cylinder mounted normal to a flat plate. *Experimental Thermal and Fluid Science*, 55, 187-199.
- HUISMAN, B. J. A., RUDOLPH, D., KANAND, A. & MÖSCHEN, M. 2009. Scour Protection Performance Of An Innovative Composite Rubber Mat At Offshore Wind Turbine Foundations. European Offshore Wind Conference & Exhibition.

- HÖLZER, A. & SOMMERFELD, M. 2008. New simple correlation formula for the drag coefficient of non-spherical particles. *Powder Technology*, 184, 361-365.
- IKEDA, S. 1982. *Lateral bed load transport on side slopes*.
- IZADINIA, E. & HEIDARPOUR, M. 2012. Simultaneous use of cable and collar to prevent local scouring around bridge pier. *International Journal of Sediment Research*, 27, 394-401.
- JAHANGIRZADEH, A., BASSER, H., AKIB, S., KARAMI, H., NAJI, S. & SHAMSHIRBAND, S. 2014. Experimental and Numerical Investigation of the Effect of Different Shapes of Collars on the Reduction of Scour around a Single Bridge Pier. *PLoS ONE*, 9, e98592.
- JONES, W. P. & LAUNDER, B. E. 1972. The prediction of laminarization with a two-equation model of turbulence. *International Journal of Heat and Mass Transfer*, 15, 301-314.
- JULIEN, P., Y. 1988. *Erosion and Sedimentation*, Cambridge University Press.
- JUNG, C.-H., KIM, C.-S. & CHOI, Y.-H. 2008. A dynamic model and numerical study on the liquid balancer used in an automatic washing machine. *Journal of Mechanical Science and Technology*, 22, 1843-1852.
- KANG, J. & YEO, Y. 2012. Shear Stress Variation at Scour Hole of Circular Pier. *Engineering*.
- KARAMI, H., BASSER, H., ARDESHIR, A. & HOSSEINI, S. H. 2012. Verification of numerical study of scour around spur dikes using experimental data. *Water and Environment Journal*.
- KHAN, I. 2014. APPLICATION OF COMMERCIAL CFD TO PREDICT INTAKE AND EXHAUST HIGH FREQUENCY NOISE. The University of Hull.
- KHOSRONEJAD, A., HILL, C., KANG, S. & SOTIROPOULOS, F. 2013. Computational and experimental investigation of scour past laboratory models of stream restoration rock structures. *Advances in Water Resources*, 54, 191-207.
- KHOSRONEJAD, A., KANG, S., BORAZJANI, I. & SOTIROPOULOS, F. 2011. Curvilinear immersed boundary method for simulating coupled flow and bed morphodynamic interactions due to sediment transport phenomena. *Advances in Water Resources*, 34, 829-843.
- KHOSRONEJAD, A., KANG, S. & SOTIROPOULOS, F. 2012. Experimental and computational investigation of local scour around bridge piers. *Advances in Water Resources*, 37, 73-85.
- KHWAIRAKPAM, P., RAY, S., DAS, S., R., D. & MAZUMDAR, A. 2012. Scour Hole Characteristics Around A Vertical Pier Under Clearwater Scour Conditions. *ARPN Journal of Engineering and Applied Sciences*.
- KNIGHTON, D. 1998. *Fluvial Forms & Processes*, Arnold Publishers.
- KOLMOGOROV, A. N. 1991. The Local Structure of Turbulence in Incompressible Viscous Fluid for Very Large Reynolds Numbers. *Proceedings: Mathematical and Physical Sciences*, 434, 9-13.
- KORKISCHKO, I. & MENEGHINI, J. 2011. Volumetric reconstruction of the mean flow around circular cylinders fitted with strakes. *Experiments in Fluids*, 51, 1109-1122.
- LARSEN, B. J. & FRIGAARD, P. 2005. Scour and Scour Protection for Windturbine Foundations: for the London Array. Department of Civil Engineering, Aalborg University.
- LAUNDER, B. E. & SPALDING, D. B. 1974. The numerical computation of turbulent flows. *Computer Methods in Applied Mechanics and Engineering*, 3, 269-289.
- LAUNDER, B. E. & SPAULDING, D. B. 1972. *Mathematical Models of Turbulence*, Academic Press.
- LEICA GEOSYSTEMS 2008. Leica Cyclone. 5.8.1 ed.
- LESSER, G. R., ROELVINK, J. A., VAN KESTER, J. A. T. M. & STELLING, G. S. 2004. Development and validation of a three-dimensional morphological model. *Coastal Engineering*, 51, 883-915.
- LI, Y.-X., QI, W.-G. & GAO, F.-P. 2016. Physical Modelling of Pile-group effect on the Local Scour in Submarine Environments. *Procedia Engineering*, 166, 212-220.
- LIANG, D., CHENG, L. & LI, F. 2005. Numerical modeling of flow and scour below a pipeline in currents: Part II. Scour simulation. *Coastal Engineering*, 52, 43-62.
- LIANG, S., ZHANG, Y. & YANG, J. 2015. An experimental study on pile scour mitigating measures under waves and currents. Science China Technological Sciences.

- LINK, O. 2006. Time Scale of Scour around a Cylindrical Pier in Sand and Gravel. *Third Chinese-German Joint Symposium on Coastal and Ocean Engineering*.
- LINK, O., PFLEGER, F. & ZANKE, U. 2008. Characteristics of developing scour-holes at a sand-embedded cylinder. *International Journal of Sediment Research*, 23, 258-266.
- LINK, O. & ZANKE, U. 2004. On the time-dependent scour-hole volume evolution at a circular pier in uniform coarse sand. *Proc. 2nd International Conference on Scour and Erosion (ICSE)*.
- LIU, X. & GARCIA, M. H. 2006. Numerical Simulation of Local Scour with Free Surface and Automatic Mesh Deformation *World Environmental and Water Resource Congress*.
- LIU, Z. 2001. *Sediment Transport*, Institute for Water, Soil and Environmental Technology. Aalborg University.
- MARGOLIN, L. G. 2005. Modelling Turbulent Flow with Implicit LES. *Joint Russian-American Five Laboratory Conference on Computational Mathematics/Physics*.
- MATUTANO, C., NEGRO, V., LÓPEZ-GUTIÉRREZ, J.-S. & ESTEBAN, M. D. 2013. Scour prediction and scour protections in offshore wind farms. *Renewable Energy*, 57, 358-365.
- MAZUMDER, B. S. & GHOSHAL, K. 2006. Velocity and concentration profiles in uniform sediment-laden flow. *Applied Mathematical Modelling*, 30, 164-176.
- MCCANN THOMSEN, J. 2006. Scour in a marine environment characterized by currents and waves
- MCGOVERN, D., ILIC, S., FOLKARD, D., MCLELLAND, S. & MURPHY, B. 2012. Evolution Of Local Scour Around A Collared Monopile Through Tidal Cycles. *International Conference on Coastal Engineering*.
- MELVILLE, B. 2008. The Physics of Local Scour at Bridge Piers. *Fourth International Conference on Scour and Erosion*.
- MELVILLE, B. & CHIEW, Y. 1999. Time Scale for Local Scour at Bridge Piers. *Journal of Hydraulic Engineering*, 125, 59-65.
- MENTER, F. 1993. Zonal Two Equation k-w Turbulence Models For Aerodynamic Flows. *23rd Fluid Dynamics, Plasmadynamics, and Lasers Conference*. American Institute of Aeronautics and Astronautics.
- MEYER-PETER, E. & MULLER, R. 1948. Formulas for the bed-load transport. *In: Report on the 2nd Meeting International Association Hydraulic Structure Research. Stockholm, Sweden, pp. 39-64.*
- MEYER-PETER, E. & MÜLLER, R. 1948. Formulas for bed load transport. *2nd Meeting , Int. Assoc. for Hydroaul. Environ. Eng. and Res. Madrid.*
- MOCKETT, C. 2009. *A comprehensive study of detached-eddy simulation* Technical University of Berlin.
- MOHAMED, T. A., NOOR, M. J., GHAZALI, A. H. & HUAT, B. K. 2005. Validation of Some Bridge Pier Scour Formulae Using Field and Laboratory Data.
- MORENO, M., MAIA, R. & COUTO, L. 2015. Effects of Relative Column Width and Pile-Cap Elevation on Local Scour Depth around Complex Piers. *Journal of Hydraulic Engineering*, 04015051.
- MUZZAMMIL, M. & GANGADHARIAH, T. 2003. The mean characteristics of horseshoe vortex at a cylindrical pier. *Journal of Hydraulic Research*, 41, 285-297.
- NIELSEN, H. L. 2013 Universal Foundation Suction Bucket. Fred. Olsen United.
- NIJDAM, J., GUO, B., FLETCHER, D. & LANGRISH, T. 2003. Lagrangian And Eulerian Models For Simulating Turbulent Dispersion And Agglomeration Of Droplets Within A Spray. *Applied Mathematical Modelling*.
- NOHANI, E., BAHADORIBRIGANI, B. & HALJISHARAFI, R. 2015. EVALUATION AND COMPARISON OF COLLAR AND COLLAR WITH SLOT METHODS IN REDUCING LOCAL SCOUR OF CYLINDRICAL BRIDGE PIERS.
- NORTEK AS. 2015. *Products, Velocimeters*. [Online]. Available: www.nortek-as.com/en/products/velocimeters/vector [Accessed 2015].
- O'NEIL, S. 2002. Three dimensional mobile bed dynamics for Sediment transport modelling.

- OLSEN, N. R. B. & KJELLESVIG, H. M. 1998. Three-dimensional numerical flow modeling for estimation of maximum local scour depth. *Journal of Hydraulic Research*, 36, 579-590.
- OZTURK, N. A., AKKOCA, A. & SAHIN, B. 2008. Flow details of a circular cylinder mounted on a flat plate. *Journal of Hydraulic Research*, 46, 344-355.
- PAOLA, C. & VOLLER, V. R. 2005. A generalized Exner equation for sediment mass balance. *Journal of Geophysical Research: Earth Surface*, 110, n/a-n/a.
- PARTHENIADES, E. 2009. *Cohesive Sediments in Open Channels: Erosion, Transport and Deposition*.
- PEDER HYLDAL SØRENSEN, S. & BO IBSEN, L. 2013. Assessment of foundation design for offshore monopiles unprotected against scour. *Ocean Engineering*, 63, 17-25.
- PETERS, K. & WERTH, K. 2012. Offshore Wind Energy Foundations - Geotextile Sand-Filled Containers as Effective Scour Protection Systems. *6th International Conference on Scour and Erosion*.
- PINNOJI, P. K., HAIDER, Z. & MAHAJAN, P. 2008. Design of ventilated helmets: computational fluid and impact dynamics studies. *International Journal of Crashworthiness*, 13, 265-278.
- PRENDERGAST, L. J. & GAVIN, K. 2014. A review of bridge scour monitoring techniques. *Journal of Rock Mechanics and Geotechnical Engineering*, 6, 138-149.
- QI, W.-G. & GAO, F.-P. 2014. Physical modeling of local scour development around a large-diameter monopile in combined waves and current. *Coastal Engineering*, 83, 72-81.
- QIAN, G., DONG, Z., LUO, W. & LU, J. 2011. Mean airflow patterns upwind of topographic obstacles and their implications for the formation of echo dunes: A wind tunnel simulation of the effects of windward slope. *Journal of Geophysical Research: Earth Surface*, 116, F04026.
- RAIKAR, R. V. & DEY, S. 2008. Kinematics of horseshoe vortex development in an evolving scour hole at a square cylinder. *Journal of Hydraulic Research*, 46, 247-264.
- RANZUGLIA, G., CALLIERI, M., DELLEPIANE, M., CIGNONI, P. & SCOPIGNO, R. 2012. Efficient and Flexible Sampling with Blue Noise Properties of Triangular Meshes *IEEE Trans. on Visualization and Computer Graphics*.
- RAO, S., K., SUMNER, D., & BALACHANDAR, R., . 2004. A visualization study of fluid-structure interaction between a circular cylinder and a channel bed. *Journal of Visualisation*.
- RASHID, S. M. H. 2010. *Effectiveness of Widely Used Critical Velocity and Bed Shear Stress Equations for Different Types of Sediment Beds*. Master of Science in Civil Engineering, Washington State University.
- RAUDKIVI, A. 1986. Functional Trends of Scour at Bridge Piers. *Journal of Hydraulic Engineering*, 112, 1-13.
- RIBBERINK, J. S. 1998. Bed-load transport for steady flows and unsteady oscillatory flows. *Coastal Engineering*, 34, 59-82.
- RICHARDSON, E. V. & DAVIS, S. R. 2001. *Evaluating Scour at Bridges*. Federal Highway Administration.
- RICHARDSON, J. F. & ZAKI, W. N. 1997. Sedimentation and fluidisation: Part I. *Chemical Engineering Research and Design*, 75, S82-S100.
- RODI, W. 1991. Experience with two-layer models combining the k-epsilon model with a one-equation model near the wall. *29th Aerospace Sciences Meeting*. American Institute of Aeronautics and Astronautics.
- RODI, W. 1997. Comparison of LES and RANS calculations of the flow around bluff bodies. *Journal of Wind Engineering and Industrial Aerodynamics*, 69-71, 55-75.
- ROULUND, A., SUMER, B., M., FREDSOE, J. & MICHELSEN, J. 2005. Numerical and experimental investigation of flow and scour around a circular pile. *Journal of Fluid Mechanics*.
- ROUSE, H. 1936. *Modern Conceptions of the Mechanics of Fluid Turbulence*, American Society of Civil Engineers.

- ROY, C. 2010. Review of Discretization Error Estimators in Scientific Computing. *48th AIAA Aerospace Sciences Meeting Including the New Horizons Forum and Aerospace Exposition*. American Institute of Aeronautics and Astronautics.
- SCHLICHTING, H. 1979. *Boundary-Layer Theory*, New York, McGraw-Hill.
- SHIELDS, A. 1936. Anwendung der Aehnlichkeitsmechanik und der Turbulenzforschung auf die Geschiebebewegung [Application of similarity mechanics and turbulence research on shear flow].
- SINGH, V. 2002. *Two Dimensional Sediment Transport using Parallel Computers*. Louisiana State University.
- SKANSKA. 2014. *Skanska Wind Energy* [Online]. www.skanska.co.uk/services/offshore-wind-energy/. [Accessed].
- SOULSBY, R. 1998. *Dynamics of Marine Sands* HR Wallingford.
- SOULSBY, R. L. & DAMGAARD, J. S. 2005. Bedload sediment transport in coastal waters. *Coastal Engineering*, 52, 673-689.
- STAHLMANN, A. 2013. *Experimental and Numerical Modelling of Scour at Offshore Wind Turbines*. Gottfried Wilhelm Leibniz Universitat Hannover.
- STAHLMANN, A. & SCHLURMANN, T. 2012. Numerical and Experimental Modeling of Scour at Tripod Foundations for Offshore Wind Turbines ICSE6.
- STAR-CCM+ 2012. Star-CCM+ 7.06.009 Help Files.
- STAR-CCM+ 2014. Star-CCM+ 9.06.009 Help Files.
- STIDE, A. H. 1982. *Offshore Tidal Sands*.
- STOKES, G. G. 1851. *On the Effect of the Internal Friction of Fluids on the Motion of Pendulums*, Pitt Press.
- STROUHAL, V. 1878. Ueber eine besondere Art der Tonerregung. *Annalen der Physik*, 241, 216-251.
- SUBSEA WORLD NEWS 2014. RotaBolt Tension Control on German OWFs.
- SUMER, B. & FREDSDØE, J. 2001. Scour around Pile in Combined Waves and Current. *Journal of Hydraulic Engineering*, 127, 403-411.
- SUMER, B. & FREDSDØE, J. 2006. *Hydrodynamics around Cylindrical Structures*, World Scientific.
- SUMER, B., FREDSDØE, J. & CHRISTIANSEN, N. 1992. Scour Around Vertical Pile in Waves. *Journal of Waterway, Port, Coastal, and Ocean Engineering*, 118, 15-31.
- SUMER, B. M. & FREDSDØE, J. 2002. *The Mechanics of Scour in the Marine Environment*, World Scientific.
- SUMER, B. M., FREDSDØE, J., CHRISTIANSEN, N. & HANSEN, S. B. 1994. Bed Shear Stress and Scour around Coastal Structures. *Coastal Engineering Proceedings; No 24 (1994): Proceedings of 24th Conference on Coastal Engineering, Kobe, Japan, 1994*.
- TANG, H. S. & KEEN, T. 2011. Hybrid Model Approaches to Predict Multiscale and Multiphysics Coastal Hydrodynamic and Sediment Transport Processes. InTech.
- TERNAT, F., BOYER, P., ANSELMET, F. & AMIELH, M. 2008. Erosion threshold of saturated natural cohesive sediments: Modeling and experiments. *Water Resources Research*, 44, W11434.
- TSOAR, H. 2001. Types of Aeolian Sand Dunes and Their Formation. *Geomorphological Fluid Mechanics*.
- TU, J., YEOH, G. H. & LIU, C. 2007. *Computational Fluid Dynamics: A Practical Approach*, Elsevier Science.
- TULIMILLI, B., R., MAJUMDAR, P. & KOSTIC, M. 2010. Development of a CFD Simulation for 3-D Flooding Flow and Scouring Around a Bridge Structure. *Latest Trends on Urban Planning and Transportation*.
- TULIMILLI, B. R., LOTTES, S. A., MAJUMDAR, P. & KOSTIC, M. Three-Dimensional Scouring Analysis For Open Channel Pressure Flow Scour Under Flooded Bridge Decks. International Mechanical Engineering Congress & Exposition, 2011.
- U.S. ARMY CORPS OF ENGINEERS 1994. Engineering and Design: Channel Stability Assessment for Flood Control Projects.

- UMEDA, S. 2011. Scour Regime and Scour Depth around a Pile in Waves. *Journal of Coastal Research*.
- UNIVERSITY OF HULL. 2013. *Total Environmental Simulator* [Online]. Available: http://www2.hull.ac.uk/science/gees/research/total_environment_simulator/facilities/flume.aspx [Accessed].
- VAN DER TEMPEL, J., DIEPEVEEN, N. F. B. & CERDA SALZMANN, D. J. 2010. Design of support structures for offshore wind turbines. In: TONG, W. (ed.) *Wind Power Generation and Wind Power Design*.
- VAN RIJN, L., C. 1987. Mathematical Modelling of Morphological Process in the case of Suspended Sediment Transport.
- VAN RIJN, L. C. 1981. The development of concentration profiles in a steady, uniform flow without initial sediment load. *IAHR Workshop on particle motion*. Rapperswil, Switzerland.
- VAN RIJN, L. C. 1984. Sediment Transport, Part II: Suspended Load Transport. *Journal of Hydraulic Engineering*.
- VAN RIJN, L. C. 1991. Sediment Transport in combined currents and waves. Netherlands: Delft Hydraulics.
- VAN RIJN, L. C. 1993. *Principles of Sediment Transport in Rivers, Estuaries and Coastal Seas*, Amsterdam, Netherlands, Aqua Publications.
- VAN RIJN, L. C. 1993 *Principles of Sediment Transport in Rivers, Estuaries and Coastal Seas*, Amsterdam, Netherlands, Aqua Publications.
- VAN RIJN, L. C., ROELVINK, J. A. & TER HORST, W. 2001. Approximation formulae for sand transport by currents and waves and implementation in DELFT-MOR. WL | Delft Hydraulics.
- VAN RIJN, L. C., WALSTRA, D. J. R., VAN ORMONDT, M., BRIÈRE, C. & TALMON, A. M. 2006. The Effects Of Bed Slope And Wave Skewness On Sediment Transport And Morphology. *Sixth International Symposium on Coastal Engineering*.
- VANONI, V., A. 1941. Velocity distribution in open channels. *Civil Engineering*.
- VANONI, V. A. & PARKER, G. 2008. ASCE Manual 54, Sedimentation Engineering.
- VERSTEEG, H. K. & MALALASEKERA, W. 1995. *An Introduction to Computational Fluid Dynamics The Finite Volume Method, 2/e*, Pearson Education.
- VICI VENTUS. 2014. *Concrete Gravity Foundations* [Online]. Available: www.viciventus.no/concrete-gravity-foundations/category132.html [Accessed August 2014].
- VIÉ, W., POURANSARI, H., ZAMANSKY, R. & MANI, A. 2014. Comparison between Lagrangian and Eulerian methods for the simulation of particle-laden flows subject to radiative heating. *Centre for Turbulence Research Annual Research Brief*.
- WARNER, J. C., SHERWOOD, C. R., SIGNELL, R. P., HARRIS, C. K. & ARANGO, H. G. 2008. Development of a three-dimensional, regional, coupled wave, current, and sediment-transport model. *Computers & Geosciences*, 34, 1284-1306.
- WASSERMAN, S. 2016. Choosing the Right Turbulence Model for Your CFD Simulation.
- WEINAN, E. & VANDEN-EIJNDEN, E. 2001. Turbulent Prandtl number effect on passive scalar advection. *Physica D: Nonlinear Phenomena*, 152–153, 636-645.
- WHITEHOUSE, R. 2004. Marine scour at large foundations. *Second International Conference on Scour and Erosion*
- WHITEHOUSE, R., HARRIS, J. & SUTHERLAND, J. 2010. Evaluating Scour at Marine Gravity Structures. *1st European IAHR Congress*.
- WHITEHOUSE, R., SUTHERLAND, J. & O'BRIEN, D. Seabed scour assessment for offshore wind farm. Third International Conference on Scour and Erosion, 2006.
- WU, B., MOLINAS, A. & JULIEN, P. 2004. Bed-Material Load Computations for Nonuniform Sediments. *Journal of Hydraulic Engineering*, 130, 1002-1012.
- WWW.OPENFOAM.COM 2016. Openfoam.

- WÖRNER, M. 2003. *A Compact Introduction to the Numerical Modeling of Multiphase Flows*, Forschungszentrum Karlsruhe.
- YALIN, M. S. 1992. *River mechanics*, Pergamon Press.
- YANG 2006. *Erosion and Sedimentation Manual*, U.S. Department of the Interior Bureau of Reclamation.
- ZAAIJER, M. 2003. Comparison of monopile, tripod, suction bucket and gravity base design for a 6 MW turbine. *OWEMES Conference*.
- ZANKE, U. C. E., HSU, T.-W., ROLAND, A., LINK, O. & DIAB, R. 2011. Equilibrium scour depths around piles in noncohesive sediments under currents and waves. *Coastal Engineering*, 58, 986-991.
- ZHANG, M., FU, Z., LIN, Y. & LI, J. 2012. CFD Study of NOx Emissions in a Model Commercial Aircraft Engine Combustor. *Chinese Journal of Aeronautics*, 25, 854-863.
- ZHANG, Z. & CHEN, Q. 2007. Comparison of the Eulerian and Lagrangian methods for predicting particle transport in enclosed spaces. *Atmospheric Environment*, 41, 5236-5248.
- ZHAO, M., CHENG, L. & ZANG, Z. 2010. Experimental and numerical investigation of local scour around a submerged vertical circular cylinder in steady currents. *Coastal Engineering*, 57, 709-721.
- ZHAO, W. & HUHE, A. 2006. Large-Eddy simulation of three-dimensional turbulent flow around a circular pier*. *Journal of Hydrodynamics, Ser. B*, 18, 765-772.
- ZHAO, Z. & FERNANDO, H. J. S. 2007. Numerical simulation of scour around pipelines using an Euler–Euler coupled two-phase model. *Environmental Fluid Mechanics*, 7, 121-142.
- ZHIYIN, Y. 2015. Large-eddy simulation: Past, present and the future. *Chinese Journal of Aeronautics*, 28, 11-24.